Doctoral Thesis

Optical Properties of 2D Carbon Based Materials

Vipin Kumar

A thesis
submitted in fulfilment of the requirements
for the degree of ***Doctor of Philosophy***

in ***Physics***

Department of Physics
Indian Institute of Technology Guwahati
Guwahati- 781 039, Assam, India

November 2015

भारतीय प्रौद्योगिकी संस्थान गुवाहाटी
Indian Institute of Technology Guwahati

Optical Properties of 2D Carbon Based Materials

A thesis
submitted in fulfilment of the requirements
for the degree of ***Doctor of Philosophy***
in ***Physics***

Department of Physics
Indian Institute of Technology Guwahati
Guwahati- 781 039, Assam, India

Author:
Vipin Kumar

Supervisor:
Prof. Girish S. Setlur

November 2015


भारतीय प्रौद्योगिकी संस्थान गुवाहाटी
Indian Institute of Technology Guwahati

Declaration of Authorship

I, **Vipin Kumar**, declare that the work contained in the thesis titled, "***Optical Properties of 2D Carbon Based Materials***" is my own. I confirm that:

- The work contained in the thesis has been done by me mainly while in candidature for a research degree at *Indian Institute of Technology Guwahati.*
- The work presented in this thesis has not previously been submitted for award of any degree or any other qualification at this institute or any other institution.
- Where I have consulted the published work of others, this is always clearly mentioned.
- Where I have quoted from the work of others, the source is always given. With the exception of such quotations, this thesis is entirely my own work.
- I have acknowledged all main sources of help.
- Where the thesis is based on work done by myself jointly with my colleges, I have clearly mentioned what has been done by others and what I have contributed myself.

Date: ______________________ ***Vipin Kumar***

Certificate

I, **Dr. Girish S. Setlur**, certify that the work contained in the thesis titled, “***Optical Properties of 2D Carbon Based Materials***” has been done by **Mr. Vipin Kumar**. I also certify that:

- The work contained in this thesis has been done mainly by **Mr. Vipin Kumar**, a Ph.D student of the department of Physics, Indian Institute of Technology Guwahati while in candidature for a research degree.
- The work of this thesis has been carried out under my supervision and, in my opinion, fulfilling the requirement for the award of degree of **Doctor of Philosophy** in accordance with the regulations of Indian Institute of Technology Guwahati.
- The work presented in this thesis has not previously been submitted for award of any degree or any other qualification at this institute or any other institution.
- Where he has consulted the published work of others, this is always clearly stated. He has acknowledged all main sources of help.
- Where the thesis is based on work done by himself jointly with his colleges, he has clearly mentioned what has been done by others and what he has contributed himself.

Date: ______________________ ***Prof. Girish S Setlur***

***Dedicated to my parents*......**

Acknowledgments

First I would like to thank my supervisor Prof. Girish S. Setlur under whom I have done my thesis research work. It is a wonderful experience to work under his guidance. Whenever I was in doubt, even for silly mistakes, he explained everything friendly. His beauty of explanation is very unique and excellent. I am highly appreciating his patience, support and way of handling during my Ph.D life. His constant support and encouragement work as a catalyst for my research motivation. He never gave me any kind of pressure for research work, I am extremely thankful to him for this type of attitude towards a research scholar. More than being a supervisor, he is also a wonderful human being from whom we can learn a lot of things about research as well as life. His unbiased attitude, frankness, sincerity and ego-less nature influenced me to a great deal. I am feeling a grate proud to see him as a best supervisor in my Ph.D life.

I am deeply thankful to my doctoral committee members, Dr. A. K. Sarma (chairman), Dr. P. Poulose (internal member) and Dr. A. Saikia (external member, Dept. of Mathematics) for their constant support, valuable comments, suggestions and encouragement during my annual review seminars and presentations. I am thankful to my chairman Dr. A. K. Sarma to give me his valuable time whenever I have approached him with my doubts and queries. His way of explanation is very good.

I am grateful to the former and present Heads of Department of Physics for supplying the full support and facilities at their best. I am thankful to IIT Guwahati for providing me the financial assistantship during my research period. Without financial support it was very difficult to survive. I thank Dr. Uma Dutta for her valuable suggestions. I am thankful to my super senior Dr. (Mrs.) V. Meera who bring this research area in my knowledge. I am also thankful to my senior Dr. Enamullah and juniors Mr. Upendra Kumar and Mr. Joy Prakash Das for their supportive and helping nature. I would like to extend my sincere thank to my all lab-mates and class-mates for the great funny moments of Ph.D life shared with one another. I wish to extend my thank to all my seniors, especially Satendra Kumar, and juniors for providing valuable suggestions from his own personal research experiences.

I am grateful to the technical staff Mr. B. B. Purakayasthya and Mr. Hemanta Medhi for their technical supports whenever I needed. I am also thankful to B. Tech. lab assistances Mr. Lokesh Chakravorty, Mr. Atul C. Deka and Mr. Aditya Kalita for their regular support whenever Department of Physics gave me responsibility of the experiment instructor for the B. Tech. students.

I am extremely indebted to my most favorite teacher and one of the best teachers (at the level of Matriculation), I have ever had in my life, Mr. K. K. Shukla and Mr. C. V. Singh to twisted my life towards science. I would like to extend my sincere thank to my favorite 'Physics' teacher (at the level of twelfth standard), Mr. R. S. Singh, who taught me physics and bring a motivational interest in me to move towards physics. He is one of the best physics teacher. I am extremely thankful to my best favorite teachers, I have found in my life, Mr. Anand Kumar Chakraborty and Dr. Abhijit Chakraborty without whome I would not be able to qualify any of the national level tests to achieve this level of academic record. I can never forget the strength and motivation I received from them during my post graduation which inspired me each and every time.

Non-human contributors in acknowledgement are Google search engine, Mathematica, Latex and Microsoft word processor.

I don't know how would I say thank to my parents, Mrs. Kanti Devi and Mr. Ram Prasad, without whom this Ph.D thesis was not possible. I am thankful for the support and care they have extended from the time of my birth. The depth of each of the words they have said to me whenever and wherever I was in need and the inspiration I got from them is not forgettable. I still remember the times when I was down with low confidence and excess stress during which their constant counseling made me cross all those adverse situations. It is my great luck to see them as my parents. I am extremely thankful to the great God to select them as my parents. My parents made full effort at their best for my education to achieve good academic record. During the writing and submission of this thesis they were a great inspiration for me. I appreciate my parents for their patience during my Ph.D life. I found them around me each and every time when I was in adversities. They have given me a great enthusiasm whenever and wherever I lost my confidence and consciousness. I am also thankful to my wife, Mrs. Reshma Devi, to care me. I have shared every good and sad moments of my Ph.D life with her. She is also motivating me every time to work hard. Occasionally, when I was lazy towards my research work she used to say that you have to pay the impact of your laziness at the end of your Ph.D. I am grateful to my elder sisters whose support was a great relief for me during my whole life.

My final and foremost thank goes to the great God for giving me life to enjoy the good moments which I enjoyed and the bad moments from which I learned so many things.

Abstract

We study novel optical phenomena that emerge from light-matter interaction. The title of the thesis itself suggests that we want to study the optical properties of two dimensional carbon based materials. There are various allotropic forms of carbon found in the universe. Graphene, a newly invented in 2004 by an experimental group of Prof. Geim, is one of them. Graphene is a two dimensional nanostructured material showing fascinating physical properties, similar to conventional semiconductors, near the Dirac points. We want to study the optical properties of graphene and related materials using theoretical techniques. The key point of the present work is the theoretical formulation of free-standing graphene-based systems. This theoretical formulation acts as the background for the subsequent studies done in substrate-graphene systems.

There are several well-known optical phenomena in quantum optics, Rabi oscillation (RO) is one of them. These oscillations were first predicted in two level atomic systems by an American scientist *Isidor Isaac Rabi*. These oscillations are defined as follows: the interaction between the atom and the electromagnetic field leads to a periodic exchange of energy between the electromagnetic field and the two-level system, known as Rabi oscillations. This effect can also be interpreted as a periodic change between absorption and stimulated emission of photons. Graphene, a semi-metal, also known as zero-gap semiconductor, is analogous to the conventional semiconductors in some sense. Therefore, we can anticipate that graphene-based systems may also exhibit the same phenomenon. Mishchenko and Ishikawa among others have studied Rabi oscillations in single flake of graphene using rotating wave approximation (RWA). RWA is valid only near resonance when the frequency of the external driving field is nearly equal to the electron-hole pair excitation frequency. The main focus of this thesis is the anomalous Rabi oscillation that is seen in graphene based system far from conventional resonance. These oscillations have no counterparts either in two-level atoms or conventional semiconductors.

To discuss the phenomenon of ROs far from resonance, a semiclassical approximation is used where the electromagnetic field interacts classically with the quantum nature of the system. This study has been done in case of free-standing monolayer graphene. It is shown that free-standing graphene exhibits a new kind of ROs in off resonance. We call these oscillations as 'anomalous' ROs where the population and polarization oscillate with the frequency of the external field and the amplitude of these oscillations oscillates with even slower frequency which is the anomalous Rabi frequency (ARF). These oscillations are obtained using an approximation which is an alternative to the RWA called the 'asymptotic' RWA (ARWA). The results obtained from this technique are corroborated with a fully numerical solution of the Bloch equations. Bilayer graphene (BLG) and few-layer graphene (FLG) can be made by the stacking of single graphene sheets one on the top of the other. Bilayer graphene and few-layer graphene also exhibit the phenomenon of anomalous Rabi oscillations far from resonance. These oscillations in bilayer graphene are associated with the second harmonic in the external driving frequency whereas in single layer graphene these oscillations are found at the first harmonic in the external driving frequency. These oscillations are unique to graphene-based systems. The origin of these oscillations is the 'pseudo-spin' degree of these systems possess. Pseudo-spin lies in the plane of the graphene sheets and describes the alternation of sublattices in monolayer graphene whereas in bilayer graphene it shows the transposition of layers. Bilayer graphene show multiple conventional harmonic resonances: first conventional harmonic resonance occurs at first harmonic in the external driving frequency whereas second conventional harmonic resonance occurs at the second harmonic due to the frequency doubling effect in the external driving frequency while single layer graphene shows only one conventional harmonic resonance at the single harmonic in the external driving frequency. The experimentally measurable current density in these systems exhibits threshold behaviour in frequency domain. The exponent at threshold is equal to the half-integral multiple of the number of layers. The frequency at threshold is just the anomalous Rabi frequency which is proportional to the square of the intensity of applied field whereas it varies linearly with intensity in case of single layer graphene. The current density in these systems shows different power law decay in time domain.

The above study is done in case of free-standing graphene based systems. The same problem is also discussed in more realistic graphene systems (graphene-substrate systems). These systems change their physical properties very drastically in presence of substrate. This motivates us to study the same phenomenon in supported graphene systems. In presence of substrate, graphene-substrate interaction may takes place which give rise a mass term. This mass term is responsible for the opening of a gap in the electronic spectrum of graphene-based systems. This problem is also studied by simply applying the same method described in case of free-standing graphene-based systems. In presence of substrate-graphene interaction inversion symmetry is broken and system becomes asymmetric. This may be also caused by an on-site energy difference of the carbon atoms between the two sublattices in the graphene sheet. In case of bilayer graphene, there are two types of asymmetries: one is the intra-layer asymmetry and second is the inter-layer asymmetry. The effect of intra-layer asymmetry on anomalous Rabi oscillations in monolayer and bilayer graphene is similar. In presence of intra-layer asymmetry these systems show Rabi-like oscillations even for the applied field strengths less than the asymmetry parameter (gap parameter). We call these oscillations as 'offset' oscillations, and the corresponding frequency may be identified with the asymmetry parameter. The value of offset frequency depends on the type of the substrates used. The effect of inter-layer asymmetry on AROs is dramatic. The ARF goes through a minimum value as a function of applied field. The experimentally measurable current density shows threshold behaviour even for vanishingly small applied fields. This threshold behaviour is solely attributable to the asymmetry parameter. In presence of asymmetry parameter the threshold frequency show a shift towards a larger value equal to the gap parameter. The study so far shows that anomalous Rabi oscillations are described in perfectly AB-stacked bilayer graphene. These systems show isotropic band structure. In bilayer graphene, we can include anisotropy in the band structure with the inclusion of trigonal warping which leads to the deformation of the Fermi surfaces. This AB-stacking of graphene sheets is an ideal situation which is very difficult to find in practical life. There may be a situation where the two layers of bilayer graphene show a small twist relative to each other. This is called the twisted bilayer graphene also known as stacking defect. The phenomenon of anomalous Rabi oscillations is studied in trigonally warped as well as in twisted bilayer graphene. It is shown that all the external effects are prominent only for the weak applied fields in the study of the AROs.

In the preceding studies coherent anomalous Rabi oscillations are described in graphene-based systems because the relaxation term is not taken into account. We are also interested to study the relaxation dynamics of carriers in these systems. The relaxation dynamics may appear in a several ways like- electron-electron interaction, screening effects and electron-phonon interaction etc. Our main focus is the study of relaxation dynamics of carriers in these systems by means of electron-phonon (optical, acoustic and flexural) interaction. This can be done by calculating the dephasing rate which is the imaginary part of the particle's self-energy. We have calculated the self-energy of the system with the help of Dyson-equation. It is found that AROs in presence of electron-phonon interaction are not damped near the Dirac point. The electron-phonon interaction plays an important role in dephasing of AROs only far away from the Dirac point.

Contents

2 Anomalous Rabi oscillations in Suspended Graphene Systems 43

3 Anomalous Rabi oscillations in Supported Graphene Systems 71

4 Band Structure Effects on AROs in Graphene Systems 95

5 Phonon assisted damping of ROs in Graphene Systems 119

List of Figures

Chapter 1

Introduction

In the introduction part, we give a historical introduction to two dimensional carbon based materials, mainly graphene and bilayer graphene. We wish to answer questions such as : How are these two systems different from one another? Why is bilayer graphene more interesting than single layer graphene? What is the band structure of these systems and how does it emerge from the tight binding model? Which peculiar physical properties of these systems can be extracted from their band structure? At the end of the introduction part, we have also given a survey of theoretical and experimental literature related to the work presented in this thesis.

1.1 Historical background

1.1.1 Graphene

Condensed matter physics, as its name suggests, is the study of the physical properties of the most familiar condensed phases of matter-solid and liquid among the other known phases of matter. It is the study of physical properties of various materials by experimental as well as theoretical techniques to understand their physical behaviour.

Solid state physics is the largest branch of condensed matter physics. It is the study of rigid phase of matter or solids. The study of solid state physics gives us an insightful view to know how the large scale properties of solid materials originate from their atomic-scale properties. In this way, the solid-state physics forms a theoretical basis to understand the materials science. The solid phase of matter, solid materials, can be formed by the densely packed atoms. These atoms interact to each other in an intense manner. The interaction among them forms the basis of new physical properties such as the electrical, mechanical (e.g. hardness and elasticity), magnetic, thermal and optical properties of solids. The arrangement of atoms in a material, depending upon the conditions in which it is prepared, may be regular, irregular or geometric pattern. The study of solid state physics, as a general theory, is based on the study of crystalline phase of solid materials because the periodicity of atoms in a crystal. Crystalline materials often have mechanical, electrical, magnetic or optical properties that have broad applications in engineering physics.

There are various known solid materials found in the universe. Carbon is one of them which was recognized as an element of periodic table in 1789 by Antoine Lavoisier [1, 2]. Carbon is a primary material of life. It is an abundant material found in the universe such as in the sun, the earth's crust, stars and so on. The recognition of carbon element gives the birth of a new branch in the subject of chemistry, which is known as 'Organic Chemistry'. Carbon is found in various allotropic forms. The most familiar allotropic forms of carbon are diamond, graphite and amorphous carbon. These allotropic forms of Carbon show different physical properties. For example, diamond is highly a transparent crystal to light and the hardest naturally-occurring known material. It has a very low electrical conductivity (an insulator). On the other hand graphite is opaque to light and soft enough to form a streak on paper. It is a very good conductor of electricity. The significance of carbon element can also be understood with the important discoveries in the field of material science in the last few decades. For example, Fullerene [3], carbon nanotubes [4] and very recently graphene [5]. These systems are also the allotropes of carbon. Among the well known allotropes of carbon diamond is a three dimensional material. Each carbon atom of diamond is sp^3 hybridized, whereas graphite is also a three dimensional material but it is composed of sp^2 hybridized carbon atoms. Carbon nanotubes (cylindrical carbon molecules) are also composed of sp^2 hybridized carbon atoms but it is one dimensional showing transport of carriers in one dimensional space while the fullerenes

---

[1] http://www.matter.org.uk/glossary/detail.asp?dbid=108,
http://www.physics.ox.ac.uk/nanotech/research/nanotubes/index.html

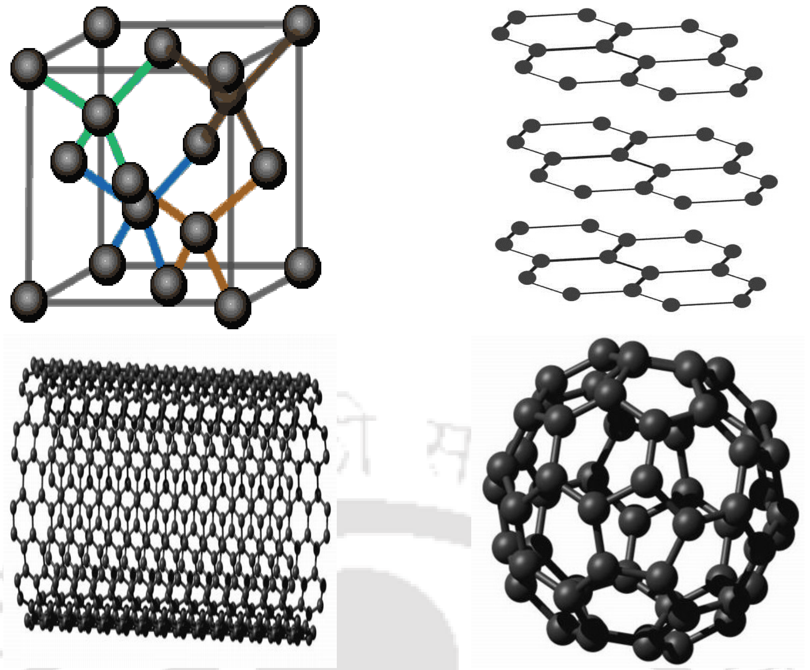

FIGURE 1.1: Allotropes of carbon[1]. Top left: Diamond, Top right: Graphite, Bottom left: Nanotube and Bottom right: Fullerene (C_{60}).

are zero dimensional compact form of carbon atoms. We have listed all the allotropes of carbon are three dimensional while the two dimensional allotrope of carbon is missing. This is because of the well-known theorem in the solid state physics called 'Mermin–Wagner theorem' [6]. This theorem states that it is impossible to find a long range crystalline order in two dimensions because of the large thermodynamic fluctuations. Even though it was a hypothetical object, the two dimensional carbon is a theoretical basis to study the allotropes of carbon in other dimensions. Experimentalists were using various methods to produce a single layer of carbon (two dimensional carbon). Making a two dimensional carbon is not only important because of its significance but also due to its two dimensional nature. Low dimensional materials are special because restricting the dimensions of these materials changes their physical properties drastically. These materials exhibit many exotic properties in comparison to the bulk materials. This may be due to the localization of carriers in low dimensions, geometry effect and absence of inter-layer interactions etc. Experimentalists were producing two dimensional carbon through intercalation compounds. However, this method was successful to some extent but making a two dimensional carbon seems impossible through

---

[2] Photo Courtesy: http://www.independent.co.uk/news/uk/politics/nobel-winner-slates-britains-stupid-immigration-reforms-8433324.html?action=gallery, http://tech.uk.msn.com/news/graphene-research-centre-to-open

FIGURE 1.2: Nobel prize winners of 2010 in physics[2]. Left: Prof. Andre Konstantin Geim. Right: Prof. Konstantin Sergeevich Novoselov.

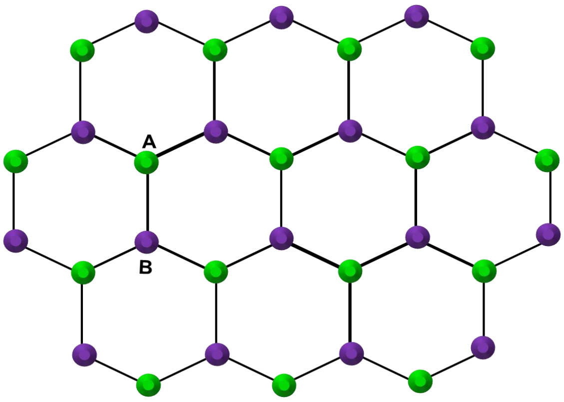

FIGURE 1.3: Schematic of graphene: an atom thick monolayer of carbon atoms.

this process. Experimenters successfully produces few-layer of carbon (few layers of graphite) with the other deposition techniques leaving the production of one atom thick monolayer of carbon atoms. The aspiration of producing a two dimensional one atom thick carbon sheet became possible in 2004 by the two researchers at Manchester University- Novoselov and Geim [5]. They were awarded Nobel prize in 2010 for their novel contribution to the physics. This is the first known two dimensional carbon allotrope named ‘Graphene’. The nomenclature of first 2D carbon allotrope of Carbon comes from graphite and suffix-ene suggested by Hanns-Peter Boehm [7]. The single-layer foil of carbon was first described in 1962 [8]. The structure of bulk graphite was solved [9] by the powder diffraction method [10] in 1916. The structure of graphite was determined from single-crystal diffraction in 1924 by Bernal [11].

The theory of single layer of graphite, known as graphene, was first explored by Wallace in 1947 [12]. The detailed study of single layer of graphite was the starting point of understanding the physical properties of bulk graphite. The Landau levels are responsible for the occurrence of anomalous integer quantum Hall effect [13–15] at the Dirac point in a magnetic field.

1.1.2 Bilayer graphene

Single layer graphene is a basic building block of understanding the other graphitic materials in different dimensions. The graphite structure can be found by the stacking of graphene sheets one on the top of the other. A simplest generalization of graphite is bilayer (graphite with two layers) [16–19]. It is also known as bilayer graphene. Bilayer graphene, as its name suggests, is a graphitic material with two graphene sheets which are arranged in a particular stacking. Single layer graphene is a zero band gap semiconductor, so it is very difficult to use it in a electronic devices whereas bilayer graphene shows a tunable band gap. Bilayer graphene can be made by the stacking of two single graphene sheets one on the top of the other in a Bernal or Rhombohedral stacking. In Bernal stacking, half the atoms in the top layer are directly above to half the atoms in the the bottom layer and vice-versa. This particular arrangement shows very different and interesting physical properties than the single layer graphene. It shows parabolic energy momentum dispersion while single graphene sheet shows a linear energy momentum dispersion. Bilayer graphene is interesting because a tunable gap can open between the

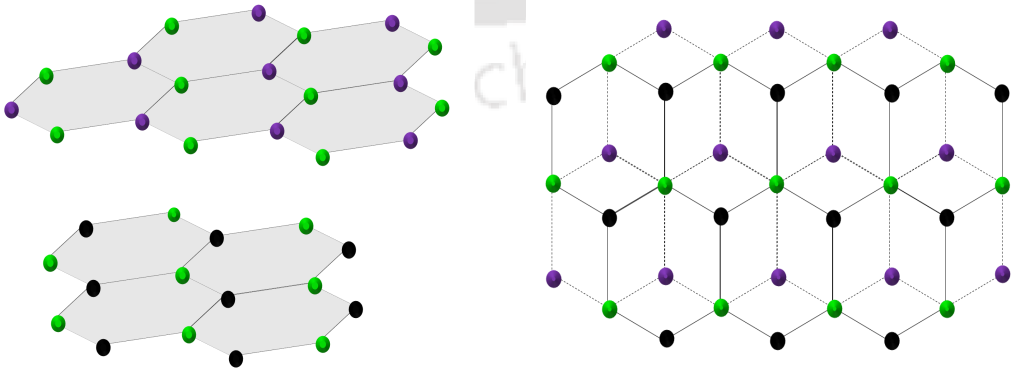

FIGURE 1.4: Schematics of bilayer graphene: Bernal stacking of two single graphene sheets. Left: lateral veiw. Right: top veiw.

conduction and valence band [20], and also the observed IQHE in bilayer graphene shows anomalies from those in single layer graphene [21]. Bilayer graphene can also be found in the twisted configuration, in addition to its Bernal stacked configuration, known as twisted bilayer graphene. In twisted bilayer graphene the two layers show a relative twist or rotation to each other. The physical property, electronic and optical, of these systems are strongly depend on stacking order and orientation. The synthesis of bilayer graphene can be done via chemical vapour deposition technique. This technique is able to produce a large area of bilayer graphene that almost exclusively conform to a Bernal stack geometry [22].

Similar to bilayer graphene, the crystal structure of few layer graphene can be made by the stacking of the graphene sheets one on the top of the other in Bernal or Rhombohedral stacking. The simplest example of few layer graphene is the Bernal stacked trilayer graphene [23, 24]. In trilayer gaphene, one type of atoms in the top most layer are directly above to the second type of atoms in the middle layer which are directly above to the third type of atoms in the bottom most layer. All the three layers are coupled by a weak Van der Waals forces.

1.2 Similarities and differences between single and bilayer graphene

In this section, we outline the similarities and the differences between single and bilayer graphene. Graphene is made of carbon atoms arranged in a honeycomb lattice. It can also be made by the interpenetration of two triangular sublattices. It has two atoms per unit cell, by the repetition of which one can obtain the whole crystal structure. Bilayer graphene is made of two graphene sheets, so it has four atoms per unit cell. Repetition of this unit cell leads to the whole crystal structure of bilayer graphene. These two layers are coupled by a weak Van der Waals forces acting between them. In single layer graphene the charge carriers are massless chiral Dirac fermions that follow the pseudo-relativistic Dirac-Weyl equation whereas the current conduction in bilayer graphene is governed by massive chiral Dirac fermions. However, the speed of massive quasi-particles in bilayer graphene is less than the velocity of the massless quasi-particles in single layer graphene. The massless quasi-particles exhibit linear energy momentum dispersion near the six corners of the hexagonal Brillouin zone. These points are known as the Dirac points. The tip of the valance band and the conduction band touch at these points. Therefore, single layer graphene is a zero-gap semiconductor [5]. In case of Bernal stacked bilayer graphene, the massive chiral quasi-particles possess parabolic energy momentum dispersion near each Dirac points in Brilloin zone in the momentum space. The valance and conduction bands touch at these points. At low energy, bilayer graphene is a zero-gap (between valance band and conduction band) semiconductor but a tunable band gap can be opened by applying a perpendicular electric field [16, 20]. The massless chiral quasi-particles in single layer graphene possess Berry phase of π [5] whereas massive chiral quasi-particles in bilayer graphene show a Berry phase of 2π [16]. The Dirac fermions in both of the graphene systems possess a pseudo-spin degree of freedom similar to the spin-$\frac{1}{2}$ elementary particles. The pseudo-spin in single layer graphene describes the alternation of the sublattices while in case of bilayer graphene the pseudo-spin shows the transposition of the layers [25]. The pseudo-spin lies in the plane of the graphene sheets in both the graphene systems.

1.3 Why is bilayer graphene interesting?

Single layer graphene is a zero-gap semiconductor that makes it difficult to use in electronic applications [5] while bilayer graphene is also a gapless semiconductor but it supports massive Dirac fermions with a tuneable band gap [16, 20]. The bilayer graphene is certainly an exciting material, having its own unique properties just like a single layer graphene, and has its niche electronic applications[3].

The electronic properties of bilayer graphene vary on a nanometre scale. Single layer graphene lacks a band gap. This implies that we cannot use it in electronic devices because it is impossible to turn 'on' and 'off' the electronic devices made from it. Thus the lack of band gap in the band structure of graphene makes it ill-suited for future nano-electronic applications. Bilayer graphene behaves more like a semiconductor when immersed in an electric field perpendicular to the plane of the graphene sheet. The band gap in the electronic spectrum of bilayer graphene can also form due to the variation of electrical potential between sheet's caused by electron-electron interaction among the graphene sheets. The gap may also be opened by the interaction of graphene sheet with

---

[3] http://phys.org/news/2011-08-bilayer-graphene electronics.html.

the non-conducting (insulating) substrate upon which the graphene sheet is deposited. Due to the mutual interaction between the graphene sheet and the substrate, the electrons and holes pools are formed in the both graphene layers. These "pools" are deeper on the bottom layer because it is closer and strongly interacted with substrate. This difference in charge density between the layers not only creates the random pattern of alternating charges [26] but also spatially varying band gap. This property of bilayer graphene gives the signature to use it in the electronic devices that can be turn on and off just like a semiconductor. According to Joseph Stroscio (NIST) if the substrate interaction can be reduced far enough, the exotic quantum properties of bilayer graphene may be used to create a new quantum field effect transistor.

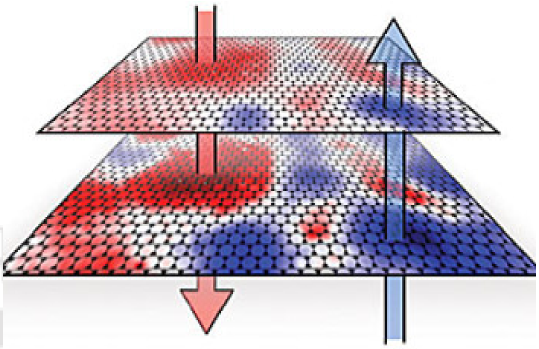

FIGURE 1.5: Electron and hole puddles in graphene bilayer[4].

Jarillo-Herrero (MIT) and Taychatanapat at Harvard [27] found that the band gap is smaller at low temperature (4 K). But this band gap still large enough to switch the electronic devices on and off. The on/off ratio found in bilayer graphene is high enough – of the order of a million – at low temperatures. However, the main problem with bilayer graphene to use as a viable semiconductor in the electronic devices is to operate at room temperature. So it is important to know what is going on at low temperature and understanding the mechanism that does not permit the electronic transport at higher temperature.

Theoretical [16, 20, 28] and experimental [29] studies of bilayer graphene shows that the on-site asymmetry between the layers leads to a gap between the conduction and the valence band. Moreover, unlike single layer graphene, the magnitude of the gap in the spectrum of bilayer graphene can be controlled using experimental techniques through the use of an external gate [30–36]. A band gap of up to $200 - 250\ meV$ can be opened in the electronic spectrum of bilayer graphene by the use of an electric field perpendicular to plane of bilayer graphene, this turns bilayer graphene into a semiconductor [31, 37]. In a recent study of Yu *et al* [38] it is reported that in a large area of bilayer graphene, more generally bilayer

---

[4] http://www.nist.gov/cnst/graphene-042611.cfm

graphene nano ribbon, a large transport gap can be opened. In this study it is also shown that how to improve the on/off ratio with several strategies. Angle-resolved photoemission spectroscopy (ARPES) [39] shows that the charge carriers in AA-stacked bilayer graphene exhibit the mixed behaviour of massive and massless Dirac fermions. The electrons behaviour in bilayer graphene in real time using time- and angle-resolved photoemission spectroscopy (TR-ARPES) is also studied by Hofmann [40], it is found that the behaviour of excited carriers in graphene bilayer is consistent with a single-particle band gap. The motion of electrons in bilayer graphene can be very efficiently understood with TR-ARPES than static ARPES. This confirms the bilayer graphene behaves like a semiconductor that opens a possibility to use it in nanoelectronic applications [41].

1.4 Crystal structure

In this section, the crystal structures of single and bilayer graphene in real and momentum (reciprocal space) space are described and a comparison between these two is presented as well.

1.4.1 Single layer graphene

Graphene is an arrangement of carbon atoms in a honeycomb pattern. Each carbon atom has $four$ valance electrons in its outer orbit three of which, one $2s$ and two 2p electrons ($2p_x$ and $2p_y$), are used to form three sigma (σ) bonds with the neighbouring atoms. These σ bonds lie in the plane of the graphene sheet with the bond angle of 120° between two neighbouring σ bonds. Therefore, each carbon atom in graphene honeycomb lattice is sp^2 hybridized. This gives rise the trigonal structure of hybridized state. The remaining electron in p_z orbital is aligned perpendicular to the plane of the graphene sheet forming the π bond. The electrons in π orbitals are free to move in the plane of the graphene sheet and responsible for the electronic and transport properties of graphene. sp^2 hybridization of carbon atoms in graphene leads to the trigonal structure. Thus graphene sheet can also be thought of as made up of two interpenetrating triangular sublattices named A and B. Therefore each of the carbon atoms in one sublattice of graphene sheet has three nearest neighbours from the second sublattice and six next-nearest neighbour from same sublattice, Fig. 1.6. The position of A and B atoms are not equivalent because it is not possible to connect them with a lattice vector of the form $\vec{R} = n_1\vec{a}_1 + n_2\vec{a}_2$, where n_1 and n_2 are integers. The lattice unit vectors of hexagonal lattice in position space can be written as [42]

$$\vec{a}_1 = \frac{3}{2}\, a_{c-c}\, \hat{x} + \frac{\sqrt{3}}{2}\, a_{c-c}\, \hat{y},\ \vec{a}_2 = \frac{3}{2}\, a_{c-c}\, \hat{x} - \frac{\sqrt{3}}{2}\, a_{c-c}\, \hat{y} \tag{1.1}$$

where $a_{c-c} \approx 1.42 \mathring{A}$ is the carbon-carbon bond length and $|\vec{a}_1| = |\vec{a}_2| = \sqrt{3}a_{c-c}$ is the lattice constant. The three nearest-neighbor vectors in real space are given by

$$\vec{\delta}_1 = \frac{1}{2}\, a_{c-c}\, \hat{x} + \frac{\sqrt{3}}{2}\, a_{c-c}\, \hat{y},\ \vec{\delta}_2 = \frac{1}{2}\, a_{c-c}\, \hat{x} - \frac{\sqrt{3}}{2}\, a_{c-c}\, \hat{y},\ \vec{\delta}_3 = -a_{c-c}\, \hat{x}$$

while the six second-nearest neighbors are located at

$$\vec{\delta}_1' = \pm\vec{a}_1,\ \vec{\delta}_2' = \pm\vec{a}_2,\ \vec{\delta}_3' = \pm(\vec{a}_2 - \vec{a}_1)$$

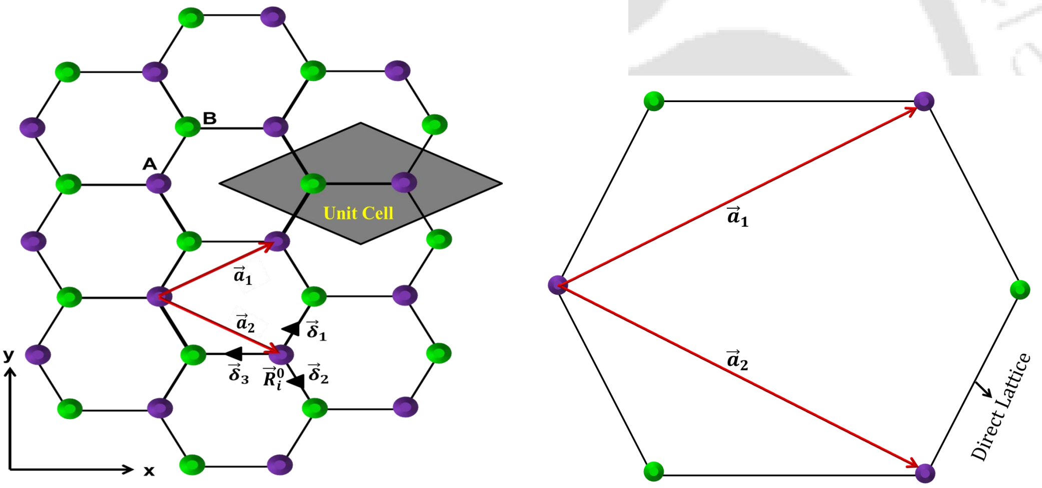

FIGURE 1.6: Left: honeycomb crystal structure of graphene, made out of two interpenetrating sublattices denoted by 'A' and 'B'. Carbon atoms on two sublattices are marked by 'green' and 'purple' color. The lattice unit vectors and nearest-neighbour vectors are denoted by $\vec{a}_1$, $\vec{a}_2$ and $\vec{\delta}_1$, $\vec{\delta}_2$ and $\vec{\delta}_3$, respectively. It has two atoms per unit cell. a_{c-c} is the carbon-carbon bond length. Right: direct lattice of honeycomb lattice.

The reciprocal lattice of direct graphene lattice can be constructed as shown in Fig. 1.7. The reciprocal lattice can also be thought of as the rotation of 90° of direct graphene lattice. The reciprocal-lattice vectors are given by

$$\vec{b}_1 = \frac{2\pi}{3\ a_{c-c}}\, \hat{x} + \frac{2\pi}{\sqrt{3}\ a_{c-c}}\, \hat{y},\ \vec{b}_2 = \frac{2\pi}{3\ a_{c-c}}\, \hat{x} - \frac{2\pi}{\sqrt{3}\ a_{c-c}}\, \hat{y} \tag{1.2}$$

The reciprocal lattice vectors $\vec{b}_1$ and $\vec{b}_2$ can be obtained from the following relation

$$\vec{a}_i \cdot \vec{b}_j = 2\pi \ \delta_{i,j}$$

The first Brillouin zone is the smallest volume in the reciprocal space bounded by the planes bisecting the vectors to the nearest reciprocal lattice points as shown in Fig. 1.7. The three points in the first Brillouin zone Γ, K and $K^{'}$ are of special interest because graphene shows interesting physics near these points. Γ point is located at the center of the first Brillouin zone while K and $K^{'}$ are at the corners of the first Brillouin zone where the valance band and conduction band touches one another. These two points are connected by time-reversal symmetry. The position of these two points in the momentum space is given by

$$\vec{K} = \frac{2\pi}{3\ a_{c-c}}\ \hat{x} + \frac{2\pi}{3\ \sqrt{3}\ a_{c-c}}\ \hat{y},\ \vec{K}^{'} = \frac{2\pi}{3\ a_{c-c}}\ \hat{x} - \frac{2\pi}{3\ \sqrt{3}\ a_{c-c}}\ \hat{y} \qquad (1.3)$$

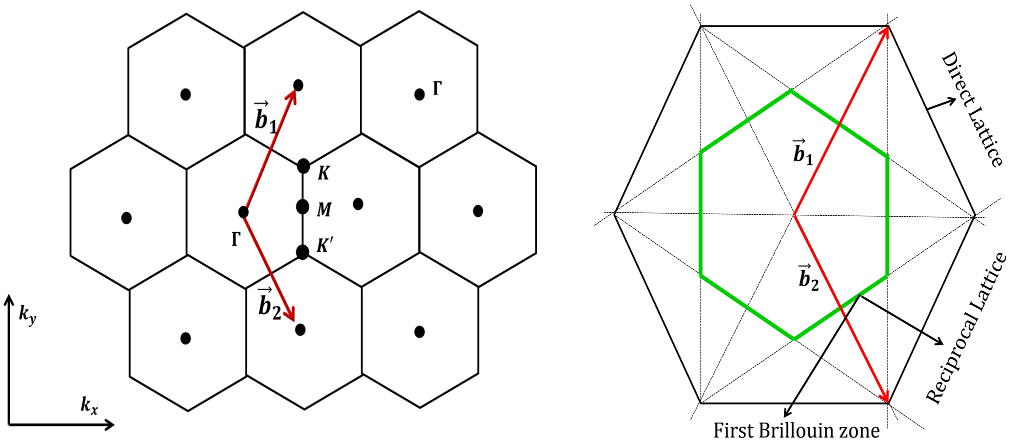

FIGURE 1.7: Left: graphene honeycomb lattice in reciprocal lattice space. $\vec{b}_1$ and $\vec{b}_2$ are the reciprocal lattice vectors. The points K and $K^{'}$ are called the Dirac points and Dirac cones are located at these points. These two points are connected by the time reversal symmetry. Γ point denotes the center of the Brillouin zone. Right: It shows the construction of reciprocal lattice from direct graphene lattice. Green hexagon shows the first Brillouin zone of graphene lattice in reciprocal space.

1.4.2 Bilayer graphene

Monolayer graphene is a building block of other graphitic materials [12]. Graphite structure can be obtained from the stacking of the graphene sheets one on the top of the other. The simplest generalization is bilayer graphene. Bilayer graphene can be thought of as made from two coupled monolayers. These two layers are separated by $3.35A^{\circ}$, the interplanar distance, and coupled by the weak Van der Waals forces. Bilayer graphene can be obtained from the stacking of two monolayers of carbon atoms in a Bernal or Rhombohedral stacking [11]. The crystal lattice structure of bilayer graphene [16–18] is given in Fig. 1.8. These two layers are arranged in a way such that one type of atoms in the lower layer, say $B1$, are directly below to an atom on the top layer, say $A2$. These two atomic sites are referred as 'dimer' sites. The atomic orbitals on dimer sites are strongly coupled by an inter-layer coupling γ_1. The atomic sites which are not directly above or below to one another called 'non-dimer' sites. The dimer sites in bilayer graphene are responsible for the formation of high energy bands [43–45] in the electronic spectrum. All four atomic sites $A1$, $B1$ in bottom layer and $A2$, $B2$ in top layer are inequivalent. Bilayer graphene has four atoms per unit cell. The reciprocal lattice of bilayer graphene is shown in Fig. 1.8 [46]. The reciprocal lattice of bilayer graphene is

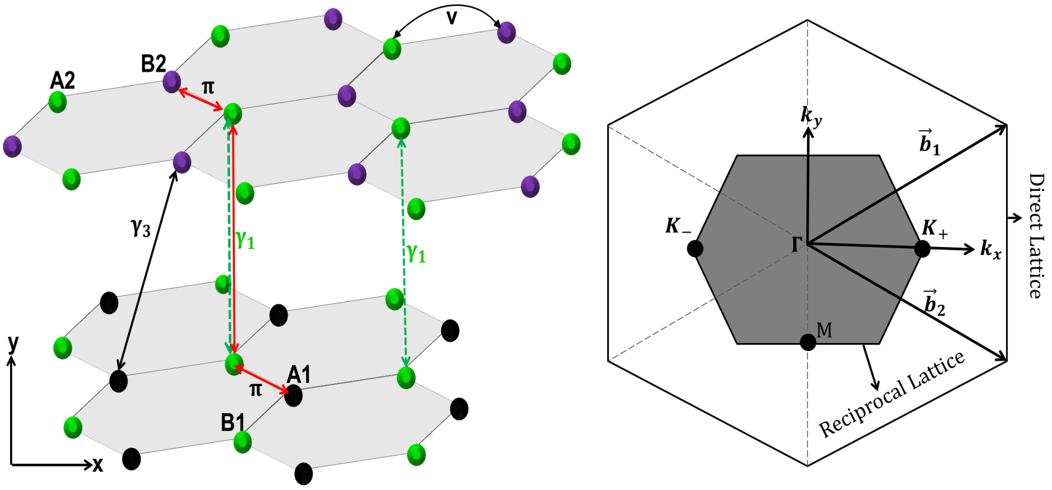

FIGURE 1.8: Left: schematic honeycomb crystal lattice of bilayer graphene, side view, containing four sites in the unit cell: A1 (black circles) and B1 (green circles) in the bottom layer, and A2 (green circles) and B2 (purple circles) in the top layer. Right: Reciprocal lattice of bilayer graphene. It is also a honeycomb lattice similar to single layer graphene. $\vec{b}_1$ and $\vec{b}_2$ are primitive reciprocal lattice vectors. The shaded hexagon is the first Brillouin zone with Γ indicating the center, K_+ and K_- showing two non-equivalent corners.

also a hexagonal lattice similar to single layer graphene. Figure 1.9 shows the

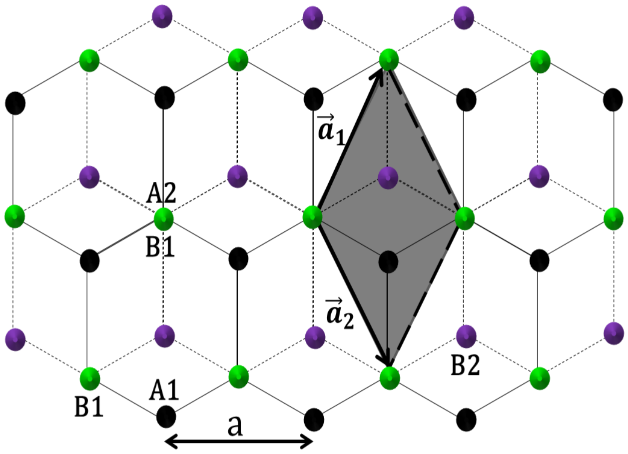

FIGURE 1.9: Schematic of the plane view of the honeycomb crystal lattice of bilayer graphene. $\vec{a}_1$, $\vec{a}_2$ are the primitive lattice vectors. Bottom layer is denoted by solid hexagons while top layer denoted by dashed hexagons. The shaded rhombus indicates the conventional unit cell. a is the lattice constant.

plane view of the graphene bilayer. The bottom and top layers are denoted by solid and dashed hexagons, respectively. The dimer sites, $B1 - A2$, are shown by green circles whereas non-dimer sites, A1 and B2, are shown by black and purple circles, respectively. Shaded region shows the conventional (non-primitive) unit cell and $a = |a_1| = |a_2|$ is the lattice constant, the distance between adjacent unit cells, $a = 2.46\mathring{A}$ [18, 47]. The lattice constant is different from the carbon-carbon bond length $a_{c-c} = a/\sqrt{3} = 1.42\mathring{A}$, which is the distance between adjacent carbon atoms. The primitive lattice vectors $\vec{a}_1$ and $\vec{a}_2$ may be defined as

$$\vec{a}_1 = \frac{a}{2}\,\hat{x} + \frac{\sqrt{3}\,a}{2}\,\hat{y},\ \vec{a}_2 = \frac{a}{2}\,\hat{x} - \frac{\sqrt{3}\,a}{2}\,\hat{y} \tag{1.4}$$

The primitive reciprocal lattice vectors $\vec{b}_1$ and $\vec{b}_2$ can be calculated from the following relation between primitive direct lattice vectors and primitive reciprocal lattice vectors.

$$\vec{a}_i \cdot \vec{b}_j = 2\ \pi\ \delta_{i,j}$$

where $\delta_{i,j} = 0\ for\ i \neq j$ and $\delta_{i,j} = 0\ for\ i = j$. The primitive reciprocal lattice vectors are given by

$$\vec{b}_1 = \frac{2\ \pi}{a}\,\hat{x} + \frac{2\ \pi}{\sqrt{3}\ a}\,\hat{y},\ \vec{b}_2 = \frac{2\ \pi}{a}\,\hat{x} - \frac{2\ \pi}{\sqrt{3}\ a}\,\hat{y} \tag{1.5}$$

As shown in Fig. 1.8, the reciprocal lattice is hexagonal lattice, and the first Brillouin zone is a hexagonal. Two of the six points, one at each corner, in the first Brillouin zone are inequivalent denoted by K_+ and K_-, also denoted by K and $K^{'}$. These two points are connected by time reversal symmetry. The physics of bilayer graphene is important at these points.These two points are called the Dirac points where the valance band and conduction band touch one another. The position vectors of Dirac points, also referred to as valleys, in first Brillouin zone are

$$\vec{K} = \frac{4}{3}\frac{\pi}{a}\hat{x}, \ \vec{K}^{'} = -\frac{4}{3}\frac{\pi}{a}\hat{x}$$

In the following section, we discuss the band structures of single and bilayer graphene. We also show how to apply the tight binding method to calculate the energy momentum dispersion for both graphene systems.

1.5 Electronic Band structure

According to band theory of solids, the electronic band structure is used to calculate the ranges of energy that are allowed for an electron within solids, these allowed ranges of energy are called allowed energy bands, and the ranges of energy which are not allowed for an electron called forbidden energy bands or simply the band gap. These allowed or forbidden electronic bands can be derived with band theory by determining the allowed wave functions for an electron in a large periodic lattice. Band theory is widely used to explain the various physical properties, such as electronic and optical. There are many methods to calculate the electronic band structure of solids [48–50]. The following sections describe how to calculate the band structures of single layer and bilayer graphene.

1.5.1 Band structure of graphene

In this section, we calculate the band structure of an electron in a hexagonal lattice made from the carbon atoms, called graphene. We employ the tight binding approximation well described in the various text books [48, 49]. This approximation is based on linear combination of atomic orbitals. In a periodic crystalline structure each atom has its atomic orbital and corresponding wave function associated with each atomic site. This wave function is not a true wave function because of the overlapping of atomic orbitals with the nearby atomic orbitals. Therefore, the wave function should be the linear combination of these atomic orbitals on each atomic site.

The tight binding approximation was first explored by Wallace in 1947 [12] to calculate the band structure of graphite using a two dimensional model of the graphitic lattice. The tight binding model of graphene was explored by assuming that the nearest and next nearest neighbors interaction for the p_z orbital which is normal to the plane of the graphene sheet. The overlap between p_z orbital wave functions centered at different atoms is also neglected. Lately it was explored by Slonczewski *et al* by taking the second nearest neighbors or more distant neighbors [51]. Semenoff [52] calculated the band structure of graphite using two dimensional hexagonal lattice of more general diatomic system by assuming that sites A and B are occupied by distinct types of atoms. The calculation of band structure of graphene using tight binding approximation is also available in literature [42, 53–58].

Graphene is a two dimensional sheet of carbon atoms arranged in a honeycomb pattern. The band structure of gaphene is calculated for unbonded p_z atomic orbital using tight binding method. The p_z orbital lies normal to the plane of the graphene sheet that can accommodate two electrons with spin projection ±1 [57]. For convenience, only the nearest neighbor hopping is considered as shown in Fig. 1.6. If we denote the orbital on atom i with spin σ by (i, σ) then the nearest neighbor tight binding Hamiltonian of graphene can be written as (we use units such that $\hbar = 1$)

$$\hat{H}_1 = -t \sum_{\langle i,j \rangle,\sigma} \left(\hat{a}^{\dagger}_{i\sigma}\, \hat{b}_{j\sigma} + h.c. \right) \tag{1.6}$$

where the subscript in left hand side stands for number of layers, i (j) are the i^{th} (j^{th}) atomic orbitals on sublattice A and B, $\hat{a}^{\dagger}_{i\sigma}$ $(\hat{b}_{j\sigma})$ creates (annihilates) an electron with spin σ $(\sigma =\uparrow, \downarrow)$ on site $\vec{R}_i$ $(\vec{R}_j)$ on sublattice A and B, $\langle i, j \rangle$ represents the hopping between nearest neighbors only, σ is pseudospin that describes the alternation of sublattices A and B, t $(\simeq 2.8\ eV)$ is the nearest-neighbor hopping energy (hopping between different sublattices). To derive an energy dispersion, we need to transform Eq. (1.6) to momentum space using the usual Fourier transformations, we may write

$$\hat{a}^{\dagger}_{i\sigma} = \frac{1}{\sqrt{N}} \sum_{\vec{k}} e^{-i\vec{k}\cdot\vec{R}^0_i}\, \hat{a}^{\dagger}_{\vec{k},i\sigma}; \qquad \hat{b}_{j\sigma} = \frac{1}{\sqrt{N}} \sum_{\vec{k}'} e^{i\vec{k}'\cdot(\vec{R}^0_i+\vec{\delta}_j)}\, \hat{b}_{\vec{k}',i\sigma} \tag{1.7}$$

where $\vec{R}_i^0$ is the reference point within the unit cell. It is a matter of convention how we choose the pair A and B and the reference point $\vec{R}_i^0$. For convenience let us choose atom A as reference point $\vec{R}_i^0$ (Fig. 1.6) then B type of atoms will be the nearest neighbors of A and separated by nearest neighbor vectors $\vec{\delta}_1$, $\vec{\delta}_2$ and $\vec{\delta}_3$ at an angle 120° with each other. Substituting Eq. (1.7) into Eq.(1.6), we obtain

$$\hat{H}_1 = -t \sum_{j,\sigma} \sum_{\vec{k}} \left(e^{i\vec{k}\cdot\vec{\delta}_j} \; \hat{a}^{\dagger}_{\vec{k},\sigma} \; \hat{b}_{\vec{k},\sigma} + h.c. \right) \tag{1.8}$$

In Eq. (1.8) sum over j denotes the nearest neighbors of A atom and sum over σ breaks the spin degeneracy in each valley. For present discussion, we are suppressing sum over σ and include the spin degeneracy in later results. Then the Hamiltonian Eq. (1.8), in matrix form, can be written as

$$\hat{H}_1 = \sum_{\vec{k}} \begin{pmatrix} \hat{a}^{\dagger}_{\vec{k}} & \hat{b}^{\dagger}_{\vec{k}} \end{pmatrix} \begin{pmatrix} 0 & -t\sum_j e^{i\vec{k}\cdot\vec{\delta}_j} \\ -t\sum_j e^{-i\vec{k}\cdot\vec{\delta}_j} & 0 \end{pmatrix} \begin{pmatrix} \hat{a}_{\vec{k}} \\ \hat{b}_{\vec{k}} \end{pmatrix} \tag{1.9}$$

Therefore, one electron tight binding Hamiltonian of graphene in momentum space can be represented in terms of purely off diagonal 2 × 2 matrix as follows

$$\hat{H}_1 = \begin{pmatrix} 0 & f(\vec{k}) \\ f^*(\vec{k}) & 0 \end{pmatrix}, \qquad f(\vec{k}) = -t \sum_{j=1}^{3} e^{i\vec{k}\cdot\vec{\delta}_j} \tag{1.10}$$

Substituting the values of three nearest neighbor lattice vectors $\vec{\delta}_j$, $j = 1, 2, 3$, we can write the explicit form of $f(\vec{k})$ as given below

$$f(\vec{k}) = -t \left[e^{i\vec{k}\cdot\vec{\delta}_1} + e^{i\vec{k}\cdot\vec{\delta}_2} + e^{i\vec{k}\cdot\vec{\delta}_3} \right]$$

$$f(\vec{k}) = -t \; e^{ik_x a_{c-c}} \left[1 + 2 \; e^{i\frac{3k_x a_{c-c}}{2}} \; Cos\left(\frac{\sqrt{3}k_y a_{c-c}}{2} \right) \right] \tag{1.11}$$

With the help of Eq. (1.11), the eigenvalues of Hamiltonian Eq. (1.10) can be written as

$$E(k) = \pm |f(\vec{k})|$$

$$E(k) = \pm \; t \sqrt{1 + 4Cos\left(\frac{3k_x a_{c-c}}{2}\right) Cos\left(\frac{\sqrt{3}k_y a_{c-c}}{2}\right) + 4Cos^2\left(\frac{\sqrt{3}k_y a_{c-c}}{2}\right)} \tag{1.12}$$

Equation (1.12) gives the energy spectrum of electrons in graphene and pictorially shown in Fig. 1.10. The plus and minus sign indicates the upper π^* band (conduction) and the lower π band (valance band), respectively. It can be seen that the energy eigenvalue depends on momentum. Let us check whether Eq. (1.12) vanishes for some value of momentum, it is equivalent to find the zeros of Eq. (1.12). Equation (1.12) has zeros whenever the following two conditions satisfied

$$\frac{3\ k_x\ a_{c-c}}{2} = 2n\pi \qquad \& \qquad Cos\left(\frac{\sqrt{3}\ k_y\ a_{c-c}}{2}\right) = -\frac{1}{2}$$

$$\frac{3\ k_x\ a_{c-c}}{2} = (2n+1)\pi \qquad \& \qquad Cos\left(\frac{\sqrt{3}\ k_y\ a_{c-c}}{2}\right) = +\frac{1}{2}$$

where n is an integer. First set of choice takes the y- component of wave vector away from the first Brillouin zone (FBZ) while second choice (with n = 0) is satisfied exactly at the corners of FBZ denoted by K and K', these points are called the Dirac points and the position of these points in FBZ is given by Eq. (1.3). The conduction band and valence band touch one another at these points, and are symmetric around $E(k) = 0$. The fermi level lies exactly at these points. It follows that for exactly half filled bands the DOS at the Fermi level is exactly zero. Thus, undoped graphene is a perfect semimetal. We are interested to know the behavior of energy spectrum and eigenfunctions close to $\vec{k} = \vec{K}$, at the Dirac point. Expanding Eq. (1.11) near $\vec{q} = 0$ for small value of wave vector $\vec{q}$ such that $\vec{q} = \vec{k} - \vec{K}$, with $|\vec{q}| \ll |\vec{K}|$ [12, 42, 57], we end up with

$$f_{\vec{K}}(\vec{q}) = 2\ e^{-iK_x a_{c-c}}\ \vec{q}\cdot\nabla_k \left[e^{i\frac{3k_x a_{c-c}}{2}} Cos\left(\frac{\sqrt{3}k_y a_{c-c}}{2}\right)\right]_{\vec{k}=\vec{K}}$$

$$f_{\vec{K}}(\vec{q}) = -\frac{3ta_{c-c}}{2} e^{-iK_x a_{c-c}} (iq_x - q_y) \tag{1.13}$$

Extracting an overall factor, $-ie^{-iK_x a_{c-c}}$, that does not affect the physical results, then we can write Eq. (1.13) as

$$f_{\vec{K}}(\vec{q}) = \hbar v_F (q_x + iq_y) \tag{1.14}$$

where $v_F = \frac{3ta_{c-c}}{2\hbar} = 10^6\ m/sec$. If we expand Eq. (1.11) around K' point, for which $K'_x = K_x$ and $K'_y = -K_y$, we will obtain

$$f_{\vec{K}'}(\vec{q}) = \hbar v_F (q_x - iq_y) = f^*_{\vec{K}}(\vec{q}) \tag{1.15}$$

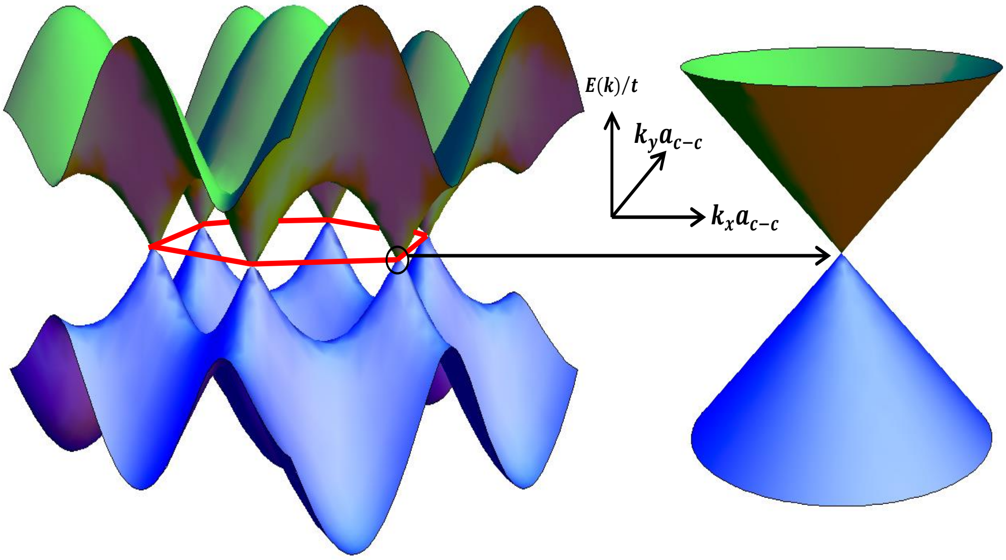

FIGURE 1.10: Schematic of the electronic band structure of graphene honeycomb lattice. Left: three dimensional plot of Eq. (1.12) between dimensionless quantities $E(k)/t$ versus $k_x a_{c-c}$ and $k_y a_{c-c}$. Upper band signifies the π^* band (conduction band) and lower band the π band (valance band). These two bands touch one another at the several points, these points are the corners of the FBZ. These points are called the Dirac points. Right: zoom in of the energy bands close to one of the Dirac point.

Therefore, in the limit of small lattice constant, known as continuum limit, the Hamiltonian of electrons in graphene near $\vec{K}$ point in FBZ can be written as

$$H_{\vec{K}} = \hbar v_F \begin{pmatrix} 0 & q_x + iq_y \\ q_x - iq_y & 0 \end{pmatrix} \equiv \hbar v_F (\hat{\sigma} \cdot \vec{q}) \tag{1.16}$$

where $\hat{\sigma}$ are the usual Pauli matrices. The energy eigenvalues of Hamiltonian Eq. (1.16) are given by

$$\epsilon(q) = \pm\, \hbar v_F |\vec{q}| \tag{1.17}$$

The Hamiltonian Eq. (1.16) is same as that of an ultra-relativistic (massless) spin-$\frac{1}{2}$ particle with the velocity of light replaced by the Fermi velocity v_F, which is equal to $\frac{c}{300}$ where c is the velocity of light. It is clear from Eq. (1.17) that the eigenvalues of Eq. (1.16) are depends only on the magnitude of $\vec{q}$, not on its direction in two dimensional space. The eigenfunctions in the vicinity of $\vec{K}$ point are

$$\psi^{\pm}_{\vec{K}}(q) = \frac{1}{\sqrt{2}} \begin{pmatrix} e^{i\theta_{\vec{q}}/2} \\ \pm e^{-i\theta_{\vec{q}}/2} \end{pmatrix}, \qquad \theta_{\vec{q}} \equiv tan^{-1}\left(q_x/q_y\right) \tag{1.18}$$

As we can see from Eq. (1.18) when $\vec{q}$ rotates once around the Dirac point, the phase of $\psi^{\pm}_{\vec{K}}(q)$ changes by π, which is the characteristic of spin-$\frac{1}{2}$ particles. The more elaborated discussion on band structure of graphene is taken from references [42, 57].

1.5.2 Band structure of bilayer graphene

Bilayer graphene contains two graphene sheets in Bernal stacking. The interplanar distance between two graphene sheets is 3.35 $\mathring{A}$. These two layers are coupled by a weak Van der Waals force acting between them [16]. The tight-binding model of bulk graphite can easily be generalized for the stacking of finite number of graphene layers, for example bilayer graphene, tri-layer graphene and so on.

The tight binding model of bilayer graphene can be constructed in a similar way as for single layer graphene, discussed in an earlier section. In case of bilayer graphene, we have two graphene sheets one on the top of the other in a Bernal stacking. As we now have two layers, we will have four atoms per unit cell and thus expect four energy bands. In bilayer graphene two types of hopping are possible: an intra-layer hopping in both graphene sheets which is similar to single layer graphene and an inter-layer hopping, hopping between atoms in one layer that lies directly above and below in the other layer. This hopping forms the 'dimer' site which is a high energy state. The tight binding Hamiltonian of graphene bilayer can be modeled in a similar way as for single layer graphene. The tight binding Hamiltonian of hopping from $A1 \rightleftarrows B1$ in lower layer can be written as

$$\hat{H}_L = -t \sum_{\langle i,j \rangle} \left(\hat{a}^{\dagger}_{1i}\, \hat{b}_{1j} + h.c. \right) \tag{1.19}$$

Equation (1.19) gives the Hamiltonian of hopping from $A1 \rightleftarrows B1$ in lower layer. $i(j)$ are the $i^{th}(j^{th})$ atomic sites on sublattice $A1$ and $B1$, $\hat{a}^{\dagger}_{1i}(\hat{b}_{1j})$ creates (annihilates) an electron on site $\vec{R}_i(\vec{R}_j)$ on sublattice $A1$ and $B1$, $\langle i,j \rangle$ represents the hopping between nearest neighbors only.

The tight binding Hamiltonian of upper layer, indexed by 2, can be written in a similar way as the tight binding Hamiltonian of lower layer (layer 1), and it is of the form

$$\hat{H}_U = -t \sum_{\langle i,j \rangle} \left(\hat{a}^{\dagger}_{2i} \, \hat{b}_{2j} + h.c. \right) \tag{1.20}$$

All the notations are similar as in Eq. (1.19), except layer index. The tight binding Hamiltonian of inter-layer hopping (hopping between two layers), hopping between $B1 \rightleftarrows A2$ (dimer site), can be written as

$$\hat{H}_{I-L} = -\gamma_1 \sum_{i} \left(\hat{a}^{\dagger}_{2i} \, \hat{b}_{1i} + h.c. \right) \tag{1.21}$$

where γ_1 is the hopping energy for transitions between sites of vertical stacking. Therefore, the total Hamiltonian of bilayer graphene can be obtained by adding Eqs. (1.19), (1.20) and (1.21), and can be written as follows

$$\hat{H}_2 = \hat{H}_L + \hat{H}_U + \hat{H}_{I-L}$$

$$\hat{H}_2 = -t \sum_{\langle i,j \rangle} \left(\hat{a}^{\dagger}_{1i} \, \hat{b}_{1j} + h.c. \right) - t \sum_{\langle i,j \rangle} \left(\hat{a}^{\dagger}_{2i} \, \hat{b}_{2j} + h.c. \right) - \gamma_1 \sum_{i} \left(\hat{a}^{\dagger}_{2i} \, \hat{b}_{1i} + h.c. \right) \tag{1.22}$$

In order to derive the electronic dispersion relation of electrons in bilayer graphene, we need to transform the Hamiltonian Eq. (1.22) to momentum space using usual Fourier transform technique, and this can be done in a similar way as described in sec. 1.5.1. When we define the Fourier transform in the standard way, the last term in Eq. (1.22) picks up no $\vec{k}-$ dependence because both operators $\hat{a}^{\dagger}_{2i}$ and $\hat{b}_{1i}$ operate at the same point in the $x - y$ plane. Then the resulting Hamiltonian of electrons in bilayer graphene in momentum space can be expressed in the form of a 4×4 matrix as follows,

$$H_{2,\vec{k}} = \begin{pmatrix} 0 & 0 & 0 & f(\vec{k}) \\ 0 & 0 & f^*(\vec{k}) & 0 \\ 0 & f(\vec{k}) & 0 & \gamma_1 \\ f^*(\vec{k}) & 0 & \gamma_1 & 0 \end{pmatrix} \tag{1.23}$$

where $f(\vec{k}) = -t \sum_{\delta} e^{i\vec{k}\cdot\delta}$ and t is an in-plane (intra-layer) hopping parameter that has relation with in-plane velocity v as, $v = (\sqrt{3}/2)ta/\hbar$. In subsequent discussion we have taken γ_0 as in-plane hopping parameter instead t. In order to parameterize tight binding couplings relevant to bilayer graphene, we have adopted the notation of the Slonczewski-Weiss-McClure (SWM) model [51, 59, 60] that is often used to describe bulk graphite. As in single layer graphene, $f(\vec{k})$ can be expanded about the $\vec{K}$ in the continuum approximation (for small lattice constant) to get $|f(\vec{q})| = \hbar vq$. Therefore, in the continuum limit, Eq. (1.23) near $\vec{K}$ point in the FBZ can be represented as

$$H_{2,\vec{K}} = \begin{pmatrix} 0 & 0 & 0 & v\pi^\dagger \\ 0 & 0 & v\pi & 0 \\ 0 & v\pi & 0 & \gamma_1 \\ v\pi^\dagger & 0 & \gamma_1 & 0 \end{pmatrix} \tag{1.24}$$

where v is the intra-layer hopping velocity in each layer, $\pi = q_x + iq_y$ and $\pi^\dagger = q_x - iq_y$. The energy eigenvalues of Eq. (1.24) in terms of $f(\vec{q})$ are given by

$$E_\alpha^2 = \frac{\gamma_1^2}{2} + |f(\vec{q})|^2 + (-1)^\alpha \sqrt{\frac{\gamma_1^4}{4} + |f(\vec{q})|^2\gamma_1^2} \tag{1.25}$$

where $|f(\vec{q})| = \hbar vq$, $\alpha = 1$ for low-energy bands and $\alpha = 2$ for high-energy bands that occur from the hopping between the dimer sites. Equation (1.24) is a 4×4 matrix, so it has four eigenvalues given by Eq. (1.25), and denoted by $E_+^{(1)}$, $E_+^{(2)}$, $E_-^{(1)}$ and $E_-^{(2)}$ in the right part of Fig. 1.11. The main low-energy physics of

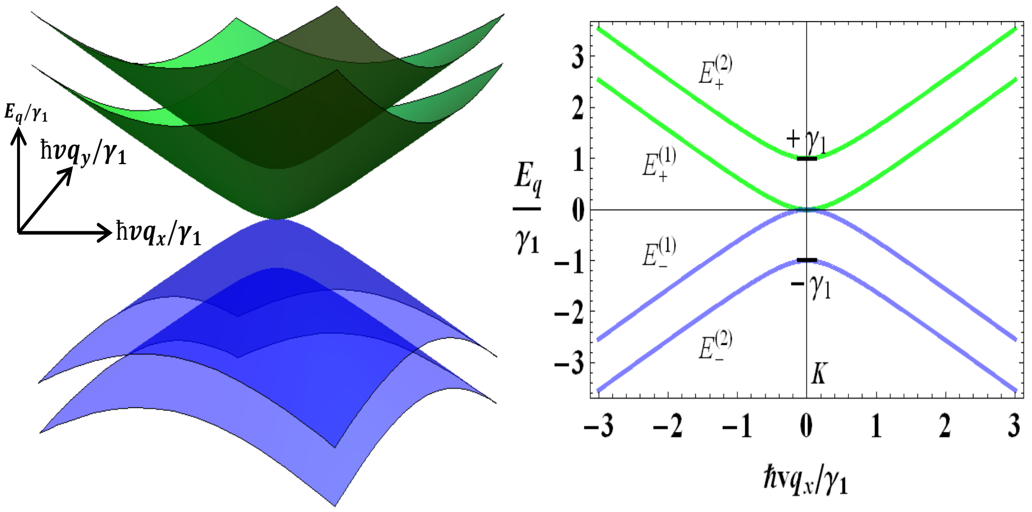

FIGURE 1.11: Bilayer graphene band structure. Left: 3D plot of energy bands in the vicinity of K valley. $\vec{q}$ measured from the center of the valley, where the valance band and conduction band touch one another. Right: 2D plot of energy $E_{\vec{q}}$ versus x-component of wave number $\vec{q}$.

electrons in bilayer graphene occurs near $\vec{K}$ and $\vec{K}'$ points, called Dirac points, in the FBZ. The band structure of bilayer graphene is now quadratic in $\vec{q}$ for low-energies while the band structure is still linear for high-energies, as clearly shown in Fig. 1.11. We now have four bands as predicted; two valance band and two conduction band. Of them, high-energy bands $E_{+}^{(2)}$ and $E_{-}^{(2)}$, occur due to dimer sites, are separated by $\pm\gamma_1$, respectively, from the Dirac point, and the low-energy bands $E_{+}^{(1)}$ and $E_{-}^{(1)}$ touch one another at Dirac point of the BZ.

Bilayer graphene Hamiltonian Eq. (1.24) is derived by assuming two types of hopping, an intra-layer hopping (an in-plane hopping in each layer) parameterized by γ_0 and a direct inter-layer hopping (hopping between dimer sites) between two graphene sheets which is parameterized by γ_1. In whole of the above discussion, we have ignored a weak direct hopping from lower layer to the upper layer (indicated by γ_3), apart from this, an on-site asymmetry in each layer and between the layers have also not been taken into account. In presence of γ_3, the band structure becomes anisotropic (directionally dependent) that gives rise to the trigonal warping of bands. On-site asymmetries have remarkable effect on the electronic spectrum of bilayer graphene. These asymmetries are responsible for opening a gap in the electronic spectrum. It becomes clear from the following discussion.

1.5.2.1 Gap opening in bilayer graphene band structure

Bilayer graphene has four atomic sites per unit cell. These sites may be held at different energies say ϵ_{A1}, ϵ_{B1}, ϵ_{A2} and ϵ_{B2}. Therefore, the Hamiltonian of bilayer graphene including on-site energy difference between four atomic sites can be written as

$$H_{2,\vec{K}} = \begin{pmatrix} \epsilon_{A1} & 0 & 0 & \upsilon\pi^{\dagger} \\ 0 & \epsilon_{B2} & \upsilon\pi & 0 \\ 0 & \upsilon\pi & \epsilon_{A2} & \gamma_1 \\ \upsilon\pi^{\dagger} & 0 & \gamma_1 & \epsilon_{B1} \end{pmatrix} \tag{1.26}$$

Three independent parameters are required to define the energy difference among four atomic sites. These independent parameters are Δ_{AB}, Δ and U describing the on-site energy difference between the sublattice sites A and B on each layer (an intra-layer asymmetry), the energy difference between dimer and non-dimer sites [61–64] and inter-layer asymmetry between the two layers caused by the application of external gates or a doping effect [16–18, 20, 28–32, 65–69], respectively. In terms of energies of four atomic sites these parameters in a unit cell can be represented as follows:

$$\begin{aligned}\Delta_{AB} &= \frac{[(\epsilon_{A1}+\epsilon_{A2})-(\epsilon_{B1}+\epsilon_{B2})]}{2}\\ \Delta &= \frac{[(\epsilon_{A1}+\epsilon_{B2})-(\epsilon_{B1}+\epsilon_{A2})]}{2}\\ U &= \frac{[(\epsilon_{A1}+\epsilon_{B1})-(\epsilon_{A2}+\epsilon_{B2})]}{2}\end{aligned} \tag{1.27}$$

The choice of these three asymmetry parameters Δ_{AB}, Δ and U is not unique. The four-component Hamiltonian Eq. (1.26) give the following energy eigenvalues (taking $U=0$, $\Delta=0$),

$$E_\alpha^2 = \frac{\Delta_{AB}^2}{4} + \frac{\gamma_1^2}{4}\left[\sqrt{1+\frac{4\gamma_0^2|f(\vec{q})|^2}{\gamma_1^2}}+(-1)^\alpha\right]^2 \tag{1.28}$$

where, $\alpha = 1$ *and* 2, accounts for the low-energy bands (degenerate bands) and

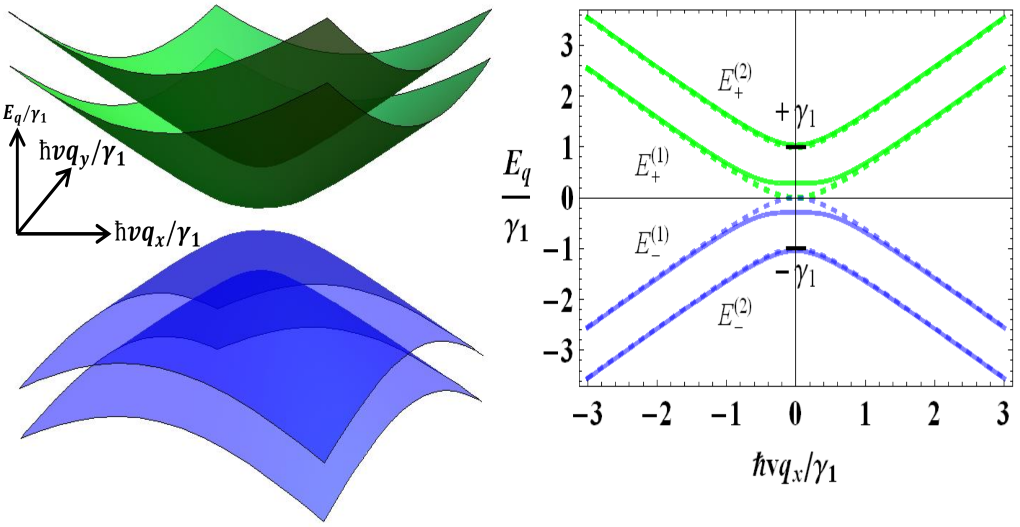

FIGURE 1.12: Bilayer graphene band structure when an intra-layer asymmetry is taken into account. Solid and dashed curves for with and without intra-layer asymmetry, respectively. For clarity, we choose large value of asymmetry, $\Delta_{AB} = 0.2\ eV$. Other parameters are $\gamma_0 = 3.0\ eV$, $\gamma_1 = 0.35\ eV$.

for the split bands (high energy bands), respectively. For small wave vector $\vec{q}$ in the vicinity of a valley, we may approximate $\gamma_0^2|f(\vec{k})|^2 = \hbar^2 v^2 q^2$. Equation (1.28) pictorially shown in Fig. 1.12. It is clear from figure that the role of Δ_{AB} is to open a gap in the electronic spectrum by a trivial shift of the energy. Thereby, lifting the degeneracy at the Dirac point. The lower ($E_+^{(1)}$) and upper ($E_-^{(1)}$) sub-band in the conduction and valance band shifted by an amount $(\pm\Delta_{AB})/2$, respectively. This gives rise a band gap of Δ_{AB} between $E_+^{(1)}$ and $E_-^{(1)}$. The high-energy bands $E_+^{(2)}$ and $E_-^{(2)}$ are almost remains unshifted.

The parameter U describes the inter-layer asymmetry between two layers arising from external gate or a doping effect. In this case, the four component Hamiltonian Eq. (1.26) gives the following energy eigenvalues (taking $\Delta_{AB} = 0$, $\Delta = 0$)

$$E_\alpha^2 = \frac{U^2}{4} + \frac{\gamma_1^2}{2} + \gamma_0^2|f(\vec{k})|^2 + (-1)^\alpha \sqrt{\frac{\gamma_1^4}{4} + \gamma_0^2|f(\vec{k})|^2(\gamma_1^2 + U^2)} \tag{1.29}$$

where all parameters have the same definition as above. The inter-layer asymmetry U is responsible for the appearance of a distinctive 'Mexican hat' structure of the degenerate bands in the electronic spectrum, as shown in Fig. 1.13. The parameter U is tuneable and strongly depends on the external applied gate voltage. The numerical value of U is explicitly calculated in bilayer graphene [20, 28]. Unlike intra-layer asymmetry, here, the high-energy bands show a remarkable shift in energy at Dirac point, and the shift is equal to the asymmetry parameter. The lower and upper sub-bands in the valance and conduction band, $E_-^{(2)}$ and $E_+^{(2)}$, shift towards slight lower and higher value of energy in each band. This shift is equal to $\mp U/2$, respectively. Inter-layer asymmetry is responsible for the 'Mexican hat' like structure in the low-energy bands which is quite different in comparison to intra-layer asymmetry in single and bilayer graphene. The appearance of 'Mexican hat' like structure in the low-energy spectrum gives the true value of the gap, say $\tilde{\Delta}$, between the conduction and valance band occurs at finite value of wave vector, $\vec{q} \neq 0$, away from the Dirac point. The value of gap $\tilde{\Delta}$

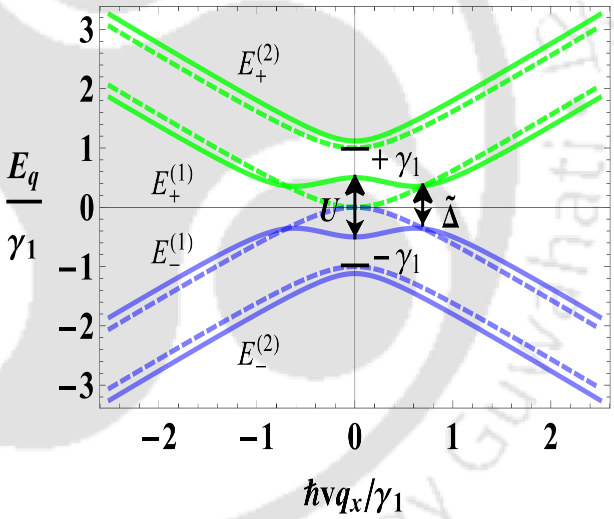

FIGURE 1.13: Bilayer graphene band structure when an inter-layer asymmetry is taken into account. Solid and dashed curves for with and without inter-layer asymmetry, respectively. For clarity, we choose large value of asymmetry, $U = \gamma_1 = 0.35\ eV$ and $\gamma_0 = 3.0\ eV$.

and the corresponding non-zero wave vector q_g is given below [17],

$$\tilde{\Delta} = \frac{|U|\gamma_1}{\sqrt{\gamma_1^2 + U^2}}, \qquad q_g = \frac{|U|}{2v}\sqrt{\frac{2\gamma_1^2 + U^2}{\gamma_1^2 + U^2}} \tag{1.30}$$

For large value of asymmetry $|U| \gg \gamma_1$, the gap saturates at $\tilde{\Delta} \approx \gamma_1$, although for intermediate value of asymmetry $|U| \ll \gamma_1$, it is simply equal to $\tilde{\Delta} \approx |U|$. Theoretical [16] and experimental [29] studies show that the inter-layer asymmetry (asymmetry between the layers) is responsible for the gap $\tilde{\Delta}$ between the otherwise degenerate conduction and valance band. Moreover, unlike monolayer graphene, here, there is an experimental possibility to control the magnitude of induced gap in the spectrum of bilayer graphene through the use of an external gate [5, 13, 15, 21, 30]. A more elaborate discussion of controlling the gap in bilayer graphene is given in the references [17, 28].

A tuneable band gap in the electronic spectrum of bilayer graphene was first observed with angle-resolved photoemission spectroscopy (ARPES) of epitaxial bilayer graphene on silicon carbide [29]. The band gap has now been observed in a number of different experiments including photoemission [29], magneto-transport [31], infrared spectroscopy [34, 35, 37, 62, 70, 71], scanning tunneling spectroscopy [72] and transport [27, 32, 73, 74]. The band structure of bilayer graphene discussed above uses four-component Hamiltonian that includes low as well high energy states. The physics of bilayer graphene at low-energy is more interesting than the physics at high-energy. The low-energy physics of massive chiral Dirac fermions in bilayer graphene is governed by two component Hamiltonian. At low-energy the band structure of bilayer graphene has only single valance band and single conduction band.

1.5.2.2 Trigonal warping of bands in bilayer graphene

Similar to the bulk graphite [63, 75, 76] the trigonal warping also occurs in bilayer graphene. In bilayer graphene the weak direct $A1 - B2$ coupling γ_3 responsible for the trigonal warping which leads to the effective velocity $v_3 \ll v$. At very low energies, the effect of trigonal warping is dramatic. It leads to a Lifshitz transition: the iso-energetic line is broken into four pockets, which can be referred to as one "central" and three "leg" parts [16, 77–80]. This transition takes place when $\epsilon_F \sim \epsilon_L = \gamma_1 v_3^2/(4v)$, where $v_3/v = 0.1$ [16]. The low-energy two-component

Hamiltonian describing effective hopping between the $A1 - B2$ sites, including the effect of weak direct coupling parameter γ_3, can be written as

$$H^{TW}_{2,\vec{K}} = -\frac{1}{2m}\begin{pmatrix} 0 & (\pi^\dagger)^2 \\ \pi^2 & 0 \end{pmatrix} + v_3 \begin{pmatrix} 0 & \pi \\ \pi^\dagger & 0 \end{pmatrix} \tag{1.31}$$

This effective Hamiltonian Eq. (1.31) is applicable within the energy range $|E| < \frac{\gamma_1}{4}$ and yields the following energy eigenvalue

$$E_1^2 = v_3^2 q^2 - \frac{2v^2 v_3 q^2}{\gamma_1} Cos3\phi + \left(\frac{v^2 q^2}{\gamma_1}\right)^2 \tag{1.32}$$

where $\phi = tan^{-1}\left(\frac{q_y}{q_x}\right)$. In presence of parameter γ_3 the band structure of bilayer graphene becomes anisotropic, it is directionally dependent. The energy eigenvalue Eq. (1.32) is pictorially shown in Fig. 1.14. It is clear from figure that the

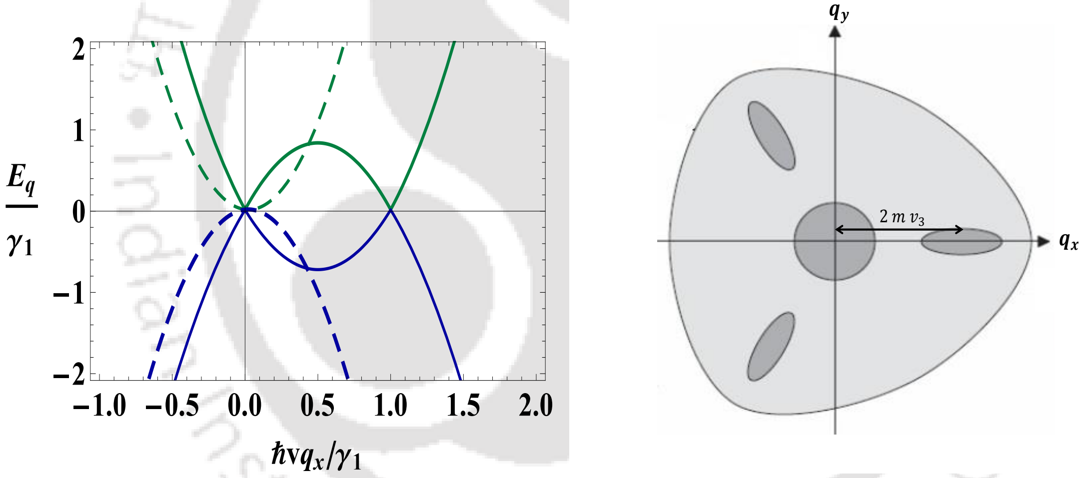

FIGURE 1.14: Left: bilayer graphene band structure in presence of weak direct inter-layer coupling parameter γ_3. The energy bands are potted along the line $q_y = 0$. Dashed and solid curves stand for without and with trigonal warping in bilayer graphene. Right: Schematic of the Fermi line in the valley $\vec{K}$ for high (light shading) and low density (dark shading). This shows the effect of trigonal warping leads to a Lifshitz transition: the iso-energetic line is broken into four pockets, one "central" and three "leg" parts.

presence of coupling parameter γ_3 gives rise a zero non-trivial minimum of energy for $q \neq 0$. At this value of wave vector dispersion-relation is linear similar to that of monolayer graphene. The trigonal warping breaks the iso-energetic line into four pockets one central and three leg parts. The central and leg parts have minimum $|E| = |U|/2$ at $q = 0$ and at $q = 2mv_3 = \gamma_1 v_3 / v^2$, angle ϕ_0, respectively.

For $\vec{K}$ valley, $\phi_0 = 0, \frac{2\pi}{3}, \frac{4\pi}{3}$, whereas for $\vec{K}'$ valley, $\phi_0 = \pi, \frac{\pi}{3}, \frac{5\pi}{3}$. For $\vec{K}$ valley, taking $q_y = 0$ and $\phi = 0$, Eq. (1.32) gives

$$E_{\pm}(q) = \pm \left| v_3 q - \frac{q^2}{2m} \right| \tag{1.33}$$

Equation (1.33) shows that, at zero energy, the leg pocket of the Fermi surface develops at $q = 2mv_3$ where the valance and conduction band overlap and the overlap is given by $2\epsilon_L \approx \frac{\gamma_1}{2}\frac{v_3^2}{v^2} \approx 2\ meV$ [55] using $\gamma_1 = 0.4\ eV$ and $v_3/v = 0.1$. Note that Berry phase 2π [16] is conserved through the Lifshitz transition; the three leg pockets each have Berry phase π while the central pocket has $-\pi$. A detailed description of Berry phase and pseudospin in single and bilayer graphene is given in the next section.

1.6 Pseudo-spin and Berry phase

1.6.1 Single layer graphene

Single layer graphene can be think of as made by the interpenetration of two triangular sublattices A and B. Consider the Hamiltonian of single layer graphene in presence of a vector potential $\vec{A}(t)$ such that $\vec{A}(t)$ is slowly varying and periodic $\vec{A}(0) = \vec{A}(t_f) = 0$. Thus a slowly time varying electric field $\vec{E}(t) = -\frac{1}{c}\dot{\vec{A}}(t)$ is turned on at $t = 0$ and finally off at $t = t_f$. We want to know how the states of the Dirac quasi-particles change with time in this case. The energy eigenvalue equation of the system can be written as

$$H\psi = E\psi \tag{1.34}$$

where H is the Hamiltonian of monolayer graphene and ψ is a two component column matrix.

$$H = v_F \begin{pmatrix} 0 & p_x - ip_y \\ p_x + ip_y & 0 \end{pmatrix} \tag{1.35}$$

with the energy eigenvalues The eigenvalues and the eigenfunction of Eq. (1.34) are

$$E = \pm v_F |p| \tag{1.36}$$

$$\psi_+(\vec{p},0) = \frac{1}{\sqrt{2}} \begin{pmatrix} 1 \\ e^{i\theta_p} \end{pmatrix}, \quad \psi_-(\vec{p},0) = \frac{1}{\sqrt{2}} \begin{pmatrix} 1 \\ -e^{i\theta_p} \end{pmatrix} \tag{1.37}$$

Another choice of eigenfunction with an additional phase factor $e^{\pm i\theta_p/2}$ is

$$\psi_+(\vec{p},0) = \frac{1}{\sqrt{2}} \begin{pmatrix} e^{-i\theta_p/2} \\ e^{i\theta_p/2} \end{pmatrix}, \quad \psi_-(\vec{p},0) = \frac{1}{\sqrt{2}} \begin{pmatrix} e^{-i\theta_p/2} \\ -e^{i\theta_p/2} \end{pmatrix} \tag{1.38}$$

where $|p|$ is the magnitude of $\vec{p}$ that makes an angle θ_p with the x- axis and ± corresponds to conduction and valance band respectively. Since vector potential $\vec{A}(t)$ is *slowly varying*, we may claim that at each time t, the state $\psi(\vec{p},t)$ is close to the eigenstate $\phi(\vec{p},t)$ of the Hamiltonian $H(t) = v_F\vec{\sigma}\cdot(\vec{p} - \frac{e}{c}\vec{A}(t))$ with energy $+v_F|\vec{p} - \frac{e}{c}\vec{A}(t)| \equiv E(t)$. The energy eigenvalue equation near one of the Dirac point can be written as,

$$H(t)\phi(\vec{p},t) = E(t)\phi(\vec{p},t)$$

$$\psi(\vec{p},0) = \phi(\vec{p},0)$$

Since each energy $+v_F|\vec{p} - \frac{e}{c}\vec{A}(t)|$ is non-degenerate, the states representing $\psi(\vec{p},t)$ and $\phi(\vec{p},t)$ are the same. This means the wave functions can differ at most by a phase $\vartheta_B(t)$. This is called the geometric phase, Pancharatnam Berry phase or simply Berry's phase. We may write,

$$\psi(\vec{p},t) = e^{i\vartheta_B(t)}\; e^{-i\int_0^t E(t^{'})dt^{'}}\; \phi(\vec{p},t)$$

The phase $\int_0^t E(t^{'})dt^{'}$ is called the dynamical phase and is expected to be there. The new contribution $\vartheta_B(t)$ is the geometric phase. Now,

$$\phi(\vec{p},t) = \frac{1}{\sqrt{2|P(t)|^2}} \begin{pmatrix} (P_x(t) - iP_y(t)) \\ P_z(t) - P(t) \end{pmatrix}$$

where $\vec{P}(t) = \vec{p} - \frac{e}{c}\vec{A}(t)$ and $P(t) = \sqrt{P_x(t)^2 + P_y(t)^2}$.

$$i\frac{\partial}{\partial t}\psi(\vec{p},t) = e^{i\vartheta_B(t)}\; E(t)\phi(\vec{p},t) - \frac{\partial\vartheta_B(t)}{\partial t}e^{i\vartheta_B(t)}\; \phi(\vec{p},t) + e^{i\vartheta_B(t)}\; i\frac{\partial}{\partial t}\phi(\vec{p},t)$$

$$= H(t)\psi(\vec{p},t) = e^{i\vartheta_B(t)}\; H(t)\phi(\vec{p},t) = e^{i\vartheta_B(t)}\; E(t)\phi(\vec{p},t)$$

$$-\frac{\partial\vartheta_B(t)}{\partial t}\; \phi(\vec{p},t) + i\frac{\partial}{\partial t}\phi(\vec{p},t) = 0$$

since $\phi^\dagger(\vec{p},t)\phi(\vec{p},t) = 1$, therefore

$$\frac{\partial \vartheta_B(t)}{\partial t} = i\phi^\dagger(\vec{p},t)\frac{\partial}{\partial t}\phi(\vec{p},t)$$

But $\phi(\vec{p},t) = \phi(\vec{P}(t),0)$. This means,

$$\frac{\partial \vartheta_B(t)}{\partial t} = i\phi^\dagger(\vec{P}(t),0)\frac{\partial}{\partial t}\phi(\vec{P}(t),0)$$

Using chain rule,

$$\frac{\partial \vartheta_B(t)}{\partial t} = i\phi^\dagger(\vec{P}(t),0)\frac{d\vec{P}(t)}{dt} \cdot \nabla_{\vec{P}(t)}\phi(\vec{P}(t),0)$$

Integrating with respect to time,

$$\vartheta_B(t_f) = i\int_{\vec{P}(0)=\vec{p}}^{\vec{P}(t_f)=\vec{p}} d\vec{P}(t) \cdot (\phi^\dagger(\vec{P}(t),0)\nabla_{\vec{P}(t)}\phi(\vec{P}(t),0))$$

$$\vartheta_B(t_f) = i\oint d\vec{p} \cdot (\phi^\dagger(\vec{p},0)\nabla_{\vec{p}}\phi(\vec{p},0)) \tag{1.39}$$

where,

$$d\vec{p} = \hat{p}\ dp + p\ d\theta\ \hat{\theta}, \quad \nabla_{\vec{p}} = \hat{p}\ \frac{d}{dp} + \hat{\theta}\ \frac{1}{p}\ \frac{d}{d\theta}$$

$$\phi^\dagger(\vec{p},0)\nabla_{\vec{p}}\phi(\vec{p},0) = \frac{1}{\sqrt{2}}\begin{pmatrix} e^{i\theta} & -1 \end{pmatrix}\left(\hat{p}\ \frac{d}{dp} + \hat{\theta}\ \frac{1}{p}\ \frac{d}{d\theta}\right)\frac{1}{\sqrt{2}}\begin{pmatrix} e^{-i\theta} \\ -1 \end{pmatrix}$$

$$= \frac{-i}{2p}\hat{\theta}$$

Therefore,

$$\vartheta_B(t_f) = i\oint d\vec{p} \cdot (\phi^\dagger(\vec{p},0)\nabla_{\vec{p}}\phi(\vec{p},0)) = i\oint d\vec{p} \cdot \frac{-i}{2p}\hat{\theta} = \pi$$

which is the Berry phase corresponding to the eigenfunctions in Eq. (1.37). If we calculate $\vartheta_B(t_f)$ using eigenfunctions in Eq. (1.38), the Berry phase comes out to be zero. It is convenient to use the wave-function of Eq. (1.38), since the effect of Berry's phase is included in the wave-function [81]. This change of phase by π under rotation is characteristic of spinors and experimentally verified by Zhang *et al.* [15]. In fact, the wave function is a two component spinor.

The eigenfunctions may be characterize by their helicity. In quantum-mechanics the helicity operator, the projection of the momentum operator along the (pseudo) spin direction, is defined as

$$\hat{h} = \frac{1}{2}\frac{\vec{\sigma}\cdot\vec{p}}{|\vec{p}|} \tag{1.40}$$

It is clear from Eq. (1.40) that the states $\psi_{\vec{K}}$ and $\psi_{\vec{K}'}$ are also the eigenfunction of the helicity operator $\hat{h}$ because, $[H, \hat{h}] = 0$. This means,

$$\hat{h}\psi_{\vec{K}} = \pm\frac{1}{2}\psi_{\vec{K}} \tag{1.41}$$

Therefore, electrons and holes have positive and negative helicity, respectively. Equation (1.41) implies that $\vec{\sigma}$ has its two eigenvalues either in the direction of momentum or against it. This property says that the states of the system close to the Dirac point have well defined chirality or helicity. Helicity is a good quantum number as long as Hamiltonian, $H = v_F\vec{\sigma}\cdot\vec{p}$ is valid. The helicity is not a good quantum number for large energies or in presence of next-nearest neighbor hopping. The chirality discussed in the context of graphene is not related to the real spin of the electron in graphene but to the pseudo-spin variable associated with the two components of the wave function, labeled by sublattice index A and B. Pseudo-spin is aligned in mutually opposite directions on two sublattices, the superposition of which lies in the plane of the graphene sheet [25].

1.6.2 Bilayer graphene

Bilayer graphene is composed of two single graphene sheets separated by 3.35 $\mathring{A}$ and coupled by a weak Van der Waals force acting between them. The low-energy eigenvalue equation of electrons in graphene bilayer can be written as

$$H\psi = E\psi \tag{1.42}$$

where H is 2×2 Hamiltonian matrix and ψ is a two component column matrix, given by

$$H = -\frac{1}{2m}\begin{pmatrix} 0 & (\pi^\dagger)^2 \\ \pi^2 & 0 \end{pmatrix}, \; \psi = \begin{pmatrix} \psi_{A1} \\ \psi_{B2} \end{pmatrix} \tag{1.43}$$

After solving Eq. (1.42) with the help of Eq. (1.43), we can write the eigenvalues and eigenfunctions as follows

$$E = \pm\frac{|p|^2}{2m} \tag{1.44}$$

$$\psi_{+}(\vec{k}) = \frac{1}{\sqrt{2}}\begin{pmatrix} 1 \\ -e^{2i\theta_k} \end{pmatrix}, \quad \psi_{-}(\vec{k}) = \frac{1}{\sqrt{2}}\begin{pmatrix} 1 \\ e^{2i\theta_k} \end{pmatrix} \tag{1.45}$$

where θ_k is angle of $\vec{k}$ that makes with the x-axis and ± stands for conduction band and valance band, respectively. The electronic wave function amplitudes on two sublattice sites $A1$ and $B2$ can be expressed in terms of pseudo-spin degree of freedom which is related to these amplitudes. If all the electronic densities are located on $A1$ or $B2$ sites, the pseudo-spin part of the wave function could be viewed as a pseudo-spin 'up' ($|\uparrow\rangle = (1,0)$) or 'down' ($|\downarrow\rangle = (0,1)$) states pointing upward and downward out of the graphene plane, respectively. However, the electronic density is usually shared equally between the two layers. Thus the pseudo-spin can be represented as a linear combination of up and down states, $|\uparrow\rangle \mp e^{2i\theta_k}|\downarrow\rangle$, and it lies in the plane of the graphene sheet. The pseuso-spin in bilayer graphene turns twice as quickly as the direction of momentum [16]. The Berry phase in bilayer graphene can also be calculated using Eq. (1.39),

$$\begin{aligned}\phi^{\dagger}(\vec{p},0)\nabla_{\vec{p}}\phi(\vec{p},0) &= \frac{1}{\sqrt{2}}\begin{pmatrix} e^{2i\theta} & -1 \end{pmatrix}\left(\hat{p}\,\frac{d}{dp} + \hat{\theta}\,\frac{1}{p}\,\frac{d}{d\theta}\right)\frac{1}{\sqrt{2}}\begin{pmatrix} e^{-2i\theta} \\ -1 \end{pmatrix} \\ &= \frac{-i}{p}\hat{\theta}\end{aligned}$$

Therefore,

$$\vartheta_B(t_f) = i\oint d\vec{p}\cdot\left(\phi^{\dagger}(\vec{p},0)\nabla_{\vec{p}}\phi(\vec{p},0)\right) = i\oint d\vec{p}\cdot\frac{-i}{p}\hat{\theta} = 2\pi$$

Thus the massive chiral quasi-particles in bilayer graphene shows a Berry phase of 2π. The 2π Berry phase of electronic wave function in bilayer graphene is same as that of conventional two dimensional electron gas (DEG) [82]. Thus the Berry phase in bilayer graphene is *not* nontrivial and is equivalent to that of a trivial Berry phase of *zero* in conventional 2-DEG.

1.7 Methods of synthesis

Graphene is a very special material because it is highly conducting as well as transparent. Graphene sheet has the property of flexibility which can be withstand high stress. Therefore it can be used to develop the flexible electronic devices, for example touch screens [83]. It is very difficult to grow low dimensional systems using usual growth mechanism because of the large thermodynamic fluctuations at high temperature during growth process. This may damage the system and even if they exist but they cannot be stable. Even though the conventional methods are not successful in the production of 2D materials, a possibility remains that they may be produced artificially. Broadly speaking, there are two ways of preparation of graphene, one is 'exfoliation method' and other is 'growth technique'. In exfoliation method the graphene can be detached from an already existing graphite crystal. This method of preparation of graphene was first used by Novoselov *et al.* in 2004 [5, 84]. In growth technique, the graphene sheet can be directly grown on the surface of substrate.

1.7.1 The "Scotch Tape Method"

FIGURE 1.15: Schematic of scotch tape method to prepare graphene[5].

This method of micromechanical exfoliation uses a adhesive tape to detach graphene layer from the graphite crystal. The graphene layers are peeling off the graphite with the help of adhesive tape. In this way the multi-layer graphene is obtained on the adhesive tape. After the multiple process of peeling the multi-layer graphene, it converted to few-layer graphene flakes. Thereafter the tape is attached to the substrate and the glue solved, e.g. by acetone, in order to detach the tape. Finally one last peeling with an unused tape is performed. The graphene flakes obtained with this process differ considerably in size and thickness. The size of obtained single layer graphene is ranges from nanometers to several tens of micrometers. Single-layer graphene has a absorption rate of 2%, nevertheless it is possible to see it under a light microscope on SiO_2/Si, due to interference effects [85]. The Scotch tape method of production of graphene is the easiest method for research purpose but not for industrial purpose. This method cannot be used to prepare the large amount of graphene sheet which limits the use of this method for the industrial purpose. The complexity of this method is

---

[5] http://www.democraticunderground.com/122820077

basically low and the quality of the prepared graphene is very high with almost no defects. Some other exfoliation methods are dispersion of graphite and graphite oxide exfoliation.

1.7.2 Growth techniques

The growth of graphene can occur in two different ways: either the carbon already exists in the substrate or it has to be added by chemical vapour deposition (CVD). Epitaxial growth of graphene can be done by simply heating and cooling down an SiC crystal [86]. Generally, single- or bi-layer graphene and few-layer graphene grow on the Si and C face of the crystal [87], respectively. The crystal structure of Ni(111) is more similar to that of graphene, with a miss match of the lattice constant at about 1.3% [88]. Thus, the graphene can also be prepared by use of the nickel diffusion method. In this method, Ni-layer is evaporated onto a SiC crystal and after heating it the carbon diffused through the Ni layer and forms a graphene or graphite layer on the surface, depending on the heating rate. The graphene prepared by this method can easily be detached from the surface than that produced by simply the growth on a simple SiC crystal without Ni [88]. The quality of graphene samples prepared by this method is not as good as that of exfoliated graphene that can only be found by growing it on a single crystal. The size of graphene layer is limited by the size of the crystal used. The large amount of production of graphene by this method is not as good as by liquid-phase exfoliation. However, the complexity of this methods is comparatively low.

Among the well-known deposition techniques, the chemical vapour deposition (CVD) is one of them. In this deposition technique the substrate is exposed to gaseous compounds. Graphene can be grown by exposing of a Ni film to a gas mixture of H_2, CH_4 and Ar at about 1000 °C [89] which a process similar to the Ni diffusion method. These graphene layers can be transferred via polymer support, which will be attached onto the top of the graphene. After etching the Ni, the graphene can be stamped onto the required substrate and the polymer support gets peeled off or etched away. Using this method several layers of graphene can be stamped onto each other in order to decrease the resistance. Single-layer graphene can also be grown using copper substrate instead nickel [90]. The optical and electrical performance of graphene prepared by CVD is very high. However, the purity of graphene samples produced by this method is not very good which is required by research purpose. On the other hand, this method allows us to produce large graphene samples in size as well as in amount. The complexity of this method is rather low. The detailed description of this section is directly taken from Ref. [91] and the references therein.

1.8 Properties of graphene and bilayer graphene

1.8.1 Electronic properties

Single layer graphene is a semi-metal or a zero-gap semiconductor whereas bilayer graphene is also a zero-gap semiconductor. The band gap in bilayer graphene is tuneable. The properties that separate these systems from one another and also from the other condensed matter systems are as follows:

Graphene, one atom thick carbon sheet, exhibits various supreme properties including exceptionally high electronic and thermal conductivities, extreme mechanical strength, impermeability to gases and so on. These physical properties among other make it highly attractive for various potential applications. The characteristics of graphene observed experimentally are very excellent than those found in any other material. The experiments based on transport measurements reveals that graphene exhibits a remarkably high electron mobility in excess of $15,000\ cm^2V^{-1}s^{-1}$ at room temperature [13, 15, 92]. Mayorov with his collaborators [93] reported the value of electron mobility in graphene is $2.5\times10^5\ cm^2V^{-1}s^{-1}$ while the theoretically calculated value of mobility is $2\times10^5\ cm^2V^{-1}s^{-1}$ [94–97]. The electron and hole mobilities in graphene are found nearly the same [98], and nearly independent of temperature between $10\ K$ and $100\ K$ [13, 94, 99]. This implies that the dominant scattering mechanism for such a high mobility is defect scattering. The room temperature mobility of carriers in graphene due to scattering by the acoustic phonon of graphene is found to be $200,000\ cm^2V^{-1}s^{-1}$ at a carrier density of $10^{12}\ cm^{-2}$ [94, 100] which is 10 times greater than copper [101]. However, the mobility of graphene deposited on SiO_2 substrates at room temperature is largely affected by the scattering of electrons in graphene caused by optical phonons of substrates than scattering by its own phonons. Under this condition the value of mobility found to be equal to $40,000\ cm^2V^{-1}s^{-1}$ [94]. The carriers (electron and hole) in graphene can travel a large distances without experiencing any scattering mechanism, even at room temperature [42]. The minimum conductivity exhibited by carriers in graphene is of the order of $4e^2/h$. The reasons of occurring such a minimum conductivity of graphene are still unknown. Several proposed theories suggest that the minimum conductivity should be $4e^2/\pi h$. However, most measurements are of the order $4e^2/h$ or greater [92] and depend on impurity concentration [102]. The mobility of bilayer sample on h-BN is better than bilayer sample on SiO_2 [94]. According to Monte Carlo calculation, the intrinsic mobility of carries in single layer graphene is better than bilayer graphene [103]. The calculated value of mobility in single and bilayer graphene is $1 \times 10^6\ cm^2V^{-1}s^{-1}$ and $1.2 \times 10^5\ cm^2V^{-1}s^{-1}$, respectively.

The well known phenomenon "Hall effect" is observed in conventional semiconductors placed in a magnetic field. The quantum Hall effect is a quantum mechanical version of the classical Hall effect. Graphene is most like a conventional semiconductor, it also exhibits the phenomenon of Hall effect. It has been observed that the high mobility graphene samples exhibit an unusual sequence of quantum Hall (QH) effects [13, 15]. Graphene shows the 'anomalous' quantum Hall effect in terms of quantization of conductivity. It is anomalous in the sense that the sequence of steps is shifted by 1/2 with respect to the standard observed sequence with an additional factor of 4 accounts for the double valley and double spin degeneracies. The observed Hall conductivity in graphene is $\sigma_{xy} = \pm 4 \cdot (N + 1/2)\, e^2/h$, where N is the Landau level (LL) [92]. The spin and valley degeneracy can be lifted by applying a high magnetic field that splits $N = 0$ LL into four sublevels, lifting spin and valley degeneracy. However, in such an experimentally accessible high magnetic field only the spin degeneracy of $N = \pm 1$ LL seems to be lifted [30], the valley degeneracy of $N = \pm 1$ LL in such a high magnetic field is still present. This response of graphene sample is a direct consequence of massless Dirac electrons in graphene. Similar to single layer graphene, the behaviour of bilayer graphene is also more like a semiconductor. It can be expected that it will also exhibit the phenomena those observed in single layer graphene. The quantum Hall effect is also observed in bilayer graphene. The quantized Hall conductivity of bilayer graphene is $\sigma_{xy} = \pm 4 \cdot N \cdot e^2/h$ which is quite different than single layer graphene. The observed Hall conductivity in bilayer graphene is similar to a conventional semiconductor. The pre-factor of 4 arising from the spin and valley degrees of freedom [12, 16, 21, 43, 63, 104, 105]. The quantum Hall effect in bilayer graphene shows anomaly those observed in single layer graphene. Unlike single layer graphene, the first plateau at $N = 0$ is absent in bilayer graphene. This indicates that bilayer graphene behaves more like a metal at the neutrality point [21, 92]. The $N = 0$ LL can be recovered with the help of chemical doping. In chemically dopped bilayer graphene the neutrality point shifts to a high value of gate voltage that creates an asymmetry gap [31].

The prediction of integral quantum Hall plateaus in graphene [13, 15] poses several questions: Does the fractional quantum Hall effect (FQHE) also occur in graphene, and, if so, what is its character? Does it resemble the integral quantum Hall effect (IQHE) in graphene? The FQHE is experimentally observed by Bolotin *et al.* in an ultra clean suspended single layer graphene [106]. A multi-component FQHE is also observed in graphene [107]. In presence of mixing of LLs the FQHE in monolayer graphene shows different results for $N = 1$ compared to $N = 0$ LL. Mixing of LLs break the particle-hole symmetry [108]. In presence of magnetic field the physics of LLs in suspended bilayer graphene even more interesting than single layer graphene. Suspended bilayer gaphene exhibits an even denominator FQHE at $\nu = -1/2$ on the hole side [109]. Kou *et al.* studied the IQHE and FQHE in electron-hole symmetry broken bilayer graphene [110]. The tuneable and unusual FQH states can be produced by the unique choice of spin, valley, and orbital degeneracies in bilayer graphene. Quantum anomalous Hall effect (QAHE) is also predicted in single and bilayer graphene in presence of exchange field and Rashba spin orbit interaction [111–113]. Single layer graphene also show a quantum spin Hall effect (QSHE) at sufficiently low energy in presence of spin-orbit (SO) interaction [114]. Recently, the QSH effect in supported and suspended graphene samples is also studied [115–117]. A detailed study of QSH effect in AB- and AA-stacked bilayer graphene is given in the refs.[118–120]

1.8.2 Optical properties

The nonlinear optics is the study of light-matter interaction in presence of strong electromagnetic field. The nonlinear optics of graphene is an active research field from theoretical as well as experimental point of view. The unique optical properties of graphene produces a high opacity for one atom thick layer. Graphene is a good absorber of red light, it absorbs almost $\pi\alpha \approx 2.3\%$ part of red light falling on it, where α is the fine-structure constant [121]. In presence of magnetic field the optical responses of large area graphene (graphene nanoribbon) are tuneable [122]. The linear and ultrafast optical properties of graphene and graphene oxide systems are tuneable because these system show electrochromic behaviour [123–127]. For the threshold value of input optical intensity such a unique absorbtion exhibits a saturation behaviour. This nonlinear optical behavior of graphene is known as saturable absorption and the threshold value, at which the absorbtion approaches to saturation, called the saturation fluence. Saturable absorption in graphene could occur at the Microwave and Terahertz band, owing to its wideband optical absorption property. The property of saturable absorbtion in graphene opens the possibilities of graphene to use it in various nanophotonic devices as described in the literature [128]. In presence of more intense laser light field graphene possess a nonlinear phase shift caused by the optical nonlinear Kerr effect exhibited by the system. The nonlinear Kerr coefficient of graphene is very large compared to bulk dielectrics. It is of the order of $10^{-7}cm^2W^{-1}$ which is very large in magnitude than that of bulk dielectrics [129]. This suggests that graphene may be used as a powerful nonlinear Kerr medium.

The theoretical background of graphene was available from almost mid of 20^{th} century. However, only after its experimental realization graphene based systems becomes very active for experimentalists as well as for theoreticians. Nowadays, researchers are trying to replace the conventional semiconductor by the graphene in the electronic devices and trying to develop graphene-based nanoelectronic, nanophotonic and optoelectronic devices operating at room temperature. The study of the optical properties of graphene based systems is an active field of research interest. There has been increasing interest in graphene-based materials for photonic applications, as well as the realization of graphene's potential in the terahertz to far infrared regime. The optical properties of graphene-based systems are seems to be more significant, interesting and more versatile than perhaps previously believed. Among the several well-known most important optical properties of graphene optical conductivity is one of them. A detailed calculated general expression of optical conductivity of graphene is given by Gusynin *et al.* [130]. The theoretical calculation of universal ac optical conductivity [131] and the sum rules for optical and Hall conductivities [132] are also well studied along with the electro- and magneto-optical response of graphene [133–136]. The conductivity of graphene has been extensively studied theoretically [137–141] and largely verified experimentally [121, 142–144]. Similarly, the optical conductivity of AB-stacked bilayer graphene is also studied theoretically [64, 145–147] and verified experimentally [34, 61, 62]. There are a number of studies which deals the substrate effects on graphene, its visible criteria, contrast analysis etc [148, 149]. Apart from the above mentioned optical properties, other optical properties involved the study of optical Stark effect, four wave mixing, photon echo and the phenomenon of Rabi oscillation. These properties are widely described in various text books available in literature [150–152]. The phenomenon of Rabi oscillations is one of the well-known optical phenomena in quantum optics [153, 154] and also in conventional semiconductors [152]. These oscillations were first predicted in a two-level atomic systems.

Experimental study of optical properties of graphene systems is based on optical spectroscopy. Single layer of graphite, graphene, was first identified with the reflection spectroscopy of graphene on SiO_2 substrate by the interference effects [5, 155]. Among the several experimental tools to study the optical properties of graphene systems Raman Spectroscopy is one of them. Raman spectroscopy is helpful to count the number of layers present in sample [156–161]. Raman spectroscopy is also used to determine the effective doping [162]. Pump-probe spectroscopy [163–169] is used to detect the coherent and incoherent optical phenomena like Rabi oscillations [150–152], four-wave mixing [150], optical dephasing [152] and relaxation dynamics of excited carriers. In pump-probe spectroscopy, two successive laser pulses are used with a variable time delay. One of them is used to prepare the system in excited state called the pump pulse other pulse of low intensity monitors the system known as probe pulse. The intensity of pump pulse is greater than the probe pulse.

1.9 Applications of graphene

So far, graphene is not used in commercial applications [170], many have been proposed and/or are under development, in areas including electronics, biological engineering, filtration, lightweight/strong composite materials, photovoltaics and energy storage [171]. Graphene is produced as a powder and as a dispersion in a polymer matrix, or adhesive, elastomer, oil and aqueous and non-aqueous solutions. The dispersion is stated by the manufacturer to be suitable for advanced composites [172], paints and coatings, lubricants, oils and functional fluids, capacitors and batteries, thermal management applications, display materials and packaging, inks and 3D-printers' materials, and barriers and films [173].

1.10 Motivations

This section describes the motivation and the back ground of my thesis work. Our main motivation is to study the coherent and incoherent optical properties of single and bilayer graphene. There are several well-known optical phenomena described in an earlier discussion. Among the well-known optical phenomena, Rabi oscillation is one of them. Rabi oscillations were first predicted in a two-level atomic systems [174] and subsequently in conventional semiconductors [152]. The phenomenon of Rabi oscillation emerges from the interaction of the electromagnetic field with the matter under consideration. The definition of Rabi oscillation is as follows: a periodic exchange of energy between the electromagnetic field and the two-level system is known as Rabi oscillation and the frequency of these oscillations referred to as Rabi frequency. This effect can also be interpreted as a periodic change between absorption and stimulated emission of photons. Graphene is also a semi-metal or a zero gap semiconductor. We can expect that graphene-based systems will also exhibit the phenomena that are observed in two-level atomic systems and conventional semiconductors. Therefore, it is worthwhile to study these phenomena in graphene and graphene-based systems because these systems are analogous to two-level atomic systems and conventional semiconductors. Our intention is to study the phenomenon of Coherent and incoherent Rabi oscillations in single and bilayer graphene. Coherent and incoherent Rabi oscillations in graphene have already been studied by a number of authors available in literature [169, 175–180]. Nonlinear optics of graphene is a nascent field. Ishikawa [181] studied the nonlinear optical response of graphene in time domain. His study shows that the nonlinear optical response is not sufficiently described neither by pure intra-band nor by pure inter-band dynamics but their interplay has to be taken into account. Romanets *et al.* [177] described the mechanisms of coherent nonlinear response of an intrinsic graphene under ultra-fast inter-band excitation. They showed that Rabi oscillations, both versus time and versus pumping intensity, can easily be observed on femtosecond time scales. Ang *et al.* [182] studied the nonlinear optics of bilayer graphene in the frequency range from the terahertz regime to the far-infrared regime and concluded that it is useful for developing graphene-based nonlinear photonics and optoelectronic devices. The optical properties of bilayer graphene are also described in references [146, 183].

In this thesis work, we will describe the phenomenon of Rabi oscillations (ROs) in suspended and supported graphene systems. Mischenko [175] has already been described the phenomenon of Rabi oscillation in resonance in single flake of graphene using rotating wave approximation. Rotating wave approximation is valid when the frequency of the external field is nearly equal to the electron-hole pair excitation frequency. We are interested in studying the phenomenon of Rabi oscillations far from resonance in graphene systems when the frequency of the applied field is very large in comparison to the electron-hole pair excitation frequency. To discuss the Rabi oscillations far from resonance we use an approximation called asymptotic rotating wave approximation (ARWA) which is alternative to rotating wave approximation (RWA). This approximation is used to describe Rabi oscillations in suspended single layer graphene [184]. We are interested to use this approximation in clean bilayer graphene and substrate-graphene systems to describe Rabi oscillations. The results obtained from this technique are corroborated with a fully numerical solution of the Bloch equations.

The above description shows the study of coherent Rabi oscillations. We are also interested in studying the phenomenon of carrier relaxation dynamics in clean suspended single and bilayer samples by determining the behaviour of Rabi oscillations in presence of electron-phonon interaction (optical, acoustic and flexural). The inclusion of electron-phonon interaction in graphene potentially leads to a damping of ROs. We have discussed the incoherent ROs by means of optical excitations (carriers excitation under applied electric field). Energetic optically excited carriers are known as hot carriers. These carriers lose their energy to lattice vibrations known as phonons resulting in what is known as dephasing of these carriers. In order to observe ROs experimentally, it is important that these oscillations are not significantly affected by the presence of electron-phonon interaction.

PART-I

Coherent Anomalous Rabi Oscillations

Chapter 2

Anomalous Rabi oscillations in Suspended Graphene Systems

This chapter deals with the light-matter interaction in suspended graphene systems. Light matter interaction in graphene systems leads to novel physical phenomena similar to that of two-level atomic systems and conventional semiconductors. Graphene systems are analogous to two-level atomic systems in some ways. The difference is that in graphene systems the levels are replaced by bands. Two-level atomic systems show novel optical phenomena in presence of an electromagnetic field. Among known optical phenomena, Rabi oscillations is one of them which is widely discussed in many text books [150, 151] of quantum optics. These oscillations in conventional semiconductors are described i. e. in the text book by Haug and Lindberg [152]. Graphene is a zero-gap semiconductor showing a linear energy momentum dispersion relation unlike conventional semiconductors. Therefore, it is worthwhile to study the same phenomenon in case of graphene systems. Rabi oscillations in graphene have already been discussed in resonance case by a number of authors using rotating wave approximation (RWA). This approximation is valid only when the frequency of the external applied field is nearly equal to the electron-hole pair excitation frequency of the system considered. Mishchenko [175] studied Rabi oscillations in clean graphene sample using RWA. The novel work of Mishchenko on ROs in conventional resonance case is the background of my thesis work. He also studied the damping of Rabi oscillations by including energy relaxation in a phenomenological way. The same phenomenon has been studied in our group in undoped single layer graphene in extreme non-resonance case (far from resonance), also known as off resonance. To discuss Rabi oscillations far from resonance an approximation is used called asymptotic rotating wave approximation (ARWA) [184] which is an alternative to RWA, the results of which is corroborated with a fully numerical solution of the Bloch equations. RWA is valid only near resonance when the frequency of the applied field is nearly equal to the electron-hole pair excitation frequency whereas ARWA is valid when the frequency of the applied field is very large in comparison to the electron-hole pair excitation frequency. These oscillations are known as ‘anomalous’ Rabi oscillations (AROs) since they are absent in two level systems and conventional semiconductors. Similar to single layer graphene, bilayer graphene is also a zero-gap semiconductor. This motivates us to study the same phenomenon in case of bilayer graphene and to see that what would be the response of bilayer graphene under the same circumstances as in single layer graphene.

One may ask a question that why we choose bilayer graphene to discuss ROs while these oscillations have already been predicted in single layer graphene. This is because of the difference in the band structure which is a very crucial point that makes the two systems very different from one another. Single layer graphene shows linear dispersion relation whereas bilayer graphene exhibits parabolic energy momentum dispersion, while both are zero gap semiconductors.

The study of ROs in bilayer graphene is generalized to include a few graphene layers (few-layer graphene). The outline of this chapter is as follows: the optical Bloch equations are derived for population and polarization on two sublattices in bilayer graphene. These Bloch equations are solved near resonance as well as far from resonance using conventional RWA and asymptotic RWA, respectively. Bilayer graphene shows multiple conventional harmonic resonances whereas a single anomalous Rabi frequency is found in off resonance. Single layer graphene on the other hand, possesses a single conventional and anomalous Rabi frequency (ignoring frequency doubling effects). Subsequently, the experimentally accessible quantity current density is calculated in both cases. Finally, this idea is generalized to few-layer graphene. The generalized n-layer expressions for Rabi frequency and current density are found. These expressions are able to reproduce the results of Rabi frequencies and current densities for the case of single layer, bilayer graphene and so on. It can easily be understood with the help of the following discussion.

2.1 Coherent optical Bloch equations of bilayer graphene

In this section we derive the coherent optical Bloch equations of bilayer graphene. The effective low-energy two-component Hamiltonian of bilayer graphene (BLG) describes the effective hopping between non-dimer sites $A1$–$B2$ (red solid arrow) through dimer sites $B1$–$A2$ (green dashed arrow), Fig. 1.8. The hopping between non-dimer sites $A1$–$B2$ includes an inter-layer hopping (γ_1). This effective low-energy Hamiltonian of bilayer graphene has been derived by McCann *et al.* [16] using Green's function method.

$$\hat{H}_2 = -\frac{1}{2m}\begin{pmatrix} 0 & k_-^2 \\ k_+^2 & 0 \end{pmatrix} \tag{2.1}$$

with the energy eigenvalues $E_{\pm}(k) = \pm\frac{|k|^2}{2m}$, $\pm$ corresponds to conduction and valance band respectively, $k_{\pm} = k_x \pm ik_y$ and m is the effective mass of massive chiral Dirac fermions, $m = \frac{\gamma_1}{2v^2} \sim 0.035\ m_e$. The eigenfunction of Hamiltonian Eq. (2.1) in K valley can be represented as $\psi^T = (\psi_{A1}\ \psi_{B2})$. A semiclassical approach is used to describe the phenomenon of ROs where radiation is treated classically and matter fields are quantum in nature. An in-plane electric field is applied through a vector potential of the form $A(t) = A(0)e^{-i\omega t}$, where $A(0) = \frac{e}{c}\left(A_x(0) + iA_y(0)\right)$ is a complex amplitude of the external applied field. This vector potential couples to BLG in a transverse gauge, and changes the momentum of massive Dirac fermions from $\vec{k}$ to $\vec{k} - \frac{e}{c}\vec{A}$. In second quantization, using two component basis eigenstates of the Hamiltonian Eq. (2.1) in momentum space of the form $\psi^T = \left(c_{A1}(\vec{k},t)\ \ c_{B2}(\vec{k},t)\right)$, the Hamiltonian Eq. (2.1) reads as

$$H = -\frac{1}{2m}\sum_{\vec{k}}\left[\left(k_- - A^*(t)\right)^2 c^\dagger_{A1}(\vec{k},t)\ \ c_{B2}(\vec{k},t) + h.c.\right] \tag{2.2}$$

where c and $c^\dagger$ are annihilation and creation operators on sublattice sites $A1$ and $B2$ in bottom and top layer respectively and vice-versa.

Now we are going to derive the Bloch equations which are nothing but the rate equations of polarization and population excess on sublattice site $A1$ and $B2$. The fundamental dynamical quantities are (i) the population difference $n_{diff}(\vec{k},t)$ in the number densities of the $A1$ sublattice site in the bottom layer and the $B2$

sublattice site in the top layer and (ii) the inter-layer polarization $p(\vec{k},t)$. In terms of creation and annihilation operators these quantities may be represented as

$$\begin{aligned} n_{diff}(\vec{k},t) &= \langle c^{\dagger}_{A1}(\vec{k},t)\ c_{A1}(\vec{k},t)\rangle - \langle c^{\dagger}_{B2}(\vec{k},t)\ c_{B2}(\vec{k},t)\rangle \\ p(\vec{k},t) &= \langle c^{\dagger}_{A1}(\vec{k},t)\ c_{B2}(\vec{k},t)\rangle \end{aligned} \tag{2.3}$$

With the help of the equations of motion for operators $i\partial_t\hat{\rho} = [\hat{\rho}, H]$, and simple anti-commutator algebra for fermions, the Bloch equations of $n_{diff}(\vec{k},t)$ and $p(\vec{k},t)$ reads as (setting $\hbar = 1$),

$$i\partial_t n_{diff}(\vec{k},t) = -\frac{1}{m}\left[\left(k_- - A^*(0)\ e^{i\omega t}\right)^2 p(\vec{k},t) - h.c.\right] \tag{2.4}$$

$$i\partial_t p(\vec{k},t) = -\frac{1}{2m}\left(k_+ - A(0)\ e^{-i\omega t}\right)^2 n_{diff}(\vec{k},t) \tag{2.5}$$

where $k_\pm = k_x \pm ik_y$, and $A(0) = \frac{e}{c}\left(A_x(0) + iA_y(0)\right)$. Equations (2.4) and (2.5) are also called the coherent optical Bloch equations. Therefore, the model presented, here, is a pure coherent process of uncorrelated fermions. In other words, we are studying the phenomenon of coherent ROs.

2.2 Solution of Bloch equations

In this section, we discuss the solution of Bloch equations in the regions of interest. We first solve these equations in conventional resonance condition using rotating wave approximation (RWA), when the external driving frequency (EDF) ω is nearly equal to the inter-band transition frequency $2\frac{|k|^2}{2m}$ of the system. Subsequently, these equations are solved in off resonance condition, when the frequency of the external field is much larger than the inter-band transition frequency of the system ($\omega \gg \frac{|k|^2}{m}$). To solve the Bloch equations in off resonance we employ 'asymptotic' RWA (ARWA), the results of which is corroborated with a fully numerical solution of the Bloch equations. This situation is quite different from the conventional case where the external driving frequency is close to the particle-hole creation frequency. The conventional resonant case in single layer graphene is already discussed in the literature [175, 181]. Here we will give only a qualitative description of this regime in the case of bilayer graphene.

2.2.1 Solution of Bloch equations near resonance, $\nu\omega \approx 2\frac{|k|^2}{2m}$

This section describes the solution of Bloch equations in the resonance regime when $\nu\omega$ is nearly equal to electron-hole pair excitation frequency. Bilayer graphene possesses a parabolic dispersion between energy and momentum. Therefore, here, there are two possible resonances – one is at the first harmonic in EDF, i.e. when $\nu = 1$ and the second resonance occurs due to the frequency doubling effect already present in the Hamiltonian due to quadratic energy momentum dispersion, i.e. when $\nu = 2$. To solve the Bloch equations in the resonance case, we invoke a rotating wave approximation [150, 151, 174] well known in the context of two-level atomic systems in quantum optics. Mischenko [175] has already been studied the phenomenon of Rabi oscillations in suspended single layer graphene for small detuning, Δ, which is the difference between external driving frequency and electron-hole pair excitation frequency. His study shows a saturation behaviour of current density. To solve the Bloch equations of bilayer graphene in resonance case, we use a change of basis for the time independent part of Hamiltonian. It can be understood from the following discussion.

The Bloch Eqs. (2.4) and (2.5) can be written in the following matrix form (suppressing $\vec{k}$ in the argument).

$$i\frac{d}{dt}\begin{pmatrix} n_d(t) \\ p(t) \\ p^*(t) \end{pmatrix} = \begin{pmatrix} 0 & \frac{-k_-^2}{m} & \frac{k_+^2}{m} \\ \frac{-k_+^2}{2m} & 0 & 0 \\ \frac{k_-^2}{2m} & 0 & 0 \end{pmatrix}\begin{pmatrix} n_d(t) \\ p(t) \\ p^*(t) \end{pmatrix} + \begin{pmatrix} 0 & \frac{K_t^*}{m} & \frac{-K_t}{m} \\ \frac{K_t}{2m} & 0 & 0 \\ \frac{-K_t^*}{2m} & 0 & 0 \end{pmatrix}\begin{pmatrix} n_d(t) \\ p(t) \\ p^*(t) \end{pmatrix}$$
$$+ \begin{pmatrix} 0 & \frac{-(A^*(t))^2}{m} & \frac{(A(t))^2}{m} \\ \frac{-(A(t))^2}{2m} & 0 & 0 \\ \frac{(A^*(t))^2}{2m} & 0 & 0 \end{pmatrix}\begin{pmatrix} n_d(t) \\ p(t) \\ p^*(t) \end{pmatrix} \tag{2.6}$$

where, $K_t = 2k_+A(t)$, $K_t^* = 2k_-A^*(t)$, $k_\pm = k_x \pm ik_y$. Diagonalizing the unperturbed Hamiltonian (time independent part of Hamiltonian) by making the following substitution

$$\begin{pmatrix} n_d(t) \\ p(t) \\ p^*(t) \end{pmatrix} = \begin{pmatrix} 0 & \frac{-2k_+}{k_-} & \frac{2k_+}{k_-} \\ \frac{k_+^2}{k_-^2} & \frac{-k_+^2}{k_-^2} & \frac{-k_+^2}{k_-^2} \\ 1 & 1 & 1 \end{pmatrix}\begin{pmatrix} \tilde{n}_d(t) \\ \tilde{p}(t) \\ \tilde{p}'(t) \end{pmatrix} \tag{2.7}$$

yields the following set of three equations

$$
\begin{aligned}
n_d(t) &= \frac{-2k_+}{k_-}\,\tilde{p}(t) + \frac{2k_+}{k_-}\,\tilde{p}^{'}(t) \\
p(t) &= \frac{k_+^2}{k_-^2}\left[\tilde{n}_d(t) - \tilde{p}(t) - \tilde{p}^{'}(t)\right], \quad p^*(t) = \tilde{n}_d(t) + \tilde{p}(t) + \tilde{p}^{'}(t)
\end{aligned}
\tag{2.8}
$$

Inserting Eq. (2.7) into Eq. (2.6) gives

$$
i\frac{d}{dt}\begin{pmatrix} \tilde{n}_d(t) \\ \tilde{p}(t) \\ \tilde{p}^{'}(t) \end{pmatrix} = \begin{pmatrix} 0 & 0 & 0 \\ 0 & \frac{-|k|^2}{m} & 0 \\ 0 & 0 & \frac{|k|^2}{m} \end{pmatrix}\begin{pmatrix} \tilde{n}_d(t) \\ \tilde{p}(t) \\ \tilde{p}^{'}(t) \end{pmatrix} +
$$

$$
\begin{pmatrix} 0 & \frac{-K_t k_-^2 + K_t^* k_+^2}{2m|k|^2} & \frac{K_t k_-^2 - K_t^* k_+^2}{2m|k|^2} \\ \frac{K_t k_-^2 - K_t^* k_+^2}{4m|k|^2} & \frac{K_t k_-^2 + K_t^* k_+^2}{2m|k|^2} & 0 \\ \frac{-K_t k_-^2 + K_t^* k_+^2}{4m\kappa^2} & 0 & \frac{-K_t k_-^2 - K_t^* k_+^2}{2m|k|^2} \end{pmatrix}\begin{pmatrix} \tilde{n}_d(t) \\ \tilde{p}(t) \\ \tilde{p}^{'}(t) \end{pmatrix} +
$$

$$
\begin{pmatrix} 0 & \frac{k_-^2 (A(t))^2 - k_+^2 (A^*(t))^2}{2m\kappa^2} & \frac{-k_-^2 (A(t))^2 + k_+^2 (A^*(t))^2}{2m\kappa^2} \\ \frac{-k_-^2 (A(t))^2 + k_+^2 (A^*(t))^2}{4m\kappa^2} & \frac{-k_-^2 (A(t))^2 - k_+^2 (A^*(t))^2}{2m\kappa^2} & 0 \\ \frac{k_-^2 (A(t))^2 - k_+^2 (A^*(t))^2}{4m\kappa^2} & 0 & \frac{k_-^2 (A(t))^2 + k_+^2 (A^*(t))^2}{2m\kappa^2} \end{pmatrix}\begin{pmatrix} \tilde{n}_d(t) \\ \tilde{p}(t) \\ \tilde{p}^{'}(t) \end{pmatrix}
$$

This gives the following set of equations

$$
\begin{aligned}
i\frac{d}{dt}\tilde{n}_d(t) &= \left[\frac{-K_t\ k_-^2 + K_t^*\ k_+^2 + k_-^2\ (A(t))^2 - k_+^2\ (A^*(t))^2}{2m|k|^2}\right]\tilde{p}(t) \\
&\quad + \left[\frac{K_t\ k_-^2 - K_t^*\ k_+^2 - k_-^2\ (A(t))^2 + k_+^2\ (A(t)^*)^2}{2m|k|^2}\right]\tilde{p}^{'}(t) \\
i\frac{d}{dt}\tilde{p}(t) &= \left[\frac{K_t\ k_-^2 - K_t^*\ k_+^2 - k_-^2\ (A(t))^2 + k_+^2\ (A^*(t))^2}{4m|k|^2}\right]\tilde{n}_d(t) \\
&\quad + \left[\frac{-2|k|^4 + K_t\ k_-^2 + K_t^*\ k_+^2 - k_-^2\ (A(t))^2 - k_+^2\ (A^*(t))^2}{2m|k|^2}\right]\tilde{p}(t) \\
i\frac{d}{dt}\tilde{p}^{'}(t) &= \left[\frac{-K_t\ k_-^2 + K_t^*\ k_+^2 + k_-^2\ (A(t))^2 - k_+^2\ (A^*(t))^2}{4m|k|^2}\right]\tilde{n}_d(t) \\
&\quad + \left[\frac{2|k|^4 - K_t\ k_-^2 - K_t^*\ k_+^2 + k_-^2\ (A(t))^2 + k_+^2\ (A^*(t))^2}{2m|k|^2}\right]\tilde{p}^{'}(t)
\end{aligned}
\tag{2.9}
$$

Now, let us assume

$$
\tilde{p}^{'}(t) = e^{\frac{-i|k|^2}{m}t}P^{'}(t), \quad \tilde{p}(t) = e^{\frac{i|k|^2}{m}t}P(t) \tag{2.10}
$$

Inserting the above assumption, we left with the following set of equations

$$
\begin{aligned}
i\frac{d}{dt}\tilde{n}_d(t) &= \left[\frac{-K_t\ k_-^2 + K_t^*\ k_+^2 + k_-^2\ (A(t))^2 - k_+^2\ (A^*(t))^2}{2m|k|^2}\right] e^{\frac{i|k|^2}{m}t} P(t) \\
&\quad + \left[\frac{K_t\ k_-^2 - K_t^*\ k_+^2 - k_-^2\ (A(t))^2 + k_+^2\ (A^*(t))^2}{2m|k|^2}\right] e^{\frac{-i|k|^2}{m}t} P^{'}(t) \\
i\frac{d}{dt}P(t) &= \left[\frac{K_t\ k_-^2 - K_t^*\ k_+^2 - k_-^2\ (A(t))^2 + k_+^2\ (A^*(t))^2}{4m|k|^2}\right] e^{\frac{-i|k|^2}{m}t} \tilde{n}_d(t) \\
&\quad + \left[\frac{K_t\ k_-^2 + K_t^*\ k_+^2 - k_-^2\ (A(t))^2 - k_+^2\ (A^*(t))^2}{2m|k|^2}\right] p(t) \\
i\frac{d}{dt}P^{'}(t) &= \left[\frac{-K_t\ k_-^2 + K_t^*\ k_+^2 + k_-^2\ (A(t))^2 - k_+^2\ (A^*(t))^2}{4m|k|^2}\right] e^{\frac{i|k|^2}{m}t} \tilde{n}_d(t) \\
&\quad - \left[\frac{K_t\ k_-^2 + K_t^*\ k_+^2 - k_-^2\ (A(t))^2 - k_+^2\ (A^*(t))^2}{2m|k|^2}\right] p^{'}(t)
\end{aligned}
$$

Writing $A(t) = A(0)e^{-i\omega t}$, $A^*(t) = A^*(0)e^{i\omega t}$ and applying rotating wave approximation (RWA), $\Delta = \nu\omega - \frac{|k|^2}{m}$, $\nu = 1, 2$ for first and second harmonic resonance, respectively. Therefore, applying RWA to get the first harmonic resonance by taking $\nu = 1$, $\Delta = \omega - \frac{|k|^2}{m}$. With this assumption the above equations reduces to the following-

$$
\begin{aligned}
i\frac{d}{dt}\tilde{n}_d(t) &= \frac{-Kk_-^2}{2m|k|^2}P(t)e^{-i\Delta t} - \frac{K^*k_+^2}{2m|k|^2}e^{i\Delta t}P^{'}(t) \\
i\frac{d}{dt}P(t) &= \frac{-K^*k_+^2}{4m|k|^2}e^{i\Delta t}\tilde{n}_d(t) \\
i\frac{d}{dt}P^{'}(t) &= \frac{-Kk_-^2}{4m\kappa^2}e^{-i\Delta t}\tilde{n}_d(t)
\end{aligned}
\tag{2.11}
$$

To solve the above set of equations, we need to make the further following assumption

$$
P^{'}(\vec{k}, t) = e^{-i\Delta t}u^{'}(\vec{k}, t), \qquad P(\vec{k}, t) = e^{i\Delta t}u(\vec{k}, t) \tag{2.12}
$$

This assumption reduces the above set of equations in the following-

$$
\begin{aligned}
i\frac{d}{dt}\tilde{n}_d(t) &= \frac{-K\ k_-^2}{2m|k|^2}u(t) - \frac{K^*\ k_+^2}{2m|k|^2}u^{'}(t) \\
i\frac{d}{dt}u(t) - \Delta u(t) &= \frac{-K^*\ k_+^2}{4m|k|^2}\tilde{n}_d(t) \\
i\frac{d}{dt}u^{'}(t) + \Delta u^{'}(t) &= -\frac{K^*\ k_-^2}{4m|k|^2}\tilde{n}_d(t)
\end{aligned}
\tag{2.13}
$$

The set of equations (2.13) may easily be solved by assuming the solution in the following from, restoring $\vec{k}$ in the argument,

$$u(\vec{k},t) = A(\vec{k})Sin(\Omega t) + B(\vec{k})(1 - Cos(\Omega t))$$

$$u^{'}(\vec{k},t) = A^{'}(\vec{k})Sin(\Omega t) + B^{'}(\vec{k})(1 - Cos(\Omega t))$$

Putting the value of u and $u^{'}$ in Eq. (2.13) and solving for unknown coefficients, we can get the solution of u and $u^{'}$ as given below,

$$\begin{aligned} u(\vec{k},t) = {} & \frac{ik_- A^*(0)|A(0)|^2 n_s(\vec{k},0)}{2m^2\Omega\omega} Sin(\Omega t) \\ & + \frac{\Delta k_- A^*(0)|A(0)|^2 n_s(\vec{k},0)}{2m^2\Omega^2\omega}(1 - Cos(\Omega t)) \end{aligned}$$

$$\begin{aligned} u^{'}(\vec{k},t) = {} & \frac{iA(0)k_-^2|A(0)|^2 n_s(\vec{k},0)}{2m^2\Omega\omega k_+} Sin(\Omega t) \\ & - \frac{\Delta A(0)k_-^2|A(0)|^2 n_s(\vec{k},0)}{2m^2\Omega^2\omega k_+}(1 - Cos(\Omega t)) \end{aligned}$$

After back substitution in Eq. (2.8), we can get the solution of Bloch equations in resonance case as given below,

$$\begin{aligned} n_{diff}(\vec{k},t) = {} & -\frac{i\;\Theta(\frac{|k|^2}{2m} - \mu)}{4m\Omega}\left[2k_+A^*(0) - 2k_-A(0)\right] Sin(\Omega t) \\ & - \frac{\Delta\;\Theta(\frac{|k|^2}{2m} - \mu)}{4m\Omega^2}\left[2k_+A^*(0)e^{i\omega t} + 2k_-A(0)e^{-i\omega t}\right][1 - Cos(\Omega t)] \end{aligned} \tag{2.14}$$

$$\begin{aligned} p(\vec{k},t) = {} & -\left[\frac{ik_+^2A^*(0)}{4m\Omega k_-}e^{i\omega t} - \frac{ik_+A(0)}{4m\Omega}e^{-i\omega t}\right] Sin(\Omega t)\;\Theta(\frac{|k|^2}{2m} - \mu) \\ & - \left[\frac{k_+^2|A(0)|^2}{m^2\Omega^2} + \frac{\Delta k_+^2A^*(0)}{4m\Omega^2 k_-}e^{i\omega t} - \frac{\Delta k_+A(0)}{4m\Omega^2}e^{-i\omega t}\right][1 - Cos(\Omega t)]\;\Theta(\frac{|k|^2}{2m} - \mu) \end{aligned} \tag{2.15}$$

where,

$$\Omega_\omega = \sqrt{\Delta^2 + \frac{2|k|^2\omega_R}{m}} \tag{2.16}$$

is the generalized conventional Rabi frequency at first harmonic resonance and $\Delta = \omega - \frac{|k|^2}{m}$ is the detuning (difference between the external driving frequency and the electron-hole pair excitation frequency). If we repeat the similar calculation for second harmonic resonance, the Rabi frequency comes out to be equal to

$$\Omega_{2\omega} = \sqrt{\Delta^2 + \omega_R^2} \tag{2.17}$$

where $\omega_R = \frac{|A(0)|^2}{2m}$. Unlike single layer graphene where only single resonance is possible which occurs at the level of first harmonic in the external driving frequency [184], here, we have seen that there are two possible resonances in case of bilayer graphene- one is at first harmonic in external driving frequency, i.e. when $\nu = 1$ and the second resonance occurs due to the frequency doubling effect, i. e. when $\nu = 2$. The frequency doubling effect is directly attributable to the quadratic dispersion relation of bilayer graphene between energy and momentum. In passing, we note that we have used complex exponential time varying vector potentials, as opposed to real sinusoidal ones used by Mishchenko [175]. These two approaches are equivalent in linear response but when including nonlinear terms as we do here, they are different. The appeal of Mishchenko's work is that he treats the external applied field as a purely physical real quantity. However, our approach of using time-varying complex exponentials renders calculations involving higher harmonics (which is the norm in BLG and MLG) quite easy and elegant. This preceding discussion was about solving the Bloch equations in the resonance case. In following section, the Bloch equations are solved far from resonance using an approximation which is an alternative to the rotating wave approximation (RWA) called asymptotic rotating wave approximation (ARWA) which has been recently used to discuss the same phenomenon in case of single layer graphene [184]. We shall also justify that the results obtained from ARWA technique are corroborated with a fully numerical solution of the Bloch equations. Here, we employ this approximation to solve the Bloch equations for the case of bilayer graphene which is quite different than single layer graphene.

2.2.2 Solution of Bloch equations far from resonance, $\omega \gg \omega_R, 2\frac{|k|^2}{2m}$

The Bloch equations are solved in the off resonance regime using ARWA [184]. For that we have to decompose $n_{diff}(\vec{k},t)$ and $p(\vec{k},t)$ (e.g. see Boyd [150]) using the ansatz,

$$n_{diff}(\vec{k},t) = n_s(\vec{k},t) + \sum_{l=1}^{2} n_{fl}(\vec{k},t)e^{-il\omega t} + \sum_{l=1}^{2} n^*_{fl}(\vec{k},t)e^{il\omega t} \tag{2.18}$$

$$p(\vec{k},t) = p_s(\vec{k},t) + \sum_{l=1}^{2} p_{l+}(\vec{k},t)e^{-il\omega t} + \sum_{l=1}^{2} p_{l-}(\vec{k},t)e^{il\omega t} \tag{2.19}$$

Here we retain terms varying as $e^{\pm i\omega t}$ and $e^{\pm 2i\omega t}$ unlike single layer graphene where we retain only the first harmonic, the underlying reason being that the AROs are associated with the second harmonic in case of BLG (at least for the population) while in SLG it is associated with the first harmonic. In BLG, the single harmonic may affect the second harmonic since multiplication of two single harmonics may give rise to the second harmonic. Hence it is necessary to keep both the harmonics in external frequency when decomposing $n_{diff}(\vec{k},t)$ and $p(\vec{k},t)$ into slow and fast terms. Moreover, if we consider the Bloch equations for the case where $\vec{k} = 0$, it is clear that we have to keep terms at least up to second harmonic in external frequency when decomposing the population and polarization into slow and fast terms. Inserting Eqs. (2.18) and (2.19) into Bloch Eqs. (2.4) and (2.5) and comparing the coefficients of the same exponential powers from both sides, we can separate the slow as well as the fast population and polarization equations. The slowly and rapidly varying polarization equations comes out to be:

$$\begin{aligned}
i\frac{\partial}{\partial t}p_s(\vec{k},t) &= -\frac{1}{2m}\left[k_+^2 n_s(\vec{k},t) + A^2(0)n^*_{f2}(\vec{k},t) - 2k_+A(0)n^*_{f1}(\vec{k},t)\right]\\
i\frac{\partial}{\partial t}p_{1+}(\vec{k},t) + \omega p_{1+}(\vec{k},t) &= -\frac{1}{2m}\left[k_+^2 n_{f1}(\vec{k},t) + A^2(0)n^*_{f1}(\vec{k},t) - 2k_+A(0)n_s(\vec{k},t)\right]\\
i\frac{\partial}{\partial t}p_{1-}(\vec{k},t) - \omega p_{1-}(\vec{k},t) &= -\frac{1}{2m}\left[k_+^2 n^*_{f1}(\vec{k},t) - 2k_+A(0)n^*_{f2}(\vec{k},t)\right]\\
i\frac{\partial}{\partial t}p_{2+}(\vec{k},t) + 2\omega p_{2+}(\vec{k},t) &= -\frac{1}{2m}\left[k_+^2 n_{f2}(\vec{k},t) + A^2(0)n_s(\vec{k},t) - 2k_+A(0)n_{f1}(\vec{k},t)\right]\\
i\frac{\partial}{\partial t}p_{2-}(\vec{k},t) - 2\omega p_{2-}(\vec{k},t) &= -\frac{1}{2m}k_+^2 n^*_{f2}(\vec{k},t)
\end{aligned}$$

The slowly and rapidly varying population equations comes out to be:

$$
\begin{aligned}
i\frac{\partial}{\partial t}n_s(\vec{k},t) &= -\frac{1}{m}\Big[k_-^2 p_s(\vec{k},t) + A^{*2}(0)p_{2+}(\vec{k},t) - 2k_-A^*(0)p_{1+}(\vec{k},t) \\
&\qquad - k_+^2 p_s^*(\vec{k},t) - A^2(0)p_{2+}^*(\vec{k},t) + 2k_+A(0)p_{1+}^*(\vec{k},t)\Big] \\
i\frac{\partial}{\partial t}n_{f1}(\vec{k},t) + \omega n_{f1}(\vec{k},t) &= -\frac{1}{m}\Big[k_-^2 p_{1+}(\vec{k},t) - 2k_-A^*(0)p_{2+}(\vec{k},t) - k_+^2 p_{1-}^*(\vec{k},t) \\
&\qquad - A^2(0)p_{1+}^*(\vec{k},t) + 2k_+A(0)p_s^*(\vec{k},t)\Big] \\
i\frac{\partial}{\partial t}n_{f1}^*(\vec{k},t) - \omega n_{f1}^*(\vec{k},t) &= -\frac{1}{m}\Big[k_-^2 p_{1-}(\vec{k},t) + A^{*2}(0)p_{1+}(\vec{k},t) - 2k_-A^*(0)p_s(\vec{k},t) \\
&\qquad - k_+^2 p_{1+}^*(\vec{k},t) + 2k_+A(0)p_{2+}^*(\vec{k},t)\Big] \\
i\frac{\partial}{\partial t}n_{f2}(\vec{k},t) + 2\omega n_{f2}(\vec{k},t) &= -\frac{1}{m}\Big[k_-^2 p_{2+}(\vec{k},t) - k_+^2 p_{2-}^*(\vec{k},t) \\
&\qquad - A^2(0)p_s^*(\vec{k},t) + 2k_+A(0)p_{1-}^*(\vec{k},t)\Big] \\
i\frac{\partial}{\partial t}n_{f2}^*(\vec{k},t) - 2\omega n_{f2}^*(\vec{k},t) &= -\frac{1}{m}\Big[k_-^2 p_{2-}(\vec{k},t) + A^{*2}(0)p_s(\vec{k},t) \\
&\qquad - 2k_-A^*(0)p_{1-}(\vec{k},t) - k_+^2 p_{2+}^*(\vec{k},t)\Big]
\end{aligned}
$$

The above set of equations is derived by neglecting the terms containing harmonics larger than those present in the Hamiltonian of the system. Now, we want to solve these set of equations. These equations may easily be solved by assuming that the external driving frequency (EDF) ω is very large compared to all other frequencies (so we can neglect the terms $\left|\frac{\partial f}{\partial t}\right|$ in comparison to $\omega|f|$). These simplifications gives the solution of the fast coefficients of population $n_{fl}(\vec{k},t)$ and polarization $p_{l+}(\vec{k},t)$ equations in terms of slow coefficients $n_s(\vec{k},t)$ and $p_s(\vec{k},t)$.

$$
\begin{aligned}
n_{f1}(\vec{k},t) &= -\frac{2k_+A(0)}{m\omega}p_s^*(\vec{k},t), \quad & n_{f1}^*(\vec{k},t) &= -\frac{2k_-A^*(0)}{m\omega}p_s(\vec{k},t) \\
n_{f2}(\vec{k},t) &= \frac{A^2(0)}{2m\omega}p_s^*(\vec{k},t), & n_{f2}^*(\vec{k},t) &= \frac{A^{*2}(0)}{2m\omega}p_s(\vec{k},t)
\end{aligned}
\tag{2.20}
$$

$$
\begin{aligned}
p_{1+}(\vec{k},t) &= \frac{1}{2m\omega}2k_+A(0)n_s(\vec{k},t) \\
p_{1-}(\vec{k},t) &= -\frac{1}{m\omega}\left[k_+^2\frac{k_-A^*(0)}{m\omega}p_s(\vec{k},t) + k_+A(0)\frac{A^{*2}(0)}{2m\omega}p_s(\vec{k},t)\right] \\
p_{2+}(\vec{k},t) &= -\frac{1}{4m\omega}A^2(0)n_s(\vec{k},t) \\
p_{2-}(\vec{k},t) &= \frac{k_+^2}{4m\omega}\frac{A^{*2}(0)}{2m\omega}p_s(\vec{k},t)
\end{aligned}
\tag{2.21}
$$

The simplified slow varying part of population and polarization equation comes out to be,

$$i\partial_t n_s(\vec{k},t) = -\frac{1}{m}\left[k_-^2\ p_s(\vec{k},t) - k_+^2\ p_s^*(\vec{k},t)\right] \tag{2.22}$$

$$i\partial_t p_s(\vec{k},t) = -\frac{1}{2m}\left[k_+^2\ n_s(\vec{k},t) + \alpha\ p_s(\vec{k},t)\right] \tag{2.23}$$

These equations may be solved by assuming that $n_s(\vec{k},t) = n_s(\vec{k},0)Cos(2\Omega t)$ and $n_s(\vec{k},0) = \frac{2|k_-|^2}{\alpha}$ is the equilibrium value of population which can be determined in mean field approximation, see Appendix A.1. This gives the solution for the slow part of polarization,

$$p_s(\vec{k},t) = \frac{k_+}{2k_-}\left[Cos(2\Omega t) + i\frac{4m\Omega}{\alpha}Sin(2\Omega t)\right] \tag{2.24}$$

$$\Omega = \left[\left(\frac{|k|^2}{2m}\right)^2 + \frac{\left(\omega_R^2 + 4\frac{|k|^2\omega_R}{m}\right)^2}{4\omega^2}\right]^{1/2},\ \alpha = \left(\frac{2m\omega_R^2}{\omega} + \frac{8|k|^2\omega_R}{\omega}\right)$$

$\Omega_{ARWA}^{BLG}(= 2\Omega)$ is the generalized anomalous Rabi frequency for BLG far from resonance. The anomalous Rabi frequency exactly at Dirac point can be found by setting $\vec{k} = 0$ in the expression of Ω and comes out to be equal to, $\Omega_{ARF} = \frac{\omega_R^2}{\omega}$ where $\omega_R = \frac{|A(0)|^2}{2m}$. This anomalous behavior of Rabi frequency in off resonance case is attributed to pseudospin degree of freedom of BLG.

We may equally easily write an approximate solution of Bloch Eqs. (2.4) and (2.5) in terms of slow coefficients $p_s(\vec{k},t)$ and $n_s(\vec{k},t)$ with the help of Eqs. (2.18) and (2.19) together with the fast coefficients.

$$\begin{aligned} n_{diff}(\vec{k},t) = n_s(\vec{k},t) &- \frac{2k_+A(0)}{m\omega}p_s^*(\vec{k},t)e^{-i\omega t} - \frac{2k_-A^*(0)}{m\omega}p_s(\vec{k},t)e^{i\omega t} \\ &+ \frac{A^2(0)}{2m\omega}p_s^*(\vec{k},t)e^{-2i\omega t} + \frac{A^{*2}(0)}{2m\omega}p_s(\vec{k},t)e^{2i\omega t} \end{aligned} \tag{2.25}$$

$$\begin{aligned} p(\vec{k},t) = p_s(\vec{k},t) &+ \frac{k_+A(0)}{m\omega}n_s(\vec{k},t)e^{-i\omega t} - \beta p_s(\vec{k},t)e^{i\omega t} - \frac{A^2(0)}{4m\omega}n_s(\vec{k},t)e^{-2i\omega t} \\ &+ \frac{k_+^2A^{*2}(0)}{8m^2\omega^2}p_s(\vec{k},t)e^{2i\omega t} \end{aligned} \tag{2.26}$$

where $p_s(\vec{k},t)$ given by Eq. (4.8),

$$\beta = \left(\frac{k_+^2 k_- A^*(0)}{m^2\omega^2} + \frac{k_+ A(0) A^{*2}(0)}{2m^2\omega^2}\right), \qquad n_s(\vec{k},t) = \frac{2|k_-|^2}{\alpha} Cos(2\Omega t)$$

Equations (2.25) and (2.26) gives the solution of Bloch Eqs. (2.4) and (2.5) far from resonance, when the external driving frequency is very large. In Eq. (2.26), third and last terms are proportional to $\mathcal{O}(\frac{1}{\omega^2})$, these terms can be neglected because we are working with very high intense optical pump field. Therefore, we have seen that bilayer graphene exhibits a second kind of Rabi oscillations far from resonance similar to single layer graphene. The difference is that the Rabi frequency has a different dependence on amplitude of external driving frequency. The frequency of these oscillations is even slower than the conventional Rabi oscillations. There is a special situation exactly at the Dirac point, $\vec{k} = 0$ where the Bloch equations may be solved exactly. The Bloch equations exactly at the Dirac point can be found by setting $\vec{k} = 0$ in Eqs. (2.4) and (2.5), as given below

$$\begin{aligned} i\partial_t n_{diff}(\vec{0},t) &= -\frac{1}{m}\left[\left(-A^*(0)\ e^{i\omega t}\right)^2 p(\vec{0},t) - h.c.\right] \\ i\partial_t p(\vec{0},t) &= -\frac{1}{2m}\left(-A(0)\ e^{-i\omega t}\right)^2 n_{diff}(\vec{0},t) \end{aligned} \tag{2.27}$$

The above set of equations reduces to the following set of ordinary differential equations with the substitution $p(\vec{0},t) = \tilde{p}(\vec{0},t)\ e^{-2i\omega t}$.

$$\begin{aligned} i\partial_t n_{diff}(\vec{0},t) &= -\frac{1}{m}\left[\left(-A^*(0)\right)^2 \tilde{p}(\vec{0},t) - h.c.\right] \\ i\partial_t \tilde{p}(\vec{0},t) + 2\omega\tilde{p}(\vec{0},t) &= -\frac{1}{2m}\left(-A(0)\right)^2 n_{diff}(\vec{0},t) \end{aligned}$$

The above equations may be solved directly by Mathematica using DSolve routine.

$$n_{diff}(\vec{0},t) = 1 + \frac{\omega_R^2}{\omega^2} Cos(\Omega t), \quad \tilde{p}(\vec{0},t) = \frac{\omega_R}{2\omega}\left(e^{i\Omega t} - 1\right) \tag{2.28}$$

where, $\Omega = \frac{\sqrt{4m^2\omega^2 + |A(0)|^4}}{m} \approx 2\omega + \frac{\omega_R^2}{\omega}$. Back substitution gives that the polarization oscillates with frequency $\frac{\omega_R^2}{\omega}$ which is the anomalous Rabi frequency exactly at the Dirac point, where $\omega_R = \frac{|A(0)|^2}{2m}$. Thus, we find that the carriers are oscillating even more slower frequency than the frequency in the resonance case.

In this way, we may conclude that Rabi oscillations in bilayer graphene show anomalous behaviour far from resonance and corresponding frequency known as

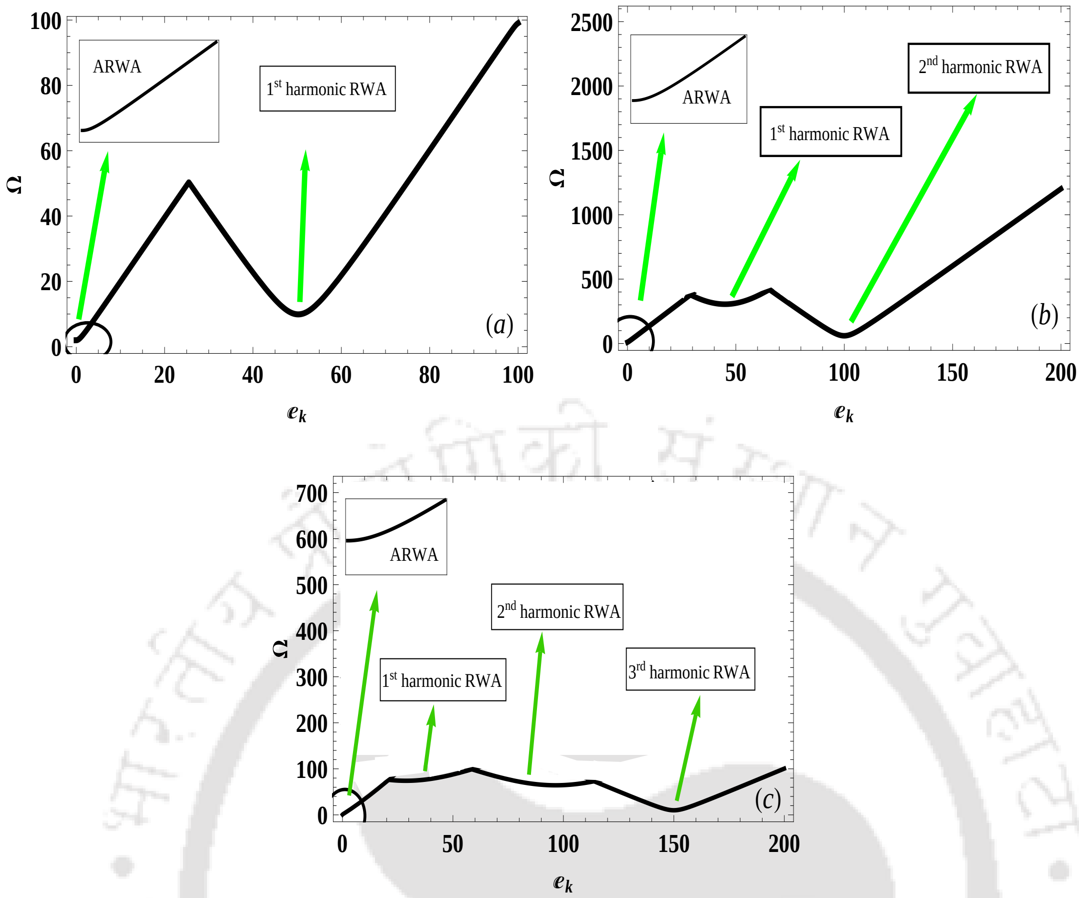

FIGURE 2.1: (a) Schematic of the effective Rabi frequency Ω versus band energy $e_k = v_F|k|$ for single layer graphene. In all three plots there is one anomalous Rabi frequency (ARF) close to $e_k = 0$. For a single layer, there is one conventional Rabi frequency (CRF) at $\omega = 2e_k$. (b) Schematic of the effective Rabi frequency Ω versus band energy $e_k = \frac{|k|^2}{2m}$ for BLG. In addition to one ARF, two resonances (CRFs) are possible, one is at single harmonic ($\omega = 2e_k$) and another is at second harmonic ($2\omega = 2e_k$) in external driving frequency. (c) Schematic of the effective Rabi frequency Ω versus band energy $e_k = \frac{v_0^3|k|^3}{\gamma_1^2}$ for trilayer graphene. In addition to one ARF, three resonances are possible at values of e_k determined by $\nu\omega = 2e_k$, $\nu = 1, 2, 3$. The ARF plot near $e_k = 0$, gets flatter as the number of layers increases. Vertical axes (ordinates) are exaggerated for clarity. The corresponding formulae are given in Appendix A.2.

anomalous Rabi frequency Ω_{ARWA}. In resonance case, bilayer graphene exhibits multiple harmonic resonances- one is at first harmonic in the external driving frequency. Second is at the second harmonic in the external driving frequency which is due to the frequency doubling effect. Frequency doubling effect is directly attributable to the quadratic dispersion of bilayer graphene. Thus the resonance case of bilayer graphene is quite different than the resonance case of single layer graphene. Bilayer graphene exhibits two harmonic resonances as explained above while in single layer graphene there is only one possible reonance [184]. This is made clearer in Fig. 2.1. Figures 2.1(a), (b) and (c) show an interpolation between RWA and ARWA regime. The resonance conditions are identified by the minimum observed in Ω versus e_k diagrams. We are interested only in the minimum of the diagrams because the amplitudes of the fast oscillations far from the minimum average out to zero. It is clear from these figures that there is only one minimum near the origin. This minimum corresponds to the anomalous resonance (far from conventional resonance) and the corresponding frequency is called anomalous Rabi frequency. Secondary minima, the minimum other than near the origin, are characterized by conventional resonances. In case of single layer graphene, there is only one secondary minimum observed that tells there is only one possible resonance in single layer graphene, Fig. 2.1(a). In case of bilayer graphene, two secondary minima are observed- one is at first harmonic resonance while second minimum occurs due to the frequency doubling effect in bilayer graphene, Fig. 2.1(b), whereas trilayer graphene exhibits three secondary minima, Fig. 2.1(c). This means trilayer graphene shows three harmonic resonances other than one minimum near the Dirac point which corresponds to the anomalous resonance. Thus we have seen that all the graphene based systems show only one anomalous minimum that means there is only one anomalous resonance possible in all graphene based systems. As the number of layers increase, the number of secondary minima increases. The number of secondary minima are directly proportional to the number of layers presented in the system considered. It means, in bilayer graphene there are two possible resonances while trilayer graphene possesses three possible conventional resonances and so on. The number of minima is directly attributable to the band structure of the system considered. In other words, we can say that the number of harmonic resonances present in the system can be directly identified with the number of harmonics appears in the Hamiltonian of the system under consideration. In the derivation of formulae of Rabi frequencies in conventional and anomalous resonances, the harmonics higher than that present in the system are ignored. If we are including the harmonics higher than the harmonics present in the system that leads to a slight modification in the original results and our approximation to the realistic results.

2.3 Current density in bilayer graphene

The natural question that arises is how to observe Rabi oscillations in RWA and ARWA regime experimentally. One way to answer this question is to calculate the current density in both the regimes. Current density is a gauge invariant and easily experimentally accessible quantity. Therefore, this section deals with the calculation of current density due to massive carriers in bilayer graphene in RWA and ARWA regimes. The current density is directly proportional to the inter-layer polarization (inter-band polarization) of carriers induced in presence of high intense applied electric field. The expression of current density can be obtained with the help of the continuity equation $\vec{\nabla} \cdot \vec{J}(\vec{r},t) = -\partial_t \rho(\vec{r},t)$, the quantum kinetic equation $i\hbar\partial_t \rho(\vec{r},t) = [\rho(\vec{r},t), H]$, $\rho(\vec{r},t)$ is the total density of carriers in the system considered, and the simple anti-commutator algebra for fermions. The compact form of current density in momentum space for bilayer graphene can be written as follows (the average current is independent of position, of course),

$$\begin{aligned}\langle \vec{J}(t) \rangle = &-\frac{1}{2\pi m}\sum_{\vec{k}} \left[(k_- - A^*(t))p(\vec{k},t) + h.c. \right] \hat{x} \\ &+ \frac{i}{2\pi m}\sum_{\vec{k}} \left[(k_- - A^*(t))p(\vec{k},t) - h.c. \right] \hat{y}\end{aligned} \tag{2.29}$$

Current density is, of course, a real quantity. A detailed calculation of Eq. (2.29) is given in appendix A.3.

2.3.1 Current density of bilayer graphene in RWA regime

As Eq. (2.29) exposes that current density solely depends on inter-layer polarization. The inter-layer polarization, in RWA regime, is given by Eq. (2.15). For small detuning Δ, the terms proportional to Δ in Eq. (2.15) can be neglected. Therefore, Eq. (2.15) reduces to the following,

$$p(\vec{k},t)|_{RWA} = -i\frac{k_+ A(0)}{4m\Omega_{RWA,\omega}} Sin(\Omega_{RWA,\omega}\ t)e^{-i\omega t} \tag{2.30}$$

Other terms will also not contribute because the contribution from other terms will be zero after integration over θ_k. Therefore, the x-component of the slow part of the current density can be written as,

$$\langle \vec{j}_x(t)\rangle = \frac{i}{2\pi m}\frac{A(0)}{4m}\sum_{\vec{k}}(k_- - A^*(t))\,\frac{k_+}{\Omega_{RWA,\omega}}Sin(\Omega_{RWA,\omega}\ t)$$

Writing $k_\pm = |k|e^{\pm i\theta_k}$ and performing integration over θ_k, all the terms drop out except the terms which oscillate with the first harmonic in external applied field. Therefore, in low-energy approximation we may write the current density in frequency domain to exhibit a threshold behavior.

$$j_x^s(\omega')|_{RWA,\omega} \approx \frac{A}{64\pi^2}\frac{A(0)}{\pi}\frac{\omega}{\sqrt{\omega'^2 - 2\omega\omega_R}}\Theta(\omega'^2 - 2\omega\omega_R) \tag{2.31}$$

where ω' is the frequency of Fourier transform of current density from time domain to frequency domain. Equation (2.31) gives the current density of bilayer graphene at first harmonic resonance. If we perform the similar calculation of current density of bilayer graphene at second harmonic resonance, we will get the following compact form of current density of bilayer graphene at second harmonic resonance.

$$j_x^s(\omega')|_{RWA,2\omega} \approx \frac{A}{16\pi^2 m}\frac{A^4(0)}{8A^*(0)}\frac{1}{\sqrt{\omega'^2 - \omega_R^2}}\Theta(\omega'^2 - \omega_R^2) \tag{2.32}$$

It is clear from Eqs. (2.31) and (2.32) that the current density in both the resonance cases shows a threshold behaviour in frequency domain. The threshold frequencies at the first and the second harmonic resonances are $\sqrt{2\omega\omega_R}$ and ω_R, respectively. In other words, we can say that the current density in the conventional resonance case shows two different kinds of threshold behaviour. This is pictorially shown in Fig. 2.2.

The asymptotic from of current density, after doing straight forward Fourier transformation from frequency to time domain of the current density Eqs. (2.31) and (2.32), in time domain can be written as follows,

$$j_x^s(t)|_{RWA,\omega} \approx \gamma\frac{Cos(\sqrt{2\omega\omega_R}\ t) - Sin(\sqrt{2\omega\omega_R}\ t)}{\sqrt{t}} \tag{2.33}$$

$$j_x^s(t)|_{RWA,2\omega} \approx \lambda\frac{Cos(\omega_R\ t) - Sin(\omega_R\ t)}{\sqrt{t}} \tag{2.34}$$

where γ and λ are constants that fit the dimension of current density. Equations (2.31) and (2.32) reveals that the slow part of current density in RWA case exhibits two different types of threshold behaviour, one is at first harmonic and another at the second harmonic in the external frequency. The corresponding Rabi frequencies are $(2\omega\omega_R)^{1/2}$ and ω_R respectively. The current density in both RWA cases has an amplitude that has a power law decay of the form $t^{-1/2}$, see Fig. 2.2.

2.3.2 Current density of bilayer graphene in ARWA regime

The current density in bilayer graphene in extreme non-resonance can be calculated in a similar way as we did in case of resonance case. The inter-layer polarization in ARWA case is given by Eq. (2.26). In this equation the terms proportional to $\mathcal{O}(\frac{1}{\omega^2})$ can be neglected because we are assuming that the frequency of the external applied field is very large. Inserting into the current density Eq. (2.29) and performing integration over θ_k, all the terms drop out except the terms which oscillate with the first harmonic in external applied field. Therefore, in low-energy approximation we may write the current density in frequency domain to exhibit a threshold behavior.

$$j_x^s(\omega^{'})|_{ARWA} \approx -\frac{A}{16\pi^2}\frac{\omega^2 A(0)}{32\omega_R^3}\left(\omega^{'}-\frac{\omega_R^2}{\omega}\right)\theta\left(\omega^{'}-\frac{\omega_R^2}{\omega}\right) \tag{2.35}$$

Near the threshold, when $\omega^{'} \approx \frac{\omega_R^2}{\omega}$, the current density exhibits a linear behaviour. The exponent at the threshold of induced current in BLG is thus found to be equal to unity whereas in SLG this exponent has been computed [184] to be equal to 1/2. The asymptotic forms of the current density in time domain in ARWA case can be written as,

$$j_x^s(t)|_{ARWA} \approx \beta\frac{e^{-i\frac{\omega_R^2}{\omega}t}}{t^2} \tag{2.36}$$

where β is a constant that fits the dimension of current density. Therefore, it is obvious from Eq. (2.36) that the slow part of the current density in off resonance oscillates with the threshold frequency $\frac{\omega_R^2}{\omega}$ with the amplitude exhibiting a power-law decay t^{-2}. The threshold behaviour of current density in off resonance case is pictorially shown in Fig. 2.2.

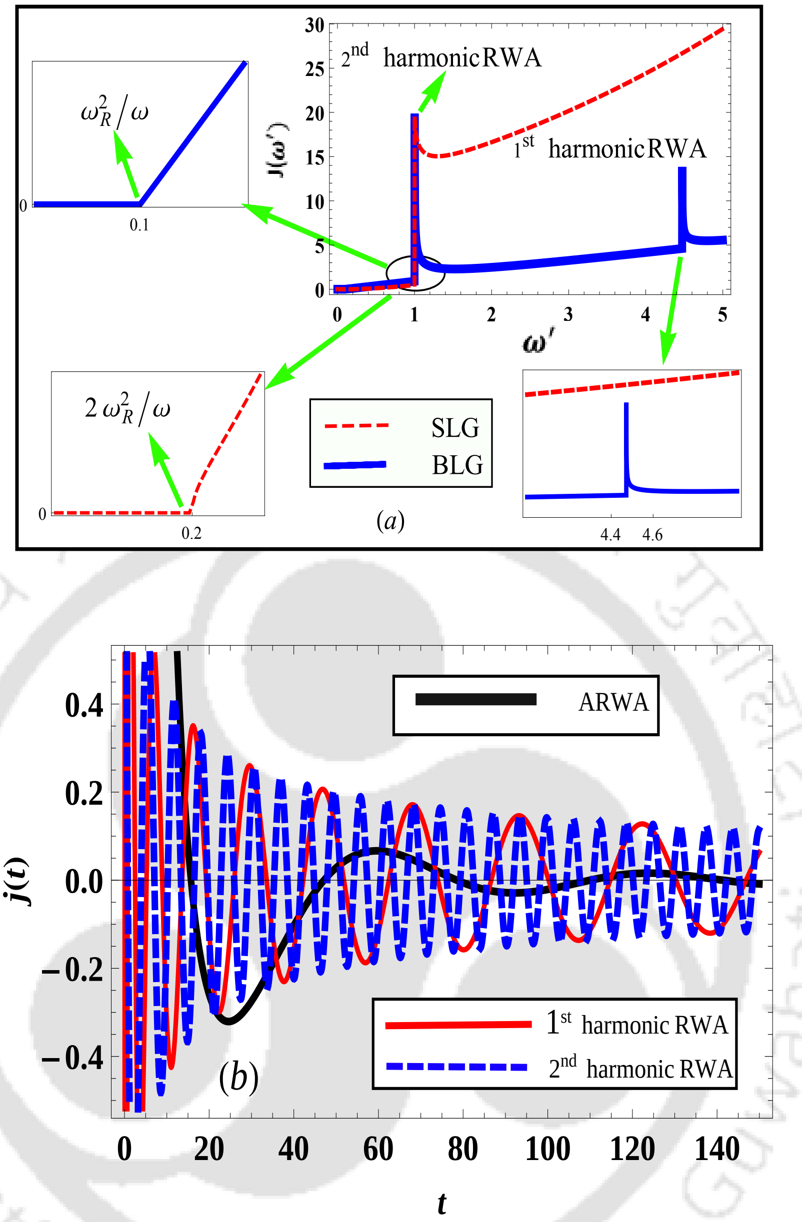

FIGURE 2.2: (a) Schematic of the variation of slow part of current density $j(\omega')$ with frequency ω' of BLG (blue solid curve) for zero detuned Rabi frequency $\omega_R = 1$ in arbitrary units. The slow part of current density exhibits threshold behavior at the anomalous Rabi frequency, ω_R^2/ω. Near threshold, the current density exhibits linear behavior unlike SLG [184] (red dashed curve) where the current is proportional to the square root of the deviation from the resonant frequency (red dashed curve shown in the inset of the diagram). (b) This plot shows the variation of current density $j(t)$ versus t. The solid thick black curve shows ARO in the time domain. The solid red and dashed blue lines show the first and second harmonic RWA case respectively. The frequency associated with solid red and dashed blue curves are $\sqrt{2\omega\omega_R}$ and ω_R, respectively.

2.4 Numerical solution of the problem

In the above study, we have solved Bloch equations analytically in different regions of interest namely- RWA and ARWA. In this section, we present a fully numerical simulation of the Bloch equations. Numerical simulation affirms the findings

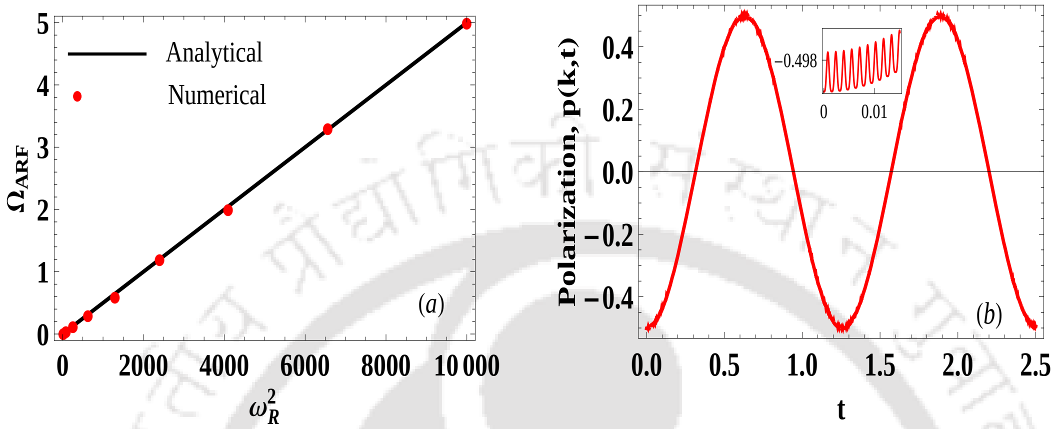

FIGURE 2.3: Fully numerical simulation (a) is a schematic of the variation of ARF versus $\omega_R^2 (= \frac{|A(0)|^4}{4m^2})$ ∼square of the intensity of the applied field. The ARF found analytically, solid black line, is in good agreement with the numerical simulation, red dots. (b) Shows the slow as well as rapidly (inset) varying part of population $p(\vec{k}, t)$ versus time t. For plotting purposes, we have chosen the parameters $\frac{k_-}{\sqrt{2m}} = 0$, $\frac{A(0)}{\sqrt{2m}} = 10$ and $\omega = 2000$, in arbitrary units. The frequency obtained from plot (b) is in complete agreement with analytical expectations.

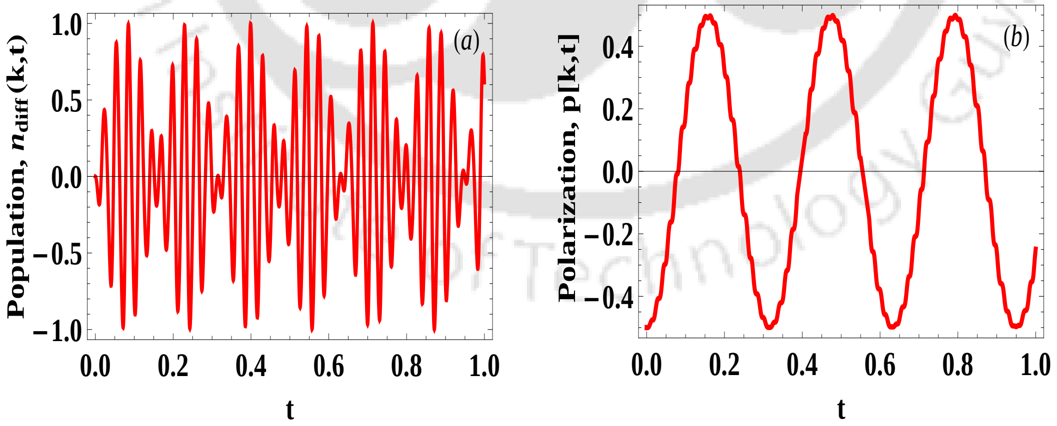

FIGURE 2.4: Schematic of the slow as well as rapidly varying population $n_{diff}(\vec{k}, t)$ and polarization $p(\vec{k}, t)$ versus time t at first harmonic resonance, respectively . The frequency of oscillation matches with the expectations from analytical solution. To plot we have chosen the parameters, $\frac{k_-}{\sqrt{2m}} = 10$, $\frac{A(0)}{\sqrt{2m}} = 1$ and $\omega = 200$.

of the other sections discussed so far. We have employed the NDSolve routine of Mathematica (Appendix A.4) on the Bloch equations to generate the plots of population and polarization with respect to time.

In this section, no approximations of any kind are involved so the results obtained would be reliable and if they agree with the approximate analytical results, it would provide immediate vindication of the approximation methods used. The analytical (black line) anomalous Rabi frequency is in excellent agreement with the numerical simulation (red dots). This is diagrammatically shown in Fig. 2.3(a). Far from resonance, the slow part of polarization oscillates exactly with the ARF that matches with the frequency inferred from numerical simulations, refer to Fig. 2.3(b). The fast oscillations are shown in inset of Fig. 2.3(b). The frequency of fast oscillations is exactly the frequency of the external field. Figure (2.4) shows the numerical solution of Bloch equations in first harmonic resonance for population and polarization, respectively. The frequency of oscillation determined from plot is consistent with the analytical result.

2.5 Anomalous Rabi oscillations in multi-layer graphene

In this section, we describe how to generalize the ideas of the previous discussion to n-layer graphene, also known as multi-layer graphene (MLG) [185]. The layered structure make it very high exceptionally anisotropic material. This section is devoted to deriving the generalized form of the formulae of the previous sections. MLG can be formed by the stacking of single graphene sheets one on the top of the other - either in ABAB... arrangement (Bernal stacking) or ABCABC.. pattern (Rhombohedral stacking), see Fig. 2.5. The MLG can be prepared by mechanical exfoliation of highly ordered pyrolytic graphite. Multi-layer graphene with less than ten layers each show different electronic band spectrum. For the present discussion, ABC-stacking is considered. These layers are weakly coupled by a Van der Waals forces.

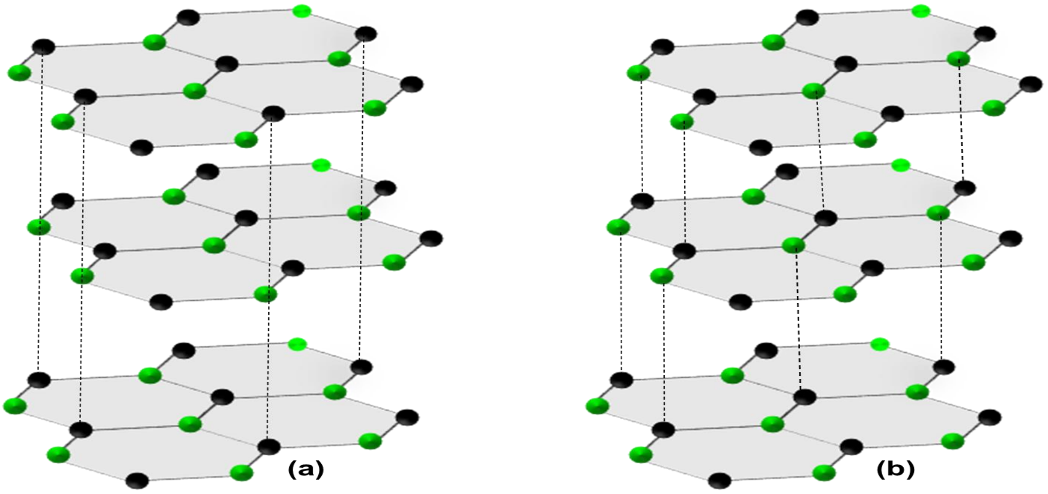

FIGURE 2.5: Schematic diagrams of few layer graphene crystal structure: (a) ABAB... arrangement (Bernal stacking) and (b) ABC.... arrangement (Rhombohedral stacking). A and B corresponds to green and black colour circles respectively.

2.5.1 Hamiltonian of multi-layer graphene

The two band model Hamiltonian [16, 23, 186] of ABC-stacked n-layer graphene can be written as follows,

$$H_n = \frac{v_0^n}{(-\gamma_1)^{(n-1)}} \begin{pmatrix} 0 & k_-^n \\ k_+^n & 0 \end{pmatrix} \tag{2.37}$$

In terms of second quantization, the effective low energy Hamiltonian Eq. (2.37) can be read as follows,

$$H_n = \lambda \sum_{\vec{k}} \sum_{j=1}^{n-1} \left[K_-^n c_{Aj}^\dagger(\vec{k},t) c_{B(j+1)}(\vec{k},t) + h.c. \right] \tag{2.38}$$

where $\lambda = v_0^n/(-\gamma_1)^{(n-1)}$, $K_- = k_- - A^*(0)e^{i\omega t}$, $K_+ = K_-^*$, $k_\pm = k_x \pm ik_y$, $A(0) = \frac{e}{c}(A_x(0) + iA_y(0))$ is the complex vector potential which couples to MLG in the transverse gauge, $(\vec{\nabla} \cdot \vec{A} = 0)$. The index n starts from $n = 2, 3, 4, ...$ for two, three, four layers respectively. The single layer $n = 1$ is a special case which we have already dealt separately [184]. Nevertheless, we may recover the single layer graphene Hamiltonian by setting $n = 1$ and removing the summation and all the indices. The symbol j denotes the effective inter-layer hopping between non-dimer states through the dimer states is accomplished by coupling the j^{th} layer to the $(j+1)^{th}$ layer.

2.5.2 Bloch equations for n-layer graphene

In this section, we derive the Bloch equation for n-layer graphene. These equations can be derived by adopting a process similar to described in case of bilayer graphene. Just as in bilayer graphene, here too, we define dynamical quantities such as population and polarization as shown below,

$$\begin{aligned} N_{\nu\,\nu+1}(\vec{k},t) &= \langle c^{\dagger}_{A\nu}(\vec{k},t)c_{A\nu}(\vec{k},t)\rangle - \langle c^{\dagger}_{B(\nu+1)}(\vec{k},t)c_{B(\nu+1)}(\vec{k},t)\rangle \\ \pi_{\nu\,\nu+1}(\vec{k},t) &= \langle c^{\dagger}_{A\nu}(\vec{k},t)c_{B(\nu+1)}(\vec{k},t)\rangle \end{aligned} \tag{2.39}$$

where the index $\nu = 1, 2, ...$ labels a layer in MLG. If $\nu = 1$, two graphene layers will be involved and if $\nu = 2$, three graphene layers will be involved and so on. The quantum kinetic equations for $n_{\nu\,\nu+1}(\vec{k},t)$ and $\pi_{\nu\,\nu+1}(\vec{k},t)$ of n-layer graphene reads,

$$\begin{aligned} i\partial_t N_{\nu\,\nu+1}(\vec{k},t) &= \lambda\left[2K^n_-\;\pi_{\nu\,\nu+1}(\vec{k},t) - h.c.\right] \\ i\partial_t \pi_{\nu\,\nu+1}(\vec{k},t) &= \lambda K^n_+\;N_{\nu\,\nu+1}(\vec{k},t) \end{aligned} \tag{2.40}$$

These are the coherent optical Bloch equations of multilayer graphene.

2.5.3 Solution of Bloch equations

In this section, the Bloch equations of n-layer graphene are solved applying a process similar used to solve the Bloch equations of bilayer graphene. These equations are solved in different regions of interest. First we solve these equations exactly at Dirac point where $\vec{k} = 0$. These equations are also solved near Dirac point in conventional as well as in off resonance case using RWA and ARWA, respectively.

Case -I: At Dirac point, $\vec{k} = 0$

At the Dirac point, $\vec{k} = 0$, the coupled Bloch equations for n-layer graphene may be solved using an ansatz, $\pi_{\nu\,\nu+1}(\vec{0},t) = \pi_{\nu\,\nu+1,\,s}(\vec{0},t)\;e^{-in\omega t}$. Making this substitution and performing a straightforward calculation we may write the solution of Bloch equations

$$\begin{aligned} N_{\nu\,\nu+1}(\vec{0},t) &= \frac{4\lambda(-A(0))^n}{n\omega}\pi^*_{\nu\,\nu+1,\,s}(\vec{0},0)\ Sin(\Omega_R t) \\ \pi^*_{\nu\,\nu+1,\,s}(\vec{0},t) &= \pi^*_{\nu\,\nu+1,\,s}(\vec{0},0)\ e^{-i\Omega_R t},\ \ \Omega_R \approx n\omega + \Omega^{MLG}_{ARF} \end{aligned} \tag{2.41}$$

where $\Omega^{MLG}_{ARF} = \frac{2\omega_R^2}{n\omega}$ is the generalized ARF for n-layer graphene at the Dirac point with which the slow part of polarization oscillates and $\omega_R = \lambda\ |A(0)|^n$. As we have been stressing, this ARF is observable only in the systems that possess a pseudospin degree of freedom. One may see that while the ARO in polarization appears to be associated with the n^{th} harmonic in the EDF ω for n-layer graphene, in reality, the overall polarization $p(\vec{0},t)$ is slowly varying on the scale of the EDF. However the population does oscillate according to the n^{th} harmonic in EDF.

Case -II: Near the Dirac point (off resonance $\omega \gg \omega_R, \lambda|k|)^n$)

This section describes how to solve the Bloch equations for n-layer graphene using the ARWA method discussed earlier. The main assumption involved in ARWA is that the EDF (ω) is the largest frequency. In order to solve the Bloch equations we decomposed population $n_{\nu\,\nu+1}(\vec{k},t)$ and polarization $\pi_{\nu\,\nu+1,\,s}(\vec{k},t)$ into slow and fast varying equations, as we did for BLG. But, this time the summation over l will run from $l = 1$ to $l = n$. Since in SLG, ARO are observed at the level of first harmonic whereas in BLG these are observed at second harmonic. Therefore, it forces us to keep all the harmonics in case of n-layer graphene to see the ARO. Inserting these equations into the Bloch equations and following a process described in case of bilayer graphene far from resonance, we may easily write the solution of rapidly varying polarization and population equations in terms of their slowly varying coefficients. The slowly varying part of population and polarization equations will be,

$$\begin{aligned} i\partial_t n_s(\vec{k},t) &= 2\lambda k_-^n \pi_s(\vec{k},t) - 2\alpha k_+^n\ \pi_s^*(\vec{k},t) \\ i\partial_t \pi_s(\vec{k},t) &= \lambda k_+^n n_s(\vec{k},t) - 2\beta\pi_s(\vec{k},t) \end{aligned} \tag{2.42}$$

The solution of these equations can easily be found by assuming the solution of the slow part of population equation in the form of $n_s(\vec{k},t) = n_s(\vec{k},0)Cos(2\Omega t)$.

The solution of the slow part of polarization equation comes out to be,

$$\begin{aligned}\pi_s(\vec{k},t) &= \pi_s(\vec{k},0)\left[-i\frac{\beta}{\Omega}Cos(2\Omega t) + Sin(2\Omega t)\right] \\ \Omega = \left[\lambda^2|k|^{2n} + \beta^2\right]^{\frac{1}{2}}, &\ \beta = \sum_{l=1}^{n}\frac{(\lambda C_l^n)^2\ |k|^{2(n-l)}\ |A(0)|^{2l}}{l\omega}\end{aligned} \tag{2.43}$$

where $\Omega^n_{ARWA}(= 2\Omega)$ is the generalized anomalous Rabi frequency for n-layer graphene and $\pi_s(\vec{k},0) = (-1)^n \frac{k_+^n}{2|k|^n}$ and $n_s(\vec{k},0) = -\frac{(-1)^n\lambda|k|^n}{\beta}$ are the equilibrium values of polarization and population, and may be determine in the mean field approximations. From these general expressions of equilibrium values of polarization and population, we can easily write the the expressions of equilibrium values of polarization and population in case of single and bilayer graphene by simply putting $n = 1$ and $n = 2$, respectively. We can reproduce the formulae of anomalous Rabi frequency of single and bilayer graphene by simply putting $n = 1$ and $n = 2$ in Eq. (2.43), respectively.

Case -III: Near resonance ($\omega \approx 2\lambda|k|)^n$)

This section deals with the solution of Bloch equations in the resonance case for small detuning, $\Delta \ll (\nu\omega - 2\lambda|k|^n)$, where ν denotes the number of resonances present in the particular graphene system i.e. if $n = 1$ then $\nu = 1$ and only one resonance will be present, for BLG $n = 2$, two resonances will occur. The one at $\nu = 1$ occurs at single harmonic in EDF and the second at $\nu = 2$ is due to the frequency doubling effect in BLG absent in SLG and so on. First, we write the Bloch equations in matrix form then find the diagonalization matrix of the time independent part of the Hamiltonian thereafter use the appropriate substitutions to solve the Bloch equations. The conventional Rabi frequency comes out to be,

$$\Omega^{MLG}_{RWA} = \sqrt{\Delta^2 + \omega_R^2},\ \omega_R = \lambda C^n_\nu |A_c(0)|^\nu |k|^{n-\nu} \tag{2.44}$$

where $C^n_\nu = \frac{n!}{\nu!(n-\nu)!}$ are combinatorial factors. Equation (2.44) is the general form of conventional Rabi frequency of n-layer graphene in resonance case. All the conventional resonance results in single and bilayer graphene can be found directly from Eq. (2.44) by simply putting $n = 1$ and $n = 1, 2$, respectively.

2.5.4 Current density in n-layer graphene

In order to compute the current density in n-layer graphene, we adopt a procedure similar to discussed in bilayer graphene. The expression of current density in n-layer graphene will be of the form, $\langle J_\nu(t)\rangle = J_x\hat{x} + J_y\hat{y}$ where J_x, J_y defined as $J_{\nu,\pm} = J_x \pm iJ_y$ where $J_{\nu,+}$ reads as,

$$\langle J_{\nu,+}(t)\rangle = \frac{2n\lambda}{2\pi}\sum_{\vec{k}}\sum_{l=0}^{n-1} C_l^{n-1} k_-^{n-1-l}(-A^*(0))^l e^{il\omega t}\ \pi_{\nu\nu+1}(\vec{k},t) \tag{2.45}$$

Inserting the value of polarization $\pi_{\nu\nu+1}(\vec{k},t)$ in above equation and doing straightforward simplification, Eq. (2.45) reduces to the following equation,

$$\langle J_{\nu,+}(t)\rangle = -\frac{n\lambda}{\pi}\sum_{\vec{k}}\frac{(-1)^n|k|^n}{(-A^*(0))}Cos(\Omega_{ARWA}^{MLG}t)e^{-i\omega t} \tag{2.46}$$

Equation (2.46) is the basic equation to find the current density in n-layer graphene. After performing integration over $\vec{k}$ in above equation, in the low-energy approximation, the general expression of current density in frequency domain comes out to be

$$\langle J_{\nu,+}(\omega')\rangle = J_0\left(\omega' - \frac{2\omega_R^2}{n\omega}\right)^{\frac{n}{2}} \tag{2.47}$$

where J_0 is constant that fit the dimension of current density. It must be stressed that the current density in Eq. (2.47) is valid only in low energy approximations and near the threshold when $\omega' \approx \frac{2\omega_R^2}{n\omega}$.

Before summarizing our results we wish to clarify that the theory presented here is not valid for bulk graphite. The term ‘n-layer’ should not be confused with ‘graphite’. It is used to describe ‘few-layer’ graphene or multi-layer graphene not ‘bulk graphite’. In the present discussion, we use RWA and ARWA on low-energy effective theory of monolayer, bilayer and few-layer graphene. Low-energy effective theory means we have considered only the nearest neighbour hopping. If we include next nearest hopping, the methodology presented in this chapter still remains valid. The next nearest hopping give rise nonlinearity in the band structure of graphene systems which includes higher energy electronic states. However, the present discussion does not include any nonlinearity. Eq. (2.37) holds only for few-layer low-energy electronic spectrum. It is not valid for bulk graphite because we are not discussing graphite using the band structure of graphene.

2.6 Summary and conclusions

In this section, we give overall summary of the work presented in this chapter. In this chapter, we have described Rabi oscillations, which is a well-known nonlinear optical phenomenon in quantum optics, in different regions of interest, namely-resonance and off resonance regimes. To describe the phenomenon of Rabi oscillations in bilayer graphene we first derived the Bloch equations for population and polarization in a similar way as in case of two-level atomic systems. Then, these equations are solved in resonance and off resonance case. Bloch equations in off resonance are solved using a new technique called asymptotic rotating (ARWA) which is an alternative approach to rotating wave approximation (RWA) well-known in quantum optics. It is found that Rabi oscillations in off resonance case show an anomalous behaviour similar to that of single layer graphene. The anomalous behaviour of Rabi oscillations is attributable to the pseudospin degree of freedom these systems possess. The anomalous Rabi frequency in these systems has a different dependence on the external electric field from the conventional one. In conventional resonance case, more than one layer graphene systems show multiple harmonic resonances depending upon the system chosen. In multi-layer graphene, multiple conventional harmonic resonances occur because of presence of multiple harmonics in the system of Hamiltonian in presence of external applied field. The number of conventional harmonic resonances present in the graphene systems are directly attributed to the dispersion relation of these systems. For example, single layer graphene possesses linear energy-momentum dispersion. Therefore, single layer graphene possesses single conventional resonance. Charge carriers in bilayer graphene show parabolic energy-momentum dispersion. So, bilayer graphene exhibits two conventional harmonic resonances- one is at first harmonics in external driving frequency and other is at second harmonics in external driving frequency which occurs due to the frequency doubling effect. Similarly, trilayer graphene exhibits three harmonic resonances and so on. This is pictorially shown in Fig. 2.1. It is seen that, the frequency of anomalous Rabi oscillations in bilayer graphene is less by the order of $\frac{1}{\omega}$ than the frequency of conventional Rabi oscillations in resonance case. In this figure, there is only one minimum is seen near $e_k = 0$ which is the anomalous Rabi frequency in each graphene systems. Whereas, the conventional resonances are shown by the secondary minima for each graphene system. There is only single secondary minimum in case of single layer graphene while as the number of layers increases the number of secondary minima increases. Number of secondary minima is directly proportional to the number of layers. There are two secondary minimum in bilayer graphene and in trilayer graphene three secondary minima are present. It means multi-layer graphene shows multiple conventional resonances whereas there is only single anomalous resonance is present in each graphene systems. In other words, we can say that multi-layer graphene exhibits only single anomalous resonance in off resonance regime while there are multiple conventional resonance are present in multi-layer graphene.

We have also calculated the experimentally accessible quantity current density in bilayer graphene. Current density in bilayer graphene shows a threshold behaviour in frequency domain that oscillates exactly with the anomalous Rabi frequency ($\frac{\omega_R^2}{\omega}$) in off resonance regime. Whereas, in resonance case current density exhibits two threshold behaviours in frequency domain- one is at first harmonic resonance and other is at second harmonic resonance. The frequency of oscillations at first and second harmonic resonances are $\sqrt{2\omega\omega_R}$ and ω_R, respectively, where $\omega_R = \frac{|A(0)|^2}{2m}$. The threshold behaviour of current density in different regions of interest is clearly shown in Fig. 2.2. The exponent at threshold in ARWA regime in bilayer graphene is computed to be equal to *unity* whereas it is equal to $\frac{1}{2}$ in case of single layer graphene. The current density in time domain shows a power law decay of the form t^{-2} in ARWA case whereas in both RWA cases it is of the form $t^{-\frac{1}{2}}$.

A fully numerical solution of Bloch equations is also presented that completely corroborates the analytical findings.

We have successfully generalized the ideas applied on single and bilayer graphene to multi-layer graphene. The results obtained in case of single and bilayer graphene can easily be recovered with the help of generalized formulae obtained in case of multi-layer graphene. It is seen that there is a single anomalous resonance present in multi-layer graphene whereas there are multiple conventional resonances present in multi-layer graphene. Number of multiple conventional resonances depend on the number of layers present in the multi-layer graphene system.

The work presented in this chapter has been taken from Ref.[187]

Chapter 3

Anomalous Rabi oscillations in Supported Graphene Systems

.

In chapter 2, we studied AROs in suspended graphene systems. Suspended graphene systems (free standing graphene systems) possess a zero gap between the valance and the conduction band. Therefore, these systems cannot be used in electronic devices. Absence of gap in electronic spectrum does not permit the turning off the electronic devices. To use graphene as a viable semiconductor in electronic devices a gap is required to turn off these devices. Therefore, to make use of graphene in electronic applications, it is very important to open a tunable and sizable band gap in the electronic spectrum of graphene. There are several methods to open a gap between the valance and the conduction band. This gap may be opened usually by symmetry breaking through extrinsic effects [188]. The electronic spectrum of gapped graphene is parabolic similar to bilayer graphene without gap which is quite different from gapless graphene. The carriers in gapped graphene no longer massless but are now massive. These massive carriers in gapped graphene possess a parabolic dispersion between energy and momentum [189]. Thus, the asymmetry breaks the valley degeneracy in monolayer graphene. The gap between the valance band and the conduction band can also be open in presence of substrate-graphene interaction upon which the graphene sheet is deposited. Several attempts have been made to open a gap by depositing graphene on different substrates and different values of the gap parameter is found in each case.

Using density functional theory, Quhe and collaborators [190] show that when single layer graphene is properly sandwiched between a pair of hexagonal boron nitride single layers, a gap of $0.16eV$ and $0.34eV$ can be opened without and with electric field, respectively. Hexagonal boron nitride consists of single layers of BN of a honeycomb structure almost commensurate to single layer graphene. Mak et al. [35] studied the gap opening in the electronic spectrum of bilayer graphene by applying a perpendicular electric field to the plane of bilayer graphene. They successfully induced a gap of $0.2eV$ in the electronic spectrum of bilayer graphene in the presence of a strong applied electric field, about $1V/nm$. In bilayer graphene two types of asymmetries are possible: intra- and inter-layer asymmetry. The effect of intra-layer symmetry on electronic spectrum is similar to gapped graphene. While, the effect of inter-layer asymmetry on electronic spectrum is very dramatic than intra-layer asymmetry. An inter-layer asymmetry gives rise to a 'Mexican-hat' like structure in the band structure of the bilayer graphene [16, 29, 65, 191, 192]. The properties of gapped monolayer and bilayer graphene are also discussed in the extensive literature available [46, 193–196].

In present chapter, we discuss the same phenomenon described in chapter 2 in gapped monolayer and bilayer graphene in presence of an intense optical pump field. The phenomenon of Rabi oscillation is analysed in two different regions of interest namely–the resonance and the off resonance case. In the case of symmetric graphene, Rabi oscillations close to resonance have already been discussed in the literature [175, 177, 181] using rotating wave approximation (RWA) [151, 152]. To analyze the phenomenon of Rabi oscillations in off resonance in gapped graphene systems, we use a similar methodology as described in Chapter 2 in symmetric graphene systems. In off resonance, the gapped graphene systems ('graphene systems' mean – monolayer and bilayer graphene) show offset oscillations even for vanishingly small applied electric fields– a feature absent in the symmetric graphene systems. These offset oscillations are characterized by the asymmetry parameter in these systems. In bilayer graphene, inter-layer asymmetry has a dramatic effect on anomalous Rabi oscillations. Conventional Rabi oscillations, however, are not significantly affected by the asymmetry parameter in these graphene systems. This is made clear from the following discussion.

3.1 Effect of asymmetry on Rabi oscillations in single layer graphene

This section describes the effect of asymmetry on Rabi oscillations in resonance as well as in off resonance case in single layer graphene. The conventional ROs (ROs in resonance case) are almost not affected by the asymmetry parameter (gap parameter). On the other hand, ROs in off resonance are very highly sensitive to the gap parameter.

3.1.1 Effective low-energy Hamiltonian of gapped single layer graphene

The low-energy Hamiltonian of graphene honeycomb lattice is derived using the tight binding model [92]. This honeycomb lattice is made from two sublattices, A and B, connected by time-reversal symmetry (SU(2) symmetry). Therefore, the Hamiltonian of gapless graphene is symmetric under the transformation of $A \longleftrightarrow B$, and the massless Dirac fermions show gapless linear energy–momentum dispersion at the Dirac points. The zero gap dispersion implies that the conduction of electrons cannot be simply toggled by the external gate voltage, and this limits the use of graphene in electronic applications. This gapless energy dispersion of graphene has been derived by assuming that the on-site energy of electrons in the sublattices A and B are equal, $H_{AA} = H_{BB}$. Whenever $H_{AA} \neq H_{BB}$, a mass term exists which is responsible for opening of a gap in the energy spectrum. This mass term breaks the symmetry between the two sublattices A and B, and graphene becomes asymmetric under the transformation of $A \longleftrightarrow B$. Now the graphene Hamiltonian will no longer be symmetric under this transformation. There are various ways to induce this mass term such as interaction of graphene sheet with the substrate upon which graphene sheet is deposited [188, 196], sandwiching a monolayer graphene between a pair of hexagonal Boron nitride layers [190] or applying an external electric field perpendicular to plane of the graphene sheet. There are experimental and theoretical [189, 193] research articles available on the topic of generation of a gap in the energy spectrum of graphene.

The effective low energy Hamiltonian [92] of gapped monolayer graphene can then be written as a pure graphene Hamiltonian and a term that describes the creation of a mass term

$$H = H_0 + H_{mt} \tag{3.1}$$

where, $H_0 = v_F(\vec{\sigma} \cdot \vec{p})$ is the intrinsic graphene Hamiltonian and $H_{mt} = v_F^2 m_t \sigma_z$ is the Hamiltonian of the mass term that may arise due to sublattice space asymmetry between A and B sublattices. The energy eigenvalues of Hamiltonian Eq. (3.1) are derived in Refs. [189, 194] as given below:

$$E_{\pm}(\vec{k}) = \sqrt{(v_F^2 m_t)^2 + \gamma_2 |f(\vec{k})|^2} \tag{3.2}$$

where $f(\vec{k}) = e^{i\frac{k_x a}{\sqrt{3}}} + 2e^{-i\frac{k_x a}{\sqrt{3}}} Cos(\frac{k_y a}{2})$ and γ is the transfer integral. Equation (3.2) gives the parabolic dispersion for the charge carriers (Fig. 3.1).

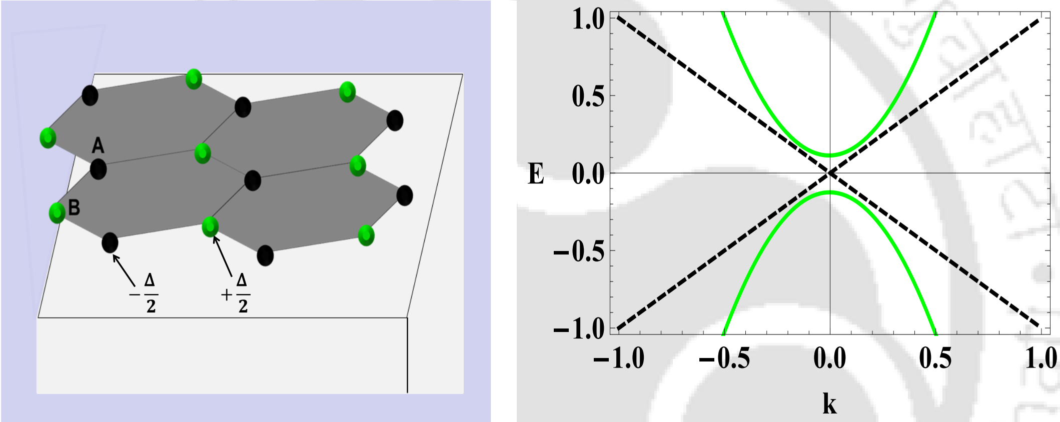

FIGURE 3.1: Left: Schematic of the graphene sheet deposited upon a substrate. Δ is the on-site energy of the atoms on sublattice sites A and B that defines the intra-layer asymmetry between two sublattices and gives rise a mass term in the monolayer graphene Hamiltonian Eq. (3.1). Right: Energy band spectrum of single layer graphene with (solid green) and without asymmetry (dashed black). The energy spectrum of asymmetric single layer graphene has a parabolic dispersion and shows a band gap between the conduction and valance band.

To describe the phenomenon of Rabi oscillations a semiclassical approximation is used, radiation is treated classically and matter fields are quantum. An in plane electric field is applied to the graphene sheet through a vector potential of the form $\vec{A}(t) = \vec{A}(0)e^{-i\omega t}$, where $\vec{A}(0) = \frac{e}{c}(A_x(0) + iA_y(0))$ is a complex amplitude of an external driving field. In second quantization, using two-component basis eigenstates of Hamiltonian Eq. (3.1) in momentum space of the form $\psi^T(\vec{k}, t) =$

$(c_A(\vec{k},t)\ c_B(\vec{k},t))$, the Hamiltonian Eq. (3.1) reads as

$$\hat{H} = \sum_{\vec{k}} \left[v_F \left(k_+ - A^*(t)\right) c_A^\dagger(\vec{k},t) c_B(\vec{k},t) + h.c. \right] \\ + v_F^2 m_t \sum_{\vec{k}} \left[c_A^\dagger(\vec{k},t) c_A(\vec{k},t) - c_B^\dagger(\vec{k},t) c_B(\vec{k},t) \right] \tag{3.3}$$

where $k_\pm = k_x \pm ik_y$, $c(c^\dagger)$ are the annihilation(creation) operators on sublattice sites A and B and vice versa. If mass term is zero, the Hamiltonian Eq. (3.1) commutes with the helicity operator $\hat{h}$ (projection of pseudo-spin in the direction of momentum) that preserves the SU(2) symmetry. In presence of a mass term, the Hamiltonian Eq. (3.1) does not commute with helicity operator $\hat{h}$. This breaks SU(2) symmetry of Hamiltonian Eq. (3.1). It means the time reversal symmetry has been broken or we can say that there exists a sublattice space asymmetry between two sublattices A and B. This also signifies that we cannot produce the crystal of graphene by simply repetition of a unit cell in two dimensions.

3.1.2 Bloch equations of gapped graphene

In this section, we derive the Bloch equations of population and polarization excess on sublattice sites A and B in gapped graphene. In second quantization, these quantities are expressed as follows,

$$\begin{aligned} n_{diff}(\vec{k},t) &= \langle c_A^\dagger(\vec{k},t)\ c_A(\vec{k},t)\rangle - \langle c_B^\dagger(\vec{k},t)\ c_B(\vec{k},t)\rangle \\ p(\vec{k},t) &= \langle c_A^\dagger(\vec{k},t)\ c_B(\vec{k},t)\rangle \end{aligned} \tag{3.4}$$

With the help of the equations of motion for operators $i\partial_t\hat{\rho} = [\hat{\rho}, H]$, and simple anti-commutator algebra for fermions, the Bloch equations of $n_{diff}(\vec{k},t)$ and $p(\vec{k},t)$ reads as (setting $\hbar = 1$),

$$i\partial_t n_{diff}(\vec{k},t) = 2v_F \left[\left(k_+ - A^*(t)\right) p(\vec{k},t) - h.c. \right] \tag{3.5}$$

$$i\partial_t p(\vec{k},t) = v_F \left(k_- - A(t)\right) n_{diff}(\vec{k},t) - 2v_F^2 m_t p(\vec{k},t) \tag{3.6}$$

These are the rate equations of the population excess $n_{diff}(\vec{k},t)$ and polarization $p(\vec{k},t)$ on sublattice site A and B. Where $k_\pm = k_x \pm ik_y$, $\vec{A}(t) = \vec{A}(0)e^{-i\omega t}$, and $\vec{A}(0) = \frac{e}{c}\left(A_x(0) + iA_y(0)\right)$. The asymmetry affects only the rate equation of polarization $p(\vec{k},t)$ while the population equation remains unchanged. It means asymmetry affects only the induced polarization in presence of an electric field while population is not affected by asymmetry. This is the main difference between the Bloch equations of gapped and without gapped single layer graphene. Now, we want to solve these equations *near resonance*, when the external driving frequency is nearly equal to the inter-band transition frequency of the system, and *far from resonance*, when the external driving frequency is very large in comparison to the inter-band transition frequency of the system. The Bloch equations in single layer graphene have already been solved in absence of gap [184]. Here, we solve these equations in presence of gap parameter (in presence of asymmetry parameter). We followed a process similar to the one described in Ref.[184].

3.1.3 Solution of Bloch equations near resonance, $\omega \approx 2E_k$

This section describes the solution of Bloch equations of gapped single layer graphene in the resonance regime when ω is nearly equal to electron-hole pair excitation frequency. Similar to bilayer graphene, gapped single layer graphene also exhibits parabolic dispersion between energy and momentum. Unlike bilayer graphene, here, there is only one resonance, similar to single layer graphene without gap, which occurs at the first harmonic in EDF . To solve the Bloch equations of gapped single layer graphene in the resonance case, we applied a rotating wave approximation [150, 151, 174] well known in the context of two-level atomic systems in quantum optics. These Bloch equations are explicitly solved in resonance regime in case of single layer graphene without gap [184]. Hence we provide only the results and their interpretation. Following a process similar to the one described in Ref.[184], we obtain the following formula of conventional Rabi frequency in gapped single layer graphene

$$\Omega_{RWA} = \sqrt{\delta^2 + \omega_R^2 + \frac{\omega_R^2}{E_k^2}\Delta\left(\Delta - 2E_k\right)} \tag{3.7}$$

where $\delta = \omega - 2E_k$ and $E_k = \sqrt{v_F^2 k^2 + \Delta^2}$. Near resonance $\omega \sim 2E_k$ and also $\Delta \ll \omega$. With these approximations, Eq. (3.7) reduces to $\Omega_{RWA} = \omega_R\left(1 - \frac{2\Delta}{\omega}\right) \approx \omega_R$ which is approximately the same as in suspended graphene. Thus, we can see that the conventional Rabi frequency near resonance is almost independent of asymmetry parameter Δ.

3.1.4 Solution of Bloch equations far from resonance, $\omega \gg \omega_R, 2E_k$

In this section, we solve the Bloch equations in off resonance case using ARWA described in refs.[184, 187]. Therefore, we highlight only the results. Note that the population equations in gapped and without gapped single layer graphene are same. This means that the solution for the population equation of gapped and without gapped single layer graphene remains unchanged. The change appears only in the solution of polarization equation. The solutions of rapidly varying part of population and polarization equations are as follows,

$$\begin{aligned} n_f(\vec{k},t) &\sim \frac{2v_F A^*(0)}{\omega} p_s^*(\vec{k},t) \\ p_+(\vec{k},t) &\sim -\frac{v_F A^*(0)}{(2v_F^2 m_t + \omega)} n_s(\vec{k},t) \\ p_-(\vec{k},t) &\sim \frac{2v_F^2 k_- A(0)}{\omega(2v_F^2 m_t - \omega)} p_s(\vec{k},t) \end{aligned} \tag{3.8}$$

The solution of slow varying part of polarization equation comes out to be equal to,

$$p_s(\vec{k},t) = n_s(\vec{k},0)\frac{\omega_{Rm}}{4v_F k_+}\left[-Cos(2\Omega t) - i\frac{2\Omega}{\omega_{Rm}}Sin(2\Omega t)\right] \tag{3.9}$$

$$\Omega_{ARWA} = 2\left[(v_F|k|)^2 + \frac{\omega_{Rm}^2}{4}\right]^{1/2}, \ \omega_{Rm} = 2v_F^2 m_t + \frac{2v_F^2|A(0)|^2}{\omega} \tag{3.10}$$

Equation (3.10) gives the anomalous Rabi frequency of gapped single layer graphene in off resonance. Exactly at the Dirac point of the Brillouin zone, the formula of anomalous Rabi frequency reduces to, $\Omega_{ARF} = 2v_F^2 m_t + \frac{2\omega_R^2}{\omega}$, where $\omega_R = v_F|A(0)|$, is the zero detuned conventional Rabi frequency. This formula turns into the anomalous Rabi frequency of suspended graphene in absence of gap parameter. In presence of mass term, monolayer graphene show Rabi-like oscillations even for vanishingly small applied field. We call these oscillations ‘offset oscillations’ and the corresponding frequency is called the offset frequency. The value of offset frequency may be identified with the asymmetry parameter. This feature of offset oscillations is absent in suspended graphene. Typically, this asymmetry parameter is due to sublattice space asymmetry Δ between A and B sublattices. Figure 3.2 depicts the offset frequency in asymmetric monolayer graphene. The actual value of offset frequency Ω_{ARF} is 0.21ω for a value of frequency $\omega = 6\pi \times 10^{14} rad/sec$ of the applied field. In addition we choose $\omega_R = 2.02 \times 10^{13} rad/sec$. This offset

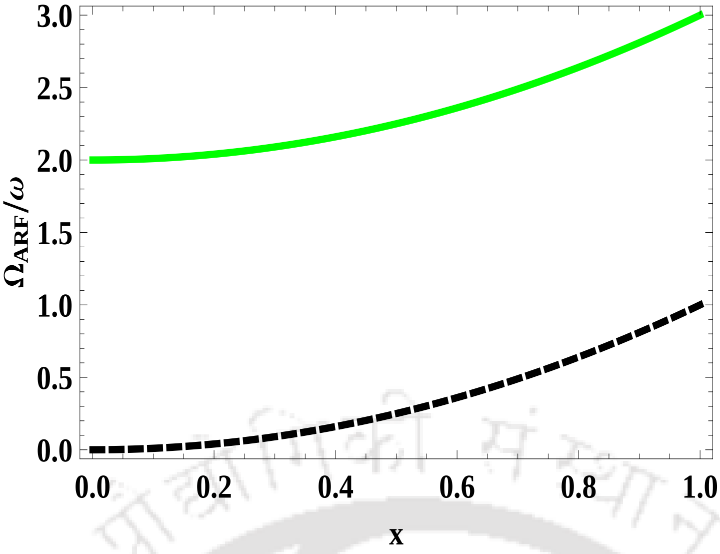

FIGURE 3.2: Schematic of the variation of the dimensionless anomalous Rabi frequency (ARF) Ω_{ARF}/ω versus a dimensionless quantity x $(= \frac{\sqrt{2}\omega_R}{\omega}, \omega_R = v_F|A(0)|)$ in case of symmetric graphene (dashed black) and asymmetric monolayer graphene (solid green), at the Dirac point of the Brillouin zone. ARF in symmetric graphene shows a zero trivial minimum in the absence of externally applied field whereas for asymmetric graphene it has a finite value. This shows that the ARF exhibits offset oscillations that may be identified with the twice the asymmetry parameter Δ. For clarity, we have chosen a large value of the offset frequency. A realistic value of the offset frequency is related to asymmetry parameter through the relation, $\frac{\Omega_{ARF}}{\omega} = \frac{2\Delta}{\hbar\omega} = 0.21$.

frequency is better observable for weak electric fields. We can see that the mass term has a remarkable effect on the anomalous Rabi frequency only for weak fields, as it is obvious from Eq. (3.10). Thus we have seen that the asymmetry parameter has no significant effect on conventional Rabi frequency while the anomalous Rabi oscillations are significantly affected by the asymmetry parameter in monolayer graphene.

3.1.5 Current density in gapped single layer graphene

The current density of suspended graphene sheet has been derived in detail in Ref.[184]. Here, we mention the key differences of behaviour of current density of gap and gapless single layer graphene. As we have seen the asymmetry has no significant effect on conventional Rabi oscillations. Therefore, our concern is to discuss the effect of asymmetry on induced current density only in off resonance case. Current density is an experimentally accessible quantity. Theoretically, this may be derived with the help of continuity equation and Hiesenberg's equation of motion for the charge density.

$$\vec{J}(t) = 4ev_F \sum_{\vec{k}} p(\vec{k},t)\vec{\sigma}_{AB} + h.c. \tag{3.11}$$

where v_F is the Fermi velocity of Dirac fermions, $\vec{\sigma}$ is the Pauli spin matrices, and the prefactor $4 = 2\times 2$ is for the spin and valley degeneracy, respectively. Inserting the value of polarization $p(\vec{k},t)$ in above equation and performing a straightforward calculation, we may easily write the slow part of current density in the frequency domain, in off-resonance case,

$$\vec{j}_s(\omega') \approx -\frac{4eAA^*(0)\vec{\sigma}_{AB}}{\omega_{Rm} v_F \omega}\left[\omega'^4 - \omega'^2\left(2\Delta + \frac{2\omega_R^2}{\omega}\right)^2\right]^{1/2} \tag{3.12}$$

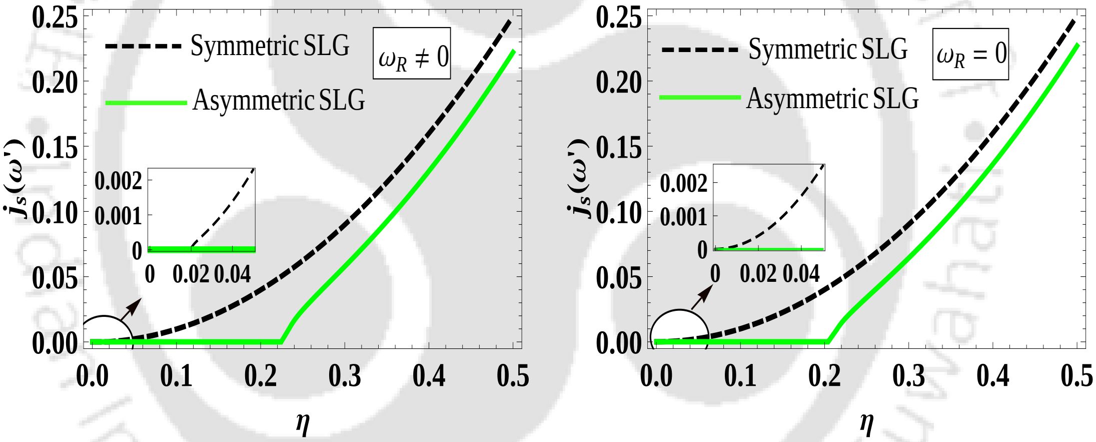

FIGURE 3.3: Schematic of the variation of the slow part of: (left) induced current versus a dimensionless quantity $\eta(=\omega'/\omega)$, in the presence of an external applied field, and (right) in the absence of an externally applied field. This figure is plotted by assuming that $\omega_R = 1$ and $\omega = 10$, in arbitrary units. It is obvious from the left part of this figure that the threshold frequency of the induced current is increased in the presence of asymmetry (solid green) in comparison to that of without asymmetry (dashed black) shown in inset for clarity. The threshold frequency $\frac{\omega'}{\omega}$ is $(\frac{2\Delta}{\hbar\omega} + \frac{2\omega_R^2}{\omega^2})$ which is the anomalous Rabi frequency at Dirac point, as may be seen from Eq. (3.10). The right part is plotted in the absence of external field. It is clear from the right part of this figure that the induced current in symmetric graphene [184] (dashed black) loses its threshold behaviour when the external field is absent whereas, asymmetric monolayer graphene (solid green) still exhibits the threshold behaviour. The frequency of offset oscillations of the current is identified by the asymmetry parameter Δ, and has the relation, $2\Delta = 0.21\hbar\omega$.

Equation (3.12) has the following explanation: the value of threshold frequency of slow part of current density, in asymmetric monolayer graphene, is increased by the asymmetry parameter (as we have seen earlier as well), and the threshold frequency $\omega^{'}$ of induced current is equal to $(2\Delta + 2\omega_R^2/\omega)$ which is exactly the anomalous Rabi frequency at the Dirac point which is obvious from Eq. (3.10). Moreover, the current density in asymmetric graphene exhibits a threshold behaviour even for vanishingly small applied fields. The asymmetry parameter does not affect the exponent at threshold but it has a remarkable effect on the value of the threshold frequency. In Fig. 3.3, we have shown the variation of the induced current with a dimensionless quantity $\eta(=\omega^{'}/\omega)$. For this, we make the quantity within the square bracket dimensionless. Realistic values of ω and ω_R are $6\pi \times 10^{12} rad/sec$ and $2.02 \times 10^{13} rad/sec$, respectively.

In the above discussion, we have observed the effect of asymmetry on Rabi oscillations as well as on the induced current in asymmetric monolayer graphene, mainly in the off resonance case. The anomalous Rabi frequency is offset by the asymmetry parameter in the off resonance case whereas asymmetry has no significant effect on the conventional Rabi frequency. The induced current in asymmetric monolayer graphene shows threshold behaviour even for vanishingly small applied fields less than the gap parameter.

The subsequent sections describe the same phenomenon in asymmetric *bilayer* graphene. In bilayer graphene, there are two asymmetries involved namely- inter-layer and intra-layer asymmetry. We investigate the effect of these asymmetries on anomalous Rabi oscillations in bilayer graphene. The intra-layer asymmetry has a similar effect on anomalous Rabi oscillations as in asymmetric monolayer graphene whereas, the effect of inter-layer asymmetry on anomalous Rabi oscillations is even more dramatic. We have already discussed anomalous Rabi oscillations in bilayer graphene without gap parameter. Therefore, the following sections describe only the results and their interpretations when the asymmetry is considered in bilayer graphene.

3.2 Effect of asymmetry on Rabi oscillations in bilayer graphene

This section describes the effect of asymmetry on ROs in bilayer graphene. Bilayer graphene is composed of two single graphene sheets in a Bernal stacking [28]. In bilayer graphene, there are two kinds of asymmetry: one is intra-layer asymmetry and second is inter-layer asymmetry. The inter-layer asymmetry may be due to doping effect or external gate-voltage whereas, intra-layer asymmetry arises due to the substrate and graphene sheet interaction upon which the graphene sheet is deposited. It could also arise due to an applied electric field perpendicular to the plane of the graphene sheet [35, 46, 191]. The effect of intra-layer asymmetry on ROs in bilayer graphene is similar to that of single layer graphene. The effect of inter-layer asymmetry on ROs is more dramatic than intra-layer asymmetry, as we will see from the following discussion. We will not discuss further details of the effect of asymmetry on conventional ROs because these oscillations do not change significantly as we have seen in case of single layer graphene. Therefore, we discuss only the effect of asymmetry in detail on ROs in off resonance case.

The effective low-energy Hamiltonian of bilayer graphene including inter- and intra-layer asymmetries may be written as follows,

$$H_2 = -\frac{1}{2m}\begin{pmatrix} 0 & k_-^2 \\ k_+^2 & 0 \end{pmatrix} + \begin{pmatrix} \Delta & 0 \\ 0 & -\Delta \end{pmatrix} + U\left(\frac{1}{2} - \frac{v^2 k_+ k_-}{\gamma_1^2}\right)\begin{pmatrix} 1 & 0 \\ 0 & -1 \end{pmatrix} \tag{3.13}$$

The first term in Eq. (3.13) is the effective low energy two component Hamiltonian of pure bilayer graphene that describes the indirect inter-layer hopping from A1 to B2 atomic site which includes direct inter-layer hopping γ_1 forming dimer-site between the atomic sites B1 and A2, and an intra-layer hopping velocity v. This two component Hamiltonian was first derived by E. McCann *et al.* [16] using the Green's function method for matrices. The second and third term in Eq. (3.13) are due to the intra- and inter-layer asymmetry that breaks the sublattice space symmetry and the symmetry between two layers, respectively. The intra-layer asymmetry opens up a gap in the low energy spectrum of bilayer graphene. The effect of inter-layer asymmetry is dramatic, it leads to a 'Mexican-hat' structure in the low energy spectrum of bilayer graphene, Fig. 3.4. Our purpose is to describe the effect of asymmetry on Rabi oscillations in the presence of an intense applied electromagnetic field. We first discuss the effect of intra-layer asymmetry on Rabi

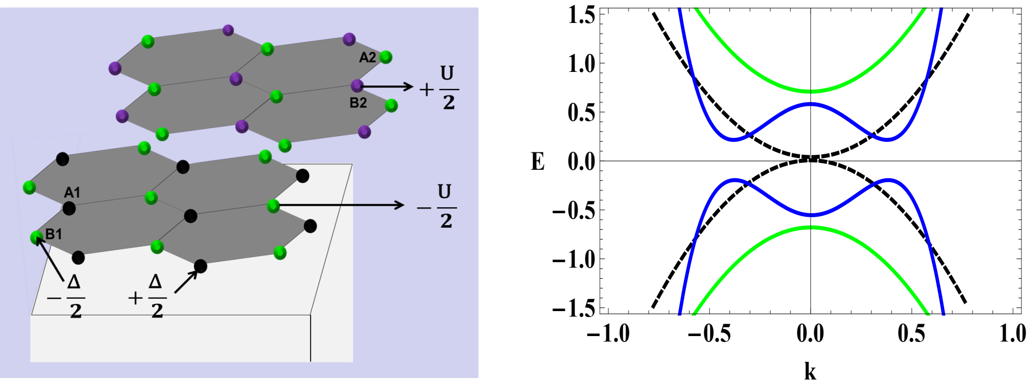

FIGURE 3.4: Left: Schematic of bilayer graphene deposited upon a substrate. Δ is the on site energy of the atoms on sublattice site $A1$ and $B1$ that defines the intra-layer asymmetry between two sublattices and opens up a gap at the Dirac point. U is the asymmetry between two layers that gives rise to a 'Mexican' hat structure in the energy spectrum. Right: Low energy spectrum of bilayer graphene with intra-layer asymmetry (solid green), without asymmetry (dashed black) and with inter-layer asymmetry (solid blue).

oscillations and the effect of inter-layer asymmetry is discussed afterwards. The low-energy electronic band spectrum in Fig. 3.4 is theoretically derived in the references [16, 17, 192] by solving a four-component Hamiltonian, that gives the following energy bands when intra- and inter-layer asymmetry have been taken into account, respectively,

$$E_\alpha^2 = \frac{\Delta^2}{4} + \frac{\gamma_1^2}{4}\left[\sqrt{1+\frac{4\gamma_0^2|f(\vec{k})|^2}{\gamma_1^2}} + (-1)^\alpha\right]^2 \tag{3.14}$$

$$E_\alpha^2 = \frac{\gamma_1^2}{2} + \frac{U^2}{4} + \gamma_0^2|f(\vec{k})|^2 + (-1)^\alpha\sqrt{\frac{\gamma_1^4}{4} + \gamma_0^2|f(\vec{k})|^2\left(\gamma_1^2 + U^2\right)} \tag{3.15}$$

where $f(\vec{k}) = e^{\frac{ik_ya}{\sqrt{3}}} + 2e^{\frac{-ik_ya}{2\sqrt{3}}}Cos(\frac{k_xa}{2})$, a is the lattice constant. $\alpha = 1, 2$ that describe low and high energy bands, respectively. Equations (3.14) and (3.15) show that intra-layer asymmetry only gives a shift in the energy whereas inter-layer asymmetry gives rise to a 'Mexican hat' structure in the energy spectrum.

3.2.1 Effect of intra-layer asymmetry on Rabi oscillations

Here, we describe the effect of intra-layer asymmetry on ROs in bilayer graphene. In presence of intra-layer asymmetry (Δ), a gap is open in the band structure of bilayer graphene as shown by solid green curve in Fig. 3.4. The effect of intra-layer asymmetry on the band structure of bilayer graphene is similar to that of single layer graphene. In presence of intra-layer asymmetry anomalous ROs show an offset oscillations similar to that of single layer graphene. The frequency of these offset oscillations can be determined by the asymmetry parameter. In other words, we can say that the frequency of offset oscillations depends on the gap parameter that depends on the type of substrates chosen. This can be clearly understood with the help of following discussion.

To discuss the effect of intra-layer asymmetry on ROs, we use a semiclassical approximation, similar to the model presented in case of asymmetric monolayer graphene. In the low-energy continuum limit, the Hamiltonian of bilayer graphene including intra-layer asymmetry, in second quantization, may be written as

$$\begin{aligned} H = -\frac{1}{2m}\sum_{\vec{k}}\left[(k_- - A^*(t))^2\, c^\dagger_{A1}(\vec{k},t)\; c_{B2}(\vec{k},t) + h.c.\right] \\ + \Delta\sum_{\vec{k}}\left[c^\dagger_{A1}(\vec{k},t)\; c_{A1}(\vec{k},t) - c^\dagger_{B2}(\vec{k},t)\; c_{B2}(\vec{k},t)\right] \end{aligned} \tag{3.16}$$

where $k_\pm = k_x \pm ik_y$, $\vec{A}(t) = \vec{A}(0)e^{-i\omega t}$ is the vector potential which couples to bilayer graphene in the Coulomb gauge and $\vec{A}(0) = \frac{e}{c}(A_x(0) + iA_y(0))$, c and $\text{c}^\dagger$ are annihilation and creation operators on sublattice sites $A1$ and $B2$. The second term in Eq. (3.16) is purely due to intra-layer asymmetry.

We follow a process similar to the single layer graphene. We first derive the Bloch equations of bilayer graphene including intra-layer asymmetry. These Bloch equations are solved in two different regions of interest- *resonance* and *off resonance*. Here, we will give a qualitative description because the process is similar to that of single layer graphene, hence, we do not want to repeat the similar calculations. Similar to single layer graphene, we discuss the effect of asymmetry on experimental accessible quantity current density.

We may write the Bloch equations of population $n_{diff}(\vec{k},t)$ and polarization $p(\vec{k},t)$ excess on sublattice site A1 in the bottom layer and B2 in the top layer when intra-layer asymmetry is taken into account as follows,

$$i\partial_t n_{diff}(\vec{k},t) = -\frac{1}{m}\left[(k_- - A^*(t))^2\, p(\vec{k},t) - h.c.\right] \tag{3.17}$$

$$i\partial_t p(\vec{k},t) = -\frac{1}{2m}\,(k_+ - A(t))^2\, n_{diff}(\vec{k},t) - 2\Delta p(\vec{k},t) \tag{3.18}$$

Now we wish to solve the rate equations of population and polarization in two different regions of interest- resonance and far from resonance, as we have already been mentioned in case of asymmetric monolayer graphene.

Solution of Bloch equations near resonance. To solve the Bloch equations near resonance, we follow a process similar to the one described in previous chapters and also in the earlier section. In bilayer graphene, there are two possible resonances- one is at the first harmonic and other is at the second harmonic in external frequency, unlike in single layer graphene [184] where there is only one possible resonance. The conventional Rabi frequencies near first and second harmonic resonances are given below, respectively,

$$\Omega_\omega = \left[\delta^2 + 2\omega_R \frac{|k|^2}{mE_k^2}\left(\frac{|k|^4}{4m^2} + 2\Delta\left(\Delta - E_k\right)\right)\right]^{1/2} \tag{3.19}$$

$$\Omega_{2\omega} = \left[\delta^2 + \frac{\omega_R^2}{E_k^2}\left(\frac{|k|^4}{4m^2} + 2\Delta(\Delta - E_k)\right)\right]^{1/2} \tag{3.20}$$

where $\delta = n\omega - 2E_k$, n defines the order of harmonic resonances and E_k is the energy eigenvalue of the system. When $\Delta = 0$, Equations (3.19) and (3.20) gives the conventional Rabi frequencies without asymmetry in bilayer graphene. Near resonance, $n\omega \approx 2E_k$, the conventional Rabi frequencies at first and second harmonic resonance reduces to the following

$$\Omega_\omega = \left(2\omega_R \frac{|k|^2}{m}\right)^{1/2}\left(1 - \frac{2\Delta}{\omega}\right), \quad \Omega_{2\omega} = \omega_R\left(1 - \frac{2\Delta}{\omega}\right)$$

Since $\Delta \ll \omega$, therefore we can see that the conventional Rabi frequencies are nearly independent of the intra-layer asymmetry. This shows that the conventional Rabi frequency in both resonance cases is nearly the same with or without asymmetry. In other words, asymmetry has no significant effect on conventional ROs. On the other hand, ROs in off resonance are significant effected by the presence of asymmetry, it may be clear from the subsequent description.

Solution of Bloch equations in off resonance case. In off resonance, when the frequency of external field is very large in comparison to the inter-band transition frequency of the system ($\omega \gg |k|^2/m$) and also from the zero detuned Rabi frequency of carriers ($\omega \gg \omega_R$), the Bloch equations are solved using an approximation called asymptotic rotating wave approximation (ARWA). In case of bilayer graphene, when we decomposed the population $n_{diff}(\vec{k}, t)$ and polarization $p(\vec{k}, t)$

into slow and fast varying, we have to keep terms up to the second harmonic in the external frequency unlike single layer graphene, where we kept only the terms that oscillate with the first harmonic in external driving frequency, as it is clear from the Hamiltonian Eq. (3.16). Following a similar process described in case of asymmetric monolayer graphene, we may write the solution of fast coefficients of population and polarization,

$$n_{f1}(\vec{k},t) = -\frac{2k_+A(0)}{m\omega}p_s^*(\vec{k},t),\ n_{f2}(\vec{k},t) = \frac{A^2(0)}{2m\omega}p_s^*(\vec{k},t)$$

$$p_{1-}(\vec{k},t) = \frac{1}{m(2\Delta-\omega)}\left[\frac{|k|^2k_+A^*(0)}{m\omega}p_s(\vec{k},t) + \frac{k_+|A(0)|^2A^*(0)}{2m\omega}p_s(\vec{k},t)\right]$$

$$p_{2-}(\vec{k},t) = -\frac{k_+^2A^{*2}(0)}{8m^2\omega(\Delta-\omega)}p_s(\vec{k},t),\ p_{1+}(\vec{k},t) = \frac{k_+A(0)}{m(2\Delta+\omega)}n_s(\vec{k},t)$$

$$p_{2+}(\vec{k},t) = -\frac{A^2(0)}{4m(\Delta+\omega)}n_s(\vec{k},t)$$

The slow varying population and polarization equations are

$$i\partial_t n_s(\vec{k},t) = -\frac{1}{m}\left[k_-^2p_s(\vec{k},t) - k_+^2p_s^*(\vec{k},t)\right]$$

$$i\partial_t p_s(\vec{k},t) = -\frac{k_+^2}{2m}n_s(\vec{k},t) - \left[2\Delta + \frac{\omega_R^2}{\omega} + 4\frac{|k|^2\omega_R}{m\omega}\right]p_s(\vec{k},t)$$

These two equations may be solved mutually by assuming that the solution of the slow part of the populations equation $n_s(\vec{k},t) = n_s(\vec{k},0)Cos(2\Omega t)$. Then the solution of the slow part of polarization equation may be written as follows

$$p_s(\vec{k},t) = \frac{k_+^2}{4mE_k}\left[Cos(2\Omega t) + i\frac{2\Omega}{\omega_{R,asy}}Sin(2\Omega t)\right],\ n_s(\vec{k},0) = \frac{|k|^4}{2m^2E_k\omega_{R,asy}}$$

$$\Omega_{ARWA} = 2\left[\left(\frac{|k|^2}{2m}\right)^2 + \frac{\omega_{R,asy}^2}{4}\right]^{1/2},\ \omega_{R,asy} = \left[2\Delta + \frac{\omega_R^2}{\omega} + 4\frac{|k|^2\omega_R}{m\omega}\right] \qquad (3.21)$$

where $\omega_R = |A(0)|^2/2m$, $E_k = (|k|^4/4m^2 + \Delta^2)^{1/2}$ is the energy eigenvalue of the system and Δ denotes the intra-layer asymmetry that opens a gap between the valance and conduction band. Equation (3.21) gives the anomalous Rabi frequency near the Dirac point of the Brillouin zone. Exactly at Dirac point, when $\vec{k} = 0$, Eq. (3.21) reduces to $\Omega_{ARF} = 2\Delta + \omega_R^2/\omega$. In absence of asymmetry, this gives the anomalous Rabi frequency of suspended bilayer graphene that varies linearly with the square of the intensity of the applied field whereas, in single layer graphene

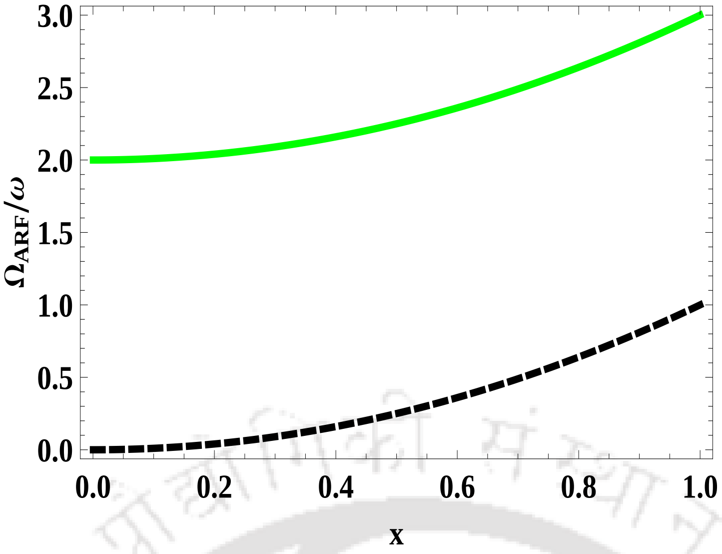

FIGURE 3.5: Schematic of the variation of the dimensionless anomalous Rabi frequency (ARF) $\frac{\Omega_{ARF}}{\omega}$ versus a dimensionless quantity x (intensity of applied field) $\left(= \frac{\omega_R}{\omega}, \omega_R = \frac{|A(0)|^2}{2m}\right)$ for symmetric (dashed black) and asymmetric bilayer graphene (solid green) respectively, at the Dirac point of the Brillouin zone. The dimensionless ARF for symmetric bilayer graphene shows a zero trivial minimum in the absence of the applied field whereas for asymmetric bilayer graphene it has a finite value. This reveals that the ARF shows offset oscillations in the absence of applied field, and these offset oscillations are observed only for weak fields. For clarity, we have chosen a large value of offset frequency. A realistic value of offset frequency is related to the asymmetry parameter by the relation, $\frac{2\Delta}{\hbar\omega} = 0.24$.

it is linear with intensity [184]. In presence of asymmetry, the system exhibits Rabi-like oscillations even for vanishingly small applied fields. It means, here also, similar to asymmetric monolayer graphene, the anomalous Rabi frequency is offset by an asymmetry parameter. The value of the offset frequency is identified with the asymmetry parameter. Realistic values of ω, ω_R and Δ are listed in the table (3.1). Offset oscillations in bilayer graphene with intra-layer asymmetry are shown in Fig. 3.5.

Effect of intra-layer asymmetry on current density. Current density in bilayer graphene is not affected directly in presence of asymmetry. Therefore, the expression of current density for symmetric and asymmetric bilayer graphene remains same, as we can see from Eqs. (2.29) and (3.22). The current density in bilayer graphene is affected by the presence of asymmetry through polarization because asymmetry modified the polarization and current density is proportional to polariation. The compact form of current density of asymmetric bilayer graphene can

Energy	*Unit(eV)*	
	SLG	BLG
$\hbar\omega_R^2/\omega$	1.4×10^{-4}	1.78×10^{-7}
$\hbar\omega_R$	0.013	4.69×10^{-4}
Δ	0.26	0.15
U	-	0.075
$\hbar\omega$	1.24	1.24

TABLE 3.1: This table contains realistic values of various energy scales in monolayer and bilayer graphene. The value of Δ and U are adopted from the references [29, 188, 197].

be derived by using a process similar to that of asymmetric single layer graphene, x-component of which can be written as

$$< J_x(t) >= -\frac{1}{2\pi m}\sum_{\vec{k}}(k_- - A^*(t))\,p(\vec{k},t) + h.c. \tag{3.22}$$

Inserting $p(\vec{k},t)$ in above equation and performing the integration over the momenta $\vec{k}$, we can write a final expression of slow part of current density in the frequency domain,

$$J_x^s(\omega') = -\left(\frac{A(0)}{16\pi^2}\right)\frac{A\omega^2}{32\omega_R^3}\left(\omega' - 2\Delta - \frac{\omega_R^2}{\omega}\right)\Theta\left(\omega' - 2\Delta - \frac{\omega_R^2}{\omega}\right) \tag{3.23}$$

Equation (3.23) gives the induced current in bilayer graphene when intra-layer asymmetry has been taken into account. If $\Delta = 0$, Eq. (3.23) gives the induced current in bilayer graphene without asymmetry. Equation (3.23) is valid only near threshold. The exponent of induced current at threshold is equal to unity whereas, in monolayer graphene [184] this computed to be equal to 1/2. The asymmetry does not affect the exponent at the threshold but changes the value of the threshold frequency. The value of threshold frequency is increased by the gap parameter. The induced current in Eq. (3.23) shows Rabi-like oscillations even in absence of external applied electric field ($\omega_R = 0$). This shows that the induced current exhibits offset oscillations- a feature absent in symmetric bilayer graphene. These offset oscillations are characterized by the asymmetry parameter Δ. This explanation will become more clear from Fig. 3.6.

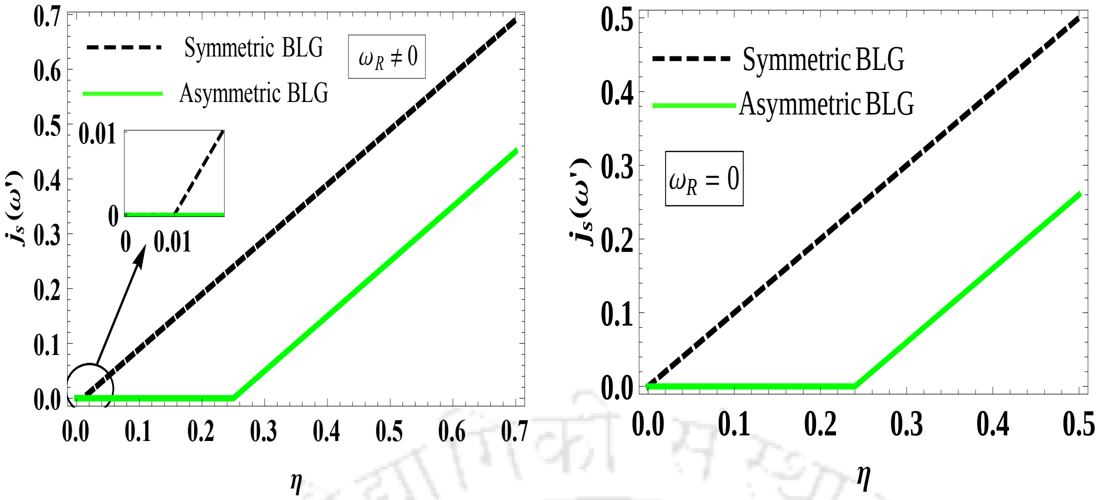

FIGURE 3.6: Schematic of the variation of the slow part of: (left) induced current versus a dimensionless quantity $\eta(=\frac{\omega'}{\omega})$, in the presence of the external applied field. This figure is plotted by assuming that $\omega_R = 1$ and $\omega = 10$, in arbitrary units. It is obvious from the left part of this figure that the threshold frequency of the induced current is increased in the presence of asymmetry (solid green) in comparison to without asymmetry (dashed black). The threshold frequency $\frac{\omega'}{\omega}$ is $(\frac{2\Delta}{\hbar\omega} + \frac{\omega_R^2}{\omega^2})$, where $\omega_R = \frac{|A(0)|^2}{2m}$. The right part is plotted in the absence of external field which shows that the induced current in symmetric bilayer graphene (dashed black) loses its threshold behaviour whereas, the asymmetric bilayer graphene (solid green) retains a threshold behaviour. The frequency of offset oscillations of the current is identified with the asymmetry parameter Δ. The offset oscillations in induced current are observable only for weak applied fields. For strong fields these parameters reduce to those without asymmetry. A realistic value of the offset frequency is $\frac{2\Delta}{\hbar\omega} = 0.24$.

3.2.2 Effect of inter-layer asymmetry on Rabi oscillations

The third term in Hamiltonian Eq. (3.16) is due to inter-layer asymmetry in bilayer graphene, where U denotes the strength of inter-layer asymmetry. The inter-layer asymmetry has a dramatic effect on the energy spectrum of bilayer graphene. A 'Mexican hat' like structure appears in the low energy spectrum of bilayer graphene that gives the true value of the energy gap [17], Fig. 3.4. In the continuum limit, the Hamiltonian of bilayer graphene with inter-layer asymmetry may be written as,

$$\begin{aligned} H = -\frac{1}{2m}\sum_{\vec{k}}\Big[(k_- - A^*(t))^2\ c^\dagger_{A1}(\vec{k})\ c_{B2}(\vec{k}) + h.c.\Big] \\ + \sum_{\vec{k}}\left[\frac{U}{2} - \frac{Uv^2}{\gamma_1^2}K_+K_-\right][c^\dagger_{A1}(\vec{k})\ c_{A1}(\vec{k}) - c^\dagger_{B2}(\vec{k})\ c_{B2}(\vec{k})] \end{aligned} \tag{3.24}$$

To discuss the effect of inter-layer asymmetry on Rabi oscillations, we follow a procedure as described in earlier section. We first derive the Bloch equations and then solve these equations *near resonance* and *far from resonance*. Upon solving the Bloch equations far from resonance, we obtain the following expression for the slowly varying part of polarization,

$$p_s(\vec{k},t) = \frac{k_+^2}{4mE_k}\left[Cos2\Omega t + i\frac{2\Omega}{\omega_R^{'}}Sin2\Omega t\right]$$

where E_k is the energy eigenvalue of bilayer graphene with inter-layer asymmetry.

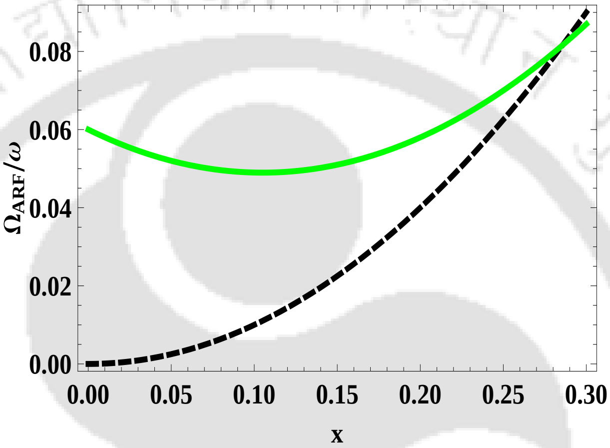

FIGURE 3.7: Schematic of the variation of the dimensionless anomalous Rabi frequency (ARF) $\frac{\Omega_{ARF}}{\omega}$ versus a dimensionless quantity x ($\sim \omega_R/\omega$) for symmetric (dashed black) and inter-layer asymmetric bilayer graphene (solid green), at the Dirac point of the Brillouin zone. The dimensionless ARF for symmetric bilayer graphene shows a zero trivial minimum in the presence of the applied field. For inter-layer asymmetric bilayer graphene, the ARF goes through a non-trivial minimum that occurs at a value of x = $\frac{U}{2\gamma_1}$, and is observed only for weak applied fields. For strong applied fields, the effect of inter-layer asymmetry becomes similar to the intra-layer asymmetry, and if we further increase the strength of the applied field the ARF tends towards to that without asymmetry. The offset frequency is related to asymmetry parameter by the relation, $\frac{\Omega_{ARF}}{\omega} = \frac{U}{\hbar\omega} = 0.06$, for a realistic value of the ratio $\frac{U}{\gamma_1} \sim 0.21$ and frequency of the applied field $\omega = 6\pi \times 10^{14} rad/sec$.

The general expression of anomalous Rabi frequency in this case comes out to be,

$$\Omega_{ARWA} = 2\sqrt{\left(\frac{|k|^2}{2m}\right)^2 + \frac{\omega_R^{'2}}{4}}$$

$$\omega_R^{'} = \left[\frac{|A(0)|^4}{4m^2\omega} + \frac{2|k|^2|A(0)|^2}{m^2\omega} + U\left(1 - \frac{v^2}{\gamma_1^2}\left(|k|^2 + |A(0)|^2\right)\right)\right] \tag{3.25}$$

Exactly at Dirac point, the above expression for anomalous Rabi frequency reduces to the following,

$$\Omega_{ARF} = U\left(1 - \frac{\omega_R}{\gamma_1}\right) + \frac{\omega_R^2}{\omega}, \ \omega_R = \frac{|A(0)|^2}{2m} \tag{3.26}$$

Unlike the anomalous Rabi frequency in bilayer graphene with intra-layer asymmetry, here we find an additional term containing ω_R that is responsible for a non-trivial minimum in the anomalous Rabi frequency. This non-trivial minimum is observed only for weak applied electromagnetic fields- a characteristic absent in symmetric and intra-layer asymmetric bilayer graphene. For strong fields, it tends towards the anomalous Rabi frequency of bilayer graphene with intra-layer asymmetry. The effect of inter-layer asymmetry on anomalous Rabi frequency in bilayer graphene at Dirac point of the Brillouin zone is shown in Fig. 3.7. The effect of inter-layer asymmetry on the slow part of induced current can be seen

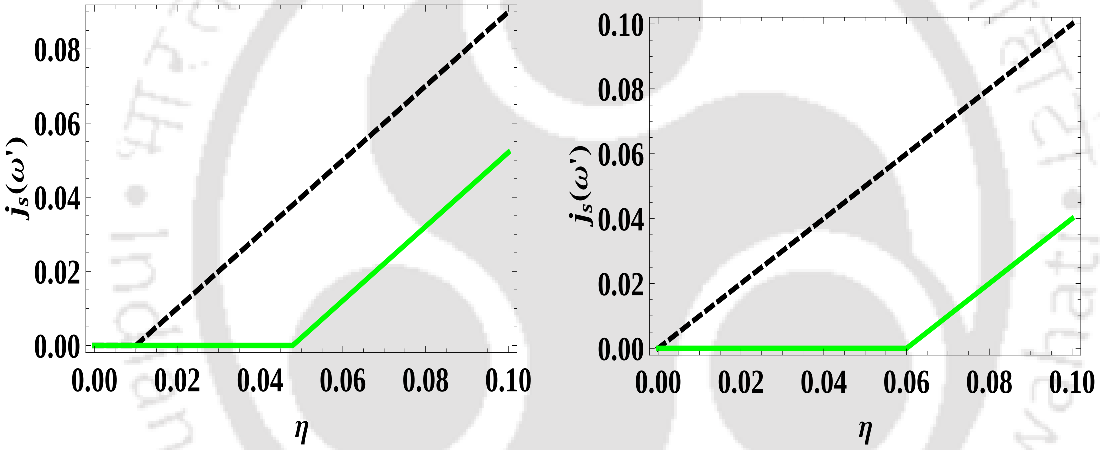

FIGURE 3.8: Schematic of the variation of the slow part of: (left) induced current versus a dimensionless quantity $\eta = \frac{\omega'}{\omega}$, in the presence and (right) in the absence of the applied field. This figure is plotted assuming that $\omega_R = 1$ and $\omega = 10$, in arbitrary units. It is obvious from the left part of this figure that the threshold frequency of the induced current is increased in the presence of asymmetry (solid green) in comparison to that of without asymmetry, similar to the intra-layer asymmetric bilayer graphene. This shift is observed only for weak fields, for strong fields, the behaviour is same as without asymmetry. The threshold frequency $\frac{\omega'}{\omega}$ is $(\frac{U}{\hbar\omega} - \frac{U\omega_R}{\omega\gamma_1} + \frac{\omega_R^2}{\omega^2})$. Right part of this figure shows that the induced current in symmetric bilayer graphene (dashed black) loses its threshold behaviour whereas, the bilayer graphene with inter-layer asymmetry (solid green) exhibits threshold behaviour even for vanishingly small external fields, and this is prominent only for the weak applied fields. The frequency of offset oscillations of the current is identified by the asymmetry parameter U, and has the relation, $U = 0.06\hbar\omega$.

from the following expression,

$$J_x^s(t) = \frac{A}{2\pi m}\frac{\gamma_1^2}{8\pi U v^2}\frac{\omega_R}{4m^2\omega}\frac{A(0)}{\left(U - \frac{U\omega_R}{\gamma_1} + \frac{\omega_R^2}{\omega}\right)}\frac{\omega' - \left(U - \frac{U\omega_R}{\gamma_1} + \frac{\omega_R^2}{\omega}\right)}{\left(\frac{4\omega_R}{m\omega} - \frac{Uv^2}{\gamma_1^2}\right)^2} \tag{3.27}$$

The induced current in bilayer graphene with inter-layer asymmetry is also offset by the asymmetry parameter- a feature absent in symmetric bilayer graphene, and the offset value is identified with the asymmetry parameter which is different than that of the intra-layer asymmetry parameter. A shift appears in the induced current from lower to higher threshold frequency and is well observed only for weak fields. Similar to the effect of intra-layer asymmetry on induced current, the inter-layer asymmetry also does not change the exponent at threshold but changes the threshold frequency with different asymmetry parameter, as can be seen from Eq. (3.27). The effect of inter-layer asymmetry on induced current in bilayer graphene can be easily understood from Fig. 3.8. The numerical values of various quantities given in table (3.1) are calculated at a fixed value of the frequency $\omega = 6\pi \times 10^{14} rad/sec$ of the external applied field, $E_{max} = 250\ kV/cm$. The value of the zero-detuned Rabi frequency and anomalous Rabi frequency at Dirac point in monolayer graphene is 10^2 and 10^3 times larger than that of bilayer graphene, respectively.

So far we have discussed the phenomenon of Rabi oscillations in monolayer and bilayer graphene deposited on a substrate, for example hexagonal boron nitride. The substrate-graphene interaction is responsible for opening of a gap, around 53 meV [198], in the electronic spectrum of these graphene systems. There are known substrates such as Ni that open a negligible gap [199, 200] or no gap [196] in the electronic spectrum. Experimenters [69, 188, 197, 201, 202] observed a gap of 260 meV in the band spectrum of epitaxial graphene on SiC substrate due to graphene-substrate interaction. A density functional theory (DFT) calculation confirmed substrate-induced symmetry breaking [203]. Their results showed a gap in the band spectra of graphene of about 200 meV, which is in agreement with recent experimental observations. Varykhalov *et al.* [196] has studied the photoemission spectrum of a single graphene sheet grown on Ni and Co substrate, and demonstrated the absence of a band gap at the Dirac point. They have shown that the effects that usually open a gap at the Dirac point may also have the adverse effect of closing it in such situations. The gap opening is also dependent on the distance between substrate and graphene sheet. So according to aforementioned literature on opening of gap in the electronic spectrum of graphene systems, the value of the gap parameter depends on the nature of substrate chosen. When there is no gap, the anomalous and conventional Rabi oscillations in these graphene systems correspond to that of gapless graphene systems, and the current density will lose its threshold behaviour for the vanishingly small applied fields. Depending upon the type of substrate, therefore, the gap parameter may increase, decrease or vanish altogether. Therefore, our results still valid even in these unusual situations with an appropriate choice of the gap parameters.

3.3 Summary and conclusions

This section summarizes the results obtained in this chapter and their conclusions. In preceding chapter, we discussed the phenomenon of Rabi oscillations in suspended bilayer graphene whereas, the present chapter describes the same phenomenon in these systems in presence of asymmetry. In other words we can say that this chapter is fully devoted to the study of ROs in supported graphene systems. The natural question arises that what are the similarities and the differences between the results obtained in these systems with or without including asymmetry. This issue is also addressed very well in this section.

We have studied the effect of intra- and inter-layer asymmetries on ROs in graphene-based systems (monolayer and bilayer). In monolayer graphene only intra-layer asymmetry is possible. Bilayer graphene possesses two kinds of asymmetries- intra- and inter-layer asymmetries. The intra-layer asymmetry in monolayer and bilayer graphene comes either from the graphene-substrate interaction or by simply applying an electric field perpendicular to plane of the graphene sheets. The intra-layer asymmetry has a dramatic effect on (anomalous) ROs far from resonance in monolayer graphene whereas, (conventional) ROs near resonance are nearly independent of asymmetry parameter. In presence of asymmetry, monolayer graphene show Rabi-like oscillations in off resonance even for vanishingly small applied electromagnetic fields- a feature absent in symmetric monolayer graphene. We called these oscillations ‘offset’ oscillations. The frequency of offset oscillations is identified with the asymmetry parameter. The offset oscillations are observable only for weak applied fields. For strong applied fields, the anomalous Rabi frequency tends towards to that without asymmetry. The induced current exhibits the threshold behaviour even for vanishingly small applied fields. Asymmetry does not change the value of exponent at threshold but changes the value of the threshold frequency. In presence of asymmetry, the value of the threshold frequency is increased by the asymmetry parameter.

A similar study is also done in case of bilayer graphene. In bilayer graphene, there are two kinds of asymmetry- intra- and inter-layer asymmetry. The effect of intra-layer asymmetry on Rabi oscillations in graphene bilayer has a similar effect as in monolayer graphene, only the difference is in the strength of the asymmetry parameter. The inter-layer asymmetry has an even more dramatic effect on Rabi oscillations in bilayer graphene. In presence of inter-layer asymmetry, anomalous Rabi frequency goes through a non-trivial minimum- a feature absent in asymmetric monolayer and intra-layer asymmetric bilayer graphene. Rabi oscillations in monolayer and bilayer graphene at extreme non-resonance are significantly affected by asymmetry, and is easily observable for weak applied fields. Usually, different substrates open gaps in the band structure whose size depends on the nature of the substrate-graphene interaction and also on type of substrate chosen. Our work is able to probe this aspect also through the phenomenon of Rabi oscillations.

The work presented in this chapter has been taken from Ref.[204]

Chapter 4

Band Structure Effects on AROs in Graphene Systems

In previous chapters, we have discussed AROs in symmetric and asymmetric graphene systems (single and bilayer graphene) mainly in off resonance. In the discussion of ROs in bilayer graphene, so far, we have considered an indirect hopping $A1$ to $B2$ between the layers on to different sublattice sites. This indirect hopping between two layers is shown in Fig. 4.1 by red arrow. Besides this indirect inter-layer hopping from $A1$ to $B2$ between two layers, there is one more

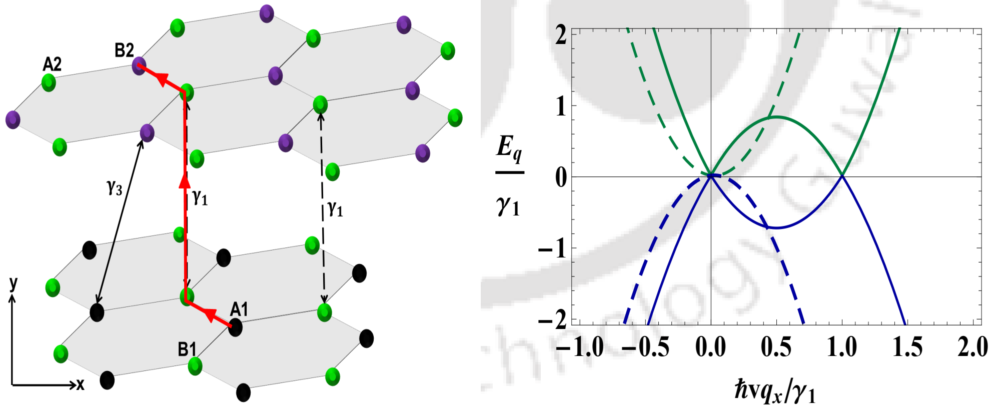

FIGURE 4.1: Left: Bilayer graphene crystal structure showing the intra-layer nearest neighbor hoping in top and bottom layer marked by red arrows. Black dashed arrows show direct inter-layer hoping, γ_1, hoping between dimer sites. Solid black arrow shows indirect inter-layer hoping, γ_3. Right: Band structure of bilayer graphene with (solid curves) and without (dashed curves) trigonal warping in the direction where $q_y = 0$. In presence of trigonal warping, a second non-trivial zero minimum appears far from the Dirac point.

possible way to do the hopping from $A1$ to $B2$ between two layers that includes direct hopping from $A1$ to $B2$ as shown by hopping parameter γ_3 (black arrow) in Fig. 4.1. This direct hopping from $A1$ to $B2$ has a remarkable effect on the band structure of bilayer graphene at very low energy. It leads to Lifshitz transitions: [16, 66, 205, 206] the iso-energetic lines are broken into four pockets, which can be referred to as one "central" and three "leg" parts [16, 77–80]. This transition takes place when $\epsilon_F \sim \epsilon_L = \gamma_1 v_3^2/(4v)$, where $v_3/v = 0.1$ [16]. The band structure of bilayer graphene when trigonal warping (γ_3) is taken into account is shown in Fig. 4.1.

In the above discussion, even in previous chapters, bilayer graphene is considered in a perfect Bernal stacking which is an ideal situation. This stacking is very difficult to find in practical life. In practical bilayer graphene samples (especially, those produced by epitaxy), these two graphene layers are not exactly AB but, there is a relative twist between the layers. Twisting, also called stacking defect, is obviously absent in monolayer graphene. The low-energy band structure of twisted bilayer graphene is drastically different from the AB-stacked bilayer and possesses intriguing electronic properties. Unlike biased AB stacked bilayer graphene [17], a potential difference between the twisted layers does not open a gap in the energy spectrum. Rather, this potential difference between the layers gives rise to a vertical shift in the energies at the degeneracy points [207]. The electronic band structure of twisted graphene bilayer has also been confirmed experimentally [208–210]. We wish to investigate what effect twisting has on a property we have been

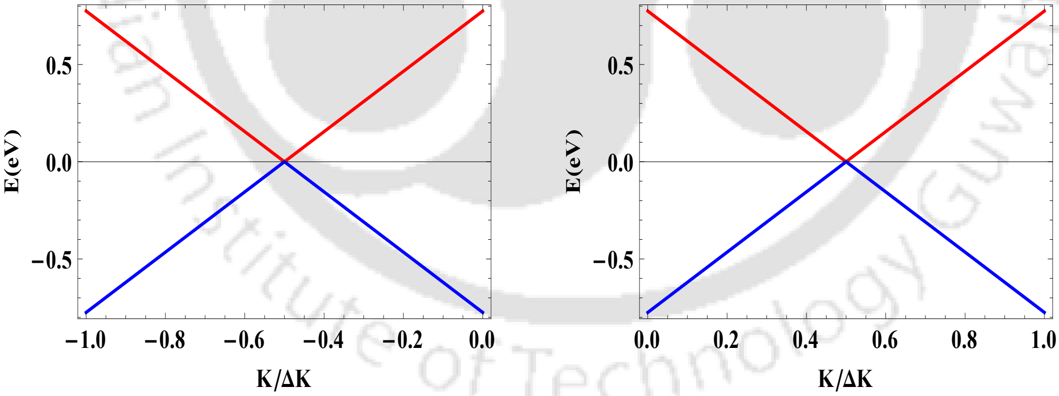

FIGURE 4.2: Schematic diagrams of band structure of twisted BLG. Left: for $q = K + \frac{\Delta K}{2}$. Right: $q = K - \frac{\Delta K}{2}$. In the presence of twist, the Dirac point splits up into two Dirac points and shift by $\pm\frac{\Delta K}{2}$. For plotting purposes, we have taken the parameters: $v_F|\Delta K| = 1.56\ eV$, twist angle $\theta = 10°$ and $t_\perp = 0.22\ eV$.

stressing is unique to graphene-based systems, i.e. anomalous Rabi oscillations (AROs). The band structure of twisted bilayer graphene is given in Fig. 4.2.

4.1 Effect of trigonal warping on ROs

In this section, we describe the phenomenon of ROs in bilayer graphene when a weak direct inter-layer hopping, γ_3, is taken into account. The effective low-energy Hamiltonian of bilayer graphene when trigonal warping is taken into account [16], can be written as follows

$$\hat{H}_2 = -\frac{1}{2m}\begin{pmatrix} 0 & (\pi^\dagger)^2 \\ (\pi)^2 & 0 \end{pmatrix} + v_3\begin{pmatrix} 0 & \pi \\ \pi^\dagger & 0 \end{pmatrix} \tag{4.1}$$

with the energy eigenvalues $E_\pm(p) = \pm|v_3 p_+ - \frac{p_-^2}{2m}|$, $\pm$ corresponds to conduction and valance band respectively, where $p_\pm = p_x \pm i p_y$. These energy eigenvalues are pictorially shown in Fig. 4.1. The first term in Hamiltonian Eq. (4.1) gives the indirect hopping from A1 to B2 that includes three hops between the atomic sites: an intra-layer hop A1-B1, followed by an inter-layer hop B1-A2 via dimer site, followed by an intra-layer hop A2-B2. The second term in Hamiltonian Eq. (4.1) describes a weak direct inter-layer hopping A1-B2, parameterized by γ_3 and $\gamma_3 \ll \gamma_0$. Since the Hamiltonian Eq. (4.1) describes the effective hopping between the non-dimer sites, A1-B2, i. e. between those atomic sites that do not lie directly above and below each other, therefore, the corresponding wave function of Hamiltonian Eq. (4.1) will be, $\psi = (\psi_{A1}, \psi_{B2})$. The weak direct inter-layer hopping parameter γ_3 has a dramatic effect on energy momentum dispersion of bilayer graphene. Similar to bulk graphite [79, 211], the effect of coupling γ_3 is to produce trigonal warping that deforms the iso-energetic lines along the direction $\phi = \phi_0$, following Fig.2 in Ref.[16]. At very low energies $|\epsilon| \ll \frac{1}{2}\gamma_1(v_3/v)^2$, the trigonal warping effect is striking. It leads to Lifshitz transitions: the iso-energetic line breaks into four pockets, which is referred to as one 'central' and three 'leg' parts [16, 17, 79]. The central part and leg parts have minimum at $p = 0$ and at $|p| = 2mv_3$, angle ϕ_0, respectively. In the continuum limit, the Hamiltonian Eq. (4.1) in the K valley may be written as,

$$H = \sum_{\vec{k}} \psi^\dagger_{\vec{k}} \hat{H}_2 \psi_{\vec{k}} \tag{4.2}$$

where $\hat{H}_2$ is given by Eq. (4.1). The eigenstates of the Hamiltonian Eq. (4.1) in momentum space will be of the form $\psi = \Big(c_{A1}(\vec{k},t) \;\; c_{B2}(\vec{k},t)\Big)$. An in-plane electric field is applied to the bilayer graphene through a vector potential of the form $\vec{A}(t) = \vec{A}(0)e^{-i\omega t}$, where $\vec{A}(0) = \frac{e}{c}\left(A_x(0) + iA_y(0)\right)$. This vector potential couples to BLG through the minimal coupling prescription $\vec{k} \rightarrow \vec{k} - \frac{e}{c}\vec{A}$. In second quantization, the Hamiltonian Eq. (4.2) reads,

$$H = -\frac{1}{2m}\sum_{\vec{k}}\left[(k_- - A^*(t))^2 c^\dagger_{A1}(\vec{k},t)c_{B2}(\vec{k},t) + h.c.\right]$$
$$+ v_3\sum_{\vec{k}}\left[(k_+ - A(t))\, c^\dagger_{A1}(\vec{k},t) \;\; c_{B2}(\vec{k},t) + h.c.\right] \tag{4.3}$$

where c and $c^\dagger$ are the annihilation and creation operators on two sublattice sites A1 and B2. The Hamiltonian Eq. (4.3) is valid only in semiclassical approximation where light is treated classically but the electronic degrees of freedom are quantum in nature.

The reason why we are interested in studying the same phenomenon in trigonally warped bilayer graphene, even when this phenomenon has already been discussed in bilayer graphene without trigonal warping effect. The main reason is the change in the low-energy Hamiltonian in presence of trigonal warping that changes the band structure drastically. Therefore, it is worthwhile to study the phenomenon of ROs in bilayer graphene, when weak direct inter-layer hopping is taken into account, even when this phenomenon has already been discussed in bilayer graphene without trigonal warping effect. To do so, we follow a strategy similar to described in previous chapters. First, we derive the Bloch equations and then these equations will be solved in conventional and in off resonance cases. To solve these equations in both the aforementioned cases, we apply a method which has already been used to solve the Bloch equations in single and bilayer graphene without trigonal warping effect. Therefore, briefly indicate the method of solution and the interpretations of the results obtained. Hence, we first will discuss the effect of trigonal warping on conventional Rabi oscillations and later treat the same phenomenon in off resonance case.

Bloch equations of trigonally warped bilayer graphene: Here, we derive the Bloch equations of bilayer graphene when trigonal warping effect is taken into account. Using Heisenberg's equation of motion and Hamiltonian Eq. (4.3), we may write the Bloch equations of trigonally warped bilayer graphene as follows

$$i\partial_t n_{diff}(\vec{k},t) = -\frac{1}{m}\left[\left(k_- - A^*(0)\, e^{i\omega t}\right)^2 p(\vec{k},t) - h.c.\right] + 2v_3\left[\left(k_+ - A(0)\, e^{-i\omega t}\right) p(\vec{k},t) - h.c.\right] \tag{4.4}$$

$$i\partial_t p(\vec{k},t) = -\frac{1}{2m}\left(k_+ - A(0)\, e^{-i\omega t}\right)^2 n_{diff}(\vec{k},t) + v_3\left(k_- - A^*(0)\, e^{i\omega t}\right) n_{diff}(\vec{k},t) \tag{4.5}$$

where,

$$n_{diff}(\vec{k},t) = \langle c^{\dagger}_{A1}(\vec{k},t)\; c_{A1}(\vec{k},t)\rangle - \langle c^{\dagger}_{B2}(\vec{k},t)\; c_{B2}(\vec{k},t)\rangle$$

$$p(\vec{k},t) = \langle c^{\dagger}_{A1}(\vec{k},t)\; c_{B2}(\vec{k},t)\rangle, \quad k_{\pm} = k_x \pm ik_y$$

Equations (4.4) and (4.5) are the coherent optical Bloch equations of bilayer graphene when trigonal warping is taken into account.

Now, we move on to discuss the solution of these equations in the different regions of interest. We first solve the Bloch equations in the conventional resonance case, when the frequency ω of the externally applied field is nearly equal to the particle-hole creation frequency. Later on, the Bloch equations are solved in the off resonance case where the external frequency ω is very large compared to all other frequencies.

Solution of Bloch equations in conventional resonance case: Here, Bloch equations (4.4) and (4.5) are solved in conventional case when $n\omega$ is nearly equal to the inter-band transition frequency of the system, where n defines the order of harmonic resonances. We adopt the well known RWA in order to solve the Bloch equations in conventional resonance case. In bilayer graphene, there are two possible resonances - single harmonic resonance occurs at the first harmonic in external frequency i.e. when $n = 1$ and a second resonance that occurs due to the frequency doubling effect i.e. when $n = 2$. Bloch equations are solved in the resonance case by using the rotating wave approximation [150–152] well-known in the context of two level atomic systems in quantum optics. Mishchenko [175] has already studied the phenomenon of Rabi oscillations in single layer graphene, for small detuning δ which is the difference between the external driving frequency, and the inter-band transition frequency of the system. For small detuning, the conventional Rabi frequency at the single and double (ω *and* 2ω) harmonic resonance are given by respectively,

$$\Omega_\omega = \left[\delta^2 + \frac{2|k|^2}{m}\omega_{R2} + \omega_{R1}^2\right]^{\frac{1}{2}}, \; \Omega_{2\omega} = \left[\delta^2 + \omega_{R2}^2\right]^{\frac{1}{2}} \tag{4.6}$$

where $\delta = n\omega - 2E_k$, and $n = 1, 2$ for the first and second harmonic resonance, respectively. $\omega_{R1} = v_3|A(0)|$, which is analogous to ω_R in case of single layer graphene only the difference is that v_F replaced by v_3 and $\omega_{R2} = \frac{|A(0)|^2}{2m}$. The above formulae have the following explanation: Ω_ω in Eq. (4.6) contains an additional factor of ω_{R1} in comparison to bilayer graphene without trigonal warping, see Eq. (2.16) in chapter 2. This term is solely due to the weak direct interlayer hopping parameter γ_3. This means, the conventional Rabi frequency at first harmonic resonance is increased by a factor of ω_{R1} in presence of trigonal warping in bilayer graphene. On the other hand, $\Omega_{2\omega}$ in Eq. (4.6) has no terms that contains ω_{R1} which means trigonal warping does not affect the conventional Rabi frequency at second harmonic resonance. Therefore, in the conventional resonance case, trigonal warping affects only the conventional Rabi frequency at first harmonic resonance while conventional Rabi frequency at second harmonic resonance remains unaffected. This is the direct consequence of the effect of trigonal warping on band structure. In Hamiltonian Eq. (4.3), the second term (trigonal warping term) contains only the first harmonics in the external deriving frequency. This shows that the trigonal warping affects the conventional Rabi frequency only at the first harmonic resonance while conventional Rabi frequency at the second harmonic resonance is not affected by the presence of trigonal term. Therefore, we can conclude that the trigonal warping affects the conventional Rabi frequency only at the first harmonic resonance while conventional Rabi frequency at the second harmonic resonance is not affected by the trigonal warping term.

Solution of Bloch equations in off resonance case: As usual, here also, we solve the Bloch equations of bilayer graphene in off resonance. The method of solving the Bloch equations in off resonance case has been described in earlier chapters hence we merely describe the results obtained and their interpretations. To solve the Bloch equations in off resonance case, we employ an approximation called the asymptotic rotating wave approximation (ARWA) described in earlier chapters, the results of which is corroborated with a fully numerical solution of the Bloch equations. To this end, we decompose $n_{diff}(\vec{k}, t)$ and $p(\vec{k}, t)$ into slow and fast terms as usual. Using this ansatz into the Bloch equations and comparing the same exponential power in the external frequency from both sides, we may easily separate the slow and fast varying population and polarization equations. In this analysis, we have neglected the terms containing higher harmonics than that present in the Hamiltonian of the system. Finally, we assumed that the frequency ω of the external field is the largest frequency. Using these simplifications, we may write the solutions of the fast varying population and polarization equations as,

$$n_{f1}(\vec{k},t) = -\frac{2k_+A(0)}{m\omega}p_s^*(\vec{k},t) - \frac{2v_3A(0)}{\omega}p_s(\vec{k},t), \quad n_{f2}(\vec{k},t) = \frac{(A(0))^2}{2m\omega}p_s^*(\vec{k},t)$$

$$p_{1+}(\vec{k},t) = \frac{k_+A(0)}{m\omega}n_s(\vec{k},t), \quad p_{1+}^*(\vec{k},t) = \frac{-v_3A^*(0)}{\omega}n_s(\vec{k},t)$$

$$p_{2+}^*(\vec{k},t) = \left(\frac{k_+^2(A^*(0))^2}{8m^2\omega^2} - \frac{5v_3k_-(A^*(0))^2}{4m\omega^2}\right)p_s(\vec{k},t) - \frac{v_3^2(A^*(0))^2}{\omega^2}p_s^*(\vec{k},t)$$

$$p_{2+}(\vec{k},t) = \frac{-A^2(0)}{4m\omega}n_s(\vec{k},t)$$

The slow varying part of population and polarization equations comes out to be,

$$i\partial_t n_s(\vec{k},t) = -\frac{1}{m}\left[k_-^2\ p_s(\vec{k},t) - k_+^2\ p_s^*(\vec{k},t)\right] + 2v_3\left[k_+\ p_s(\vec{k},t) - k_-\ p_s^*(\vec{k},t)\right] \tag{4.7}$$

$$i\partial_t p_s(\vec{k},t) = -\left(\frac{k_+^2}{2m} - v_3k_-\right)\ n_s(\vec{k},t) - \omega_{R12}\ p_s(\vec{k},t) \tag{4.8}$$

$$\omega_{R12} = \left(\frac{\omega_{R2}^2}{\omega} + \frac{4|k|^2\omega_{R2}}{m\omega} - \frac{2\omega_{R1}^2}{\omega}\right), \ \omega_{R2} = \frac{|A(0)|^2}{2m}$$

$\omega_{R1} = v_3|A(0)|$, is the zero detuned Rabi frequency of the trigonal warping term which is similar to that of the single layer graphene, and ω_{R2} is the zero detuned conventional Rabi frequency of bilayer graphene without trigonal warping. Equations (4.7) and Eq.(4.8) may be solved by assuming that $n_s(\vec{k},t) = n_s(\vec{k},0)Cos(2\Omega t)$ and $n_s(\vec{k},0) = \frac{2E_k}{\omega_{R12}}$, is the equilibrium value of population that can be determined in mean field approximation. $E_k = |\frac{k_+^2}{2m} - v_3k_-|$, is the energy eigenvalue of the Hamiltonian Eq. (4.1). Using this simplification, we may write the solution of the slow part of polarization equation as,

$$p_s(\vec{k},t) = p_0(\vec{k})\left[Cos(2\Omega t) + i\frac{2\Omega}{\omega_{R12}}Sin(2\Omega t)\right]$$

$$\Omega_{ARWA} = 2\Omega = 2\left[E_k^2 + \frac{(\omega_{R12})^2}{4}\right]^{1/2}, \quad \omega_{R12} = \left(\frac{\omega_{R2}^2}{\omega} + \frac{4|k|^2\omega_{R2}}{m\omega} - \frac{2\omega_{R1}^2}{\omega}\right)$$

where $p_0(\vec{k}) = E_k/\left(\frac{k_-^2}{m} - 2v_3k_+\right)$ is the equilibrium value of polarization. Ω_{ARWA}

is the generalized anomalous Rabi frequency (ARF) for bilayer graphene in the off resonance case when trigonal warping effect is taken into account.

Moreover, there is a *special* situation at the *Dirac point*, $\vec{k} = 0$, of the Brillouin zone where the Bloch equations may be solved easily by the above process. The ARF at the *Dirac point* is given by,

$$\Omega_{ARF} = \left| \frac{\omega_{R2}^2}{\omega} - \frac{2\omega_{R1}^2}{\omega} \right| \tag{4.9}$$

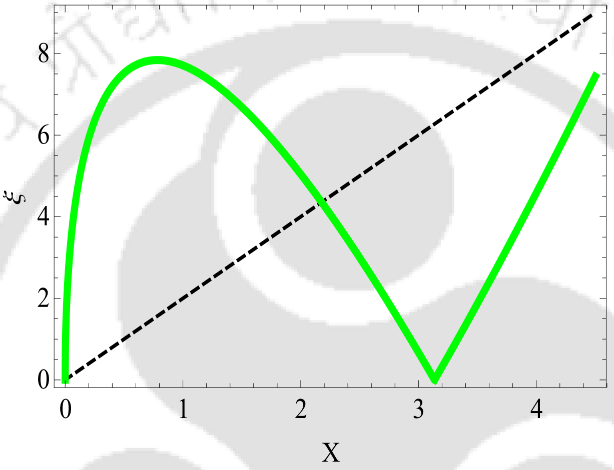

FIGURE 4.3: Schematic of the variation of dimensionless ARF $\xi\,(=10^5\Omega_{ARF}/\omega)$ versus a dimensionless quantity $\eta\,(=10^5X \text{ and } X=\omega_{R2}^2/\omega^2)$. Bilayer graphene without TW effect (black dashed curve) shows a zero trivial minimum at a zero value of the applied field whereas, when the TW effect is taken into account, it shows a zero non-trivial minimum (solid green curve). This zero non-trivial minimum occurs at a strength of the field that corresponds to a value of the momentum where the 'leg pocket' of the Fermi surface develops, and thereafter varies linearly with the square of the intensity of the applied field consistent with bilayer graphene without TW effect.

The above ARF has following explanation: if we ignore the trigonal warping effect, (set the parameter $v_3 \sim 0$), the first term in Eq. (4.9) is present, but the second term is zero since $\omega_{R1} = v_3|A(0)|$. That yields the anomalous Rabi frequency of bilayer graphene without trigonal warping, at the Dirac point of the Brillouin zone. The second term in Eq. (4.9) is purely due to trigonal warping, and this term has an analogy with the zero detuned conventional Rabi frequency of single layer graphene with some minor differences. The single layer graphene Hamiltonian [92] and the second term in the Hamiltonian Eq.(4.1) are nearly identical, the only difference [16, 18] being that in single layer graphene $v_F \sim 10^6\ m/s$ whereas in bilayer graphene $v_3 \sim 9.7 \times 10^4\ m/s$.

It is clear from Fig. 4.3 that the ARF varies linearly with a dimensionless quantity X (∼ square of intensity) and exhibits a zero trivial minimum (black dashed curve) whereas it shows a zero non-trivial minimum (solid green curve) when trigonal warping effect has been taken into account. The zero non-trivial minimum occurs at a value of the intensity that corresponds to a value of the momentum where the 'leg pocket' of the Fermi surface develops, described in the pioneering work of E. McCann *et al.* [16, 17]. A realistic value of X is 1.4×10^{-7} at an applied external field $E_{max} = 250\ KV/cm$ for a frequency of the applied field, $\omega = 6\pi \times 10^{14}\ rad/s$. It can be seen that the trigonal warping effect is significant only for weak applied electric fields. For a weak applied field, ARF of bilayer graphene with trigonal warping is similar to that of single layer graphene. As the strength of the applied field increases, the behaviour of ARF tends towards the bilayer graphene without trigonal warping and varies linearly with the square of the intensity. This transition occurs where the 'leg pocket' of the Fermi surface develops.

So far we have discussed the effect of trigonal warping on ROs in bilayer graphene when trigonal warping is taken into account while we have neglected the effect of on-site asymmetry. This asymmetry may be caused by the substrate-graphene interaction or it may be due to an applied field perpendicular to the graphene sheet. The effect of asymmetry on AROs, when trigonal warping is not taken into account, is well described in chapter 3. When asymmetry is taken into account, the Hamiltonian Eq. (4.1) has to be modified by the inclusion of an additional term $\sigma_z\,\Delta$. This term is responsible for opening a gap at the Dirac point in the electronic spectrum of graphene bilayer. Now the Hamiltonian Eq. (4.1) has three terms- the first term which describes the parabolic dispersion at the Dirac points of the Brillouin zone, the second term describes the trigonal warping effect and the third term which is proportional to σ_z describes the on-site asymmetry. Using the modified Hamiltonian (that includes on-site asymmetry) we re-derive the Bloch equations and solve these equations far from resonance by a process similar to the one already discussed. We then obtain the following expression for the anomalous Rabi frequency at the Dirac point,

$$\Omega_{ARF}^{asy} =\mid 2\Delta + \frac{\omega_{R2}^2}{\omega} - \frac{2\omega_{R1}^2}{\omega} \mid \tag{4.10}$$

Equation (4.10) gives the effective ARF at Dirac point in graphene bilayer when both trigonal warping and on-site asymmetry have been taken into account. It is clear from Eq. (4.10) that graphene bilayer exhibits Rabi-like oscillations (offset oscillations) even for applied field strengths less than the gap parameter. As the strength of the applied field increases, the ARF smoothly decreases to a zero minimum value. This minimum occurs when $\Omega_{ARF}^{asy} = 0$. The phenomenon of offset oscillation is pictorially shown in Fig. 4.4.

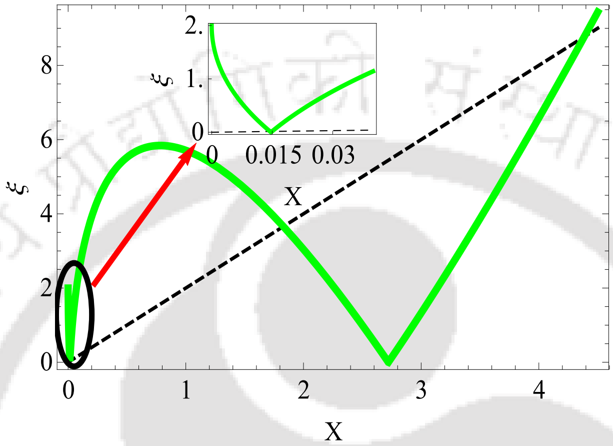

FIGURE 4.4: Schematic of the variation of dimensionless ARF ξ versus a dimensionless quantity η, in presence of on-site asymmetry. Bilayer graphene without any effect (black dashed curve) and with the trigonal warping and asymmetry effect (solid green curve). Without any effect ARF shows a zero trivial minimum at the origin. When on-site asymmetry is also taken into account, the ARF exhibits Rabi-like oscillations (inset) even for applied field strengths less than the gap parameter. For clarity, we have chosen a large value of gap parameter. The realistic value of the offset frequency is related to the gap parameter through the relation $2\Delta/\hbar\omega = 0.24$.

Similar to bilayer graphene without trigonal warping effect, here, we have also calculated the experimentally measurable and gauge invariant quantity current density when trigonal warping effect is taken into account in bilayer graphene. To calculate the current density, we apply a usual method described in previous chapters. The expression of current density for the bilayer graphene with trigonal warping may be derived using the continuity equation $\vec{\nabla} \cdot \vec{J}(\vec{r}, t) = -\partial_t \rho(\vec{r}, t)$ and quantum kinetic equation $i\hbar\partial_t \rho(\vec{r}, t) = [\rho(\vec{r}, t), H]$ along with the Hamiltonian Eq. (4.3). The real part of the current density, in momentum space, is given by (the average current is independent of position)

$$< Re\left(\vec{J}(t)\right) >= -\frac{1}{2\pi m}\sum_{\vec{k}}\left(k_- - A^*(t)\right)p(\vec{k}, t) + \frac{v_3}{2\pi}\sum_{\vec{k}}p(\vec{k}, t) + c.c. \tag{4.11}$$

Inserting $p(\vec{k}, t)$ into Eq. (4.11), writing $k_\pm = |k|e^{\pm i\theta_k}$, and upon integration over θ_k all terms drop out except the one that oscillates with the frequency of the external field. Performing a Fourier transform of this and integrating over $|k|$, we obtain a closed formula for the current density in the frequency domain,

$$\langle J_x^s(\omega^{'})\rangle \approx \alpha \left(\omega^{'} - \frac{1}{\omega}\left(\omega_{R2}^2 - 2\omega_{R1}^2\right)\right) \tag{4.12}$$

where $\omega^{'} > \left(\omega_{R2}^2 - 2\omega_{R1}^2\right)/\omega$ and $\langle J_x^s(\omega^{'})\rangle = 0$ otherwise. Eq. (4.12) is valid only near the threshold, $\omega' \approx \frac{\omega_{R2}^2 - 2\omega_{R1}^2}{\omega}$, evaluated using $E_k \ll \omega_{R12}/2$ and $v_3 \ll v$ as in Ref.[16]. Close to the threshold, the induced current exhibits linear behaviour in the frequency $\omega^{'}$ measured from the threshold. The exponent at the threshold is equal to unity unlike the single layer graphene where this exponent has been computed [184] to be equal to 1/2. The current density at the first and second harmonic resonance in frequency domain, respectively, given by,

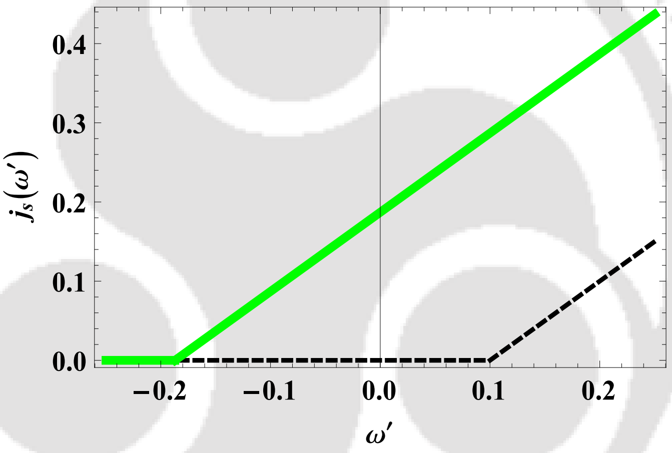

FIGURE 4.5: Schematic of the variation of the slow part of the current density in bilayer graphene in the frequency domain, in the extreme-non resonance case, without (black dashed curve) and with TW (solid green curve). Black dashed curve is plotted at a fixed value of $\omega_{R2} = 1$ and $\omega = 10$ (in arbitrary units). Solid green curve is plotted by fixing the value of the ratio (realistic) $\omega_{R2}/\omega_{R1} = 0.36$, $\omega = 10$ and $\omega_{R1} = 1$ (in arbitrary units). The frequency threshold with TW shows a shift towards a smaller value of the threshold and this shift is prominent for weak applied fields. The threshold frequencies of solid green and black dashed curve are $\left(\omega_{R2}^2 - 2\omega_{R1}^2\right)/\omega$ and ω_{R2}^2/ω, respectively, and the exponent at threshold is equal to unity in both cases.

$$j_x^s(\omega')|_\omega \approx \frac{A_r}{64\pi^2}\frac{\omega A(0)}{\sqrt{\omega'^2 - (2\omega\omega_{R2} + \omega_{R1}^2)}}, \quad j_x^s(\omega')|_{2\omega} \approx \frac{A_r}{16\pi^2 m}\frac{(A(0))^4}{16A^*(0)}\frac{1}{\sqrt{\omega'^2 - \omega_{R2}^2}}$$

The current density in time domain in resonance and off resonance case can be written as follows,

$$j^s_x(t)|_{ARWA} \approx \frac{\alpha}{2\pi}\frac{e^{-i\left(\frac{\omega^2_{R2}-2\omega^2_{R1}}{\omega}\right)t}}{t^2} \tag{4.13}$$

$$j^s_x(t)|_{\omega} \approx \beta\frac{Cos(\Omega\ t) - Sin(\Omega\ t)}{\sqrt{t}}, \quad j^s_x(t)|_{RWA,2\omega} \approx \gamma\frac{Cos(\omega_{R2}\ t) - Sin(\omega_{R2}\ t)}{\sqrt{t}} \tag{4.14}$$

$$\alpha = -\frac{A_r}{16\pi^2}\frac{\omega A(0)}{32\omega_{R2}}\frac{1}{\left(\frac{\omega^2_{R2}}{\omega} - \frac{2\omega^2_{R1}}{\omega}\right)}, \ \Omega = \sqrt{2\omega\omega_{R2} + \omega^2_{R1}}$$

$$\beta = \frac{A_r A(0)}{64\pi^2}\frac{\omega}{2\sqrt{\pi}(2\omega\omega_{R2} + \omega^2_{R1})^{1/4}}, \quad \gamma = \frac{A_r}{16\pi^2 m}\frac{(A(0))^4}{16\sqrt{\pi}A^*(0)}\frac{1}{\sqrt{\omega_{R2}}}$$

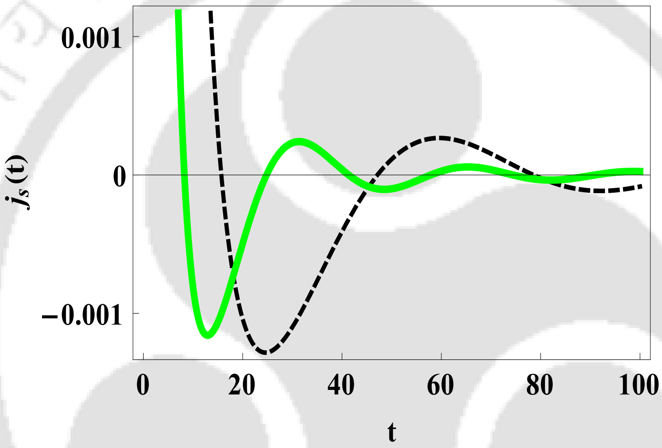

FIGURE 4.6: Shows the variation of the slow part of the current density in the time domain, in the extreme non-resonance case. Black dashed and solid green corresponds to, respectively, without and with TW. The frequency of oscillation of the current density with TW is increased relative to without TW. The current density in off resonance case shows a power law decay of the form t^{-2}.

Figures 4.5, 4.6 and 4.7 have been plotted keeping in mind that the values of ω_{R1} and ω_{R2} are such that the ratio (realistic) $\omega_{R2}/\omega_{R1} = 0.36$ is fixed, $\omega_{R1} = 1$ and $\omega = 10$, in arbitrary units. However, the realistic values of ω and ω_{R1} are $6\pi \times 10^{14}\ rad/sec$ and $1.96 \times 10^{12}\ rad/sec$, respectively, and the corresponding value of applied field is, $E = 250\ kV/cm$. Therefore, it is clear that TW effect plays a major role only for weak fields. If the value of the applied field is increased, the threshold behaviour of bilayer graphene with TW tends towards the threshold behaviour of the bilayer graphene without TW, as can be seen from Fig. 4.5, and this occurs at a very high value of the applied electric field, approximately $1375\ kV/cm$. Equation (4.14) reveal that the slow part of current density in both the resonance cases exhibit a different threshold behaviour, one is at the

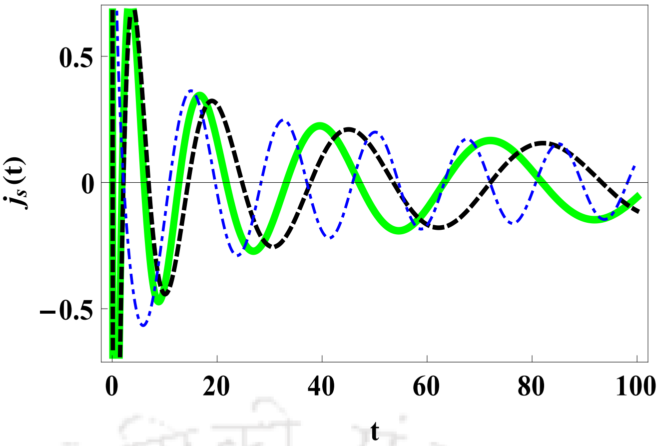

FIGURE 4.7: Shows the variation of the slow part of the current density in the time domain, in the near resonance case. Black dashed and solid green corresponds to without and with TW at the first harmonic resonance whereas, blue dot dashed corresponds to the second harmonic resonance. The threshold frequencies at first and second harmonic resonance are $(2\omega\omega_{R2}+\omega_{R1}^2)^{1/2}$ and ω_{R2}, respectively. The current density in both the resonance cases shows a power law decay of the form $t^{-1/2}$.

first harmonic resonance and another one at second harmonic resonance in the external frequency. The corresponding frequencies are $(2\omega\omega_{R2}+\omega_{R1}^2)^{1/2}$ and ω_{R2}, respectively. The threshold behaviour of current density at the second harmonic resonance is not affected by trigonal warping, it is clear from the second term of Eq. (4.6) and also from the Hamiltonian Eq. (4.3). The frequency of oscillations of the current density at first harmonic resonance is enhanced, and this increment is equal to the square of the zero detuned Rabi frequency due to the trigonal warping effect. The current density in both the resonance cases shows a power law decay of the form $t^{-1/2}$ while, for off resonance case it is of the form t^{-2} as Eqs. (4.13) and (4.14) reveals. The power law behaviour of the current density is not affected by trigonal warping i. e. the current density has the same power law decay in the bilayer graphene, either with or without trigonal warping.

So far, we have discussed the analytical solution of Bloch equations in different regions of interest. Our main motivation is to investigate the behaviour of induced current in the off resonance case, which is proportional to the inter-layer polarization in presence of an intense applied pump field. The induced current exhibits threshold behaviour in the frequency domain, and the corresponding threshold frequency may be identified with the ARF of the system. We have justified our predictions numerically by solving the Bloch equations. We have used the NDSolve routine of Mathematica to solve the Bloch equations and generate the plot of polarization versus time, Figs 4.8 and 4.9. The frequency obtained from the fully analytical method is consistent with the frequency inferred from the fully numerical solution of the Bloch equations.

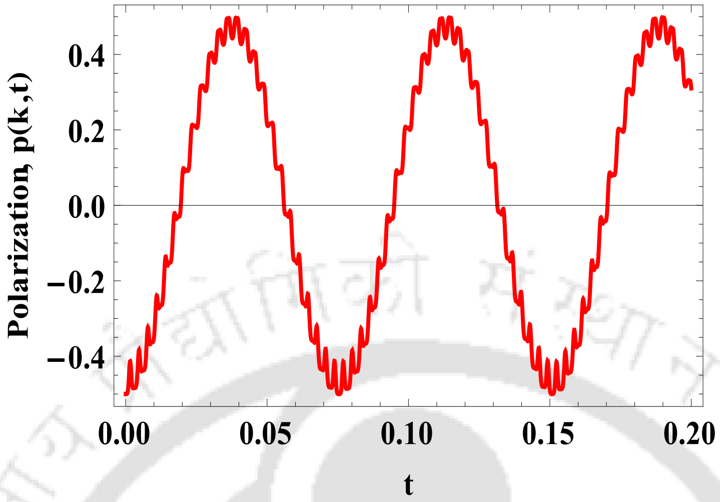

FIGURE 4.8: Schematic of the numerical plot of polarization $p(\vec{k}, t)$ versus time (t) far from resonance. It shows slow as well as rapidly varying oscillations. The frequency of oscillation of the slow part of the polarization exactly matches the analytically calculated anomalous Rabi frequency. To generate the plot we have taken the parameters $\frac{k_-}{\sqrt{2m}} = v_3 k_- = 0$, $\frac{A(0)}{\sqrt{2m}} = 10$, $v_3 A(0) = 300$ and $\omega = 2000$.

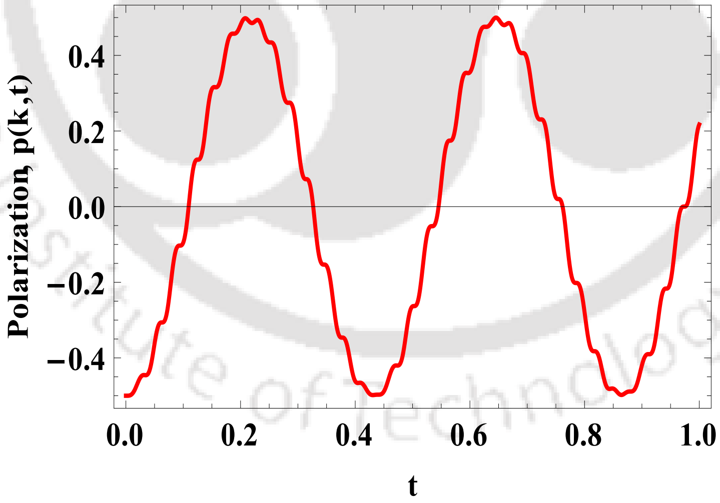

FIGURE 4.9: Schematic of the numerical plot of polarization $p(\vec{k}, t)$ versus time (t) at resonance. In this case, our numerical result favours the analytical result, as well. For plotting purposes, we have chosen $\frac{k_-}{\sqrt{2m}} = \sqrt{50}$, $v_3 k_- = 100$, $\frac{A(0)}{\sqrt{2m}} = 1$, $v_3 A(0) = 1$ and $\omega = 100$.

Similar trigonal warping effect is also found in case of single layer graphene in presence of Rashba spin orbit interaction. Bilayer graphene with weak direct inter-layer hopping γ_3 is similar to that of single layer graphene with Rashba spin orbit interaction. Therefore, we wish to remark that the results obtained above in bilayer graphene with the trigonal warping effect and that found in single layer graphene with Rashba spin-orbit interaction are quite similar to one another. The Hamiltonian of the single layer graphene when Rashba spin-orbit [111, 114, 212, 213] interaction is taken into account may be written as,

$$H = \begin{pmatrix} 0 & v_F\pi^\dagger & 0 & -v_\lambda\pi \\ v_F\pi & 0 & 3i\lambda_R & 0 \\ 0 & -3i\lambda_R & 0 & v_F\pi^\dagger \\ -v_\lambda\pi^\dagger & 0 & v_F\pi & 0 \end{pmatrix} \tag{4.15}$$

where $v_F = 3\gamma_0 d/(2\hbar)$, $v_\lambda = 3\lambda_R d/(2\hbar)$ with $v_\lambda \ll v_F$ as in given in Ref.[213], $\pi = p_x + ip_y$ and $\pi^\dagger = p_x - ip_y$ with d being the nearest neighbor distance. Also, λ_R represents the strength of spin-orbit coupling which may be due to a perpendicularly applied electric field or due to a graphene-substrate interaction.

The bilayer graphene Hamiltonian including weak direct inter-layer hopping γ_3 (trigonal warping effect) [16] near the center of the $\vec{K}$ valley in a basis corresponding to the atomic wave function $\psi = (\psi_{A1}, \psi_{B2}, \psi_{A2}, \psi_{B1})$ will be of the form;

$$H = \begin{pmatrix} 0 & v_3\pi & 0 & v\pi^\dagger \\ v_3\pi^\dagger & 0 & v\pi & 0 \\ 0 & v\pi^\dagger & 0 & \gamma_1 \\ v\pi & 0 & \gamma_1 & 0 \end{pmatrix} \tag{4.16}$$

The Hamiltonian in Eq. (4.15) has the same components as the Hamiltonian in Eq. (4.16) (apart from some relabeling). This result is remarkable since these systems are completely different. The matrix elements H_{14} and H_{41}, in Hamiltonian Eq. (4.15), are very small in comparison to the matrix elements that are proportional to v_F. These terms are responsible for the trigonal warping of the bands at low energy that changes the topology of the bands close to the Dirac points [213]. The energy momentum dispersion of both systems - single layer graphene with Rashba spin-orbit interaction and bilayer graphene with trigonal warping effect - is quite similar to one another. For a comparison of band diagram of both the systems we refer to Fig. 1(a) and 1(c) in Ref.[213] and Fig. 7(b) and 7(c) in Ref.[17].

Thus the results (ARO and conventional Rabi oscillations) that are obtained in case of BLG with trigonal warping will also be found in SLG with Rashba spin-orbit interaction.

Therefore, we can conclude that the anomalous Rabi frequency (ARF) is dramatically affected by trigonal warping since the ARF goes through a zero non-trivial minimum as a function of the applied field. This zero non-trivial minimum occurs at a strength of the applied field that corresponds to a situation where energy bands undergo trigonal warping. This happens at a value of the band momentum where the 'leg pockets' of the Fermi surface develop. Trigonal warping has a significant effect only for weak applied fields. When on-site asymmetry is also taken into account, graphene bilayer exhibits Rabi-like oscillations even for the field strengths less than the gap parameter. We call this ARF 'offset' frequency and is observable only for the weak applied fields. For strong applied field strengths, all the effects (trigonal warping and on-site asymmetry) go away and the system behaves like a bilayer graphene without any effect. Moreover, the threshold behaviour of the induced current in the off resonance case and in the first harmonic resonance case are significantly changed by trigonal warping whereas trigonal warping has no effect on the induced current or on the conventional Rabi frequency near the second harmonic resonance.

4.2 Effect of twisting on ROs in bilayer graphene

The previous chapters and the preceding section in this chapter are dealt with the phenomenon of ROs in perfect AB-stacked bilayer graphene (BLG). This section describes the same phenomenon, when relative twist between the layers is taken into account. Twisting, also called stacking defect, is unique to graphene with two or more layers. Twisted BLG shows quite different electronic properties than perfectly AB-stacked BLG, as we have already mentioned. We show that the ARF strongly depends on twist angle, and this dependence is most prominent for weak applied fields. The effective low-energy two component Hamiltonian of twisted BLG [207, 214, 215] can be written as follows,

$$H^{eff}_{2,twist} = -\frac{2v_F^2}{15\tilde{t}_\perp}\begin{pmatrix} 0 & k_-^2 - \left(\frac{\Delta K_-}{2}\right)^2 \\ k_+^2 - \left(\frac{\Delta K_+}{2}\right)^2 & 0 \end{pmatrix} \tag{4.17}$$

where $k_\pm = k_x \pm ik_y$, $\Delta K_\pm = \Delta K_x \pm i\Delta K_y$, v_F and $\tilde{t}_\perp$ is the Fermi velocity of the carriers and inter-layer coupling, respectively. ΔK_x and ΔK_y define the relative shift between the corresponding Dirac points of the twisted BLG. Unlike in untwisted BLG, the band minimum in twisted BLG splits up into two and show a linear band spectrum in the vicinity of these points. Expanding Hamiltonian Eq. (4.17) near $\frac{\Delta K_\pm}{2}$ by defining, $k_\pm = q_\pm + \frac{\Delta K_\pm}{2}$, keeping terms up to quadratic in q, Hamiltonian Eq. (4.17) reduces to the following form

$$H^{eff}_{2,twist} = -\frac{2v_F^2}{15\tilde{t}_\perp}\begin{pmatrix} 0 & q_-^2 + q_-\Delta K_- \\ q_+^2 + q_+\Delta K_+ & 0 \end{pmatrix} \tag{4.18}$$

Using Hamiltonian Eq. (4.18) and following the same process as described in earlier chapters, we can find anomalous Rabi frequency in off resonance case as given below

$$\Omega_{ARWA} = 2\sqrt{E_q^2 + \frac{\left(\frac{|\alpha A^2(0)|^2}{\omega} + \frac{2\alpha^2}{\omega}|(2q_+A(0) + A(0)\Delta K_+)|^2\right)^2}{4}} \tag{4.19}$$

where $E_{\vec{q}}(\pm) = \pm|q_-^2 + q_-\Delta K_-|$ is the energy eigenvalue of the twisted BLG

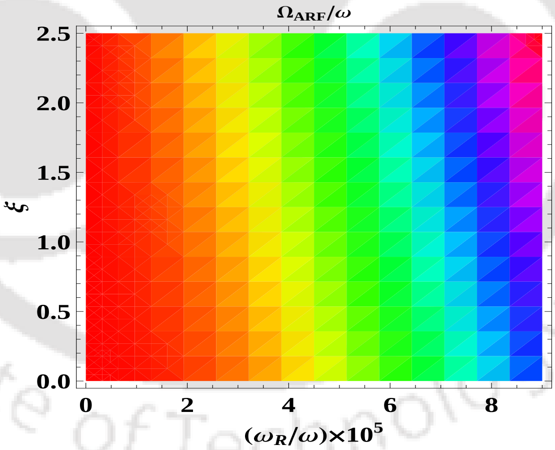

FIGURE 4.10: This density plot shows dimensionless anomalous Rabi frequency Ω_{ARF}/ω versus ω_R/ω and $\xi(= \hbar\alpha|\Delta K|^2/\omega)$ at the shifted Dirac point. It is clear from figure that twisting is prominent for weak applied fields. The value of $\hbar\Omega_{ARF}$ for red, green and blue colours are $3.7 \times 10^{-5}eV$, $1.84 \times 10^{-4}eV$ and $2.97 \times 10^{-4}eV$, respectively, at a fixed value of $\xi = 1.5$.

and $\alpha = \frac{2v_F^2}{15\tilde{t}_\perp}$. Eq. (4.19) gives the anomalous Rabi frequency near the shifted Dirac points in twisted BLG. If twist $\Delta K = 0$, we can get back the anomalous Rabi frequency of bilayer graphene without twist. Exactly at the shifted Dirac point, the Eq. (4.19) reduces to, $\Omega_{ARF} = \left[\frac{\omega_R^2}{\omega} + \frac{2\omega_R}{\omega}\alpha|\Delta K|^2\right]$. The variation of anomalous Rabi frequency at the shifted Dirac point with an external applied field and with the twist angle is clearly shown in the density plot in Fig. 4.10. It is seen that the anomalous Rabi frequency depends sensitively on the twist for weak applied fields (small ω_R).

We have also solved the Bloch equations of twisted BLG in the resonant case. A similar process is adopted to solve the Bloch equations as described earlier. The conventional Rabi frequency near first and second harmonic resonance found to be, respectively,

$$\Omega_\omega = \sqrt{\Delta^2 + \omega_R\left(\alpha|q_+|^2 + \alpha|\Delta K_-|^2 + \alpha q_+\Delta K_- + \alpha q_-\Delta K_+\right)}$$

$$\Omega_{2\omega} = \sqrt{\Delta^2 + \omega_R^2}$$

$$\Delta = \omega - 2E_k,\ E_k = |\alpha q_-^2 + \alpha q_-\Delta K_-|,\ \omega_R = \alpha|A(0)|^2,\ \alpha = \frac{2v_F^2}{15\tilde{t}_\perp}$$

Similar to BLG, twisted BLG also shows harmonic resonances. Twist has effect only on first harmonic resonance while second harmonic resonance is not affected by twisting as we can see from Eq. (4.18). We just saw that the anomalous Rabi frequency is greatly affected by the twist whereas conventional Rabi frequency is less affected. This is because at resonance q is not small rather it is given by the condition $2|\alpha q_-^2 + \alpha q_-\Delta K_-| = \omega$. Thus we see that while the anomalous Rabi frequency with twist is $\propto \omega_R$ for small fields and $\propto \omega_R^2$ without twist, the conventional Rabi frequency continues to have the form $\propto \sqrt{(..) + \omega_R(..)}$ both with and without twist.

Lastly, we examine the effect of a small voltage between layers. The low-energy electronic spectrum of twisted BLG in presence of a small bias (voltage) ($V \ll v_F|\Delta K|$) between the layers has already been discussed by Lopes *et al.* [207]. They find that the system continues to be gapless and the dispersion is linear with the same Fermi velocity as twisted bilayer without bias, but the Dirac points shift vertically by $\sim \pm V/3$.

Thus our predictions for the anomalous Rabi frequency in this case are unchanged. A comparison between the various parameters in single layer, bilayer and twisted bilayer graphene has been given in the following table:

Energy	*Unit*(*eV*)		
	SLG	BLG	TBLG
$\hbar\omega_R^2/\omega$	1.4×10^{-4}	1.78×10^{-7}	8.8×10^{-8}
$\hbar\omega_R$	1.3×10^{-2}	4.69×10^{-4}	1.05×10^{-4}
$\hbar\Omega_{ARF}$	2.8×10^{-4}	1.78×10^{-7}	5.02×10^{-5}
$\hbar(\hbar\alpha\|\Delta K\|^2)$	–	0	2.9
$\hbar\omega$	1.24	1.24	1.24

Table 4.1: This table contains realistic values of various energy scales in monolayer, bilayer and twisted BLG. The numerical values of all parameters are determined at a fixed value of external frequency, $\omega = 6\pi \times 10^{14} rad/sec$ and an applied electric field, $|E| = 250kV/cm$.

4.3 Summary and conclusions

This section includes a summary and conclusions of the present chapter. In previous chapters, we have studied the phenomenon of ROs in perfect AB-stacked bilayer graphene. This indirect inter-layer hopping includes a direct inter-layer hopping γ_1. In this discussion, we have not considered any direct inter-layer hopping between the layers of perfect AB-stacked bilayer graphene. In this chapter, we have taken into account a weak direct inter-layer hopping γ_3 between the layers and studied the phenomenon of ROs in bilayer graphene. This weak direct inter-layer hopping produces trigonal warping of bands at very low-energy in the band structure of the bilayer graphene. The behaviour of bilayer graphene with trigonal warping is intermediate to those of single layer graphene and bilayer graphene. The present chapter also describes the phenomenon of ROs if the two layers in bilayer graphene are not in perfect AB-stacking. In other words, the effect of a relative twist between layers on Rabi oscillations is studied in this chapter. This twisting is sometimes also known as a stacking defect.

In this chapter, first, we have described the effect of trigonal warping on ROs. Off resonance ROs (anomalous ROs) are dramatically affected by the presence of trigonal warping. Off resonance Rabi frequency as a function of intensity of applied field exhibits a zero non-trivial minimum far from origin. This zero non-trivial minimum appears solely due to the presence of a weak direct inter-layer hopping γ_3. This zero non-trivial minimum occurs at a strength of the applied field that corresponds to a value of the momentum where the 'leg pocket' of the

Fermi surface develops, and thereafter varies linearly with the square of the intensity of the applied field consistent with bilayer graphene without trigonal warping effect. It can be seen that the trigonal warping effect is significant only for weak applied electric fields. For a weak applied field, ARF of bilayer graphene with trigonal warping is similar to that of single layer graphene. As the strength of the applied field increases, the behaviour of ARF tend towards the bilayer graphene without trigonal warping and varies linearly with the square of the intensity. This transition occurs where the 'leg pocket' of the Fermi surface develops. This effect is pictorially shown in Fig. 4.3. In presence of trigonal warping and on-site asymmetry in each layer, bilayer graphene exhibits Rabi-like oscillations (offset oscillations) even for applied field strengths less than the gap parameter. This effect is same as in asymmetric bilayer graphene. In other words, we can say that if the on-site asymmetry is present in the graphene systems, these systems necessarily will show Rabi-like oscillations. For strong applied field strengths, all the effects (trigonal warping and on-site asymmetry) go away and the system behaves like an ideal bilayer graphene. The effect of asymmetry on off resonance ROs in trigonally warped bilayer graphene is pictorially shown in Fig. 4.4. The trigonal warping affects only the first harmonic conventional Rabi frequency whereas the second harmonic conventional Rabi frequency is not affected by the trigonal warping. This is because the trigonal warping term depends only on the first harmonic in the external driving frequency, as we can see from Eq. (4.6). Similar to the discussion in other chapters, here also, we have determined the effect of trigonal warping on experimentally measurable quantity current density. In presence of trigonal warping, the frequency threshold in extreme non-resonance case shows a shift towards a smaller value of the threshold and this shift is prominent for weak applied fields. This is diagrammatically shown in Fig. 4.5. Even in presence of trigonal warping effect the exponent at threshold is equal to unity. It means that the presence of trigonal warping does not changes the exponent at threshold, it changes only the frequency threshold, it is clear from Eq. (4.12). The frequency of oscillations of current density, in time domain in off resonance and at the first conventional harmonic resonance in presence of trigonal warping, is increased relative to without trigonal warping whereas the frequency of oscillations of current density at second conventional harmonic resonance remains unaffected. This is shown in Figs. 4.6 and 4.7. Equations (4.13) and (4.14) show that the off resonance current density shows a power law decay of the form t^{-2} whereas the current density in the conventional resonance shows a power law decay of the form $t^{-1/2}$, respectively. The power law decay of current density with and without trigonal warping is same in both cases. In other words, we can say that the effect of trigonal warping does not affect the power law decay of current density. We have also given a fully numerical solution of the Bloch equations that fully corroborates the analytical findings. We have used the NDSolve routine of Mathematica to solve the Bloch equations and generate the plot, Figs. 4.8 and 4.9, of polarization versus time. The frequency obtained from the fully analytical method is consistent with the frequency inferred from the fully numerical solution of the Bloch equations.

We have also studied the effect of twisting, also known as stacking defect, on ROs in bilayer graphene. Twisting means, the two layers in bilayer graphene are not exactly in AB-stacking but they are twisted by a small twist angle relative to each other. In this study, it is found that the off resonance Rabi frequency is significantly affected by the presence of a small relative twist between the layers. This phenomenon is pictorially shown in Fig. 4.10. It is seen that the off resonance Rabi frequency depends sensitively on twist only for weak applied fields (small ω_R). The Bloch equations of twisted bilayer graphene are also solved in conventional resonance case, and found that twist has effect only on first harmonic resonance while second harmonic resonance is not affected by twisting. The form of formulae of conventional Rabi frequencies remains same.

All the details of this chapter are taken from references [187, 216]

PART-II

Incoherent Anomalous Rabi Oscillations

Chapter 5

Phonon assisted damping of ROs in Graphene Systems

The previous chapters describe the phenomenon of coherent ROs in graphene-based systems. It is referred to as coherent because of absence of relaxation term or energy dissipation. The optical properties of graphene-based systems are rich and varied. Nevertheless, a basic question still remains unsolved: What is the effect of electron-phonon interaction on these optical properties? Specifically, does damping due to phonons make Rabi oscillations in general and anomalous Rabi oscillations in particular, unobservable?

The electron-phonon interaction is one of the most important fundamental physical problems in any new electronic material. The impact of electron-phonon coupling on the ac conductivity of monolayer graphene is studied by Wright et al. [217]. It is shown that electron-LO phonon interactions cause an increase in the absorption of monolayer graphene of as much as 20% at room temperature. Resonance Raman scattering (RRS) from metallic single-wall carbon nanotubes [218] and by inelastic x-ray scattering from a graphite flake [219] revealed that the phonon modes of certain symmetries in graphitic materials exhibit a frequency softening. This frequency softening is attributed to Kohn anomalies in two-dimensional graphite [220] and occurs when electrons at the Fermi surface screen the phonon mode in a graphene sheet. Generally, electron-phonon scattering in graphene expected to be weak due to very high phonon frequencies [221]. Phonon modes in bilayer graphene are strongly affected by the presence of a potential difference between the layers which is due to an applied electric field. In presence of potential difference between the layers symmetric and asymmetric phonon modes strongly mixed with each other [222]. The performance of proposed graphene-based devices (electronic and optical) depends on carrier and phonon scattering as well as relaxation dynamics. The optical phonons in graphene-based systems can decay in two main ways. First is that the optical phonons may be absorbed by electrons and holes. Second is that optical phonons can decay into other phonons via anharmonic interactions and lattice defects. The relaxation dynamics of hot optical phonons in few-layer and multi-layer graphene films grown by epitaxy on silicon carbide substrates and by chemical vapour deposition on nickel substrates is studied using ultra-fast optical spectroscopy, and it is shown that optical phonon cooling on short time scale is independent of graphene growth technique, the number of layers, and the type of the substrate [168]. Electron-phonon coupling is an important effect in monolayer as well as in bilayer graphene. Electron phonon interaction in monolayer graphene exhibits interesting phenomena such as the Kohn anomalies [220], breakdown of the adiabatic approximation (Born-Oppenheimer) [162], and renormalization of the phonon energy [223] have been reported. In AB-stacked bilayer graphene, the effect of electron-phonon interaction is expected to be more interesting where both the band structure and the Fermi level can be tuned through the applied electrical gates [35, 37, 61], allowing for the control of a delicate interplay between electrons, phonons, and photons [34, 224, 225]. Inter-layer asymmetry qualitatively changes the electron-phonon interaction in bilayer graphene absent in monolayer graphene [222].

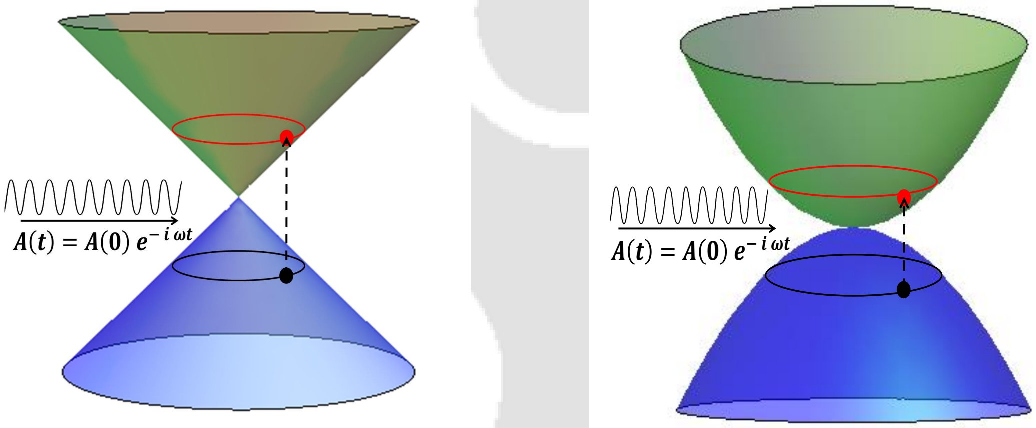

FIGURE 5.1: Left and right shows the transitions between the valence and the conduction band in monolayer and bilayer graphene, respectively, induced by externally applied electric field of frequency ω.

In this chapter, our main focus is the study of carrier relaxation dynamics on optical response in bilayer as well as in monolayer graphene in presence of highly oscillating electric field. Graphene-based systems exhibit novel quantum optical phenomena under applied electromagnetic field. Mishchenko [175] determined the ac conductivity in monolayer graphene by studying Rabi oscillations and revealed that the induced current under strong applied field shows a saturation phenomenon upon inclusion of relaxation dynamics. In his study the energy relaxation is introduced in a phenomenological way and the calculation performed 'near resonance', when the frequency of the external field is nearly equal to the electron-hole pair excitation frequency, using the well-known rotating wave approximation (RWA) [150, 151]. We have also studied Rabi oscillations in graphene-based systems 'far from resonance', when the frequency of applied field is very large compared to electron-hole pair excitation frequency, using a new approximation called 'asymptotic' rotating wave approximation [184, 187]. We successfully showed that Rabi oscillations in graphene-based systems exhibit 'anomalous' behavior far from resonance (off resonance). This chapter is devoted to the study of relaxation dynamics in bilayer as well as in monolayer graphene, not by including the energy relaxation in a phenomenological way, but by explicit calculation of electron-phonon scattering rate. In other words, we are interested in studying the phenomenon of carrier relaxation in a clean bilayer sample by determining the behaviour of Rabi oscillations in presence of electron-phonon interaction (optical, acoustic and flexural). Energetic optically excited carriers are known as hot carriers. These carriers lose their energy to lattice vibrations known as phonons resulting in a relaxation of these carriers. The main conclusions of our findings is that the combination of the constraints of energy and momentum conservation in phonon scattering in the region of the Brillouin zone relevant to ARO means that there is a momentum threshold for carrier phonon scattering. In other words, very long wavelength anomalous Rabi oscillations remain undamped. This is in contrast to the situation with conventional Rabi oscillations that occur at a wave number determined by the resonance condition which is large enough that these oscillations become heavily damped. This another indication that anomalous (rather than conventional) Rabi oscillations are an ideal probe of the low energy band structure of graphene based materials.

5.1 Optical phonon damped AROs in graphene-systems

In this section, we wish to study the relaxation dynamics of massive chiral quasi-particles in bilayer graphene with electron-optical phonon interaction in presence of intense optical pump field. Optical phonons in graphene have been discussed in the context of a valence-force field model [226, 227]. We restrict ourselves to work in the long-wavelength limit. There are two optical modes in graphene bilayer, symmetric and antisymmetric with displacement of two layers oscillating in phase and out of phase, respectively [222]. These modes can be represented by a relative displacement of two sublattice atoms A and B in layer one, given by

$$u(\vec{r}) = \sum_{\vec{q},\nu} \sqrt{\frac{\hbar}{4NM\omega_0}} (b_{\vec{q},\nu} + b^{\dagger}_{-\vec{q},\nu}) e_{\nu}(\vec{q}) e^{i\vec{q}\cdot\vec{r}} \tag{5.1}$$

where N is the number of unit cells, M is the mass of a carbon atom, ω_0 is the optical phonon frequency at the Γ point, ν stands for longitudinal (l) and transverse (t) modes of the phonon, b and $b^{\dagger}$ are the annihilation and creation operators, respectively.

$$\begin{aligned} e_l(\vec{q}) &= i(q_x/|\vec{q}|, q_y/|\vec{q}|), \quad q_x = |\vec{q}|\ cos\phi(\vec{q}) \\ e_t(\vec{q}) &= i(-q_y/|\vec{q}|, q_x/|\vec{q}|), \quad q_y = |\vec{q}|\ sin\phi(\vec{q}) \end{aligned} \tag{5.2}$$

The corresponding optical phonon hamiltonian can be written as follows,

$$H_{ph} = \sum_{\vec{q},\nu} \hbar\omega_0 \left(b^{\dagger}_{\vec{q},\nu} b_{\vec{q},\nu} + \frac{1}{2} \right) \tag{5.3}$$

The displacement in second layer is exactly same as in layer one. These two layers are coupled by a weak Van der Waals forces so the phonons in two layers are also weakly coupled to one another. These weakly coupled phonons form symmetric and antisymmetric modes with slightly different frequencies. For the present discussion we have ignored such small effect. The symmetry between transverse and longitudinal mode of phonons is not destroyed due to equal charge distribution between A and B sublattices and the isotropic nature in the long-wavelength limit. Therefore, we omit the subscript ν in the present discussion. The interaction Hamiltonian between the optical phonon and an electron [226] at one of the Dirac points, say $\vec{K}$, can be written as

$$H_{e-oph} = \chi \sum_{\vec{k},\vec{q}} \left[X_{\vec{q}}(t)\ \frac{q_-}{|\vec{q}|}\ c^{\dagger}_{A1}(\vec{k},t) c_{B2}(\vec{k}-\vec{q},t) + h.c. \right] \tag{5.4}$$

$$\chi = \sqrt{2}\frac{\beta\gamma}{b^2}\sqrt{\frac{\hbar}{4NM\omega_0}}, \quad X_{\vec{q}} = (b_{\vec{q}} + b^{\dagger}_{-\vec{q}})$$

where $b = a/\sqrt{3}$ is the equilibrium bond length. The dimensionless parameter β is given by $\beta = d(ln\ \gamma_0)/d(ln\ b)$, M is the mass of the carbon atom.

The Hamiltonian [16] of bilayer graphene in presence of an electromagnetic field can be written as follows,

$$H_2 = -\frac{1}{2m} \sum_{\vec{k}} \left[c^{\dagger}_{A1}(\vec{k},t)(k_- - A(t))^2 c_{B2}(\vec{k},t) + h.c. \right] \tag{5.5}$$

where, $k_{\pm} = k_x \pm i k_y$, $c(c^{\dagger})$ are annihilation(creation) operators on sublattice site $A1$ and $B2$ and vice-versa. $\vec{A}(t)$ is a complex vector potential applied that couples to bilayer graphene through a Coulomb gauge, where $\vec{A}(t) = \frac{e}{c}\vec{A}(0)e^{-i\omega t}$ and $\vec{A}(0) = \frac{e}{c}(A_x(0) + iA_y(0))$. Therefore, the full Hamiltonian of bilayer graphene including electron-optical phonon interaction can be written as,

$$\begin{aligned} H_{full} = &-\frac{1}{2m} \sum_{\vec{k}} \left[c^{\dagger}_{A1}(\vec{k},t)(k_- - A(t))^2 c_{B2}(\vec{k},t) + c^{\dagger}_{B2}(\vec{k},t)(k_+ - A^*(t))^2 c_{A1}(\vec{k},t) \right] \\ &+ \chi \sum_{\vec{k},\vec{q}} \left[X_{\vec{q}}(t)\ \frac{q_-}{|\vec{q}|}\ c^{\dagger}_{A}(\vec{k},t) c_B(\vec{k}-\vec{q},t) + X_{-\vec{q}}(t)\ \frac{q_+}{|\vec{q}|}\ c^{\dagger}_{B}(\vec{k},t) c_A(\vec{k}+\vec{q},t) \right] \\ &+ \sum_{\vec{q}} \omega_0 \left(b^{\dagger}_{\vec{q}} b_{\vec{q}} + \frac{1}{2} \right) \end{aligned} \tag{5.6}$$

As usual we decompose Hamiltonian Eq. (5.6) and corresponding eigenfunctions into slow as well as fast terms as follows,

$$H = \sum_{m=0,\pm1,....} H_m\ e^{-im\omega t}, \qquad \psi = \sum_{n=0,\pm1,....} \psi_n\ e^{-in\omega t} \tag{5.7}$$

Inserting Eq. (5.7) into Eq. (5.6) and comparing the coefficients of same exponential powers from both sides and then using Schrödinger equation of motion, $i\frac{\partial\psi}{\partial t} = [\psi, H]$, and simple anti-commutator algebra for fermions, we can write the slow part of Hamiltonian Eq. (5.6) as,

$$
\begin{aligned}
H_{eff} = & -\frac{1}{2m}\sum_{\vec{k}}\left[k_-^2\ c^\dagger_{A1,0}(\vec{k},t)c_{B2,0}(\vec{k},t) + k_+^2\ c^\dagger_{B2,0}(\vec{k},t)c_{A1,0}(\vec{k},t)\right] \\
& -\sum_{\vec{k}}\left(\frac{2k^2}{m}\frac{\omega_R}{\omega}+\frac{\omega_R^2}{2\omega}\right)\ (c^\dagger_{A1,0}(\vec{k},t)c_{A1,0}(\vec{k},t) - c^\dagger_{B2,0}(\vec{k},t)c_{B2,0}(\vec{k},t)) \\
& +\chi\sum_{\vec{k},\vec{q}}\left[X_{\vec{q}}(t)\ \frac{q_-}{|\vec{q}|}\ c^\dagger_{A1,0}(\vec{k},t)c_{B2,0}(\vec{k}-\vec{q},t) + X_{-\vec{q}}(t)\ \frac{q_+}{|\vec{q}|}\ c^\dagger_{B2,0}(\vec{k},t)c_{A1,0}(\vec{k}+\vec{q},t)\right] \\
& +\sum_{\vec{q}}\omega_0\left(b^\dagger_{\vec{q}}b_{\vec{q}}+\frac{1}{2}\right)
\end{aligned}
\tag{5.8}
$$

We wish to study the dephasing of ROs under the problem consideration. This is easily be done by calculating the self energy of the system considered, which is generally a complex quantity. The real part of the self-energy gives the physical energy of particles (also referred as particle's self energy) whereas the imaginary part of the self energy is identified as scattering rate or dephasing rate. The inverse of the imaginary part is a measure for the lifetime of the particle under investigation. The self energy operator is related to the bare and dressed propagators, often denoted by G_0 and G, respectively, via the Dyson equation as follows,

$$
G = G_0 + G_0\Sigma G \quad or \quad G = (1 - G_0\Sigma)^{-1}\cdot G_0 \tag{5.9}
$$

where G'^s are defined as,

$$
\begin{aligned}
G_{ab}(\vec{k},t) &= -i\frac{\langle\ T\ S\ c_a(\vec{k},t)c_b^\dagger(\vec{k},t')\ \rangle_0}{\langle\ TS\ \rangle_0} \\
S &= Exp\left[-i\int_c \hat{H}_{e-ph}(t_1)dt_1\right]
\end{aligned}
\tag{5.10}
$$

where T is the time ordering symbol, S represents the $S-$ matrix expansion. A second order expansion of $S-$ matrix is required because the expectation value of first order expansion is zero due to presence of phonon operator $X_{\vec{q}}$ in the interacting part of Hamiltonian. Using Eqs. (5.9) and (5.10), we can calculate the imaginary part of the self energy which gives the dephasing rate.

$$
\Gamma_{k,R} = \sum_{\vec{q}}\frac{\pi\ \chi^2\ \alpha_{\vec{k}}\ \alpha_{\vec{k}+\vec{q}}}{2\ \Omega_{\vec{k}}\ \Omega_{\vec{k}+\vec{q}}}\ \delta(\omega_0 - \Omega_{\vec{k}} + \Omega_{\vec{k}+\vec{q}}) \tag{5.11}
$$

where

$$\Omega_{\vec{k}} = 2\sqrt{\frac{|k|^4}{4m^2} + \alpha_{\vec{k}}^2},\ \alpha_{\vec{k}} = \left(\frac{2|k|^2}{m}\frac{\omega_R}{\omega} + \frac{\omega_R^2}{2\omega}\right)$$

The delta function in Eq. (5.11) is responsible for energy conservation of system under consideration. According to energy conservation, this delta function will survive only when anomalous Rabi frequency $\Omega_{\vec{k}}$ is greater than the optical phonon frequency ω_0. In this case, the carriers in bilayer graphene show an energy relaxation by throwing away their energy to produce lattice vibrations known as optical phonons. This happens only when the carriers are highly energetic and these carriers are known as hot carriers (electron and hole). Inserting the values of $\Omega_{\vec{k}}$ and $\alpha_{\vec{k}}$ in Eq. (5.11) and assuming that $\frac{|k|^2}{m} > \omega_0$, after straightforward calculation Eq. (5.11) reduces to the following

$$\Gamma_{k,R} = \frac{A\chi^2}{2}\frac{m\omega_R^2}{2\omega^2\hbar^3} \tag{5.12}$$

It is clear form Eq.(5.12) that beyond the threshold, the relaxation rate of carriers by optical phonons in bilayer graphene is independent of electron wave number.

Monolayer and bilayer graphene possess similarities and differences, which is addressed in Sec.1.2. The relaxation dynamics of carriers in bilayer graphene by

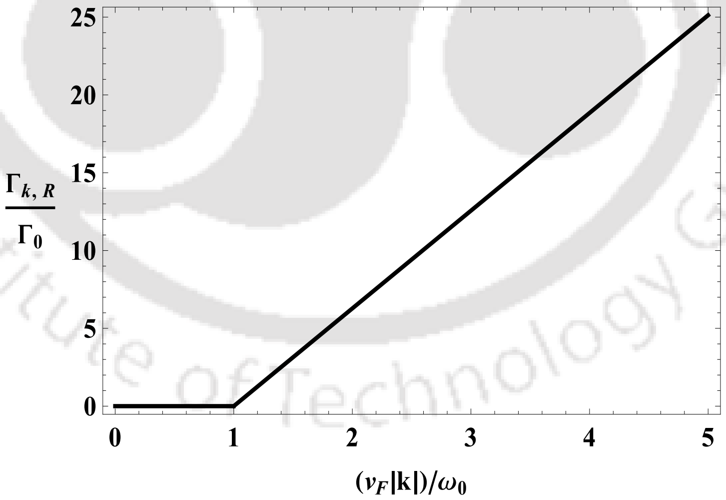

FIGURE 5.2: This schematic figure shows the variation of $\frac{\Gamma_{k,R}}{\Gamma_0}$ with respect to a dimensionless quantity $\frac{v_F|k|}{\omega_0}$. It is clear from figure that the scattering rate exhibit a threshold behaviour that can be identified with the electron wave number, $|k| = \frac{\omega_0}{2v_F}$ and zero otherwise. Thereafter, $\Gamma_{k,R}$ varies linearly with k. It shows that for the electron wave numbers $|k| < \frac{\omega_0}{2v_F}$, the optical phonons are insensitive in dephasing of AROs.

the optical phonon is discussed above. Below, the same phenomenon is described in monolayer graphene. To discuss the relaxation of carriers by optical phonons in monolayer graphene, we have adopted a similar method as described in case of bilayer graphene. The electron-optical phonon interacting Hamiltonian in bilayer and monolayer graphene has the same form [222, 223]. In case of monolayer graphene, the scattering rate is given by

$$\Gamma_{k,R} = \Gamma_0 \left(\frac{v_F k}{\omega_0}\right)(2\pi Sin\theta_k), \quad \theta_k = \cos^{-1}\left(\sqrt{\frac{2\omega_0(v_F k) - \omega_0^2}{v_F^2 k^2}}\right) \tag{5.13}$$

where $\Gamma_0 = \frac{A}{(2\pi)^2}\frac{\chi^2}{2\hbar^2}\frac{\omega_0}{v_F^2}$. It is clear from Eq. (5.13) that the electron-optical phonon interaction in monolayer graphene is prominent in dephasing of AROs only for the electron wave numbers $v_F|k| \geq \omega_0$ and zero otherwise. This is pictorially shown in Fig. 5.2. Therefore, we have seen that the effect of electron-optical phonon interaction on AROs in monolayer graphene is very different from bilayer graphene. In bilayer graphene, the scattering rate is constant (independent of electron wave number) while in case of monolayer graphene it varies linearly with electron wave number. Figure 5.3 shows the variation of Rabi cycles with respect to electron wave number. This clearly shows that carriers in monolayer graphene exhibit energy relaxation in presence of electron-optical phonon interaction far from the

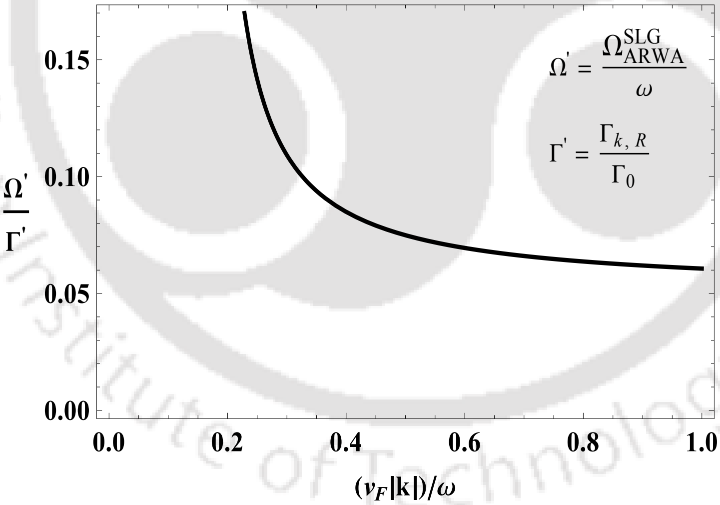

FIGURE 5.3: This figure shows the variation of number of Rabi cycles within a unit decay time $\frac{\Omega'}{\Gamma'}$ with respect to a dimensionless quantity $\frac{v_F|k|}{\omega_0}$. For $k = 0$, there are a huge number of Rabi cycles present in the system considered. As k increases, number of Rabi cycles decreases because Γ' increases linearly with increase in electron wave number. For large value of electron wave number, the number of Rabi cycles becomes constant and shows no further decay.

Dirac point. For small values of electron wave number there are huge number of Rabi cycles present in the system before these oscillations decay away. It means optical phonons are ineffective in dephasing of AROs near the Dirac point.

The effect of acoustic and flexural phonons on AROs in these systems is described in the subsequent sections.

5.2 Acoustic phonon damped AROs in graphene-systems

This section describes the damping of AROs in monolayer and bilayer graphene by means of electron-acoustic phonon interaction. Long-wavelength acoustic phonon may be treated with continuum theories to a good approximation. The dominant form of electron-phonon coupling for long-wavelength acoustic phonon modes is due to the deformation potential [227–229]. The deformation potential for in-plane acoustic phonon mode is of the form $D\vec{\nabla}\cdot u(\vec{r})$, where $u(\vec{r})$ is an in-plane displacement vector and D is the coupling constant and $D = 10-50\ eV$ [229–232] The deformation potential is non zero only for longitudinal acoustic (LA) modes. The electron-acoustic phonon interacting Hamiltonian, in second quantized form, can be written as follows

$$H_{e-acph} = \sum_{\vec{k},\vec{q}} \chi_{\vec{q}}\ X_{\vec{q}}(t)\ \frac{q_-^2}{|q|}\ c^\dagger_{A1}(\vec{k},t)\ c_{B2}(\vec{k}-\vec{q},t) + h.c. \tag{5.14}$$

$$\chi_{\vec{q}} = \sqrt{\frac{\hbar}{2M\omega_q}}D$$

where $M = A\rho$ is the total mass, $\omega_q = v_a|q|$ is the LA phonon dispersion and $v_a = 2\times10^4 m/s$, is the velocity of sound. Acoustic phonon Hamiltonian is similar to optical phonon Hamiltonian only the difference is that the frequency of optical phonon ω_0 is replaced by acoustic phonon frequency ω_q. To calculate the dephasing rate in presence of electron-acoustic phonon interaction in bilayer graphene we employ a similar strategy as we did in previous section. The modified form of $\Gamma_{k,R}$ for the case of acoustic phonon modes in bilayer graphene is given by

$$\Gamma_{k,R} = \sum_{\vec{q}} q^2 \frac{\pi\ \chi_q^2\ \alpha_{\vec{k}}\ \alpha_{\vec{k}+\vec{q}}}{2\ \Omega_{\vec{k}}\ \Omega_{\vec{k}+\vec{q}}}\ \delta\left(\omega_{\vec{q}} - \Omega_{\vec{k}} + \Omega_{\vec{k}+\vec{q}}\right) \tag{5.15}$$

All symbols have their usual meanings. Due to energy conservation law, the delta function in above expression will survive only when $\omega_q < \Omega_{\vec{k}}$. The acoustic phonons may create even with very small amount of energy which is in contrast to optical phonons. Creation of acoustic phonons depend on the value of phonon wave vector $\vec{q}$. In the present case, the magnitude of acoustic phonon wave vector is $q = q_{min} + \alpha(k - k_{min})$, where $\alpha = -2cos\theta$, $k > k_{min} = -\frac{0.01134}{cos\theta}$ and $q_{min} = 0.01512$. These values are found by taking the realistic values in Eq. (5.15) and solving the quantity within the delta function numerically. A numerical plot of $\Gamma_{k,R}$ versus electron wave number is given in Fig. 5.4. Figure 5.4 clearly depicts that the

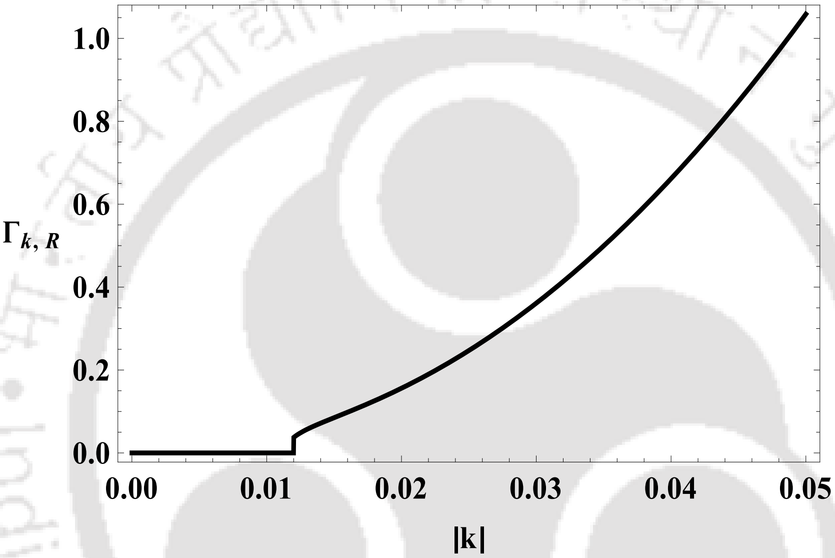

FIGURE 5.4: This is a schematic numerical plot of $\Gamma_{k,R}$ versus $|k|$ (in arbitrary units) for the case of acoustic phonos in bilayer graphene. $\Gamma_{k,R}$ increases beyond a threshold value of electron wave number $k_{min} = 0.01134$, zero otherwise.

acoustic phonons are ineffective in dephasing of AROs in bilayer graphene near the Dirac point. It is prominent for large values of electron wave vector. In other words, acoustic phonons play an important role in dephasing of AROs in bilayer graphene far from Dirac point. It means ARO is a robust nonlinear optical phenomenon in graphene like systems.

If we perform a similar calculation in case of monolayer graphene, the value of $\Gamma_{k,R}$ comes out to be equal to

$$\Gamma_{k,R} = \frac{\xi^2}{2} \sum_{\vec{q}} q^2 \frac{\Omega_{\vec{k}}\;(\Omega_{\vec{k}} - \omega_{\vec{q}}) - \Omega_0^2}{\omega_{\vec{q}}\;\Omega_{\vec{k}}\;(\Omega_{\vec{k}} - \omega_{\vec{q}})}\;\delta(\omega_{\vec{q}} - \Omega_{\vec{k}} + \Omega_{\vec{k}+\vec{q}}) \tag{5.16}$$

where $\xi = \sqrt{\frac{\hbar}{2M}}D$ and $\Omega_{\vec{k}} = \frac{1}{\omega}\sqrt{(v_F|k|\omega)^2 + \omega_R^4}$, is the anomalous Rabi frequency of monolayer graphene. All parameters have their usual meaning as before. A numerical plot of $\Gamma_{k,R}$ versus electron wave number for the case of monolayer graphene is given in Fig. 5.5. Figure 5.5 shows that the scattering rate increases after a finite value of electron wave number and zero otherwise. Thus acoustic phonons too are insensitive in dephasing of AROs near the Dirac point in monolayer graphene. Acoustic phonons are prominent in dephasing of AROs only far from the Dirac point. The following discussion deals with the effect of electron-flexural phonon interaction in dephasing of AROs in bilayer graphene.

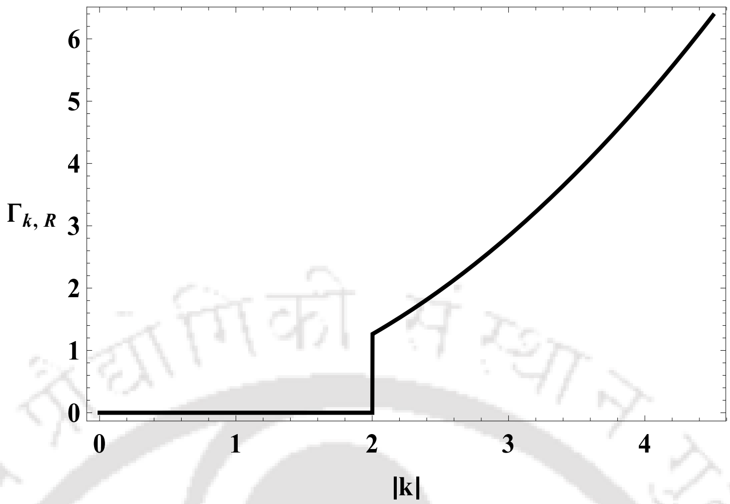

FIGURE 5.5: This is a schematic numerical plot of $\Gamma_{k,R}$ versus $|k|$ (in arbitrary units) for the case of acoustic phonons in monolayer graphene.

5.3 Flexural phonon damped AROs in graphene-systems

In presence of mechanical deformation, uniaxial strain, the graphene lattice couples to the electronic properties in two ways [228, 229, 233–236]. First is that the presence of deformation can change the bond length which leads to change in the hopping parameters results in corrections to the matrix elements of the Hamiltonian. This leads to a shift in the momenta analogous to the inclusion of a vector potential. As a result, mechanical deformations translate into fictitious gauge fields in the Dirac Hamiltonian.

Second, the elastic deformation involving local variations in areas which induces the fluctuations in the electronic densities [229, 237] that translates into a scalar potential in each layer. Consequently, symmetric deformations between two layers gives rise to a global scalar potential in bilayer graphene Hamiltonian. Whereas, asymmetric deformations yields to a potential difference between two layers. This produces similar effect as inter-layer electric fields [238–240]. There are two types of deformations in bilayer membrane- in-plane $\vec{u}(\vec{r})$ and out-of-plane $h(\vec{r})$. Here, $\vec{u}(\vec{r})$ is the vector field describing in-plane deformations and $h(\vec{r})$ is the scalar field associated with out-of-plane deformations, also known as flexural distortions. Under the deformation of bilayer membrane, the atoms in the membrane are shifted. The atom at position $\vec{r}$ under flexural deformation shifts from $\vec{r}$ to $\vec{r} + \vec{u}^{(n)}(\vec{r}) + \hat{z}h^{(n)}(\vec{r})$, where n denotes the layer number. Flexural deformation come in two categories- symmetric and antisymmetric. Therefore, it is convenient to introduce symmetric (S) and antisymmetric (A) deformations in the layer index as follows:

$$\begin{aligned} h^{(S/A)}(\vec{r}) &= \frac{h^{(2)}(\vec{r}) \pm h^{(1)}(\vec{r})}{2} \\ \vec{u}^{(S/A)}(\vec{r}) &= \frac{\vec{u}^{(2)}(\vec{r}) \pm \vec{u}^{(1)}(\vec{r})}{2} \end{aligned} \tag{5.17}$$

where, ± corresponds to symmetric and antisymmetric flexural deformations, respectively. For this study, it is worthwhile to discuss the dispersion of phonons in bilayer graphene. The phonon dispersion in bilayer graphene can be easily obtained with the help of elastic Lagrangian density [241]

$$\begin{aligned} \mathcal{L} &= \sum_{n=1,2} \mathcal{L}_n + \mathcal{L}_c \\ \mathcal{L}_n &= \frac{1}{2}\rho_0 \left[\dot{u}^{(n)2} + \dot{h}^{(n)2}\right] - \frac{1}{2}\left[2\mu u_{ij}^{(n)2} + \lambda u_{kk}^{(n)2}\right] \\ &\quad - \frac{1}{2}\left[\kappa[\nabla^2 h^{(n)}]^2 + \Gamma[\nabla h^{(n)}]^2\right] \\ \mathcal{L}_c &= -\frac{1}{2}\rho_0\omega_{in}^2[\mathbf{u}^{(1)} - \mathbf{u}^{(2)}]^2 - \frac{1}{2}\rho_0\omega_F^2[h^{(1)} - h^{(2)}]^2 \end{aligned}$$

where, μ and λ are the Lamé coefficients for in-plane streching, κ is the bending energy, ρ_0 is the mass density in each layer and Γ is the sample specific coefficient. $\mathcal{L}_c$ is a harmonic cofinement for the sliding of one layer with respect ot the other as well as for the modification of the inter-layer distance. Our intention is to study the effect of symmetric flexural phonons on anomalous Rabi oscillations in bilayer graphene. Upon solving the Euler-Lagrange equations for the elastic

Lagrangian at harmonic level for symmetric deformation, the dispersion [239] of flexuaral phonons may be written as

$$\omega_q^{S,F} = \sqrt{\frac{\kappa q^4 + \gamma q^2}{\rho_0}} \tag{5.18}$$

The above result is valid in the absence of coupling between the layers. The coupling between the layers stiffen the bending coefficient κ, which is happening in the case of realistic bilayer membrane.

To describe the effect of electron-flexural phonon interaction on AROs, we consider the gauge field term proportional to $F_3^{(\tau)}$ as described in Ref.[239]. The relevant electron-flexural phonon coupling Hamiltonian in one valley can be expressed as a 2 × 2 off diagonal matrix.

$$H_{el-Fph} = \begin{pmatrix} 0 & F_3 \\ F_3^\dagger & 0 \end{pmatrix} \tag{5.19}$$

$$\begin{aligned} F_3 &\simeq g_3\,(\partial_y - i\partial_x)\, h^{(s)}(x,y) \\ h^s(x,y) &= \frac{1}{L}\sum_{\vec{q}} \xi_{\vec{q}}\,(b_{\vec{q}} + b^\dagger_{-\vec{q}})\, e^{i\vec{k}\cdot\vec{r}} \end{aligned} \tag{5.20}$$

where, $g_3 = \frac{3ac}{2\tilde{c}}\frac{\partial\gamma_3}{\partial\tilde{c}}$ is the coupling strength. The interacting Hamiltonian in second quantized language can be written as

$$\begin{aligned} H_{el-Fph} &= \frac{g_3}{L}\sum_{\vec{k},\vec{q}} q_+\ \xi_{\vec{q}}\ X_{\vec{q}}(t)\ c^\dagger_{A1}(\vec{k},t)\ c_{B2}(\vec{k}-\vec{q},t) + h.c. \\ X_{\vec{q}}(t) &= (b_{\vec{q}} + b^\dagger_{-\vec{q}}), \qquad \xi_{\vec{q}} = \sqrt{\frac{\hbar}{2M\omega_q}} \end{aligned} \tag{5.21}$$

where, ω_q is given by Eq. (5.18). The full Hamiltonian of bilayer graphene including electron-flexural phonon interaction can be then written as

$$\begin{aligned} H_{full} = &-\frac{1}{2m}\sum_{\vec{k}} c^\dagger_{A1}(\vec{k},t)(k_- - A(t))^2 c_{B2}(\vec{k},t) \\ &+ \frac{g_3}{L}\sum_{\vec{k},\vec{q}} q_+\ \xi_{\vec{q}}\ X_{\vec{q}}(t)\ c^\dagger_{A1}(\vec{k},t)\ c_{B2}(\vec{k},t) + h.c. \end{aligned} \tag{5.22}$$

The Hamiltonian in Eq. (5.22) can be broken into slow and fast varying terms by following a similar methodology to the one described in Sec.5.1. Therefore, the slow part of Hamiltonian Eq. (5.22) can be written as follows,

$$\begin{aligned} H_{eff} = &-\sum_{\vec{k}} \frac{1}{2m} k_-^2\ c^\dagger_{A1,0}(\vec{k},t) c_{B2,0}(\vec{k},t) - \sum_{\vec{k}} \frac{1}{2m} k_+^2\ c^\dagger_{B2,0}(\vec{k},t) c_{A1,0}(\vec{k},t) \\ &+ \sum_{\vec{q}} \omega_{\vec{q}}\ b^\dagger_{\vec{q}} b_{\vec{q}} - \sum_{\vec{k}} \omega'_R \left(c^\dagger_{A1,0}(\vec{k},t) c_{A1,0}(\vec{k},t) - c^\dagger_{B2,0}(\vec{k},t) c_{B2,0}(\vec{k},t) \right) \\ &+ \frac{g_3}{L} \sum_{\vec{k},\vec{q}} \left[q_+ X_{\vec{q}}(t) \xi_{\vec{q}} c^\dagger_{A1,0}(\vec{k},t) c_{B2,0}(\vec{k}-\vec{q},t) + q_- X_{-\vec{q}}(t) \xi_{\vec{q}} c^\dagger_{B2,0}(\vec{k},t) c_{A1,0}(\vec{k}+\vec{q},t) \right] \end{aligned} \tag{5.23}$$

$$\omega'_R = \frac{1}{m^2\omega} \frac{e^2}{c^2} k^2 |A_c(0)|^2 + \frac{1}{8m^2\omega} \frac{e^4}{c^4} |A_c(0)|^4$$

Using Hamiltonian Eq. (5.23) and performing a similar calculation described in previous sections, we can write the imaginary part of self energy, which gives the scattering rate or dephasing rate, as follows

$$\Gamma_{k,R} = \frac{\pi g_3^2}{2L^2} \sum_{\vec{q}} q^2 \frac{\alpha_{\vec{k}}\ \alpha_{\vec{k}+\vec{q}}\ \xi_{\vec{q}}^2\ \Omega_{\vec{k}}}{\Omega_{\vec{k}+\vec{q}}\ \omega_{\vec{q}}^2}\ \delta(-\Omega_{\vec{k}} + \Omega_{\vec{k}+\vec{q}} + \omega_{\vec{q}}) \tag{5.24}$$

After solving integration over $\vec{q}$ straightforwardly, we obtain a compact form of $\Gamma_{k,R}$ as given below

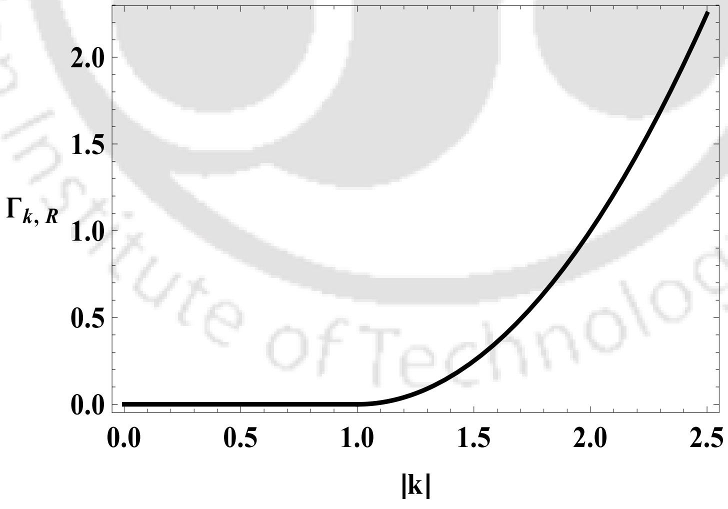

FIGURE 5.6: This plot shows variation of $\Gamma_{k,R}$ versus $|k|$ (in arbitrary units) for the case of flexural phonons in bilayer graphene. For plotting purposes we have chosen $k_{th} = 1$ in arbitrary units.

$$\Gamma_{k,R} \propto (k - k_{th})^2\, \Theta\,(k - k_{th}) \tag{5.25}$$

where $k_{th} = \frac{m\omega\left|2\sqrt{\frac{\gamma}{\rho_0}}\right|}{8\omega_R}$ is the threshold value of electron wave number. It is clear from Eq. (5.25) $\Gamma_{k,R}$ is non-zero whenever $k > k_{th}$. Integration over q in Eq. (5.24) is done for long wavelength phonons, where the dispersion relation is linear, $\omega_q = \sqrt{\frac{\gamma}{\rho_0}}q$. It is clear from Fig. 5.6 that scattering rate shows a threshold behaviour with respect to electron wave number. $\Gamma_{k,R} > 0$ for $k > k_{th}$, and zero otherwise. It means the flexural phonons are also ineffective in dephasing AROs near the Dirac point. Flexural phonons are important in daphasing of AROs only far from the Dirac point.

5.4 Summary and conclusions

This section summarizes the results obtained in the present chapter. In this chapter, we studied the effect of electron-phonon interaction on AROs in graphene-based systems. It is found that electron-phonon interaction does not play a major role in dephasing of AROs near Dirac point while these oscillations are damped far from Dirac point in presence of electron-phonon interaction.

This chapter describes the effect of electron-phonon interaction on AROs via three types of phonons- optical, acoustic and flexural. The effect of electron-optical phonon interaction on AROs is studied in Sec.5.1. This is done by calculating the scattering rate or dephasing rate which is the imaginary part of the self-energy. The self energy is calculated with the help of Dyson equation. In case of bilayer graphene, the electron-optical phonon interaction shows a constant dephasing of AROs, it is independent of electron wave vector. While, the effect of electron-optical phonon interaction on AROs in monolayer graphene is very dramatic than bilayer graphene. In monolayer graphene, AROs show a damping phenomenon far from the Dirac point in presence of electron-optical phonon interaction. However, these oscillations remain unaffected near the Dirac point. The damping of AROs by electron-optical phonon interaction in monolayer graphene is pictorially shown in Fig. 5.2. There are huge number of Rabi cycles present near the Dirac point in monolayer graphene (Fig. 5.3). This signifies that near Dirac point AROs are not damped. As the value of wave vector increases number of Rabi cycles decreases rapidly. Further increase in electron wave number the Rabi cycles are not affected. This tells that AROs are not going to be destroyed completely by means of electron-optical phonon interaction in monolayer graphene.

The above study shows the damping of AROs in presence of electron-optical phonon interaction in monolayer and bilayer graphene. We have also studied the effect of electron-acoustic phonon interaction on AROs. In this study, we follow a similar strategy to calculate the self energy of the system. From the self energy expression we extract the imaginary part which is the scattering rate or dephasing rate. It is given in Eq. (5.15). A schematic numerical plot of this equation is pictorially shown in Fig. 5.4. It is clear from figure that the dephasing rate is zero for some minimum value of electron wave number and afterwards increases slowly. This minimum value of electron wave number is $k_{min} = 0.01134$, calculated numerically. The dephasing rate is zero below k_{min}. A similar calculation in monolayer has also been done. This study is also able to show that AROs are not damped near Dirac point whereas the electron-acoustic phonon interaction plays an important role in dephasing of AROs far from Dirac point. This is pictorially shown in Fig. 5.5.

The above discussion shows the effect of electron phonon, optical and acoustic, interaction on AROs in monolayer and bilayer graphene. The last section, Sec.5.3, in the present chapter describes the effect of electron-flexural phonon interaction on AROs in bilayer graphene. Deformation potential in the layer or between the layers causes the flexural phonons. To describe the damping phenomenon of AROs in bilayer graphene in presence of gauge field induced flexural phonons, we follow a similar method described in Secs.5.1 and 5.2 and calculate the imaginary part of the self-energy to obtain a compact formula of scattering rate or dephasing rate. A numerical plot of scattering rate with respect to electron wave number is shown in Fig. 5.6. It is clear from figure that the scattering rate shows a threshold behaviour with electron wave number. It has a finite value for $k > k_{th}$ and is zero otherwise. The exponent at threshold is computed to be equal to 2. Therefore, like optical and acoustic phonons, flexural phonons are also ineffective in dephasing AROs near Dirac point. Similar to optical and acoustic phonons, flexural phonons are also plays an important role in dephasing of AROs far from Dirac point. Like optical and acoustic phonons, the scattering rate in flexural phonons show a threshold behaviour in momentum. The threshold value of the momentum varies inversely with the intensity of the applied field at a fixed value of frequency of the applied field.

The detailed calculation of this chapter has been taken from Ref.[242].

Chapter 6

Summary and outlook

As the title of the thesis itself suggests, the work presented is based on the study of optical properties of two dimensional carbon materials. There are various allotropes of carbon that exit in the nature but all allotropes are three dimensional like- graphite, diamond etc. Till 2004, it was believed that it is impossible to find long range crystalline order in two dimensions, due to large thermodynamics fluctuations in two dimensions. In 2004, Prof. Geim and Prof. Novoselov at University of Manchester made it possible to synthesize the first two dimensional allotrope of carbon material named graphene by ‘Scotch Tape Method’. They were awarded with the Nobel prize in 2010 for their novel contribution to physics. Graphene is defined as one atom thick, densely packed two dimensional flat carbon sheet in which all carbon atoms are arranged in a hexagonal pattern forming a honeycomb lattice. This newly discovered material shows very unusual physical properties than other known materials in condensed matter, and has wide potential applications. There are various theoretical and experimental studies are available in literature on this material. The study of optical properties of this material is one of them. There are several theoretical and experimental studies that are ongoing on the optical properties of this material. Nevertheless, the optical properties of this particular material is less explored compared to electronic and transport properties. Graphene derivatives like- bilayer graphene, few-layer graphene and graphene nanoribbons etc, and these systems with support show very different physical properties than graphene. They also emerge as their own research field in condensed matter physics. After the inventional of world’s thinnest first two dimensional material ‘graphene’, several attempts were made to prepare other two dimensional materials as well.

The optical studies of monolayer and bilayer graphene is the main focus of this thesis. This thesis contains two parts- in the first part coherent optical study is done in these systems, and the second part of the thesis describes the incoherent optical study in the same systems. Among well-known optical phenomenon in optics Rabi oscillations one of them. Coherent and incoherent Rabi oscillations have already been discussed by a number of authors available in literature. All of them used a well-known rotating wave approximation to describe Rabi oscillations which is valid near resonance. Recently, the same phenomenon is also studied in suspended monolayer graphene by one of the member in our group in the extreme non-resonance case by invoking a new technique called 'asymptotic' rotating wave approximation which is valid far from resonance. Using the method applied on suspended monolayer graphene, we did a similar study (coherent ROs) in suspended bilayer graphene and supported-graphene systems. The coherent ROs are described in chapters after the introductory chapter of this thesis whereas penultimate chapter is devoted to describing incoherent ROs in monolayer and bilayer graphene. Coherent and incoherent ROs in these systems are studied in presence of an intense classical electromagnetic field. However, the electronic states of the system considered are quantum in nature. Therefore, the phenomenon studied in the present thesis is purely semiclassical.

In chapter 1, a historical background of these systems is given including theoretical and experimental studies based on electronic and optical properties along with corresponding references wherever needed. This also includes the literature survey relevant to our work presented in this thesis.

In chapter 2, the system under study is suspended AB-stacked bilayer graphene which is taken to be intrinsic without any defects or disorders. Bilayer graphene can be modeled as stacking of two monolayer one on the top of the other in AB-stacking. The system under study in this chapter is exposed to a plane electromagnetic field which is propagating perpendicular to the plane of graphene system under consideration. The Bloch equations of the system under study are derived using Heisenberg's equation of motion and simple anti-commutator algebra for fermions. These coupled differential equations are solved in two different regions of interest- resonance and extreme non-resonance. The main focus of this chapter is to study the behaviour of AROs in extreme non-resonance. The AROs are studied using asymptotic rotating wave approximation. This method is valid only when the frequency of the external applied field is very large compared to the other frequencies involved in the problem under consideration. We have shown that ROs in bilayer graphene also show anomalous behaviour similar to single layer graphene. This anomalous behaviour of ROs in extreme non-resonance is attributable to the pseudospin degree of freedom of system possesses. We have also calculated the experimentally measurable quantity current density in both cases- resonance as well as extreme non-resonance. It is found that current density in extreme non-resonance case show a threshold behaviour in frequency domain. The exponent at threshold is different to the one calculated in monolayer graphene. The frequency at threshold varies parabolically with the intensity of the applied field whereas in monolayer graphene it is linear with intensity. The current density in time domain shows a power law decay which is quite different from monolayer graphene. As the number of layers increases, multi-layer graphene shows multiple harmonic resonance whereas there is only single anomalous resonance present in these systems. Except solving the Bloch equations analytically, these equations are also solved numerically using NDSolve routine of Mathematica. The results obtained analytically are in full agreement with the results obtained by numerical approach. At the end of this chapter, we have also described the same phenomenon in n-layer graphene which is nothing but the generalization of ideas applied on bilayer graphene. The results obtained in multi-layer graphene are able to reproduce the results of monolayer, bilayer, tri-layer graphene and so on.

Chapter 2 describes the phenomenon of AROs in freely suspended graphene bilayer which is not supposed to have any disorder effects due to the presence of substrate material. The natural question now arises that what will be effect on these oscillations when these systems are placed on substrate material. Therefore, the study of Chapter 2 is extended to the graphene-substrate graphene systems. This is presented in Chapter 3. In presence of substrate a mass term exists which is responsible of opening a gap in the electronic spectrum of these systems. It is found that gapped monolayer and bilayer graphene (asymmetric monolayer graphene) show Rabi-like oscillations even in presence of vanishingly small applied fields less than the gap parameter. These oscillations are called ‘offset’ oscillations. The frequency of these oscillations may be identified with the gap parameter. In presence of inter-layer asymmetry in bilayer graphene, anomalous Rabi frequency shows a minimum value with respect to intensity of the applied field- a feature absent in monolayer and also in bilayer graphene. Conventional Rabi oscillations in these systems are almost not affected in presence of asymmetry parameter. Current density in substrate-graphene systems show a threshold behaviour even for vanishingly small applied fields which can be identified with gap parameter. The threshold frequency in presence of gap parameter is increased by an amount equal to the gap parameter. The effect of different types of substrates on AROs is also addressed in this chapter.

Chapters 2 and 3 describe AROs in perfectly AB-stacked bilayer graphene excluding any direct hopping between the layers. The carries in bilayer graphene can also make a direct inter-layer hopping between two layers. This weak direct hopping parameter defined by γ_3. The perfect AB-stacking of bilayer graphene is very difficult to find in practical life. These two layers may be twisted relative to each other. This twisting is also called the stacking defect. These two issues are also addressed in chapter 4 in more detail. In presence of trigonal warping, anomalous Rabi frequency (ARF) at Dirac point goes through a zero non-trivial minimum in addition to a zero trivial minimum. This zero non-trivial minimum is attributable to the trigonal warping term due to weak direct coupling parameter γ_3. This zero non-trivial minimum in ARF appears at a value of the applied field which corresponds to the value of the momentum where the leg pocket of the Fermi surfaces develops. The threshold value of experimentally measured quantity current density show shift towards a smaller value. Conventional Rabi frequencies in presence of trigonal warping preserve their same form as without trigonal. At the end of this chapter, we mentioned the effect of twisting on AROs in bilayer graphene which is, of course, absent in monolayer graphene. In twisted bilayer graphene it is shown that AROs are significantly affected whereas conventional Rabi oscillations are not affected significantly in presence of relative small twist between the layers. The effect of twisting on AROs is observable only for weak applied electric fields.

Chapters 2, 3 and 4 describe the phenomenon of AROs in absence of relaxation term. The relaxation is responsible for the dephasing of AROs. It means, so far, coherent AROs are described in graphene based systems. One may ask a question how are these oscillations affected in presence of relaxation term. This issue is addressed in chapter 5. We wish to study the dephasing of AROs in monolayer and bilayer graphene by means of electron-phonon (optical, acoustic and flexural phonons) interaction. The study of dephasing of AROs in these systems can be done by calculating the dephasing rate which is the imaginary part of the self-energy. The self energy is calculated with the help of Dyson equation.

It is found that electron-optical phonon interaction in bilayer graphene show a constant dephasing of AROs whereas in monolayer graphene, AROs are damped far from the Dirac point while they are undamped near the Dirac point. It means electron-optical phonon interaction in monolayer graphene plays an important role in dephasing of AROs only far from the Dirac point. Similar study is also done in these systems in presence of electron-acoustic phonon interaction. It is seen that acoustic phonons in these systems too are ineffective in dephasing of AROs near the Dirac point, these are important only far away from the Dirac point. Even flexural phonons in bilayer graphene are not dephasing AROs near the Dirac point, these are significant only far from the Dirac point. In this way, we have seen that electron-phonon interaction in these systems are not capable to dephase the AROs near the Dirac point while these are significant only far from the Dirac point.

This study further can be extended to other similar materials such as Topological insulators (TI), Weyl semimetals, nanotubes and graphene nanoribbons etc. The other optical properties to be studied are- four-wave mixing, photon echo and optical Stark effect. The work presented in this thesis excludes the carrier-carrier interaction (Coulomb interaction), screening effects. These are the future directions of the research work.

Appendix A

Detailed calculations of chapter 2

A.1 Calculation of equilibrium values of polarization and population

This section describes how can we calculate the equilibrium values of polarization and population using mean field approximation as we argued in chapter 2. In second quantization, the Hamiltonian of bilayer graphene in absence of external applied field is

$$H = -\frac{1}{2m}\sum_{\vec{p}}\left[c^{\dagger}_{A1}(\vec{p})p^2_{-}\; c_{B2}(\vec{p}) + c^{\dagger}_{B2}(\vec{p})p^2_{+}\; c_{A1}(\vec{p})\right] \tag{A.1}$$

If we assume that our system is in grand canonical ensemble, the expectation value of a general operator $\hat{O}$ can be defined as

$$\langle O\rangle = \frac{Tr(e^{-\beta(H-\mu N)}\hat{O})}{Z} \tag{A.2}$$

where, $Z = Tr(e^{-\beta(H-\mu N)})$ is the grand canonical partition function, μ is the chemical potential, $\beta = 1/(KT)$, T is temperature and $N = \sum_{\vec{p}}(c^{\dagger}_{A1}(\vec{p})c_{A1}(\vec{p}) + c^{\dagger}_{B2}(\vec{p})c_{B2}(\vec{p}))$ is the number operator. We want to calculate the polarization density as well as population density. Using Eq. (A.2), the expectation value of the density operator (polarization and population) can be defined as follows,

$$\langle c^{\dagger}_{s}(\vec{p})c_{s'}(\vec{p})\rangle = \frac{Tr(e^{-\beta(H-\mu N)}c^{\dagger}_{s}(\vec{p})c_{s'}(\vec{p}))}{Z}$$

$$\langle c_s^\dagger(\vec{p}) c_{s'}(\vec{p})\rangle = \frac{Tr(c_{s'}(\vec{p}) e^{-\beta(H-\mu N)} c_s^\dagger(\vec{p}))}{Z}$$

$$\langle c_s^\dagger(\vec{p}) c_{s'}(\vec{p})\rangle = \frac{Tr(e^{-\beta(H-\mu N)}\ f(\beta, s')\ c_s^\dagger(\vec{p}))}{Z} \tag{A.3}$$

where s and $s^{'}$ stands for two sublattice sites $A1$ and $B2$ and vice-versa. In above equation, we use the cyclic property of trace i. e. Tr(ABC..) = Tr(CAB..) = Tr(BAC..) and we defined

$$f(\beta, s') = e^{\beta(H-\mu N)} c_{s'}(\vec{p}) e^{-\beta(H-\mu N)}$$

The equation of motion of above quantity is

$$\frac{\partial f(\beta, s')}{\partial \beta} = e^{\beta(H-\mu N)}[(H-\mu N), c_{s'}(\vec{p})] e^{-\beta(H-\mu N)}$$

Using the anti-commutator algebra of composite fermions, we easily can write the equations of motion for 'f' on two sublattices $A1$ and $B2$ with the help of above equation as follows,

$$\frac{\partial f(\beta, A1)}{\partial \beta} = e^{\beta(H-\mu N)} \left(\frac{p_-^2}{2m} c_{B2}(\vec{p}) + \mu c_{A1}(\vec{p})\right) e^{-\beta(H-\mu N)}$$

$$\frac{\partial f(\beta, B2)}{\partial \beta} = e^{\beta(H-\mu N)} \left(\frac{p_+^2}{2m} c_{A1}(\vec{p}) + \mu c_{B2}(\vec{p})\right) e^{-\beta(H-\mu N)}$$

Using the definition of f, the above equations can be written into two coupled linear differential equation as given below,

$$\frac{\partial f(\beta, A1)}{\partial \beta} = \frac{p_-^2}{2m} f(\beta, B2) + \mu f(\beta, A1)$$

$$\frac{\partial f(\beta, B2)}{\partial \beta} = \frac{p_+^2}{2m} f(\beta, A1) + \mu f(\beta, B2)$$

These coupled linear differential equations may be solved using DSolve routine of Mathematica. The solution of these coupled differential equations comes out to be,

$$f(\beta, A1) = c_1 e^{\beta\mu} Cosh[\beta \frac{p^2}{2m}] + c_2 \frac{p^2}{p_+^2} e^{\beta\mu} Sinh[\beta \frac{p^2}{2m}]$$

$$f(\beta, B2) = c_2 e^{\beta\mu} Cosh[\beta \frac{p^2}{2m}] + c_1 \frac{p^2}{p_-^2} e^{\beta\mu} Sinh[\beta \frac{p^2}{2m}]$$

where c_1 and c_2 are constants. These constants can be calculated with initial condition assuming that temperature is very high so that $\beta \rightarrow 0$. It gives,

$$f(0, A1) = c_1 \; f(0, B2) = c_2$$

$$f(0, s') = c_{s'}(\vec{p}) \Rightarrow f(0, A1) = c_{A1}(\vec{p}) = c_1 \; and \; f(0, B2) = c_{B2}(\vec{p}) = c_2$$

$$f(\beta, A1) = c_{A1}(\vec{p}) e^{\beta\mu} Cosh[\beta \frac{p^2}{2m}] + c_{B2}(\vec{p}) \frac{p^2}{p_+^2} e^{\beta\mu} Sinh[\beta \frac{p^2}{2m}]$$

$$f(\beta, B2) = c_{B2}(\vec{p}) e^{\beta\mu} Cosh[\beta \frac{p^2}{2m}] + c_{A1}(\vec{p}) \frac{p^2}{p_-^2} e^{\beta\mu} Sinh[\beta \frac{p^2}{2m}]$$

$$\begin{aligned} f(\beta, A1) &= e^{\beta\mu} \left(c_{A1}(\vec{p}) Cosh[\beta \frac{p^2}{2m}] + c_{B2}(\vec{p}) \frac{p^2}{p_+^2} Sinh[\beta \frac{p^2}{2m}] \right) \\ f(\beta, B2) &= e^{\beta\mu} \left(c_{B2}(\vec{p}) Cosh[\beta \frac{p^2}{2m}] + c_{A1}(\vec{p}) \frac{p^2}{p_-^2} Sinh[\beta \frac{p^2}{2m}] \right) \end{aligned} \tag{A.4}$$

Equation (A.3) can be written in the form of two sublattice sites $A1$ and $B2$ by expanding one of two indices as folows,

$$\begin{aligned} \langle c_s^\dagger(\vec{p}) c_{A1}(\vec{p}) \rangle &= \frac{Tr(e^{-\beta(H-\mu N)} \; f(\beta, A1) \; c_s^\dagger(\vec{p}))}{Z} \\ \langle c_s^\dagger(\vec{p}) c_{B2}(\vec{p}) \rangle &= \frac{Tr(e^{-\beta(H-\mu N)} \; f(\beta, B2) \; c_s^\dagger(\vec{p}))}{Z} \end{aligned} \tag{A.5}$$

Inserting Eq. (A.4) in to Eq. (A.5), we can obtain

$$\langle c_s^\dagger(\vec{p}) c_{A1}(\vec{p}) \rangle = \frac{Tr\left(e^{-\beta(H-\mu N)} e^{\beta\mu} (c_{A1}(\vec{p}) Cosh[\beta \frac{p^2}{2m}] + c_{B2}(\vec{p}) \frac{p^2}{p_+^2} Sinh[\beta \frac{p^2}{2m}]) c_s^\dagger(\vec{p}) \right)}{Z}$$

$$\langle c_s^\dagger(\vec{p}) c_{B2}(\vec{p}) \rangle = \frac{Tr\left(e^{-\beta(H-\mu N)} e^{\beta\mu} (c_{B2}(\vec{p}) Cosh[\beta \frac{p^2}{2m}] + c_{A1}(\vec{p}) \frac{p^2}{p_-^2} Sinh[\beta \frac{p^2}{2m}]) c_s^\dagger(\vec{p}) \right)}{Z}$$

Using Eq. (A.2), the above coupled equations can be written as

$$\langle c_s^\dagger(\vec{p}) c_{A1}(\vec{p}) \rangle = e^{\beta\mu} \left(\langle c_{A1}(\vec{p}) c_s^\dagger(\vec{p}) \rangle Cosh[\beta \frac{p^2}{2m}] + \frac{p^2}{p_+^2} \langle c_{B2}(\vec{p}) c_s^\dagger(\vec{p}) \rangle Sinh[\beta \frac{p^2}{2m}] \right)$$

$$\langle c_s^\dagger(\vec{p}) c_{B2}(\vec{p}) \rangle = e^{\beta\mu} \left(\langle c_{B2}(\vec{p}) c_s^\dagger(\vec{p}) \rangle Cosh[\beta \frac{p^2}{2m}] + \frac{p^2}{p_-^2} \langle c_{A1}(\vec{p}) c_s^\dagger(\vec{p}) \rangle Sinh[\beta \frac{p^2}{2m}] \right)$$

The quantity on right hand side in above equations can also be written in the following using anti-commutation relations

$$\langle c_{A1}(\vec{p})c_s^\dagger(\vec{p})\rangle = \delta_{s,A1} - \langle c_s^\dagger(\vec{p})c_{A1}(\vec{p})\rangle$$

$$\langle c_{B2}(\vec{p})c_s^\dagger(\vec{p})\rangle = \delta_{s,B2} - \langle c_s^\dagger(\vec{p})c_{B2}(\vec{p})\rangle$$

Inserting above equations into preceding equations and solving these two coupled simultaneous equations using Solve routine of Mathematica, we obtain

$$\langle c_s^\dagger(\vec{p})c_{A1}(\vec{p})\rangle = \delta_{s,A1} + \frac{p_-^2(\delta_{s,B2}e^{\beta\mu}p^2 Sinh[\beta\frac{p^2}{2m}] - \delta_{s,A1}(1+e^{\beta\mu}Cosh[\beta\frac{p^2}{2m}])p_+^2)}{-e^{2\beta\mu}p^4 Sinh[\beta\frac{p^2}{2m}]^2 + (1+e^{\beta\mu}Cosh[\beta\frac{p^2}{2m}])^2 p_-^2 p_+^2}$$

Further simplification of the above equation gives,

$$\langle c_s^\dagger(\vec{p})c_{A1}(\vec{p})\rangle = \delta_{s,A1} + \frac{\delta_{s,B2}\frac{p_-^2}{p^2}Sinh[\beta\frac{p^2}{2m}] - \delta_{s,A1}e^{-\beta\mu} - \delta_{s,A1}Cosh[\beta\frac{p^2}{2m}]}{e^{\beta\mu} + e^{-\beta\mu} + 2Cosh[\beta\frac{p^2}{2m}]}$$

For equilibrium zero temperature distribution, $\beta \to 0$, the above equation reduces to

$$\langle c_s^\dagger(\vec{p})c_{A1}(\vec{p})\rangle = \delta_{s,A1} + \frac{\frac{1}{2}(\delta_{s,B2}\frac{p_-^2}{p^2} - \delta_{s,A1})}{1 + e^{-\beta(\frac{p^2}{2m}-\mu)}} \tag{A.6}$$

Similarly, we can obtain,

$$\langle c_s^\dagger(\vec{p})c_{B2}(\vec{p})\rangle = \delta_{s,B2} + \frac{\frac{1}{2}(\delta_{s,A1}\frac{p_+^2}{p^2} - \delta_{s,B2})}{1 + e^{-\beta(\frac{p^2}{2m}-\mu)}} \tag{A.7}$$

If the energy of the system is greater than the chemical potential $\left(\frac{|p|^2}{2m} > \mu\right)$, Eqs. (A.6) and (A.7) gives

$$\langle c_s^\dagger(\vec{p})c_{A1}(\vec{p})\rangle = \frac{1}{2}\left(\delta_{s,A1} + \delta_{s,B2}\frac{p_-^2}{p^2}\right); \quad \langle c_s^\dagger(\vec{p})c_{B2}(\vec{p})\rangle = \frac{1}{2}\left(\delta_{s,B2} + \delta_{s,A1}\frac{p_+^2}{p^2}\right)$$

If the energy of the system is less than the chemical potential $\left(\frac{|p|^2}{2m} < \mu\right)$, Eqs. (A.6) and (A.7) gives

$$\langle c_s^\dagger(\vec{p})c_{A1}(\vec{p})\rangle = \delta_{s,A1}; \quad \langle c_s^\dagger(\vec{p})c_{B2}(\vec{p})\rangle = \delta_{s,B2}$$

Therefore, the equlibrium zero temperature distributions comes out to be

$$\langle c_s^\dagger(\vec{p})c_{A1}(\vec{p})\rangle = \Theta\left(\frac{p^2}{2m}-\mu\right)\frac{1}{2}\left(\delta_{s,A1}+\delta_{s,B2}\frac{p_-^2}{p^2}\right)+\Theta\left(\mu-\frac{p^2}{2m}\right)\delta_{s,A1} \tag{A.8}$$

$$\langle c_s^\dagger(\vec{p})c_{B2}(\vec{p})\rangle = \Theta\left(\frac{p^2}{2m}-\mu\right)\frac{1}{2}\left(\delta_{s,B2}+\delta_{s,A1}\frac{p_+^2}{p^2}\right)+\Theta\left(\mu-\frac{p^2}{2m}\right)\delta_{s,B2} \tag{A.9}$$

Equations (A.8) and (A.9) gives the equilibrium temperature distribution of polarization and population densities.

A.2 Formulae used to plot Fig. 2.1

This section describes the analytical expressions used to generate the central result of our work viz. Fig. 2.1. All the three parts of Fig. 2.1 are obtained through a numerical solution of the nonlinear equation for the eigenfrequency (see our earlier work [184]). In our earlier work, we showed that the plots are equally well given by a simple smooth interpolation of subplots applicable in different regimes where analytical expressions are possible. Here too we adopt the same strategy to obtain, for single layer graphene (a):

$$\Omega_{SLG}\left(v_F|k|<\frac{\omega}{4}\right)=2\sqrt{\left(v_F|k|\right)^2+\frac{\omega_R^4}{\omega^2}}$$

$$\Omega_{SLG}\left(\frac{\omega}{4}<v_F|k|\right)=\sqrt{\left(\omega-2v_F|k|\right)^2+\omega_R^2}$$

The conventional Rabi frequency is related to the fields in case of single layer graphene through, $\omega_R = v_F|\frac{e}{c}\vec{\sigma}_{BA}\cdot\vec{A}(0)|$.
For BLG (b):

$$\Omega_{BLG}\left(\frac{|k|^2}{2m}<\frac{\omega}{4}\right)=2\sqrt{\left(\frac{|k|^2}{2m}\right)^2+\frac{\left(\omega_R^2+8\frac{|k|^2\omega_R}{2m}\right)^2}{4\omega^2}}$$

$$\Omega_{BLG}\left(\frac{\omega}{4}<\frac{|k|^2}{2m}<\frac{3\omega}{4}\right)=\sqrt{\left(\omega-2\frac{|k|^2}{2m}\right)^2+4\frac{|k|^2\omega_R}{2m}}$$

$$\Omega_{BLG}\left(\frac{3\omega}{4}<\frac{|k|^2}{2m}\right)=\sqrt{\left(2\omega-2\frac{|k|^2}{2m}\right)^2+\omega_R^2},\ \omega_R=\frac{|A(0)|^2}{2m}$$

Finally for trilayer graphene (c):

$$\Omega_{TLG}\left(\alpha|k|^3 < \frac{\omega}{4}\right) = 2\frac{\sqrt{\left(\omega_R'\right)^2 + \alpha^2|k^3|^2\omega^2}}{\omega}$$

$$\omega_R' = \left(9\alpha^2|k|^4\left(\frac{\omega_R}{\alpha}\right)^{2/3} + \frac{9}{2}\alpha^2|k|^2\left(\frac{\omega_R}{\alpha}\right)^{4/3} + \frac{1}{3}\omega_R^2\right)$$

$$\Omega_{TLG}\left(\frac{\omega}{4} < \alpha|k|^3 < \frac{3\omega}{4}\right) = \sqrt{\Delta^2 + 9\omega_R^{2/3}\left(\alpha|k|^3\right)^{4/3}}$$

$$\Omega_{TLG}\left(\frac{3\omega}{4} < \alpha|k|^3 < \frac{5\omega}{4}\right) = \sqrt{\Delta^2 + 9\omega_R^{4/3}\left(\alpha|k|^3\right)^{2/3}}$$

$$\Omega_{TLG}\left(\frac{5\omega}{4} < \alpha|k|^3\right) = \sqrt{\Delta^2 + \omega_R^2},\ \omega_R = \frac{v_0^3}{\gamma_1^2}\left|A(0)\right|^3$$

where $\Delta = (\nu\omega - 2\alpha|k|^3)$. $\nu = 1, 2, 3$ for first, second and third harmonic resonance, respectively. These formulae clearly show the harmonic resonances associated with conventional Rabi oscillations.

A.3 Calculation of current density in bilayer graphene

The low-energy Hamiltonian of bilayer graphene in second quantization in absence of external applied electric field, in spatial co-ordinates, can be written as follows

$$H = \frac{-1}{2m}\int d^2\vec{r}'\left(\psi^\dagger_{A1}(\vec{r}',t)p_-'^2\psi_{B2}(\vec{r}',t) + \psi^\dagger_{B2}(\vec{r}',t)p_+'^2\psi_{A1}(\vec{r}',t)\right)$$

The charge density in two sublattice site $A1$ and $B2$ in bilayer graphene is defined as follows,

$$\rho(\vec{r},t) = \psi^\dagger_{A1}(\vec{r},t)\psi_{A1}(\vec{r},t) + \psi^\dagger_{B2}(\vec{r},t)\psi_{B2}(\vec{r},t)$$

To calculate the current density in bilayer graphene we make the use of continuity equation

$$\vec{\nabla}\cdot\vec{J}(\vec{r},t) = -\frac{\partial\rho(\vec{r},t)}{\partial t},$$

and Heisenberg's equation of motion which states that

$$\frac{\partial\hat{A}}{\partial t} = -\frac{i}{\hbar}\left[\hat{A}, H\right]$$

Now we are going to calculate the commutation relation between current density and Hamiltonian of bilayer graphene, this can be written as follows,

$$\begin{aligned}[\rho(\vec{r},t),H] &= [\psi^\dagger_{A1}(\vec{r},t)\psi_{A1}(\vec{r},t), \frac{-1}{2m}\int \psi^\dagger_{A1}(\vec{r}',t)p_-^{'2}\psi_{B2}(\vec{r}',t)d^2\vec{r}'] \\ &+ [\psi^\dagger_{B2}(\vec{r},t)\psi_{B2}(\vec{r},t), \frac{-1}{2m}\int \psi^\dagger_{A1}(\vec{r}',t)p_-^{'2}\psi_{B2}(\vec{r}',t)d^2\vec{r}'] \\ &+ [\psi^\dagger_{A1}(\vec{r},t)\psi_{A1}(\vec{r},t), \frac{-1}{2m}\int \psi^\dagger_{B2}(\vec{r}',t)p_+^{'2}\psi_{A1}(\vec{r}',t)d^2\vec{r}'] \\ &+ [\psi^\dagger_{B2}(\vec{r},t)\psi_{B2}(\vec{r},t), \frac{-1}{2m}\int \psi^\dagger_{B2}(\vec{r}',t)p_+^{'2}\psi_{A1}(\vec{r}',t)d^2\vec{r}']\end{aligned} \tag{A.10}$$

Therefore,

$$\begin{aligned}[\rho(\vec{r},t),H] = &-\frac{1}{2m}[\psi^\dagger_{A1}(\vec{r},t)p_-^2\psi_{B2}(\vec{r},t) - p_+^{'2}\psi^\dagger_{B2}(\vec{r},t)\psi_{A1}(\vec{r},t)] \\ &-\frac{1}{2m}[-p_-^2\psi^\dagger_{A1}(\vec{r},t)\psi_{B2}(\vec{r},t) + \psi^\dagger_{B2}(\vec{r},t)p_+^2\psi_{A1}(\vec{r},t)]\end{aligned}$$

we can write,

$$\psi^\dagger_{A1}(\vec{r},t)p_-^2\psi_{B2}(\vec{r},t) = p_-(\psi^\dagger_{A1}(\vec{r},t)(p_-\psi_{B2}(\vec{r},t))) - (p_-\psi^\dagger_{A1}(\vec{r},t))(p_-\psi_{B2}(\vec{r},t))$$

Applying similar process on the other three terms also, we can write

$$[\rho(\vec{r},t),H] = \frac{-1}{2m}[p_-Q_- + p_+Q_+] \tag{A.11}$$

where,

$$\begin{aligned}Q_- &= \psi^\dagger_{A1}(\vec{r},t)p_-\psi_{B2}(\vec{r},t) - p_-\psi^\dagger_{A1}(\vec{r},t)\psi_{B2}(\vec{r},t) \\ Q_+ &= \psi^\dagger_{B2}(\vec{r},t)p_+\psi_{A1}(\vec{r},t) - p_+\psi^\dagger_{B2}(\vec{r},t)\psi_{A1}(\vec{r},t)\end{aligned}$$

Using continuity equation and Hiesenberg's equation of motion, we can write

$$-i\vec{\nabla}\cdot\vec{J} = [\rho(\vec{r},t),H] = -i\frac{\partial J_x}{\partial x} - i\frac{\partial J_y}{\partial y}$$

$$p_+ = p_x + ip_y = -i\frac{\partial}{\partial x} + \frac{\partial}{\partial y}$$

Similarly,

$$p_- = p_x - ip_y = -i\frac{\partial}{\partial x} - \frac{\partial}{\partial y}$$

Therefore,

$$p_+ + p_- = -2i\frac{\partial}{\partial x},\ p_+ - p_- = 2\frac{\partial}{\partial y}$$

Hence,

$$[\rho(\vec{r},t),H]=\frac{p_++p_-}{2}J_x+\frac{p_+-p_-}{2i}J_y \tag{A.12}$$

Therefore from Eqs. (A.11) and (A.12),

$$\frac{-1}{2m}[p_-Q_-+p_+Q_+]=\frac{p_++p_-}{2}J_x+\frac{p_+-p_-}{2i}J_y$$

Now comparing the co-efficient of p_+ and p_-, we will end up with,

$$J_x-iJ_y=-\frac{Q_+}{m},\;\; J_x+iJ_y=-\frac{Q_-}{m}$$

From the above equation we can write the expression for J_x and J_y

$$J_x=\frac{-1}{2m}[Q_++Q_-],\;\; J_y=\frac{i}{2m}[-Q_++Q_-]$$

Therefore, the expression for current density in spatial co-ordinates comes out to be equal to

$$\begin{aligned}\vec{J}(\vec{r},t)=&-\frac{1}{2m}\Big[\psi^\dagger_{B2}(\vec{r},t)p_+\psi_{A1}(\vec{r},t)-p_+\psi^\dagger_{B2}(\vec{r},t)\psi_{A1}(\vec{r},t)\\&+\psi^\dagger_{A1}(\vec{r},t)p_-\psi_{B2}(\vec{r},t)-p_-\psi^\dagger_{A1}(\vec{r},t)\psi_{B2}(\vec{r},t)\Big]\hat{i}\\&+\frac{i}{2m}\Big[-\psi^\dagger_{B2}(\vec{r},t)p_+\psi_{A1}(\vec{r},t)+p_+\psi^\dagger_{B2}(\vec{r},t)\psi_{A1}(\vec{r},t)\\&+\psi^\dagger_{A1}(\vec{r},t)p_-\psi_{B2}(\vec{r},t)-p_-\psi^\dagger_{A1}(\vec{r},t)\psi_{B2}(\vec{r},t)\Big]\hat{j}\end{aligned}$$

Applying the Fourier transform to get the expression for current density in Fourier space (momentum space)

$$\psi_{A1(B2)}(\vec{r},t)=\frac{1}{\sqrt{A_r}}\sum_k e^{-i\vec{k}\cdot\vec{r}}c_{A1(B2)}(\vec{r},t)$$

$$p_+\psi_{A1(B2)}(\vec{r},t)=-i\frac{1}{\sqrt{A_r}}\sum_k ik_+e^{i\vec{k}\cdot\vec{r}}c_{A1(B2)}(\vec{r},t)$$

Therefore, the expectation value of current density can be written as,

$$\begin{aligned}\langle\vec{J}(t)\rangle=&-\frac{1}{2m}\frac{1}{A_r}\sum_{\vec{k}}[2k_+p^*(\vec{k},t)+2k_-p(\vec{k},t)]\hat{i}\\&+\frac{i}{2m}\frac{1}{A_r}\sum_{\vec{k}}[-2k_+p^*(\vec{k},t)+2k_-p(\vec{k},t)]\hat{j}\end{aligned} \tag{A.13}$$

In presence of external applied electric field, the current density in bilayer graphene is given by the following equation

$$\begin{aligned}\langle \vec{J}(t)\rangle = &-\frac{1}{mA_r}\sum_{\vec{k}}\left[(z_k - A^*(t))p(\vec{k},t) + (z_k^* - A(t))p^*(\vec{k},t)\right]\hat{i}\\ &+ i\frac{1}{mA_r}\sum_{\vec{k}}\left[(z_k - A^*(t))p(\vec{k},t) - (z_k^* - A(t))p^*(\vec{k},t)\right]\hat{j}\end{aligned} \tag{A.14}$$

A.4 Details of numerical solution of Bloch equations, Sec. 2.4

In the numerical solution of Bloch equations, we have used NDSolve routine of Mathematica to generate the plots. According to the user manual of Mathematica, it uses 'Non-stiff Adams method or a Stiff Gear backward differentiation formula'. The Mathematica program is given below,

The Bloch equations are

$$Eq1 := ID[p[t],t] == -\left[\frac{k_+}{\sqrt{2m}} - \frac{A(0)e^{-i\omega t}}{\sqrt{2m}}\right]^2 nd[t]$$

$$Eq2 := ID[ps[t],t] == \left[\frac{k_-}{\sqrt{2m}} - \frac{A^*(0)e^{i\omega t}}{\sqrt{2m}}\right]^2 nd[t]$$

$$\begin{aligned}Eq3 := ID[nd[t],t] == &-2\left[\frac{k_-}{\sqrt{2m}} - \frac{A^*(0)e^{i\omega t}}{\sqrt{2m}}\right]^2 p[t]\\ &+2\left[\frac{k_+}{\sqrt{2m}} - \frac{A(0)e^{-i\omega t}}{\sqrt{2m}}\right]^2 ps[t]\end{aligned}$$

For plotting purpose, we have chosen the value of parameters in RWA and ARWA case, respectively, as tabulated below:

RWA case: $\omega = 2\frac{\lvert k\rvert^2}{2m}$	ARWA case: $\omega \gg 2\frac{\lvert k\rvert^2}{2m}$
$\frac{k_\pm}{\sqrt{2m}} = 10$	$\frac{k_\pm}{\sqrt{2m}} = 0$
$\frac{A(0)}{\sqrt{2m}} = 1 = \frac{A^*(0)}{\sqrt{2m}}$	$\frac{A(0)}{\sqrt{2m}} = 10 = \frac{A^*(0)}{\sqrt{2m}}$
$\omega = 200$	$\omega = 2000$

NDSolve routine is used as follows,
Input:

$$s = NDSolve[\{Eq1, Eq2, Eq3, nd[0] == 0, p[0] == -1/2, ps[0] == -1/2\},$$

$$\{nd, p, ps\}, \{t, 0, 500\}, MaxSteps \to 10000000]$$

Output:

$$\{\{nd \to InterpolatingFunction[\{\{0.0, 500.0\}\}, <>],$$

$$p \to InterpolatingFunction[\{\{0.0, 500.0\}\}, <>],$$

$$ps \to InterpolatingFunction[\{\{0.0, 500.0\}\}, <>]\}\}$$

Then, we generate plots of nd and p using ‘Plot’ command of Mathematica as given below,

Plot[Re[nd[t]]/.s, { t, 0, 1 }, PlotRange→All, Frame→True, FrameLable→{“t”, “Population, $n_{diff}[k, t]$”}, PlotStyle→ {Red, Thickness[0.008]}, LableStyle→Directive[Bold, Black, FontSize→15]]

Plot[Evaluate[Re[p[t]]/.s], { t, 0, 1 }, PlotRange→All, Frame→True, FrameLable→{“t”, “Polarization, $p[k, t]$”}, PlotStyle→ {Red, Thickness[0.008]}, LableStyle→Directive[Bold, Black, FontSize→15]]

Appendix B

Detailed calculations of chapter 5

B.1 Electron-optical phonon Hamiltonian

The phonons are characterized by the relative atomic displacement from their equilibrium positions. The relative displacement of two sublattice atoms in bilayer graphene can be written as

$$u(\vec{r}) = \sum_{\vec{q},\nu} \sqrt{\frac{\hbar}{4NM\omega_0}} (b_{\vec{q},\nu} + b^{\dagger}_{-\vec{q},\nu}) e_{\nu}(\vec{q}) e^{i\vec{q}\cdot\vec{r}} \tag{B.1}$$

The meaning of the symbols used are described in corresponding chapter. where,

$$e_l(\vec{q}) = i(Cos\phi(\vec{q}), Sin\phi(\vec{q})), \qquad e_t(\vec{q}) = i(-Sin\phi(\vec{q}), Cos\phi(\vec{q}))$$

The electron-optical phonon interacting Hamiltonian [226] at one of the Dirac point is given by

$$H_{e-oph} = -\sqrt{2}\frac{\beta\gamma}{b^2}(\vec{\sigma} \times u(\vec{r})) = -\sqrt{2}\frac{\beta\gamma}{b^2}\left[\sigma_x u_y(\vec{r}) - \sigma_y u_x(\vec{r})\right] \tag{B.2}$$

where

$$\sigma_x u_y(\vec{r}) = \begin{pmatrix} 0 & 1 \\ 1 & 0 \end{pmatrix} \times \sum_{\vec{q},\nu} \sqrt{\frac{\hbar}{4NM\omega_0}} (b_{\vec{q},\nu} + b^{\dagger}_{-\vec{q},\nu})(i\frac{q_y}{q}) e^{i\vec{q}\cdot\vec{r}}$$

$$\sigma_y u_x(\vec{r}) = \begin{pmatrix} 0 & -i \\ i & 0 \end{pmatrix} \times \sum_{\vec{q},\nu} \sqrt{\frac{\hbar}{4NM\omega_0}} (b_{\vec{q},\nu} + b^{\dagger}_{-\vec{q},\nu})(i\frac{q_x}{q}) e^{i\vec{q}\cdot\vec{r}}$$

The symmetry between transverse and longitudinal mode of phonons is not destroyed due to equal charge distribution between A and B sublattices and the isotropic nature in the long-wavelength limit. Therefore, we can omit the subscript ν in the present discussion. Inserting these into Eq. (B.2), we obtain

$$H_{e-oph} = -\sqrt{2}\frac{\beta\gamma}{b^2}\sum_{\vec{q}}\sqrt{\frac{\hbar}{4NM\omega_0}}(b_{\vec{q}}+b^{\dagger}_{-\vec{q}})\begin{pmatrix} 0 & -\frac{q_-}{q} \\ \frac{q_+}{q} & 0 \end{pmatrix} e^{i\vec{q}\cdot\vec{r}} \tag{B.3}$$

In continuum limit, the Hamiltonian Eq. (B.3) can be written as

$$H_{e-oph} = -\sqrt{2}\frac{\beta\gamma}{b^2}\int d\vec{r}\psi^{\dagger}(\vec{r})\sum_{\vec{q}}\sqrt{\frac{\hbar}{4NM\omega_0}}(b_{\vec{q}}+b^{\dagger}_{-\vec{q}})\begin{pmatrix} 0 & -\frac{q_-}{q} \\ \frac{q_+}{q} & 0 \end{pmatrix} e^{i\vec{q}\cdot\vec{r}}\psi(\vec{r}) \tag{B.4}$$

where, ψ is an eigenfunction of Hamiltonian and it can be written in terms of the eigenfunctions of two atomic sites $A1$ and $B2$ as follows,

$$\psi(\vec{r}) = \frac{1}{L}\sum_{\vec{k}'}\begin{pmatrix} c_A(\vec{k}') \\ c_B(\vec{k}') \end{pmatrix} e^{i\vec{k}'\cdot\vec{r}}$$

Inserting ψ in Eq. (B.4) and doing further simplification, Eq. (B.4) reduces to

$$\begin{aligned} H_{e-oph} &= -\sqrt{2}\frac{\beta\gamma}{b^2}\frac{1}{L^2}\sum_{\vec{k},\vec{k}',\vec{q}}\sqrt{\frac{\hbar}{4NM\omega_0}}(b_{\vec{q}}+b^{\dagger}_{-\vec{q}}) \\ &\times\int d\vec{r}\cdot\left[\ c^{\dagger}_B(\vec{k}')\tfrac{q_+}{|\vec{q}|}c_A(\vec{k}) - c^{\dagger}_A(\vec{k}')\tfrac{q_-}{|\vec{q}|}c_B(\vec{k})\ \right] e^{i(\vec{k}-\vec{k}'+\vec{q})\cdot\vec{r}} \end{aligned}$$

Using the definition of Delta function,

$$\delta_{\vec{k}-\vec{k}'+\vec{q},0} = \frac{1}{L^2}\int d\vec{r}\ e^{i(\vec{k}-\vec{k}'+\vec{q})\cdot\vec{r}},$$

the above equation can be written as

$$H_{e-oph} = \chi\sum_{\vec{k},\vec{q}}\left[X_{\vec{q}}\ c^{\dagger}_A(\vec{k})\frac{q_-}{|\vec{q}|}\ c_B(\vec{k}-\vec{q}) + h.c.\right]$$

$$\chi = \sqrt{2}\frac{\beta\gamma}{b^2}\sqrt{\frac{\hbar}{4NM\omega_0}},\quad X_{\vec{q}} = b_{\vec{q}}+b^{\dagger}_{-\vec{q}}$$

This is the electron-optical phonon Hamiltonian, we used it in calculation in Sec. 5.1 of chapter 5.

B.2 Extraction of slow part of Hamiltonian

Here, we give the detailed calculation to obtain the slow part of Hamiltonian Eq. (5.8) from full Hamiltonian Eq. (5.6), used in Sec. 5.1. The Hamiltonian Eq. (5.6) is,

$$\begin{aligned} H_{full} = &-\frac{1}{2m}\sum_{\vec{k}}\left[c^{\dagger}_{A1}(\vec{k},t)(k_{-}-A(t))^{2}c_{B2}(\vec{k},t)+c^{\dagger}_{B2}(\vec{k},t)(k_{+}-A^{*}(t))^{2}c_{A1}(\vec{k},t)\right] \\ &+\chi\sum_{\vec{k},\vec{q}}\left[X_{\vec{q}}(t)\frac{q_{-}}{|\vec{q}|}c^{\dagger}_{A}(\vec{k},t)c_{B}(\vec{k}-\vec{q},t)+X_{-\vec{q}}(t)\frac{q_{+}}{|\vec{q}|}c^{\dagger}_{B}(\vec{k},t)c_{A}(\vec{k}+\vec{q},t)\right] \\ &+\sum_{\vec{q}}\omega_{0}\left(b^{\dagger}_{\vec{q}}b_{\vec{q}}+\frac{1}{2}\right) \end{aligned} \tag{B.5}$$

We can write Hamiltonian Eq. (B.5) and wave function in 'slow' as well as 'fast' harmonic terms.

$$H = \sum_{m=0,\pm1,....} H_{m}\ e^{-im\omega t},\ \psi = \sum_{n=0,\pm1,....} \psi_{n}\ e^{-in\omega t} \tag{B.6}$$

Using Heisenberg equation of motion we can write the equation of motion for ψ as,

$$\begin{aligned} i\partial_{t}\psi_{0}+\sum_{n=\pm1,\pm2,...} e^{-in\omega t}\psi_{n} &= \left[\psi_{0}+\sum_{n=\pm1,\pm2,...} e^{-in\omega t}\psi_{n},\ H_{0}+\sum_{m=\pm1,\pm2,...} e^{-im\omega t}H_{m}\right] \\ &= [\psi_{0},H_{0}]+\sum_{n=\pm1,\pm2,...}\left[\psi_{0},e^{-im\omega t}H_{m}\right]+\sum_{n=\pm1,\pm2,...} e^{-in\omega t}\left[\psi_{n},H_{0}\right] \\ &\quad +\sum_{n=\pm1,\pm2,...} e^{-i(n+m)\omega t}\left[\psi_{n},H_{m}\right] \end{aligned}$$

Comparing the coefficients of same exponential powers from both sides. The coefficients of e^{i0t} is

$$i\partial_{t}\psi_{0} = \sum_{n=0,\pm1,\pm2,...}\left[\psi_{n},H_{-n}\right]$$

Similarly we can collect the coefficients of $e^{\pm i\omega t}$ and $e^{\pm 2i\omega t}$, and solving them assuming that the external driving frequency is very large. This assumption allows us to neglect the terms containing $1/\omega^{2}$ in comparison to the terms containing

$1/\omega$. This simplification gives us,

$$\psi_1 = \frac{[\psi_0, H_1]}{\omega}, \quad \psi_{-1} = -\frac{[\psi_0, H_{-1}]}{\omega}$$
$$\psi_2 = \frac{[\psi_0, H_2]}{2\omega}, \quad \psi_{-2} = -\frac{[\psi_0, H_{-2}]}{2\omega} \tag{B.7}$$

Therefore, the equation of motion of ψ_0 comes out to be

$$i\partial_t\psi_0 = \sum_{n=0,\pm1,\pm2,\ldots} [\psi_n, H_{-n}]$$

$$i\partial_t\psi_0 = [\psi_0, H_0] + [\psi_1, H_{-1}] + [\psi_{-1}, H_1] + [\psi_2, H_{-2}] + [\psi_{-2}, H_2] \tag{B.8}$$

Inserting the vales of $\psi's$ in above equation, we will obtain a equation of motion of ψ_0 which is fully in terms of ψ_0. This is,

$$i\partial_t\psi_0 = [\psi_0, H_0] + \frac{1}{\omega}[[\psi_0, H_1], H_{-1}] - \frac{1}{\omega}[[\psi_0, H_{-1}], H_1]$$
$$+\frac{1}{2\omega}[[\psi_0, H_2], H_{-2}] - \frac{1}{2\omega}[[\psi_0, H_{-2}], H_2]$$

This way, we get rid off from the fast varying coefficients in wavefunction. The remaining is how to get rid off from the fast coefficients of Hamiltonian. This is explained below:

The interacting part of Hamiltonian Eq. (B.5) has no harmonics in external driving field. Therefore, our focus will only be on the rest part of the Hamiltonian. The bilayer graphene Hamiltonian without electron-phonon interaction is given by,

$$H = -\frac{1}{2m}\sum_{\vec{k}}\Big[c^\dagger_{A1}(\vec{k},t)(k_-^2 + (-\frac{e}{c}A(0))^2e^{-2i\omega t} + 2k_-(-\frac{e}{c}A(0))e^{-i\omega t})c_{B2}(\vec{k},t)\Big]$$
$$-\frac{1}{2m}\sum_{\vec{k}}\Big[c^\dagger_{B2}(\vec{k},t)(k_+^2 + (-\frac{e}{c}A^*(0))^2e^{2i\omega t} + 2k_+(-\frac{e}{c}A^*(0))e^{i\omega t})c_{A1}(\vec{k},t)\Big] \tag{B.9}$$

Now decomposing the creation and annihilation operators in slow and fast terms as follows,

$$c = c_0 + c_{+1}e^{-i\omega t} + c_{-1}e^{i\omega t} + c_{+2}e^{-2i\omega t} + c_{-2}e^{2i\omega t}$$
$$c^\dagger = c_0 + c^\dagger_{+1}e^{i\omega t} + c^\dagger_{-1}e^{-i\omega t} + c^\dagger_{+2}e^{2i\omega t} + c^\dagger_{-2}e^{-2i\omega t}$$

Inserting these equations in Eq. (B.9) and comparing the same exponential powers from both sides. The term of e^{i0t}:

$$
\begin{aligned}
H_0 = &-\sum_{\vec{k}} \frac{k_-^2}{2m}\left(c^\dagger_{A1,0}c_{B2,0} + c^\dagger_{A1,+1}c_{B2,+1} + c^\dagger_{A1,-1}c_{B2,-1} + c^\dagger_{A1,+2}c_{B2,+2} + c^\dagger_{A1,-2}c_{B2,-2}\right) \\
&-\frac{1}{2m}\sum_{\vec{k}}(-\frac{e}{c}A(0))^2\left(c^\dagger_{A1,0}c_{B2,-2} + c^\dagger_{A1,+1}c_{B2,-1} + c^\dagger_{A1,+2}c_{B2,0}\right) \\
&-\sum_{\vec{k}}\frac{2k_-(-\frac{e}{c}A(0))}{2m}\left(c^\dagger_{A1,0}c_{B2,-1} + c^\dagger_{A1,+1}c_{B2,0} + c^\dagger_{A1,-1}c_{B2,-2} + c^\dagger_{A1,+2}c_{B2,+1}\right) \\
&-\frac{1}{2m}\sum_{\vec{k}} k_+^2\left(c^\dagger_{B2,0}c_{A1,0} + c^\dagger_{B2,+1}c_{A1,+1} + c^\dagger_{B2,-1}c_{A1,-1} + c^\dagger_{B2,+2}c_{A1,+2} + c^\dagger_{B2,-2}c_{A1,-2}\right) \\
&-\frac{1}{2m}\sum_{\vec{k}}(-\frac{e}{c}A^*(0))^2\left(c^\dagger_{B2,0}c_{A1,+2} + c^\dagger_{B2,-1}c_{A1,+1} + c^\dagger_{B2,-2}c_{A1,0}\right) \\
&-\frac{1}{2m}\sum_{\vec{k}} 2k_+(-\frac{e}{c}A^*(0))\left(c^\dagger_{B2,0}c_{A1,+1} + c^\dagger_{B2,+1}c_{A1,+2} + c^\dagger_{B2,-1}c_{A1,0} + c^\dagger_{B2,-2}c_{A1,-1}\right)
\end{aligned}
$$

Similarly the coefficients of $e^{\mp i\omega t}$ and $e^{\mp 2i\omega t}$ are $H_{\pm1}$ and $H_{\pm2}$, respectively, and given by,

$$
\begin{aligned}
H_{+1} &= -\frac{1}{2m}\sum_{\vec{k}} 2k_-\left(-\frac{e}{c}A(0)\right)c^\dagger_{A1,0}c_{B2,0}, \;\; H_{-1} = H^\dagger_{+1} \\
H_{+2} &= -\frac{1}{2m}\sum_{\vec{k}}\left(-\frac{e}{c}A(0)\right)^2 c^\dagger_{A1,0}c_{B2,0}, \;\; H_{-2} = H^\dagger_{+2}
\end{aligned}
\qquad (B.10)
$$

Using Eq. (B.10) along with Eq. (B.7), we can calculate the various fast terms contained in the expression of H_0. Inserting these fast coefficients into the expression of H_0, it comes out to be

$$
\begin{aligned}
H_0 = &-\frac{1}{2m}\sum_{\vec{k}} k_-^2 c^\dagger_{A1,0}(\vec{k},t)c_{B2,0}(\vec{k},t) - \frac{1}{2m}\sum_{\vec{k}} k_+^2 c^\dagger_{B2,0}(\vec{k},t)c_{A1,0}(\vec{k},t) \\
&-\frac{|\frac{e}{c}A(0)|^2}{m^2\omega}\sum_{\vec{k}}|k|^2 c^\dagger_{A1,0}(\vec{k},t)c_{A1,0}(\vec{k},t) + \frac{|\frac{e}{c}A^*(0)|^2}{m^2\omega}\sum_{\vec{k}}|k|^2 c^\dagger_{B2,0}(\vec{k},t)c_{B2,0}(\vec{k},t) \\
&-\frac{|\frac{e}{c}A(0)|^4}{8m^2\omega}\sum_{\vec{k}} c^\dagger_{A1,0}(\vec{k},t)c_{A1,0}(\vec{k},t) + \frac{|\frac{e}{c}A^*(0)|^4}{8m^2\omega}\sum_{\vec{k}} c^\dagger_{B2,0}(\vec{k},t)c_{B2,0}(\vec{k},t)
\end{aligned}
\qquad (B.11)
$$

Equation (B.11) gives the slow part of Hamiltonain we used in calculation in chapter 5.

B.3 Green's function

This section describes how to calculate the Green's function of bilayer graphene. The full Green function is defined as

$$G = (1 - G_0\Sigma)^{-1} \cdot G_0 \tag{B.12}$$

where G_0 is defined as

$$G_0(\vec{k}, t - t^{'}) = (-i)\langle\, T\ c_{b,0}(\vec{k}, t)c^{\dagger}_{a,0}(\vec{k}, t^{'})\ \rangle_0 \tag{B.13}$$

The equations of motion of $\langle\, T\ c_{b,0}(\vec{k}, t)c^{\dagger}_{a,0}(\vec{k}, t^{'})\ \rangle_0$ on two sublttice sites will be of the form

$$i\partial_t\langle\, T\ c_{A1,0}(\vec{k}, t)c^{\dagger}_{a,0}(\vec{k}, t^{'})\ \rangle_0 = i\delta_{a,A1}\delta(t - t^{'}) - \frac{1}{2m}k_-^2\ \langle\, T\ c_{B2,0}(\vec{k}, t)c^{\dagger}_{a,0}(\vec{k}, t^{'})\ \rangle_0$$
$$- \left[\frac{1}{m^2\omega}\frac{e^2}{c}k^2|A_c(0)|^2 + \frac{1}{8m^2\omega}\ \frac{e^4}{c^4}|A_c(0)|^4\right]\ \langle\, T\ c_{A1,0}(\vec{k}, t)c^{\dagger}_{a,0}(\vec{k}, t^{'})\ \rangle_0$$

and,

$$i\partial_t\langle\, T\ c_{B2,0}(\vec{k}, t)c^{\dagger}_{a,0}(\vec{k}, t^{'})\ \rangle_0 = i\delta_{a,B2}\delta(t - t^{'}) - \frac{1}{2m}\ k_+^2\ \langle\, T\ c_{A1,0}(\vec{k}, t)c^{\dagger}_{a,0}(\vec{k}, t^{'})\ \rangle_0$$
$$+ \left[\frac{k^2}{m^2\omega}\ \frac{e^2}{c^2}|A_c(0)|^2 + \frac{1}{8m^2\omega}\frac{e^4}{c^4}|A_c(0)|^4\right]\langle\, T\ c_{B2,0}(\vec{k}, t)c^{\dagger}_{a,0}(\vec{k}, t^{'})\ \rangle_0$$

Using the following fourier transform

$$\langle\, T\ c_{a,0}(\vec{k}, t)c^{\dagger}_{b,0}(\vec{k}, t^{'})\ \rangle_0 = \sum_n e^{z_n(t-t^{'})}\ \langle\, T\ c_{a,0}(\vec{k}, n)c^{\dagger}_{b,0}(\vec{k}, n)\ \rangle_0$$

the above two coupled equations turn into two coupled simultaneous linear equations. These equations may easily be solved using Solve routine of Mathematica, this gives

$$\langle\, T\ c_{A1,0}(\vec{k}, n)c^{\dagger}_{a,0}(\vec{k}, n)\ \rangle_0 = \frac{2m(2im(z_n + i\alpha_k)\delta_{a,A1} - k_-^2\delta_{a,B2})}{(k^4 + 4m^2(z_n^2 + \alpha_k^2))\beta}$$

$$\langle\ T\ c_{B2,0}(\vec{k},n)c^{\dagger}_{a,0}(\vec{k},n)\ \rangle_0 = \frac{2m(-k_+^2\delta_{a,A1} + 2im(z_n - i\alpha_k)\delta_{a,B2})}{(k^4 + 4m^2(z_n^2 + \alpha_k^2))\beta}$$

Therefore, the Green functions on two sublattice sites can easily be written using Eq. (B.13),

$$\begin{aligned} G_{0,A1,a}(\vec{k},n) &= \frac{2m(2m(z_n + i\alpha_k)\delta_{a,A1} + ik_-^2\delta_{a,B2})}{(k^4 + 4m^2(z_n^2 + \alpha_k^2))\beta} \\ G_{0,B2,a}(\vec{k},n) &= \frac{2m(ik_+^2\delta_{a,A1} + 2m(z_n - i\alpha_k)\delta_{a,B2})}{(k^4 + 4m^2(z_n^2 + \alpha_k^2))\beta} \end{aligned} \tag{B.14}$$

Therefore, G_0 can be written as,

$$G_0 = \begin{pmatrix} G_{A1A1,0} & G_{A1B2,0} \\ G_{B2A1,0} & G_{B2B2,0} \end{pmatrix} = \begin{pmatrix} \frac{2m(2m(z_n+i\alpha_k))}{(k^4+4m^2(z_n^2+\alpha_k^2))\beta} & \frac{2m(ik_-^2)}{(k^4+4m^2(z_n^2+\alpha_k^2))\beta} \\ \frac{2m(ik_+^2)}{(k^4+4m^2(z_n^2+\alpha_k^2))\beta} & \frac{2m(2m(z_n-i\alpha_k))}{(k^4+4m^2(z_n^2+\alpha_k^2))\beta} \end{pmatrix} \tag{B.15}$$

$$G_0\Sigma = \begin{pmatrix} \frac{2m(2m(z_n+i\alpha_k))}{(k^4+4m^2(z_n^2+\alpha_k^2))\beta} & \frac{2m(ik_-^2)}{(k^4+4m^2(z_n^2+\alpha_k^2))\beta} \\ \frac{2m(ik_+^2)}{(k^4+4m^2(z_n^2+\alpha_k^2))\beta} & \frac{2m(2m(z_n-i\alpha_k))}{(k^4+4m^2(z_n^2+\alpha_k^2))\beta} \end{pmatrix} \begin{pmatrix} \Sigma_{A1A1} & \Sigma_{A1B2} \\ \Sigma_{B2A1} & \Sigma_{B2B2} \end{pmatrix}$$

$$(1 - G_0\Sigma)^{-1} = \frac{1}{Denfull}$$

$$\times \begin{pmatrix} Den(Den - 2m(ik_+^2\Sigma_{A1B2} + 2m(z_n - i\alpha_k)\Sigma_{B2B2})) & (2m)Den(2m(z_n + i\alpha_k)\Sigma_{A1B2} + ik_-^2\Sigma_{B2B2}) \\ (2m)Den(ik_+^2\Sigma_{A1A1} + (2m)(z_n - i\alpha_k)\Sigma_{B2A1}) & Den(Den - 2m(2m(z_n + i\alpha_k)\Sigma_{A1A1} + ik_-^2\Sigma_{B2A1})) \end{pmatrix}$$

$$Denfull = Den^2 + 4m^2(k^4 + 4m^2(z_n^2 + \alpha_k^2))(-\Sigma_{A1B2}\Sigma_{B2A1} + \Sigma_{A1A1}\Sigma_{B2B2})$$

$$-2im\ Den(k_+^2\Sigma_{A1B2} + k_-^2\Sigma_{B2A1} + 2m(\alpha_k(\Sigma_{A1A1} - \Sigma_{B2B2}) - iz_n(\Sigma_{A1A1} + \Sigma_{B2B2})))$$

$$Den = (k^4 + 4m^2(z_n^2 + \alpha_k^2))\beta$$

Therefore, the full Green function in Eq. (B.12) can be written as

$$G = \frac{1}{DenfullNew} \begin{pmatrix} \Big((2m)^2(z_n + i\alpha_k)\Big) - \frac{(2m)^2}{\beta}\Sigma_{B2B2} & (2m(ik_-^2)) + \frac{(2m)^2}{\beta}\Sigma_{A1B2} \\ (2m(ik_+^2)) + \frac{(2m)^2}{\beta}\Sigma_{B2A1} & \Big((2m)^2(z_n - i\alpha_k)\Big) - \frac{(2m)^2}{\beta}\Sigma_{A1A1} \end{pmatrix}$$

$$DenfullNew = Den + \frac{4m^2}{\beta}\left(-\Sigma_{A1B2}\Sigma_{B2A1} + \Sigma_{A1A1}\Sigma_{B2B2}\right)$$
$$-\,2im\ \left[k_+^2\Sigma_{A1B2} + k_-^2\Sigma_{B2A1} + 2m(\alpha_k(\Sigma_{A1A1} - \Sigma_{B2B2}) - iz_n(\Sigma_{A1A1} + \Sigma_{B2B2}))\right] \tag{B.16}$$

B.4 Self-energy

$$-\infty \;\text{————————}\; t_4 \;\text{————————}\!\rightarrow\!\text{————————}\; t_3 \;\text{————————}\; +\infty$$
$$-\infty \;\text{————————}\; t_1 \;\text{————————}\!\leftarrow\!\text{————————}\; t_2 \;\text{————————}\; +\infty$$

$$t_1 > t_2,\ \ t_1, t_2 > t_3, t_4,\ \ t_3 > t_4$$

The time on bottom line is always greater than the time on top line.

The generalized one particle Green's function is defined as

$$G_{ab}(\vec{k}, t - t^{'}) = (-i)\frac{\langle T\ S\ c_a(\vec{k}, t)c_b^{\dagger}(\vec{k}, t^{'})\rangle_0}{\langle\ TS\ \rangle_0} \tag{B.17}$$

Here T is the time ordered parameter and S represents the S-matrix given by

$$S = Exp[-i\int_c \hat{H}_{e-oph}(t_1)dt_1]$$

Expanding S-matrix perturbatively,

$$S = 1 + (-i)\int_c \hat{H}_{e-oph}(t_1)dt_1 + \frac{(-i)^2}{2}\int_c\int_c \langle\hat{H}_{e-oph}(t_1)\hat{H}_{e-oph}(t_2)\rangle dt_1dt_2$$

The first order expansion will be zero because the expectation value of phonon operator X is zero. The integrant of second term can be expanded by inserting the electron-optical phonon Hamiltonian.

$$\langle\hat{H}_{e-oph}(t_1)\hat{H}_{e-oph}(t_2)\rangle =$$

$$= \chi^2\sum_{\vec{k}',\vec{q}',\vec{k}'',\vec{q}''} X_{q'}(t_1)\frac{q_-^{'}}{q^{'}}c_A^{\dagger}(\vec{k}^{'}, t_1)c_B(\vec{k}^{'} - \vec{q}^{'}, t_1)\times X_{q''}(t_2)\frac{q_-^{''}}{q^{''}}c_A^{\dagger}(\vec{k}^{''}, t_2)c_B(\vec{k}^{''} - \vec{q}^{''}, t_2)$$

$$+\chi^2\sum_{\vec{k}',\vec{q}',\vec{k}'',\vec{q}''} X_{q'}(t_1)\frac{q_-^{'}}{q^{'}}c_A^{\dagger}(\vec{k}^{'}, t_1)c_B(\vec{k}^{'} - \vec{q}^{'}, t_1)\times X_{-q''}(t_2)\frac{q_+^{''}}{q^{''}}c_B^{\dagger}(\vec{k}^{''}, t_2)c_A(\vec{k}^{''} + \vec{q}^{''}, t_2)$$

$$+\chi^2 \sum_{\vec{k}',\vec{q}',\vec{k}'',\vec{q}''} X_{-q'}(t_1)\frac{q'_+}{q'}c^\dagger_B(\vec{k}',t_1)c_A(\vec{k}'+\vec{q}',t_1)\times X_{q''}(t_2)\frac{q''_-}{q''}c^\dagger_A(\vec{k}'',t_2)c_B(\vec{k}''-\vec{q}'',t_2)$$

$$+\chi^2 \sum_{\vec{k}',\vec{q}',\vec{k}'',\vec{q}''} X_{-q'}(t_1)\frac{q'_+}{q'}c^\dagger_B(\vec{k}',t_1)c_A(\vec{k}'+\vec{q}',t_1)\times X_{-q''}(t_2)\frac{q''_+}{q''}c^\dagger_B(\vec{k}'',t_2)c_A(\vec{k}''+\vec{q}'',t_2)$$

Using above expansion the Green's function in Eq. (B.17) comes out to be

$$G_{ab}(\vec{k},t-t') - G_{ab,0}(\vec{k},t-t') =$$

$$\frac{(-i)^3}{2!}\int_C dt_1 \int_C dt_2\ \chi^2 \sum_{\vec{k}',\vec{q}'\,;\ \vec{k}'',\vec{q}''} \frac{q'_-}{q'}\frac{q''_-}{q''}\langle\ T\ X_{q'}(t_1)X_{q''}(t_2)\ \rangle\times$$

$$\langle\ T\ c^\dagger_A(\vec{k}',t_1)c_B(\vec{k}'-\vec{q}',t_1)c^\dagger_A(\vec{k}'',t_2)c_B(\vec{k}''-\vec{q}'',t_2)c_a(\vec{k},t)c^\dagger_b(\vec{k},t')\ \rangle_0$$

$$+\frac{(-i)^3}{2!}\int_C dt_1 \int_C dt_2\ \chi^2 \sum_{\vec{k}',\vec{q}'\,;\ \vec{k}'',\vec{q}''} \frac{q'_-}{q'}\frac{q''_+}{q''}\langle\ T\ X_{q'}(t_1)X_{-q''}(t_2)\ \rangle\times$$

$$\langle\ T\ c^\dagger_A(\vec{k}',t_1)c_B(\vec{k}'-\vec{q}',t_1)c^\dagger_B(\vec{k}'',t_2)c_A(\vec{k}''+\vec{q}'',t_2)c_a(\vec{k},t)c^\dagger_b(\vec{k},t')\ \rangle_0$$

$$+\frac{(-i)^3}{2!}\int_C dt_1 \int_C dt_2\ \chi^2 \sum_{\vec{k}',\vec{q}'\,;\ \vec{k}'',\vec{q}''} \frac{q'_+}{q'}\frac{q''_-}{q''}\langle\ T\ X_{-q'}(t_1)X_{q''}(t_2)\ \rangle\times$$

$$\langle\ T\ c^\dagger_B(\vec{k}',t_1)c_A(\vec{k}'+\vec{q}',t_1)c^\dagger_A(\vec{k}'',t_2)c_B(\vec{k}''-\vec{q}'',t_2)c_a(\vec{k},t)c^\dagger_b(\vec{k},t')\ \rangle_0$$

$$+\frac{(-i)^3}{2!}\int_C dt_1 \int_C dt_2\ \chi^2 \sum_{\vec{k}',\vec{q}'\,;\ \vec{k}'',\vec{q}''} \frac{q'_+}{q'}\frac{q''_+}{q''}\langle\ T\ X_{-q'}(t_1)X_{-q''}(t_2)\ \rangle\times$$

$$\langle\ T\ c^\dagger_B(\vec{k}',t_1)c_A(\vec{k}'+\vec{q}',t_1)c^\dagger_B(\vec{k}'',t_2)c_A(\vec{k}''+\vec{q}'',t_2)c_a(\vec{k},t)c^\dagger_b(\vec{k},t')\ \rangle_0$$

Only the connected parts will survive, and in grouping we will use the following

$$\langle Tc^\dagger_{k_1}(t_1)c_{k_2}(t_2)\rangle = -\delta_{k_1=k_2}\langle Tc_{k_1}(t_2)c^\dagger_{k_1}(t_1)\rangle$$

$$G_{ab}(\vec{k},t-t^{'})-G_{ab,0}(\vec{k},t-t^{'})=$$

$$\frac{(-i)^3}{2!}\int_C dt_1\int_C dt_2\ \chi^2\sum_{\vec{k}',\vec{q}'\,;\ \vec{k}'',\vec{q}''}\frac{q^{'}_{-}}{q^{'}}\frac{q^{''}_{-}}{q^{''}}\langle\ T\ X_{q'}(t_1)X_{q''}(t_2)\ \rangle\times$$

$$\langle\ T\ c_B(\vec{k}''-\vec{q}'',t_2)c^{\dagger}_A(\vec{k}',t_1)\ \rangle_0\langle\ T\ c_B(\vec{k}'-\vec{q}',t_1)c^{\dagger}_b(\vec{k},t^{'})\ \rangle_0\langle\ T\ c_a(\vec{k},t)c^{\dagger}_A(\vec{k}'',t_2)\ \rangle_0$$

$$+\frac{(-i)^3}{2!}\int_C dt_1\int_C dt_2\ \chi^2\sum_{\vec{k}',\vec{q}'\,;\ \vec{k}'',\vec{q}''}\frac{q^{'}_{-}}{q^{'}}\frac{q^{''}_{-}}{q^{''}}\langle\ T\ X_{q'}(t_1)X_{q''}(t_2)\ \rangle\times$$

$$\langle\ T\ c_a(\vec{k},t)c^{\dagger}_A(\vec{k}',t_1)\ \rangle_0\langle\ T\ c_B(\vec{k}'-\vec{q}',t_1)c^{\dagger}_A(\vec{k}'',t_2)\ \rangle_0\langle\ T\ c_B(\vec{k}''-\vec{q}'',t_2)c^{\dagger}_b(\vec{k},t^{'})\ \rangle_0$$

$$+\frac{(-i)^3}{2!}\int_C dt_1\int_C dt_2\ \chi^2\sum_{\vec{k}',\vec{q}'\,;\ \vec{k}'',\vec{q}''}\frac{q^{'}_{-}}{q^{'}}\frac{q^{''}_{+}}{q^{''}}\langle\ T\ X_{q'}(t_1)X_{-q''}(t_2)\ \rangle\times$$

$$\langle\ T\ c_A(\vec{k}''+\vec{q}'',t_2)c^{\dagger}_A(\vec{k}',t_1)\ \rangle_0\langle\ T\ c_B(\vec{k}'-\vec{q}',t_1)c^{\dagger}_b(\vec{k},t^{'})\ \rangle_0\langle\ T\ c_a(\vec{k},t)c^{\dagger}_B(\vec{k}'',t_2)\ \rangle_0$$

$$+\frac{(-i)^3}{2!}\int_C dt_1\int_C dt_2\ \chi^2\sum_{\vec{k}',\vec{q}'\,;\ \vec{k}'',\vec{q}''}\frac{q^{'}_{-}}{q^{'}}\frac{q^{''}_{+}}{q^{''}}\langle\ T\ X_{q'}(t_1)X_{-q''}(t_2)\ \rangle\times$$

$$\langle\ T\ c_a(\vec{k},t)c^{\dagger}_A(\vec{k}',t_1)\ \rangle_0\langle\ T\ c_B(\vec{k}'-\vec{q}',t_1)c^{\dagger}_B(\vec{k}'',t_2)\ \rangle_0\langle\ T\ c_A(\vec{k}''+\vec{q}'',t_2)c^{\dagger}_b(\vec{k},t^{'})\ \rangle_0$$

$$+\frac{(-i)^3}{2!}\int_C dt_1\int_C dt_2\ \chi^2\sum_{\vec{k}',\vec{q}'\,;\ \vec{k}'',\vec{q}''}\frac{q^{'}_{+}}{q^{'}}\frac{q^{''}_{-}}{q^{''}}\langle\ T\ X_{-q'}(t_1)X_{q''}(t_2)\ \rangle\times$$

$$\langle\ T\ c_B(\vec{k}''-\vec{q}'',t_2)c^{\dagger}_B(\vec{k}',t_1)\ \rangle_0\langle\ T\ c_A(\vec{k}'+\vec{q}',t_1)c^{\dagger}_b(\vec{k},t^{'})\ \rangle_0\langle\ T\ c_a(\vec{k},t)c^{\dagger}_A(\vec{k}'',t_2)\ \rangle_0$$

$$+\frac{(-i)^3}{2!}\int_C dt_1\int_C dt_2\ \chi^2\sum_{\vec{k}',\vec{q}'\,;\ \vec{k}'',\vec{q}''}\frac{q^{'}_{+}}{q^{'}}\frac{q^{''}_{-}}{q^{''}}\langle\ T\ X_{-q'}(t_1)X_{q''}(t_2)\ \rangle\times$$

$$\langle\ T\ c_a(\vec{k},t)c^{\dagger}_B(\vec{k}',t_1)\ \rangle_0\langle\ T\ c_A(\vec{k}'+\vec{q}',t_1)c^{\dagger}_A(\vec{k}'',t_2)\ \rangle_0\langle\ T\ c_B(\vec{k}''-\vec{q}'',t_2)c^{\dagger}_b(\vec{k},t^{'})\ \rangle_0$$

$$+\frac{(-i)^3}{2!}\int_C dt_1\int_C dt_2\ \chi^2\sum_{\vec{k}',\vec{q}'\,;\ \vec{k}'',\vec{q}''}\frac{q^{'}_{+}}{q^{'}}\frac{q^{''}_{+}}{q^{''}}\langle\ T\ X_{-q'}(t_1)X_{-q''}(t_2)\ \rangle\times$$

$$\langle\ T\ c_A(\vec{k}''+\vec{q}'',t_2)c^{\dagger}_B(\vec{k}',t_1)\ \rangle_0\langle\ T\ c_A(\vec{k}'+\vec{q}',t_1)c^{\dagger}_b(\vec{k},t^{'})\ \rangle_0\langle\ T\ c_a(\vec{k},t)c^{\dagger}_B(\vec{k}'',t_2)\ \rangle_0$$

$$+\frac{(-i)^3}{2!}\int_C dt_1\int_C dt_2\ \chi^2\sum_{\vec{k}',\vec{q}'\,;\ \vec{k}'',\vec{q}''}\frac{q^{'}_{+}}{q^{'}}\frac{q^{''}_{+}}{q^{''}}\langle\ T\ X_{-q'}(t_1)X_{-q''}(t_2)\ \rangle\times$$

$$\langle\ T\ c_a(\vec{k},t)c^{\dagger}_B(\vec{k}',t_1)\ \rangle_0\langle\ T\ c_A(\vec{k}'+\vec{q}',t_1)c^{\dagger}_B(\vec{k}'',t_2)\ \rangle_0\langle\ T\ c_A(\vec{k}''+\vec{q}'',t_2)c^{\dagger}_b(\vec{k},t^{'})\ \rangle_0$$

Integrating over $\vec{k}'$, $\vec{k}''$ and $\vec{q}''$ using momentum conservation, this gives:

$$
\begin{gathered}
G_{ab}(\vec{k},t-t') - G_{ab,0}(\vec{k},t-t') = \\
\frac{(-i)^3}{2!}\int_C dt_1 \int_C dt_2\ \chi^2 \sum_{\vec{q}'} (-\frac{q_-'^2}{q'^2}) \langle\ T\ X_{q'}(t_1) X_{-q'}(t_2)\ \rangle \times \\
\langle\ T\ c_B(\vec{k}+\vec{q}',t_2) c_A^\dagger(\vec{k}+\vec{q}',t_1)\ \rangle_0 \langle\ T\ c_B(\vec{k},t_1) c_b^\dagger(\vec{k},t')\ \rangle_0 \langle\ T\ c_a(\vec{k},t) c_A^\dagger(\vec{k},t_2)\ \rangle_0 \\
+\frac{(-i)^3}{2!}\int_C dt_1 \int_C dt_2\ \chi^2 \sum_{\vec{q}'} (-\frac{q_-'^2}{q'^2}) \langle\ T\ X_{q'}(t_1) X_{-q'}(t_2)\ \rangle \times \\
\langle\ T\ c_a(\vec{k},t) c_A^\dagger(\vec{k},t_1)\ \rangle_0 \langle\ T\ c_B(\vec{k}-\vec{q}',t_1) c_A^\dagger(\vec{k}-\vec{q}',t_2)\ \rangle_0 \langle\ T\ c_B(\vec{k},t_2) c_b^\dagger(\vec{k},t')\ \rangle_0 \\
+\frac{(-i)^3}{2!}\int_C dt_1 \int_C dt_2\ \chi^2 \sum_{\vec{q}'} \frac{q_-'}{q'}\frac{q_+'}{q'} \langle\ T\ X_{q'}(t_1) X_{-q'}(t_2)\ \rangle \times \\
\langle\ T\ c_A(\vec{k}+\vec{q}',t_2) c_A^\dagger(\vec{k}+\vec{q}',t_1)\ \rangle_0 \langle\ T\ c_B(\vec{k},t_1) c_b^\dagger(\vec{k},t')\ \rangle_0 \langle\ T\ c_a(\vec{k},t) c_B^\dagger(\vec{k},t_2)\ \rangle_0 \\
+\frac{(-i)^3}{2!}\int_C dt_1 \int_C dt_2\ \chi^2 \sum_{\vec{q}'} \frac{q_-'}{q'}\frac{q_+'}{q'} \langle\ T\ X_{q'}(t_1) X_{-q'}(t_2)\ \rangle \times \\
\langle\ T\ c_a(\vec{k},t) c_A^\dagger(\vec{k},t_1)\ \rangle_0 \langle\ T\ c_B(\vec{k}-\vec{q}',t_1) c_B^\dagger(\vec{k}-\vec{q}',t_2)\ \rangle_0 \langle\ T\ c_A(\vec{k},t_2) c_b^\dagger(\vec{k},t')\ \rangle_0 \\
+\frac{(-i)^3}{2!}\int_C dt_1 \int_C dt_2\ \chi^2 \sum_{\vec{q}'} \frac{q_+'}{q'}\frac{q_-'}{q'} \langle\ T\ X_{-q'}(t_1) X_{q'}(t_2)\ \rangle \times \\
\langle\ T\ c_B(\vec{k}-\vec{q}',t_2) c_B^\dagger(\vec{k}-\vec{q}',t_1)\ \rangle_0 \langle\ T\ c_A(\vec{k},t_1) c_b^\dagger(\vec{k},t')\ \rangle_0 \langle\ T\ c_a(\vec{k},t) c_A^\dagger(\vec{k},t_2)\ \rangle_0 \\
+\frac{(-i)^3}{2!}\int_C dt_1 \int_C dt_2\ \chi^2 \sum_{\vec{q}'} \frac{q_+'}{q'}\frac{q_-'}{q'} \langle\ T\ X_{-q'}(t_1) X_{q'}(t_2)\ \rangle \times \\
\langle\ T\ c_a(\vec{k},t) c_B^\dagger(\vec{k},t_1)\ \rangle_0 \langle\ T\ c_A(\vec{k}+\vec{q}',t_1) c_A^\dagger(\vec{k}+\vec{q}',t_2)\ \rangle_0 \langle\ T\ c_B(\vec{k},t_2) c_b^\dagger(\vec{k},t')\ \rangle_0 \\
+\frac{(-i)^3}{2!}\int_C dt_1 \int_C dt_2\ \chi^2 \sum_{\vec{q}'} \frac{q_+'}{q'}(-\frac{q_+'}{q'}) \langle\ T\ X_{-q'}(t_1) X_{q'}(t_2)\ \rangle \times \\
\langle\ T\ c_A(\vec{k}-\vec{q}',t_2) c_B^\dagger(\vec{k}-\vec{q}',t_1)\ \rangle_0 \langle\ T\ c_A(\vec{k},t_1) c_b^\dagger(\vec{k},t')\ \rangle_0 \langle\ T\ c_a(\vec{k},t) c_B^\dagger(\vec{k},t_2)\ \rangle_0 \\
+\frac{(-i)^3}{2!}\int_C dt_1 \int_C dt_2\ \chi^2 \sum_{\vec{q}'} \frac{q_+'}{q'}(-\frac{q_+'}{q'}) \langle\ T\ X_{-q'}(t_1) X_{q'}(t_2)\ \rangle \times \\
\langle\ T\ c_a(\vec{k},t) c_B^\dagger(\vec{k},t_1)\ \rangle_0 \langle\ T\ c_A(\vec{k}+\vec{q}',t_1) c_B^\dagger(\vec{k}+\vec{q}',t_2)\ \rangle_0 \langle\ T\ c_A(\vec{k},t_2) c_b^\dagger(\vec{k},t')\ \rangle_0
\end{gathered}
\tag{B.18}
$$

The self-energy of the systems in terms of bare and dressed operators is defined as

$$G = G_0 + G_0\Sigma G \Rightarrow G - G_0 = G_0\Sigma G \tag{B.19}$$

This can be expanded, using $(G_0\Sigma G)_{ab} = \sum_{\lambda\lambda'} G_{a\lambda,0}\Sigma_{\lambda\lambda'}G_{\lambda' b}$, as

$$\begin{aligned}
&(G_{ab}(\vec{k}, t - t^{'}) - G_{ab,0}(\vec{k}, t - t^{'})) \approx \\
&\frac{1}{(-i\beta)^2}\oint dt_1 \oint dt_2\; G_{aA1,0}(\vec{k}, t - t_1)\Sigma_{A1A1}(\vec{k}, t_1 - t_2)G_{A1b,0}(\vec{k}, t_2 - t^{'}) \\
&+\frac{1}{(-i\beta)^2}\oint dt_1 \oint dt_2\; G_{aA1,0}(\vec{k}, t - t_1)\Sigma_{A1B2}(\vec{k}, t_1 - t_2)G_{B2b,0}(\vec{k}, t_2 - t^{'}) \\
&+\frac{1}{(-i\beta)^2}\oint dt_1 \oint dt_2\; G_{aB2,0}(\vec{k}, t - t_1)\Sigma_{B2A1}(\vec{k}, t_1 - t_2)G_{A1b,0}(\vec{k}, t_2 - t^{'}) \\
&+\frac{1}{(-i\beta)^2}\oint dt_1 \oint dt_2\; G_{aB2,0}(\vec{k}, t - t_1)\Sigma_{B2B2}(\vec{k}, t_1 - t_2)G_{B2b,0}(\vec{k}, t_2 - t^{'})
\end{aligned} \tag{B.20}$$

But,

$$\begin{aligned}
&G_{ab}(\vec{k}, t - t^{'}) - G_{ab,0}(\vec{k}, t - t^{'}) = \\
&\frac{(-i)^3}{2!}\int_C dt_1 \int_C dt_2\; \chi^2 \sum_{\vec{q}'} \Big(-\frac{q_-^{'2}}{q^{'2}}\Big)\langle\, T\; X_{q'}(t_1)X_{-q'}(t_2)\,\rangle \times \\
&\langle\, T\; c_B(\vec{k}+\vec{q}', t_2)c_A^\dagger(\vec{k}+\vec{q}', t_1)\,\rangle_0 \langle\, T\; c_B(\vec{k}, t_1)c_b^\dagger(\vec{k}, t^{'})\,\rangle_0 \langle\, T\; c_a(\vec{k}, t)c_A^\dagger(\vec{k}, t_2)\,\rangle_0 \\
&+\frac{(-i)^3}{2!}\int_C dt_1 \int_C dt_2\; \chi^2 \sum_{\vec{q}'} \Big(-\frac{q_-^{'2}}{q^{'2}}\Big)\langle\, T\; X_{q'}(t_1)X_{-q'}(t_2)\,\rangle \times \\
&\langle\, T\; c_a(\vec{k}, t)c_A^\dagger(\vec{k}, t_1)\,\rangle_0 \langle\, T\; c_B(\vec{k}-\vec{q}', t_1)c_A^\dagger(\vec{k}-\vec{q}', t_2)\,\rangle_0 \langle\, T\; c_B(\vec{k}, t_2)c_b^\dagger(\vec{k}, t^{'})\,\rangle_0 \\
&+\frac{(-i)^3}{2!}\int_C dt_1 \int_C dt_2\; \chi^2 \sum_{\vec{q}'} \frac{q_-^{'}}{q^{'}}\frac{q_+^{'}}{q^{'}}\langle\, T\; X_{q'}(t_1)X_{-q'}(t_2)\,\rangle \times \\
&\langle\, T\; c_A(\vec{k}+\vec{q}', t_2)c_A^\dagger(\vec{k}+\vec{q}', t_1)\,\rangle_0 \langle\, T\; c_B(\vec{k}, t_1)c_b^\dagger(\vec{k}, t^{'})\,\rangle_0 \langle\, T\; c_a(\vec{k}, t)c_B^\dagger(\vec{k}, t_2)\,\rangle_0 \\
&+\frac{(-i)^3}{2!}\int_C dt_1 \int_C dt_2\; \chi^2 \sum_{\vec{q}'} \frac{q_-^{'}}{q^{'}}\frac{q_+^{'}}{q^{'}}\langle\, T\; X_{q'}(t_1)X_{-q'}(t_2)\,\rangle \times \\
&\langle\, T\; c_a(\vec{k}, t)c_A^\dagger(\vec{k}, t_1)\,\rangle_0 \langle\, T\; c_B(\vec{k}-\vec{q}', t_1)c_B^\dagger(\vec{k}-\vec{q}', t_2)\,\rangle_0 \langle\, T\; c_A(\vec{k}, t_2)c_b^\dagger(\vec{k}, t^{'})\,\rangle_0 \\
&+\frac{(-i)^3}{2!}\int_C dt_1 \int_C dt_2\; \chi^2 \sum_{\vec{q}'} \frac{q_+^{'}}{q^{'}}\frac{q_-^{'}}{q^{'}}\langle\, T\; X_{-q'}(t_1)X_{q'}(t_2)\,\rangle \times \\
&\langle\, T\; c_B(\vec{k}-\vec{q}', t_2)c_B^\dagger(\vec{k}-\vec{q}', t_1)\,\rangle_0 \langle\, T\; c_A(\vec{k}, t_1)c_b^\dagger(\vec{k}, t^{'})\,\rangle_0 \langle\, T\; c_a(\vec{k}, t)c_A^\dagger(\vec{k}, t_2)\,\rangle_0
\end{aligned}$$

$$+\frac{(-i)^3}{2!}\int_C dt_1\int_C dt_2\ \chi^2\sum_{\vec{q}'}\frac{q'_+}{q'}\frac{q'_-}{q'}\langle\ T\ X_{-q'}(t_1)X_{q'}(t_2)\ \rangle\times$$

$$\langle\ T\ c_a(\vec{k},t)c^\dagger_B(\vec{k},t_1)\ \rangle_0\langle\ T\ c_A(\vec{k}+\vec{q}',t_1)c^\dagger_A(\vec{k}+\vec{q}',t_2)\ \rangle_0\langle\ T\ c_B(\vec{k},t_2)c^\dagger_b(\vec{k},t')\ \rangle_0$$

$$+\frac{(-i)^3}{2!}\int_C dt_1\int_C dt_2\ \chi^2\sum_{\vec{q}'}\frac{q'_+}{q'}(-\frac{q'_+}{q'})\langle\ T\ X_{-q'}(t_1)X_{q'}(t_2)\ \rangle\times$$

$$\langle\ T\ c_A(\vec{k}-\vec{q}',t_2)c^\dagger_B(\vec{k}-\vec{q}',t_1)\ \rangle_0\langle\ T\ c_A(\vec{k},t_1)c^\dagger_b(\vec{k},t')\ \rangle_0\langle\ T\ c_a(\vec{k},t)c^\dagger_B(\vec{k},t_2)\ \rangle_0$$

$$+\frac{(-i)^3}{2!}\int_C dt_1\int_C dt_2\ \chi^2\sum_{\vec{q}'}\frac{q'_+}{q'}(-\frac{q'_+}{q'})\langle\ T\ X_{-q'}(t_1)X_{q'}(t_2)\ \rangle\times$$

$$\langle\ T\ c_a(\vec{k},t)c^\dagger_B(\vec{k},t_1)\ \rangle_0\langle\ T\ c_A(\vec{k}+\vec{q}',t_1)c^\dagger_B(\vec{k}+\vec{q}',t_2)\ \rangle_0\langle\ T\ c_A(\vec{k},t_2)c^\dagger_b(\vec{k},t')\ \rangle_0$$

We can change the time from $t_1 \leftrightarrow t_2$, it will not change the value of the expression

$$G_{ab}(\vec{k},t-t')-G_{ab,0}(\vec{k},t-t')=$$

$$\frac{(-i)^3}{2!}\int_C dt_1\int_C dt_2\ \chi^2\sum_{\vec{q}'}(-\frac{q'^2_-}{q'^2})\langle\ T\ X_{q'}(t_2)X_{-q'}(t_1)\ \rangle\times$$

$$\langle\ T\ c_B(\vec{k}+\vec{q}',t_1)c^\dagger_A(\vec{k}+\vec{q}',t_2)\ \rangle_0\langle\ T\ c_a(\vec{k},t)c^\dagger_A(\vec{k},t_1)\ \rangle_0\langle\ T\ c_B(\vec{k},t_2)c^\dagger_b(\vec{k},t')\ \rangle_0$$

$$+\frac{(-i)^3}{2!}\int_C dt_1\int_C dt_2\ \chi^2\sum_{\vec{q}'}(-\frac{q'^2_-}{q'^2})\langle\ T\ X_{q'}(t_1)X_{-q'}(t_2)\ \rangle\times$$

$$\langle\ T\ c_B(\vec{k}-\vec{q}',t_1)c^\dagger_A(\vec{k}-\vec{q}',t_2)\ \rangle_0\langle\ T\ c_a(\vec{k},t)c^\dagger_A(\vec{k},t_1)\ \rangle_0\langle\ T\ c_B(\vec{k},t_2)c^\dagger_b(\vec{k},t')\ \rangle_0$$

$$+\frac{(-i)^3}{2!}\int_C dt_1\int_C dt_2\ \chi^2\sum_{\vec{q}'}\frac{q'_-}{q'}\frac{q'_+}{q'}\langle\ T\ X_{q'}(t_2)X_{-q'}(t_1)\ \rangle\times$$

$$\langle\ T\ c_A(\vec{k}+\vec{q}',t_1)c^\dagger_A(\vec{k}+\vec{q}',t_2)\ \rangle_0\langle\ T\ c_a(\vec{k},t)c^\dagger_B(\vec{k},t_1)\ \rangle_0\langle\ T\ c_B(\vec{k},t_2)c^\dagger_b(\vec{k},t')\ \rangle_0$$

$$+\frac{(-i)^3}{2!}\int_C dt_1\int_C dt_2\ \chi^2\sum_{\vec{q}'}\frac{q'_+}{q'}\frac{q'_-}{q'}\langle\ T\ X_{-q'}(t_1)X_{q'}(t_2)\ \rangle\times$$

$$\langle\ T\ c_a(\vec{k},t)c^\dagger_B(\vec{k},t_1)\ \rangle_0\langle\ T\ c_A(\vec{k}+\vec{q}',t_1)c^\dagger_A(\vec{k}+\vec{q}',t_2)\ \rangle_0\langle\ T\ c_B(\vec{k},t_2)c^\dagger_b(\vec{k},t')\ \rangle_0$$

$$+\frac{(-i)^3}{2!}\int_C dt_1\int_C dt_2\ \chi^2\sum_{\vec{q}'}\frac{q'_-}{q'}\frac{q'_+}{q'}\langle\ T\ X_{q'}(t_1)X_{-q'}(t_2)\ \rangle\times$$

$$\langle\ T\ c_B(\vec{k}-\vec{q}',t_1)c^\dagger_B(\vec{k}-\vec{q}',t_2)\ \rangle_0\langle\ T\ c_a(\vec{k},t)c^\dagger_A(\vec{k},t_1)\ \rangle_0\langle\ T\ c_A(\vec{k},t_2)c^\dagger_b(\vec{k},t')\ \rangle_0$$

$$+\frac{(-i)^3}{2!}\int_C dt_1\int_C dt_2\ \chi^2\sum_{\vec{q}'}\frac{q'_+}{q'}\frac{q'_-}{q'}\langle\ T\ X_{-q'}(t_2)X_{q'}(t_1)\ \rangle\times$$

$$\langle\ T\ c_B(\vec{k}-\vec{q}^{\,'},t_1)c_B^\dagger(\vec{k}-\vec{q}^{\,'},t_2)\ \rangle_0\langle\ T\ c_a(\vec{k},t)c_A^\dagger(\vec{k},t_1)\ \rangle_0\langle\ T\ c_A(\vec{k},t_2)c_b^\dagger(\vec{k},t')\ \rangle_0$$

$$+\frac{(-i)^3}{2!}\int_C dt_1\int_C dt_2\ \chi^2\sum_{\vec{q}^{\,'}}\frac{q_+^{'}}{q^{'}}(-\frac{q_+^{'}}{q^{'}})\langle\ T\ X_{-q'}(t_2)X_{q'}(t_1)\ \rangle\times$$

$$\langle\ T\ c_A(\vec{k}-\vec{q}^{\,'},t_1)c_B^\dagger(\vec{k}-\vec{q}^{\,'},t_2)\ \rangle_0\langle\ T\ c_a(\vec{k},t)c_B^\dagger(\vec{k},t_1)\ \rangle_0\langle\ T\ c_A(\vec{k},t_2)c_b^\dagger(\vec{k},t')\ \rangle_0$$

$$+\frac{(-i)^3}{2!}\int_C dt_1\int_C dt_2\ \chi^2\sum_{\vec{q}^{\,'}}\frac{q_+^{'}}{q^{'}}(-\frac{q_+^{'}}{q^{'}})\langle\ T\ X_{-q'}(t_1)X_{q'}(t_2)\ \rangle\times$$

$$\langle\ T\ c_a(\vec{k},t)c_B^\dagger(\vec{k},t_1)\ \rangle_0\langle\ T\ c_A(\vec{k}+\vec{q}^{\,'},t_1)c_B^\dagger(\vec{k}+\vec{q}^{\,'},t_2)\ \rangle_0\langle\ T\ c_A(\vec{k},t_2)c_b^\dagger(\vec{k},t')\ \rangle_0$$

Comparing the above equation with Eq. (B.20), we get

$$\Sigma_{A1B2}(\vec{k},t_1-t_2)=(-i)(-i\beta)^2\ \chi^2\sum_{\vec{q}^{\,'}}(-\frac{q_-^{'2}}{q^{'2}})\langle\ T\ X_{-q'}(t_1)X_{q'}(t_2)\ \rangle\langle\ T\ c_B(\vec{k}+\vec{q}^{\,'},t_1)c_A^\dagger(\vec{k}+\vec{q}^{\,'},t_2)\ \rangle_0$$

$$\Sigma_{B2B2}(\vec{k},t_1-t_2)=(-i)(-i\beta)^2\ \chi^2\sum_{\vec{q}^{\,'}}\frac{q_-^{'}}{q^{'}}\frac{q_+^{'}}{q^{'}}\langle\ T\ X_{-q'}(t_1)X_{q'}(t_2)\ \rangle\langle\ T\ c_A(\vec{k}+\vec{q}^{\,'},t_1)c_A^\dagger(\vec{k}+\vec{q}^{\,'},t_2)\ \rangle_0$$

$$\Sigma_{A1A1}(\vec{k},t_1-t_2)=(-i)(-i\beta)^2\ \chi^2\sum_{\vec{q}^{\,'}}\frac{q_-^{'}}{q^{'}}\frac{q_+^{'}}{q^{'}}\langle\ T\ X_{q'}(t_1)X_{-q'}(t_2)\ \rangle\langle\ T\ c_B(\vec{k}-\vec{q}^{\,'},t_1)c_B^\dagger(\vec{k}-\vec{q}^{\,'},t_2)\ \rangle_0$$

$$\Sigma_{B2A1}(\vec{k},t_1-t_2)=(-i)(-i\beta)^2\ \chi^2\sum_{\vec{q}^{\,'}}\frac{q_+^{'}}{q^{'}}(-\frac{q_+^{'}}{q^{'}})\langle\ T\ X_{q'}(t_1)X_{-q'}(t_2)\ \rangle\langle\ T\ c_A(\vec{k}-\vec{q}^{\,'},t_1)c_B^\dagger(\vec{k}-\vec{q}^{\,'},t_2)\ \rangle_0$$

$$\langle\ T\ X_{q'}(t_1)X_{-q'}(t_2)\ \rangle=\sum_n e^{w_n(t_1-t_2)}\ \langle\ T\ X_{q'}(n)X_{-q'}(-n)\ \rangle$$

This means,

$$\langle\ T\ X_{q'}(t_1)X_{-q'}(t_2)\ \rangle=\theta(t_1-t_2)\ e^{-i\omega_0(t_1-t_2)}+\theta(t_2-t_1)\ e^{-i\omega_0(t_2-t_1)}$$

Here, we use

$$X_q(t_1)X_{-q}(t_2)=(b_q(t_1)+b_{-q}^\dagger(t_1))(b_{-q}(t_2)+b_q^\dagger(t_2))$$

$$=b_q(t_1)b_{-q}(t_2)+b_q(t_1)b_q^\dagger(t_2)+b_{-q}^\dagger(t_1)b_{-q}(t_2)+b_{-q}^\dagger(t_1)b_q^\dagger(t_2)$$

In Heisenberg representation,

$$b(t)=e^{-i\omega_0 t}b(0)$$

Because,

$$H=\omega b^\dagger b,\ \ b(t)=e^{iHt}b(0)e^{-iHt}$$

Using expansion of $e^{B}Ae^{-B}$ we will get the required result. Therefore,

$$\langle b(t)b^{\dagger}(t')\rangle = e^{-i\omega_0(t-t^{'})}\langle b(0)b^{\dagger}(0)\rangle = e^{-i\omega_0(t-t^{'})}\langle G|b(0)b^{\dagger}(0)|G\rangle$$

$$= e^{-i\omega_0(t-t^{'})}$$

$$\delta(t_1-t_2) = \frac{1}{-i\beta}\sum_{n} e^{w_n(t_1-t_2)}$$

$$\theta(t_1-t_2) = \frac{1}{-i\beta}\sum_{n} \frac{e^{w_n(t_1-t_2)}}{w_n+i\delta}$$

$$\sum_{n} e^{w_n(t_1-t_2)} \langle\ T\ X_{q^{'}}(n)X_{-q^{'}}(-n)\ \rangle = \frac{1}{-i\beta}\sum_{n}\frac{e^{w_n(t_1-t_2)}}{w_n+i\omega_0+i\delta} + \frac{1}{-i\beta}\sum_{n}\frac{e^{w_n(t_1-t_2)}}{-w_n+i\omega_0+i\delta}$$

$$\langle\ T\ X_{q'}(n^{'})X_{-q'}(-n^{'})\ \rangle = \frac{1}{\beta}\left(\frac{1}{-iw_{n'}+\omega_0+\delta} + \frac{1}{iw_{n'}+\omega_0+\delta}\right) = \frac{1}{\beta}F(w_{n'})$$

$$\langle\ T\ c_{a,0}(\vec{k},t)c^{\dagger}_{b,0}(\vec{k},t^{'})\ \rangle_0 = \sum_{n} e^{z_n(t-t^{'})}\ \langle\ T\ c_{a,0}(\vec{k},n)c^{\dagger}_{b,0}(\vec{k},n)\ \rangle_0$$

$$\Sigma_{ab}(\vec{k},t-t^{'}) = \sum_{n} e^{z_n(t-t^{'})}\ \Sigma_{ab}(\vec{k},n)$$

Therefore, the expressions of self-energy comes out to be

$$\Sigma_{A1B2}(\vec{k},n) = (-i)(-i\beta)^2\ \chi^2\sum_{\vec{q}^{'}}\left(-\frac{q_{-}^{'2}}{q^{'2}}\right)\sum_{n^{'}}\langle\ T\ X_{-q^{'}}(n^{'})X_{q^{'}}(-n^{'})\ \rangle\langle\ T\ c_B(\vec{k}+\vec{q}^{'},n-n^{'})c^{\dagger}_A(\vec{k}+\vec{q}^{'},n-n^{'})\ \rangle_0$$

$$\Sigma_{B2B2}(\vec{k},n) = (-i)(-i\beta)^2\ \chi^2\sum_{\vec{q}^{'}}\frac{q^{'}_{-}}{q^{'}}\frac{q^{'}_{+}}{q^{'}}\sum_{n^{'}}\langle\ T\ X_{-q^{'}}(n^{'})X_{q^{'}}(-n^{'})\ \rangle\langle\ T\ c_A(\vec{k}+\vec{q}^{'},n-n^{'})c^{\dagger}_A(\vec{k}+\vec{q}^{'},n-n^{'})\ \rangle_0$$

$$\Sigma_{A1A1}(\vec{k},n) = (-i)(-i\beta)^2\ \chi^2\sum_{\vec{q}^{'}}\frac{q^{'}_{-}}{q^{'}}\frac{q^{'}_{+}}{q^{'}}\sum_{n^{'}}\langle\ T\ X_{q^{'}}(n^{'})X_{-q^{'}}(-n^{'})\ \rangle\langle\ T\ c_B(\vec{k}-\vec{q}^{'},n-n^{'})c^{\dagger}_B(\vec{k}-\vec{q}^{'},n-n^{'})\ \rangle_0$$

$$\Sigma_{B2A1}(\vec{k},n) = (-i)(-i\beta)^2\ \chi^2\sum_{\vec{q}^{'}}\frac{q^{'}_{+}}{q^{'}}\left(-\frac{q^{'}_{+}}{q^{'}}\right)\sum_{n^{'}}\langle\ T\ X_{q^{'}}(n^{'})X_{-q^{'}}(-n^{'})\ \rangle\langle\ T\ c_A(\vec{k}-\vec{q}^{'},n-n^{'})c^{\dagger}_B(\vec{k}-\vec{q}^{'},n-n^{'})\ \rangle_0$$

Inserting the known values in the above equations,

$$\Sigma_{A1B2}(\vec{k},n) = (-i)(-i\beta)^2\ \chi^2\sum_{\vec{q}}\left(-\frac{q_{-}^2}{q^2}\right)\sum_{n^{'}}\frac{1}{\beta}F(w_{n^{'}})\frac{2m(-(k_{+}+q_{+})^2)}{\left((\vec{k}+\vec{q})^4+4m^2((z_n-w_{n^{'}})^2+\alpha^2_{\vec{k}+\vec{q}})\right)\beta}$$

$$\Sigma_{B2B2}(\vec{k},n) = (-i)(-i\beta)^2\ \chi^2\sum_{\vec{q}}\frac{q_{-}}{q}\frac{q_{+}}{q}\sum_{n^{'}}\frac{1}{\beta}F(w_{n^{'}})\frac{2m(2im((z_n-w_{n^{'}})+i\alpha_{\vec{k}+\vec{q}}))}{\left((\vec{k}+\vec{q})^4+4m^2((z_n-w_{n^{'}})^2+\alpha^2_{\vec{k}+\vec{q}})\right)\beta}$$

$$\Sigma_{A1A1}(\vec{k},n) = (-i)(-i\beta)^2\ \chi^2\sum_{\vec{q}}\frac{q_{-}}{q}\frac{q_{+}}{q}\sum_{n^{'}}\frac{1}{\beta}F(w_{n^{'}})\frac{2m(2im((z_n-w_{n^{'}})-i\alpha_{\vec{k}-\vec{q}}))}{\left((\vec{k}-\vec{q})^4+4m^2((z_n-w_{n^{'}})^2+\alpha^2_{\vec{k}-\vec{q}})\right)\beta}$$

$$\Sigma_{B2A1}(\vec{k},n) = (-i)(-i\beta)^2\ \chi^2\sum_{\vec{q}}\left(-\frac{q_{+}^2}{q^2}\right)\sum_{n^{'}}\frac{1}{\beta}F(w_{n^{'}})\frac{2m(-(k_{-}-q_{-})^2)}{\left((\vec{k}-\vec{q})^4+4m^2((z_n-w_{n^{'}})^2+\alpha^2_{\vec{k}-\vec{q}})\right)\beta}$$

$$\Sigma_{A1B2}(\vec{k},n) = (-i)(-i\beta)^2\ \chi^2 \sum_{\vec{q}} (-\frac{q_-^2}{q^2})(i\beta) \int_{-\infty}^{\infty} \frac{dw_{n'}}{2\pi i} \frac{1}{\beta} F(w_{n'}) \frac{2m(-(k_+ + q_+)^2)}{\left((\vec{k}+\vec{q})^4 + 4m^2((z_n - w_{n'})^2 + \alpha^2_{\vec{k}+\vec{q}})\right)\beta}$$

$$\Sigma_{B2B2}(\vec{k},n) = (-i)(-i\beta)^2\ \chi^2 \sum_{\vec{q}} \frac{q_-}{q}\frac{q_+}{q}(i\beta) \int_{-\infty}^{\infty} \frac{dw_{n'}}{2\pi i} \frac{1}{\beta} F(w_{n'}) \frac{2m(2im((z_n - w_{n'}) + i\alpha_{\vec{k}+\vec{q}}))}{\left((\vec{k}+\vec{q})^4 + 4m^2((z_n - w_{n'})^2 + \alpha^2_{\vec{k}+\vec{q}})\right)\beta}$$

$$\Sigma_{A1A1}(\vec{k},n) = (-i)(-i\beta)^2\ \chi^2 \sum_{\vec{q}} \frac{q_-}{q}\frac{q_+}{q}(i\beta) \int_{-\infty}^{\infty} \frac{dw_{n'}}{2\pi i} \frac{1}{\beta} F(w_{n'}) \frac{2m(2im((z_n - w_{n'}) - i\alpha_{\vec{k}-\vec{q}}))}{\left((\vec{k}-\vec{q})^4 + 4m^2((z_n - w_{n'})^2 + \alpha^2_{\vec{k}-\vec{q}})\right)\beta}$$

$$\Sigma_{B2A1}(\vec{k},n) = (-i)(-i\beta)^2\ \chi^2 \sum_{\vec{q}} (-\frac{q_+^2}{q^2})(i\beta) \int_{-\infty}^{\infty} \frac{dw_{n'}}{2\pi i} \frac{1}{\beta} F(w_{n'}) \frac{2m(-(k_- - q_-)^2)}{\left((\vec{k}-\vec{q})^4 + 4m^2((z_n - w_{n'})^2 + \alpha^2_{\vec{k}-\vec{q}})\right)\beta}$$

where,

$$F(w_{n'}) = \left(\frac{1}{-iw_{n'} + \omega_0 + \delta} + \frac{1}{iw_{n'} + \omega_0 + \delta}\right)$$

Solving the values of integrations using Integrate route of Mathematica, we will get

$$\Sigma_{A1B2}(\vec{k},n) = (-i)(-i\beta)^2\ \chi^2 \sum_{\vec{q}} (-\frac{q_-^2}{q^2}) \times -\frac{2m(k_+ + q_+)^2\,[NumA1B2]}{\beta\sqrt{(\vec{k}+\vec{q})^4 + 4m^2\alpha^2_{\vec{k}+\vec{q}}}\left((\vec{k}+\vec{q})^4 + 4m^2\left(\alpha^2_{\vec{k}+\vec{q}} - (\omega_0 + iz_n)^2\right)\right) DenA1B2}$$

$$NumA1B2 = (\vec{k}+\vec{q})^4 - 2m\left(iz_n\sqrt{(\vec{k}+\vec{q})^4 + 4m^2\alpha^2_{\vec{k}+\vec{q}}} + 2m\left(-\alpha^2_{\vec{k}+\vec{q}} + \omega_0^2 + i\omega_0 z_n\right)\right)$$

$$DenA1B2 = \left(\sqrt{(\vec{k}+\vec{q})^4 + 4m^2\alpha^2_{\vec{k}+\vec{q}}} + 2m(\omega_0 - iz_n)\right)$$

$$\Sigma_{B2B2}(\vec{k},n) = (-i)(-i\beta)^2\ \chi^2 \sum_{\vec{q}} \frac{q_-}{q}\frac{q_+}{q} \times \frac{4m^2\,[NumB2B2]}{\beta\left((\vec{k}+\vec{q})^4 + 4m^2\alpha^2_{\vec{k}+\vec{q}}\right)\left((\vec{k}+\vec{q})^4 + 4m^2\left(\alpha^2_{\vec{k}+\vec{q}} - (\omega_0 + iz_n)^2\right)\right) DenB2B2}$$

$$NumB2B2 = (\vec{k}+\vec{q})^4\left[2mz_n(i\alpha_{\vec{k}+\vec{q}} - i\omega_0 + z_n) - (\alpha_{\vec{k}+\vec{q}} - iz_n)\sqrt{(\vec{k}+\vec{q})^4 + 4m^2\alpha^2_{\vec{k}+\vec{q}}}\right]$$

$$+4m^2\alpha_{\vec{k}+\vec{q}}(-\alpha_{\vec{k}+\vec{q}} + \omega_0 + iz_n)\left[(\alpha_{\vec{k}+\vec{q}} + \omega_0)\sqrt{(\vec{k}+\vec{q})^4 + 4m^2\alpha^2_{\vec{k}+\vec{q}}} - 2imz_n\alpha_{\vec{k}+\vec{q}}\right]$$

$$DenB2B2 = \left(\sqrt{(\vec{k}+\vec{q})^4 + 4m^2\alpha^2_{\vec{k}+\vec{q}}} + 2m(\omega_0 - iz_n)\right)$$

$$\Sigma_{A1A1}(\vec{k},n) = (-i)(-i\beta)^2\ \chi^2 \sum_{\vec{q}} \frac{q_-}{q}\frac{q_+}{q} \times \frac{4m^2\,[NumA1A1]}{\beta\left((\vec{k}-\vec{q})^4 + 4m^2\alpha^2_{\vec{k}-\vec{q}}\right)\left((\vec{k}-\vec{q})^4 + 4m^2\left(\alpha^2_{\vec{k}-\vec{q}} - (\omega_0 + iz_n)^2\right)\right) DenA1A1}$$

$$NumA1A1 = (\vec{k}-\vec{q})^4\left[(\alpha_{\vec{k}-\vec{q}} + iz_n)\sqrt{(\vec{k}-\vec{q})^4 + 4m^2\alpha^2_{\vec{k}-\vec{q}}} - 2imz_n(\alpha_{\vec{k}-\vec{q}} + \omega_0 + iz_n)\right]$$

$$+4m^2\alpha_{\vec{k}-\vec{q}}(\alpha_{\vec{k}-\vec{q}} + \omega_0 + iz_n)\left[(\alpha_{\vec{k}-\vec{q}} - \omega_0)\sqrt{(\vec{k}-\vec{q})^4 + 4m^2\alpha^2_{\vec{k}-\vec{q}}} - 2imz_n\alpha_{\vec{k}-\vec{q}}\right]$$

$$DenA1A1 = \left(\sqrt{(\vec{k}-\vec{q})^4 + 4m^2\alpha^2_{\vec{k}-\vec{q}}} + 2m(\omega_0 - iz_n)\right)$$

$$\Sigma_{B2A1}(\vec{k},n) = (-i)(-i\beta)^2\ \chi^2 \sum_{\vec{q}} (-\frac{q_+^2}{q^2}) \times -\frac{2m(k_- - q_-)^2\,[NumB2A1]}{\beta\sqrt{(\vec{k}-\vec{q})^4 + 4m^2\alpha^2_{\vec{k}-\vec{q}}}\left((\vec{k}-\vec{q})^4 + 4m^2\left(\alpha^2_{\vec{k}-\vec{q}} - (\omega_0 + iz_n)^2\right)\right) DenB2A1}$$

$$NumB2A1 = (\vec{k}-\vec{q})^4 - 2m\left(iz_n\sqrt{(\vec{k}-\vec{q})^4 + 4m^2\alpha^2_{\vec{k}-\vec{q}}} + 2m\left(-\alpha^2_{\vec{k}-\vec{q}} + \omega_0^2 + i\omega_0 z_n\right)\right)$$

$$DenB2A1 = \left(\sqrt{(\vec{k}-\vec{q})^4 + 4m^2\alpha^2_{\vec{k}-\vec{q}}} + 2m(\omega_0 - iz_n)\right)$$

We can find the following quantities by simply using Mathematica,

$$\Sigma_{A1A1}(\vec{k},n) + \Sigma_{B2B2}(\vec{k},n) = (-i)(-i\beta)^2\ \chi^2 \sum_{\vec{q}} \frac{q_-}{q}\frac{q_+}{q} \times \frac{8im^2zn}{\left[(\vec{k}+\vec{q})^4 + 4m\left(m(\omega_0^2 + z_n^2 + \alpha^2_{\vec{k}+\vec{q}}) + \omega_0\sqrt{(\vec{k}+\vec{q})^4 + 4m^2\alpha^2_{\vec{k}+\vec{q}}}\right)\right]\beta}$$

$$\Sigma_{A1A1}(\vec{k},n) - \Sigma_{B2B2}(\vec{k},n) = (-i)(-i\beta)^2\ \chi^2 \sum_{\vec{q}} \frac{q_-}{q}\frac{q_+}{q} \times \frac{8m^2\alpha_{\vec{k}+\vec{q}}\,[NumSA1A1MSB2B2]}{\sqrt{(\vec{k}+\vec{q})^4 + 4m^2\alpha^2_{\vec{k}+\vec{q}}}\ DenSA1A1MSB2B2\ \beta}$$

where,

$$NumSA1A1MSB2B2 = (\vec{k}+\vec{q})^4 - 2m(2m(\omega_0^2 + i\omega_0 z_n - \alpha^2_{\vec{k}+\vec{q}}) + iz_n\sqrt{(\vec{k}+\vec{q})^4 + 4m^2\alpha^2_{\vec{k}+\vec{q}}})$$

$$DenSA1A1MSB2B2 = \left((\vec{k}+\vec{q})^4 + 4m^2(-(\omega_0 + iz_n)^2 + \alpha^2_{\vec{k}+\vec{q}})\right)\left(2m(\omega_0 - iz_n) + \sqrt{(\vec{k}+\vec{q})^4 + 4m^2\alpha^2_{\vec{k}+\vec{q}}}\right)$$

$$Den = (k^4 + 4m^2(z_n^2 + \alpha_k^2))\beta$$

We are looking for the most singular part of G, putting it to zero,

$$DenfullNew = Den + \frac{4m^2}{\beta}(-\Sigma_{A1B2}\Sigma_{B2A1} + \Sigma_{A1A1}\Sigma_{B2B2})$$

$$-2im\,\left[k_+^2\Sigma_{A1B2} + k_-^2\Sigma_{B2A1} + 2m(\alpha_k(\Sigma_{A1A1} - \Sigma_{B2B2}) - iz_n(\Sigma_{A1A1} + \Sigma_{B2B2}))\right] = 0$$

This gives,

$$\beta\left(k^4 + (2m)^2(z_n^2 + \alpha_k^2)\right) - i(2m)^2\alpha_k\left(\Sigma_{A1A1}(\vec{k},n) - \Sigma_{B2B2}(\vec{k},n)\right) - (2m)^2 z_n\left(\Sigma_{A1A1}(\vec{k},n) + \Sigma_{B2B2}(\vec{k},n)\right) = 0$$

Inserting known values,

$$\begin{aligned}&\beta\left[k^4 + (2m)^2\left(z_n^2 + \alpha_k^2\right)\right]\\ &-i(2m)^2\alpha_k \times (-i)(-i\beta)^2\ \chi^2\sum_{\vec{q}}\frac{8m^2\alpha_{\vec{k}+\vec{q}}[Num1T]}{\sqrt{(\vec{k}+\vec{q})^4 + 4m^2\alpha^2_{\vec{k}+\vec{q}}}\left((\vec{k}+\vec{q})^4 + 4m^2(-(\omega_0 + iz_n)^2 + \alpha^2_{\vec{k}+\vec{q}})\right)\ Den1T\ \beta}\\ &-(2m)^2 z_n \times (-i)(-i\beta)^2\ \chi^2\sum_{\vec{q}}\frac{8im^2zn}{\left[(\vec{k}+\vec{q})^4 + 4m\left(m(\omega_0^2 + z_n^2 + \alpha^2_{\vec{k}+\vec{q}}) + \omega_0\sqrt{(\vec{k}+\vec{q})^4 + 4m^2\alpha^2_{\vec{k}+\vec{q}}}\right)\right]\beta} = 0\end{aligned} \tag{B.21}$$

where,

$$Num1T = (\vec{k}+\vec{q})^4 - 2m(2m(\omega_0^2 + i\omega_0 z_n - \alpha^2_{\vec{k}+\vec{q}}) + iz_n\sqrt{(\vec{k}+\vec{q})^4 + 4m^2\alpha^2_{\vec{k}+\vec{q}}})$$

$$Den1T = \left(2m(\omega_0 - iz_n) + \sqrt{(\vec{k}+\vec{q})^4 + 4m^2\alpha^2_{\vec{k}+\vec{q}}}\right)$$

$$Den = (k^4 + 4m^2(z_n^2 + \alpha_k^2))\beta = 0$$

Hence,

$$z_n = \pm i\sqrt{\frac{k^4}{4m^2} + \alpha_k^2} = \pm i\Omega_{\vec{k}}$$

Putting, the relaxation term in z_n in a phenomenological way and assuming it is a complex quantity,

$$z_n = \pm i\Omega_{\vec{k}} + \Gamma_{k,C}, \qquad \Gamma_{C,k} = \Gamma_{k,R} + i\ \Gamma_{k,I}$$

Therefore,

$$z_n = \pm i\Omega_{\vec{k}} + \Gamma_{k,R} + i\ \Gamma_{k,I}$$

Inserting this in Eq. (B.21), after some simplification we obtain

$$\begin{aligned}&\beta\left[k^4 + (2m)^2\left((-i\Omega_{\vec{k}} + \Gamma_{k,R} + i\ \Gamma_{k,I})^2 + \alpha_k^2\right)\right]\\ &+(2m)^2\alpha_k\beta^2\ \chi^2\sum_{\vec{q}}\frac{8m^2\alpha_{\vec{k}+\vec{q}}[T1N]}{\sqrt{(\vec{k}+\vec{q})^4 + 4m^2\alpha^2_{\vec{k}+\vec{q}}}\left((\vec{k}+\vec{q})^4 - 4m^2(\omega_0 + \Omega_{\vec{k}} + i\ \Gamma_{k,R} - \Gamma_{k,I})^2 + 4m^2\alpha^2_{\vec{k}+\vec{q}}\right)\ T1D\ \beta}\\ &-(2m)^2(\Omega_{\vec{k}} + i\ \Gamma_{k,R} - \Gamma_{k,I})\beta^2\ \chi^2\sum_{\vec{q}}\frac{8m^2(\Omega_{\vec{k}} + i\ \Gamma_{k,R} - \Gamma_{k,I})}{\left[(\vec{k}+\vec{q})^4 + 4m\ (T2D)\right]\beta} = 0\end{aligned}$$

$$T1N = (\vec{k}+\vec{q})^4 - 4m^2(\omega_0^2 + i\omega_0(-i\Omega_{\vec{k}} + \Gamma_{k,R} + i\ \Gamma_{k,I}) - \alpha^2_{\vec{k}+\vec{q}}) - 2m(\Omega_{\vec{k}} + i\ \Gamma_{k,R} - \Gamma_{k,I})\sqrt{(\vec{k}+\vec{q})^4 + 4m^2\alpha^2_{\vec{k}+\vec{q}}}$$

$$T1D = \left(2m(\omega_0 - \Omega_{\vec{k}} - i\ \Gamma_{k,R} + \Gamma_{k,I}) + \sqrt{(\vec{k}+\vec{q})^4 + 4m^2\alpha^2_{\vec{k}+\vec{q}}}\right)$$

$$T2D = m(\omega_0^2 + (-i\Omega_{\vec{k}} + \Gamma_{k,R} + i\ \Gamma_{k,I})^2 + \alpha^2_{\vec{k}+\vec{q}}) + \omega_0\sqrt{(\vec{k}+\vec{q})^4 + 4m^2\alpha^2_{\vec{k}+\vec{q}}}$$

From above equation, first two terms can be written as

$$\beta\left[k^4+(2m)^2\left((-i\Omega_{\vec{k}}+\Gamma_{k,R}+i\Gamma_{k,I})^2+\alpha_{\vec{k}}^2\right)\right]$$

$$+(2m)^2\alpha_k\beta^2\ \chi^2\sum_{\vec{q}}\frac{8m^2\alpha_{\vec{k}+\vec{q}}(T1N)}{\sqrt{(\vec{k}+\vec{q})^4+4m^2\alpha^2_{\vec{k}+\vec{q}}}\ \beta}\frac{1}{\left(\sqrt{(\vec{k}+\vec{q})^4+4m^2\alpha^2_{\vec{k}+\vec{q}}}-2m(\omega_0+\Omega_{\vec{k}}+i\Gamma_{k,R}-\Gamma_{k,I})\right)}$$

$$\times\frac{1}{\left(\sqrt{(\vec{k}+\vec{q})^4+4m^2\alpha^2_{\vec{k}+\vec{q}}}+2m(\omega_0+\Omega_{\vec{k}}+i\Gamma_{k,R}-\Gamma_{k,I})\right)}\frac{1}{\left(2m(\omega_0-\Omega_{\vec{k}}-i\Gamma_{k,R}+\Gamma_{k,I})+\sqrt{(\vec{k}+\vec{q})^4+4m^2\alpha^2_{\vec{k}+\vec{q}}}\right)}=0$$

Using ComplexExpand routine of Mathematica, we can easily separate the real and imaginary parts of above equation, the real and imaginary parts comes out to be, respectively,

$$-4m^2\beta\Gamma^2_{kI}+4m^2\beta\Gamma^2_{kR}+8m^2\beta\Gamma_{k,I}\Omega_k=-\sum_{\vec{q}}\frac{(8m^2\alpha_k\alpha_{k+q}\beta\chi^2(\omega_0+\Omega_{k+q})(\Gamma^2_{k,R}-(\Gamma_{k,I}-\Omega_k)^2+(\omega_0+\Omega_{k+q})^2))}{\Omega_{k+q}(\Gamma^2_{k,R}+(\Gamma_{k,I}+\omega_0-\Omega_k+\Omega_{k+q})^2)(\Gamma^2_{k,R}+(-\Gamma_{k,I}+\omega_0+\Omega_k+\Omega_{k+q})^2)}$$

and,

$$(8m^2\beta\Gamma_{k,I}\Gamma_{k,R}-8m^2\beta\Gamma_{k,R}\Omega_k)=\sum_{\vec{q}}\frac{16m^2\alpha_k\alpha_{k+q}\beta\Gamma_{k,R}\chi^2(\Gamma_{k,I}-\Omega_k)(\omega_0+\Omega_{k+q})}{\Omega_{k+q}(\Gamma^2_{k,R}+(\Gamma_{k,I}+\omega_0-\Omega_k+\Omega_{k+q})^2)(\Gamma^2_{k,R}+(-\Gamma_{k,I}+\omega_0+\Omega_k+\Omega_{k+q})^2)}$$

Using partial fraction, the above equations can be written as

$$-4m^2\beta\Gamma^2_{kI}+4m^2\beta\Gamma^2_{kR}+8m^2\beta\Gamma_{k,I}\Omega_k=-\sum_{\vec{q}}\frac{(8m^2\alpha_k\alpha_{k+q}\beta\chi^2(\omega_0+\Omega_{k+q}))}{4\Omega_{k+q}(\Gamma_{k,I}-\Omega_k)(\omega_0+\Omega_{k+q})}\times\left[\frac{(x)^2}{(\Gamma^2_{k,R}+(x)^2)}-\frac{(y)^2}{(\Gamma^2_{k,R}+(y)^2)}\right]$$

$$+\sum_{\vec{q}}\left[(\Gamma_{k,I}-\Omega_k)^2-(\omega_0+\Omega_{k+q})^2\right]\times\frac{(8m^2\alpha_k\alpha_{k+q}\beta\chi^2(\omega_0+\Omega_{k+q}))}{4\Omega_{k+q}(\Gamma_{k,I}-\Omega_k)(\omega_0+\Omega_{k+q})}\times\left[\frac{1}{(\Gamma^2_{k,R}+(y)^2)}-\frac{1}{(\Gamma^2_{k,R}+(x)^2)}\right]$$

and,

$$(8m^2\beta\Gamma_{k,I}\Gamma_{k,R}-8m^2\beta\Gamma_{k,R}\Omega_k)=\sum_{\vec{q}}\frac{16m^2\alpha_k\alpha_{k+q}\beta\chi^2(\Gamma_{k,I}-\Omega_k)(\omega_0+\Omega_{k+q})}{\Omega_{k+q}\ 4(\Gamma_{k,I}-\Omega_k)(\omega_0+\Omega_{k+q})}\left[\frac{\Gamma_{k,R}}{\Gamma^2_{k,R}+(y)^2}-\frac{\Gamma_{k,R}}{\Gamma^2_{k,R}+(x)^2}\right]$$

$$x=\Gamma_{k,I}+\omega_0-\Omega_k+\Omega_{k+q}$$

$$y=-\Gamma_{k,I}+\omega_0+\Omega_k+\Omega_{k+q}$$

Using the following identity,

$$\frac{p}{p^2+a^2}=\pi\delta(a)$$

the above equations can be written in terms of Delta function,

$$-4m^2\beta\Gamma^2_{kI}+4m^2\beta\Gamma^2_{kR}+8m^2\beta\Gamma_{k,I}\Omega_k=-\sum_{\vec{q}}\frac{(8m^2\alpha_k\alpha_{k+q}\beta\chi^2(\omega_0+\Omega_{k+q}))}{4\Omega_{k+q}(\Gamma_{k,I}-\Omega_k)(\omega_0+\Omega_{k+q})}\frac{\pi}{\Gamma_{k,R}}\times\left[(x)^2\delta(x)-(y)^2\delta(y)\right]$$

$$+\sum_{\vec{q}}\left[(\Gamma_{k,I}-\Omega_k)^2-(\omega_0+\Omega_{k+q})^2\right]\times\frac{(8m^2\alpha_k\alpha_{k+q}\beta\chi^2(\omega_0+\Omega_{k+q}))}{4\Omega_{k+q}(\Gamma_{k,I}-\Omega_k)(\omega_0+\Omega_{k+q})}\times\frac{\pi}{\Gamma_{k,R}}\left[\delta(y)-\delta(x)\right]$$

and,

$$(8m^2\beta\Gamma_{k,I}\Gamma_{k,R}-8m^2\beta\Gamma_{k,R}\Omega_k)=\sum_{\vec{q}}\frac{16m^2\alpha_k\alpha_{k+q}\beta\chi^2(\Gamma_{k,I}-\Omega_k)(\omega_0+\Omega_{k+q})}{\Omega_{k+q}\ 4(\Gamma_{k,I}-\Omega_k)(\omega_0+\Omega_{k+q})}\times\pi\left[\delta(y)-\delta(x)\right]$$

Simplifying the above equations assuming that $\Gamma_{k,I}\ll\omega_0$,

$$\Gamma_{k,I}\Omega_k=\sum_{\vec{q}}\frac{(\alpha_k\alpha_{k+q}\chi^2)}{\Omega_{k+q}}\frac{(-\Omega_k)^2-(\omega_0+\Omega_{k+q})^2}{-\Omega_k)}\times\frac{\pi}{\Gamma_{k,R}}\left[-\delta(\omega_0-\Omega_k+\Omega_{k+q})\right]$$

$$-\Gamma_{k,R}\Omega_k=\sum_{\vec{q}}\frac{\alpha_k\alpha_{k+q}\chi^2}{2\Omega_{k+q}}\times\pi\left[-\delta(\omega_0-\Omega_k+\Omega_{k+q})\right]$$

Our focus is only on the real part of Γ,

$$\Gamma_{k,R} = \sum_{\vec{q}} \frac{\pi\chi^2 \alpha_k \alpha_{k+q}}{2\Omega_k \Omega_{k+q}} \times \delta(\omega_0 - \Omega_k + \Omega_{k+q}) \tag{B.22}$$

Delta function gives,

$$-\omega_0 + \Omega_k = \Omega_{k+q}$$

Inserting all known values in Eq. (B.22) along with the above condition and assuming that the energy of the system is very large, Eq. (B.22) reduces to

$$\Gamma_{k,R} = \sum_{\vec{q}} \frac{\pi\chi^2 \left(\frac{2|k|^2}{m}\frac{\omega_R}{\omega}\right)\left(\frac{2|k+q|^2}{m}\frac{\omega_R}{\omega}\right)}{2 \times \frac{|k|^2}{m} \times \left(-\omega_0 + \frac{|k|^2}{m}\right)} \times \delta\left(\omega_0 - \frac{|k|^2}{m} + \frac{|k+q|^2}{m}\right)$$

For our easiness keeping $k_y = 0$ and taking $k_x = k$, the above equation can be written as,

$$\Gamma_{k,R} = \sum_{\vec{q}} \frac{\pi\chi^2 \left(\frac{2k^2}{m}\frac{\omega_R}{\omega}\right)\left(\frac{2(k^2+q_x^2+2kq_x+q_y^2)}{m}\frac{\omega_R}{\omega}\right)}{2 \times \frac{k^2}{m} \times \left(-\omega_0 + \frac{k^2}{m}\right)} \times \delta\left(\omega_0 - \frac{k^2}{m} + \frac{(k^2 + q_x^2 + 2kq_x + q_y^2)}{m}\right)$$

$$\Gamma_{k,R} = \sum_{\vec{q}} \frac{\pi\chi^2 \left(\frac{2k^2}{m}\frac{\omega_R}{\omega}\right)\left(2\left(-\omega_0 + \frac{k^2}{m}\right)\frac{\omega_R}{\omega}\right)}{2 \times \frac{k^2}{m} \times \left(-\omega_0 + \frac{k^2}{m}\right)} \times \delta\left(\omega_0 - \frac{k^2}{m} + \frac{(k^2 + q_x^2 + 2kq_x + q_y^2)}{m}\right)$$

$$\Gamma_{k,R} = \sum_{\vec{q}} \pi\chi^2 \frac{\omega_R^2}{\omega^2} \times \delta\left(\omega_0 + \frac{(q^2 + 2kqcos\theta)}{m}\right)$$

$$\Gamma_{k,R} = \sum_{\vec{q}} \pi\chi^2 \frac{\omega_R^2}{\omega^2} \times \int_0^{2\pi} d\theta \left[\int_0^{\infty} q\ dq \quad \times \delta\left(\omega_0 + \frac{(q^2 + 2kqcos\theta)}{m}\right)\right]$$

$$\Gamma_{k,R} = \sum_{\vec{q}} \pi\chi^2 \frac{\omega_R^2}{\omega^2} \times \int_0^{2\pi} d\theta I_q$$

where

$$I_q = \int_0^{\infty} q\ dq \quad \times \delta\left(\omega_0 + \frac{(q^2 + 2kqcos\theta)}{m}\right)$$

The integration over q can easily be solved using the following property of delta function

$$q\delta[f(q)] = \sum_i q_i \ \frac{\delta(q - q_i)}{|f'(q_i)|}$$

$$q\ \delta\left(\omega_0 + \frac{(q^2 + 2kqcos\theta)}{m}\right) = \frac{q}{|\frac{2k\cos(\theta)+2q}{m}|}\delta\left(q - \frac{1}{2}(-2k\cos(\theta) \pm \sqrt{2}\sqrt{k^2 - 2m\omega_0 + k^2\cos(2\theta)})\right)$$

Therefore,

$$I_{q\pm} = \int_0^{\infty} q\ dq \quad \times \delta\left(\omega_0 + \frac{(q^2 + 2kqcos\theta)}{m}\right)$$

$$= \int_0^{\infty} \ dq \ \frac{q}{\left|\pm\frac{2k\cos(\theta)+2q}{m}\right|}\delta\left(q - \frac{1}{2}\left(-2k\cos(\theta) \pm \sqrt{2}\sqrt{k^2 - 2m\omega_0 + k^2\cos(2\theta)}\right)\right)$$

$$= \frac{\frac{1}{2}\left(-2k\cos(\theta) \pm \sqrt{2}\sqrt{k^2 - 2m\omega_0 + k^2\cos(2\theta)}\right)}{\left|\frac{2k\cos(\theta)+2\times\frac{1}{2}\left(-2k\cos(\theta)\pm\sqrt{2}\sqrt{k^2-2m\omega_0+k^2\cos(2\theta)}\right)}{m}\right|} = \frac{-k\cos(\theta) \pm k\sqrt{\cos^2(\theta) - \frac{m\omega_0}{k^2}}}{2k\frac{\sqrt{\cos^2(\theta) - \frac{m\omega_0}{k^2}}}{m}}$$

Therefore, after integration over q, $\Gamma_{k,R}$ comes out to be

$$\Gamma^{\pm}_{k,R} = \frac{A}{(2\pi)^2}\pi\chi^2\frac{\omega_R^2}{\omega^2}\int_0^{2\pi} d\theta \times m\frac{-\sqrt{2}k\cos(\theta) \pm \sqrt{2}k\sqrt{\cos^2(\theta) - \frac{m\omega_0}{k^2}}}{2\sqrt{2}k\sqrt{\cos^2(\theta) - \frac{m\omega_0}{k^2}}}$$

This can also be written as,

$$\Gamma^{+}_{k,R} = \frac{A}{(2\pi)^2}\pi\chi^2\frac{\omega_R^2}{\omega^2} \times \frac{m}{2}\int_0^{2\pi} d\theta \times \frac{-\cos(\theta) + \sqrt{\cos^2(\theta) - \cos^2(\theta_k)}}{\sqrt{\cos^2(\theta) - \cos^2(\theta_k)}} \tag{B.23}$$

where,

$$\theta_k = Cos^{-1}\left(\sqrt{\frac{m\omega_0}{k^2}}\right)$$

The integration over θ in Eq. (B.23) will be valid only when both of the following conditions satisfied simultaneously,

$$\cos^2(\theta) > \cos^2(\theta_k); \qquad -\cos(\theta) + \sqrt{\cos^2(\theta) - \cos^2(\theta_k)} > 0$$

These two conditions are satisfied only some particular ranges of θ, these ranges of θ can be found by using Reduce route of Mathematica, that comes out to be,

$$\pi - \theta_k < \theta < \pi + \theta_k; \qquad 0 < \theta_k < \frac{\pi}{2}$$

Integrating over θ for the above ranges, we obtain

$$\Gamma^{+}_{k,R} = \frac{A}{(2\pi)^2}\pi\chi^2\frac{\omega_R^2}{\omega^2} \times \frac{m}{2} \times (\pi + 2\theta_k)$$

$$\Gamma^{-}_{k,R} = \frac{A}{(2\pi)^2}\pi\chi^2\frac{\omega_R^2}{\omega^2} \times \frac{m}{2} \times (\pi - 2\theta_k)$$

Therefore,

$$\Gamma_{k,R} = \Gamma^{+}_{k,R} + \Gamma^{-}_{k,R}$$

B.5 Electron-flexural phonon Hamiltonian

Mechanical deformations causes fictitious gauge field induced phonons known as flexural phonons. The relavant electronic and electron-phonon coupling Hamiltonians in one valley are given by

$$H_{el} = \frac{-1}{2m}\begin{pmatrix} 0 & p_-^2 \\ p_+^2 & 0 \end{pmatrix}, \qquad H_{el-ph} = \begin{pmatrix} 0 & F_3^{(+)} \\ F_3^{(+)\dagger} & 0 \end{pmatrix}$$

where, $p_\pm = p_x \pm ip_y$ and F_3^+ is the dominant coupling due to symmetric flexural deformations, given by

$$F_3^+ = g_3\left[\partial_y - i\partial_x\right] h^{(s)}$$

with $g_3 = \frac{3ac}{2\tilde{c}}\frac{\partial\gamma_3}{\partial\tilde{c}}$ the coupling strength. $h^{(s)}$ is a scalar field responsible for out-of-plane distortion.

$$h^{(s)}(\vec{r}) = \frac{1}{L}\sum_{\vec{q}} \xi_{\vec{q}}\; e^{i\vec{k}\cdot\vec{r}}(b_{\vec{q}} + b^\dagger_{-\vec{q}})$$

$$F_3 = g_3(\partial_y - i\partial_x) \times \frac{1}{L}\sum_{\vec{q}} \xi_{\vec{q}} e^{i\vec{q}\cdot\vec{r}}(b_{\vec{q}} + b^\dagger_{-\vec{q}}) = \frac{g_3}{L}\sum_{\vec{q}} \xi_{\vec{q}}(iq_y - iiq_x)e^{i\vec{q}\cdot\vec{r}}(b_{\vec{q}} + b^\dagger_{-\vec{q}})$$

$$= \frac{g_3}{L}\sum_{\vec{q}} \xi_{\vec{q}}(q_x + iq_y)e^{i\vec{q}\cdot\vec{r}}(b_{\vec{q}} + b^\dagger_{-\vec{q}}) = \frac{g_3}{L}\sum_{\vec{q}} \xi_{\vec{q}} q_+ e^{i\vec{q}\cdot\vec{r}}(b_{\vec{q}} + b^\dagger_{-\vec{q}})$$

$$H^{AB}_{el-ph} = \frac{g_3}{L}\sum_{\vec{q}} \xi_{\vec{q}} q_+ e^{i\vec{q}\cdot\vec{r}}(b_{\vec{q}} + b^\dagger_{-\vec{q}})$$

Similarly, we can also find H^{BA}_{el-ph}. In continuum limit,

$$H^{AB}_{e-ph} = \int \psi^\dagger F_3 \psi, \quad \psi(\vec{k}) = \frac{1}{L}\sum_{\vec{k}} e^{i\vec{k}\cdot\vec{r}}c, \quad \psi^\dagger(\vec{k}') = \frac{1}{L}\sum_{\vec{k}'} e^{-i\vec{k}'\cdot\vec{r}}c^\dagger$$

$$H^{AB}_{e-ph} = \int dr \frac{1}{L}\sum_{\vec{k}'} e^{-i\vec{k}'\cdot\vec{r}}c^\dagger(\vec{k}') \cdot \frac{g_3}{L}\sum_{\vec{q}} \xi_{\vec{q}} q_+ e^{i\vec{q}\cdot\vec{r}}(b_{\vec{q}} + b^\dagger_{-\vec{q}}) \cdot \frac{1}{L}\sum_{k} e^{i\vec{k}\cdot\vec{r}}c(\vec{k})$$

$$= \frac{g_3}{L}\sum_{\vec{k},\vec{k}',\vec{q}} \xi_{\vec{q}} q_+ (b_{\vec{q}} + b^\dagger_{-\vec{q}})c^\dagger(\vec{k}')c(\vec{k}) \cdot \left(\frac{1}{L^2}\int dr e^{i(\vec{k}-\vec{k}'+\vec{q})\cdot\vec{r}}\right)$$

$$= \frac{g_3}{L}\sum_{\vec{k},\vec{k}',\vec{q}} \xi_{\vec{q}} q_+ (b_{\vec{q}} + b^\dagger_{-\vec{q}})c^\dagger(\vec{k}')c(\vec{k}) \cdot \delta_{\vec{k}-\vec{k}'+\vec{q},0} = \frac{g_3}{L}\sum_{\vec{k},\vec{q}} \xi_{\vec{k}} q_+ (b_{\vec{q}} + b^\dagger_{-\vec{q}})c^\dagger(\vec{k}+\vec{q})c(\vec{k})$$

$$H^{AB}_{e-ph} = \frac{g_3}{L}\sum_{\vec{k},\vec{q}} q_+ X_{\vec{q}}(t)\xi_{\vec{q}} c^\dagger_{A1,0}(\vec{k},t)c_{B2,0}(\vec{k}-\vec{q},t)$$

where,

$$X_{\vec{q}} = (b_{\vec{q}} + b^{\dagger}_{-\vec{q}})$$

Bibliography

[1] Senese and Fred. Who discovered carbon? *Frostburg State University*, 2000. URL http://antoine.frostburg.edu/chem/senese/101/inorganic/faq/discovery-of-carbon.shtml.

[2] History of carbon. Retrieved 2013-01-10. URL http://www.caer.uky.edu/carbon/history/carbonhistory.shtml.

[3] S. Iijima. *J. Cryst. Growth*, **50**:675, 1980.

[4] S. Iijima. *Nature*, **354**:56, 1991.

[5] K. S. Novoselov, A. K. Geim, S. V. Morozov, D. Jiang, Y. Zhang, S. V. Dubonose, I. V. Grigorieva, and A. A. Firsov. *Science*, **306**:666, 2004.

[6] N. D. Mermin. *Phys. Rev.*, **176**:250, 1968.

[7] H. P. Boehm, R. Setton, and E. Stumpp. *Pure and Applied Chemistry*, **66**: 1893, 1994.

[8] H. P. Boehm, A. Clauss, G. O. Fischer, and U. Hofmann. *Zeitschrift für anorganische und allgemeine Chemie (in German)*, **316**:119, 1962.

[9] P. Debije and P. Scherrer. *Physikalische Zeitschrift (in German)*, **17**:277, 1916.

[10] W. Friedrich. *Physikalische Zeitschrift (in German)*, **14**:317, 1913.

[11] J. D. Bernal. *Proc. R. Soc. Lond.*, **A106**:749, 1924.

[12] P. R. Wallace. *Phys. Rev.*, **71**:622, 1947.

[13] K. S. Novoselov, A. K. Geim, S. V. Morozov, D. Jiang, M. I. Katsnelson, I. V. Grigorieva, S. V. Dubonose, and A. A. Firsov. *Nature (London)*, **438**: 197, 2005.

[14] V. P. Gusynin and S. G. Sharapov. *Phys. Rev. Lett.*, **95**:146801, 2005.

[15] Y. Zhang, Y. W. Tan, H. L. Stormer, and P. Kim. *Nature (London)*, **438**: 201, 2005.

[16] E. McCann and V. I. Fal'ko. *Phys. Rev. Lett.*, **96**:086805, 2006.

[17] E. McCann, D. S. L. Abergel, and V. I. Fal'ko. *Eup. Phys. J. Special Topics*, **148**:91, 2007.

[18] M. Mucha-Kruczynski, E. McCann, and V. I. Fal'ko. *Semicond. Sci. Technol.*, **25**:033001, 2006.

[19] L. M. Malard, J. Nilsson, D. C. Elias, J. C. Brant, F. Plentz, E. S. Alves, A. H. Castro, and M. A. Pimenta. *Phys. Rev. B*, **76**:201401 (R), 2007.

[20] H. Min, B. Sahu, S. Banerjee, and A. MacDonald. *Phys. Rev. B.*, **75**:155115, 2007.

[21] K. S. Novoselov, E. McCann, S. V. Mozorov, V. I. Fal'ko, M. I. Katsnelson, U. Zeitler, D. Jiang, F. Schedin, and A. K. Geim. *Nat. Phys.*, **2**:177, 2006.

[22] L. Min, R. Havden, P. Haung, M. Wojcik, A. D. Muller, and J. Park. *NanoLetters*, **12**:1609, 2012.

[23] F. Zhang, B. Sahu, H. Min, and A. H. MacDonald. *Phys. Rev. B*, **82**:035409, 2010.

[24] J. Jung and A. H. MacDonald. *Phys. Rev. B*, **88**:075408, 2013.

[25] A. H. MacDonald, J. Jung, and F. Zhang. *Phys. Scr.*, **T 146**:014012, 2012.

[26] G. M. Rutter, S. Jung, N. N. Klimov, D. B. Newell, N. B. Zhitenev, and J. A. Stroscio. *Nat. Phys.*, **7**:649, 2011.

[27] T. Taychatanapat and P. J.-Herrero. *Phys. Rev. Lett.*, **105**:166601, 2010.

[28] E. McCann. *Phys. Rev. B*, **74**:161403(R), 2006.

[29] T. Ohta, A. Bostwick, T. Seyller, K. Horn, and E. Rotenberg. *Science*, **313**: 951, 2006.

[30] Y. Zhang, Z. Jiang, J. P. Small, M. S. Purewal, Y. W. Tan, M. Fazcollahi, J. D. Chudow, J. A. Jaszczak, H. L. Stormer, and P. Kim. *Phys. Rev. Lett.*, **96**:136806, 2006.

[31] E. V. Castro, K. S. Novoselov, S. V. Morozov, N. M. R. Peres, J. M. B. Lopes dos Santos, J. Nilsson, F. Guinea, A. K. Geim, and A. H. Castro Neto. *Phys. Rev. Lett.*, **99**:216802, 2007.

[32] J. B. Oostinga, H. B. Heersche, X. Liu, A. F. Morpurgo, and L. M. K. Vandersypen. *Nat. Mater.*, **7**:151, 2007.

[33] J. Nilsson, A. H. Castro Neto, F. Guinea, and N. M. R. Peres. *Phys. Rev. B*, **76**:165416, 2007.

[34] A. B. Kuzmenko, E. van Heumen, D. van der Marel, P. Lerch, P. Blake, K. S. Novoselov, and A. K. Geim. *Phys. Rev. B*, **79**:115441, 2009.

[35] K. F. Mak, C. H. Lui, J. Shan, and T. F. Heinz. *Phys. Rev. Lett.*, **102**: 256405, 2009.

[36] M. Mucha-Kruczyński, D. S. L. Abergel, E. McCann, and V. I. Fal'ko. *J. Phys. Condens. Matter*, **21**:344206, 2009.

[37] Y. Zhang, T-Ta Tang, C. Girit, Z. Hao, M. C. Martin, A. Zettl, M. F. Crommie, Y. R. Shen, and F. Wang. *Nat. Lett.*, **459**:820, 2009.

[38] W. J. Yu and X. Duan. *Scientific Reports*, **3**:1248, 2013.

[39] K. S. Kim, A. L. Walter, L. Moreschini, T. Seyller, K. Horn, E. Rotenberg, and A. Bostwick. *Nat. Mater.*, **12**:887, 2013.

[40] S. Ulstrup, J. Christian, F. Cilento, J. A. Miwa, A. Crepaldi, M. Zacchigna, C. Cacho, R. chapman, E. Springate, S. Mammadov, F. Fromm, C. Raidel, T. Seyller, F. Parmigiani, M. Grioni, P. D. C. king, and P. Hofmann. *Phys. Rev. Lett.*, **112**:257401, 2014.

[41] L. Perfetti. *Physics*, **7**:68, 2014.

[42] A. H. Castro Neto, F. Guinea, N. M. R. Peres, K. S. Novoselov, and A. K. Geim. *Rev. Mod. Phys.*, **81**:109, 2009.

[43] S. B. Trickey, F. Müller-Plathe, G. H. F. Diercksen, and J.C. Boettger. *Phys. Rev. B*, **45**:4460, 1992.

[44] K. Yoshizawa, T. Kato, and T. Yamabe. *J. Chem. Phys.*, **105**:2099, 1996.

[45] T. Yumura and K. Yoshizawa. *Chem. Phys.*, **279**:111, 2002.

[46] E. McCann and M. Koshino. *Rep. Prog. Phys.*, **76**:056503, 2013.

[47] R. Saito, M. S. Dresselhaus, and G. Dresselhaus. *Physical Properties of Carbon Nanotubes (London: Imperial College Press)*, 1998.

[48] N. W. Ashcroft and N. D. Mermin. *Solid State Physics*, Harcourt Brace, FortWorth, 1976.

[49] C. Kittel. *Introduction to Solid State Physics*, 7th edition, John Wiley and Sons, Singapore, 1996.

[50] A. J. Dekker. *Solid State Physics*, Prentice-Hall, 1958.

[51] J. C. Slonczewski and P. R. Weiss. *Phys. Rev.*, **109**:272, 1958.

[52] G. W. Semenoff. *Phys. Rev. Lett.*, **53**:2449, 1984.

[53] S. Reich, J. Maultzsch, and C. Thomsen. *Phys. Rev. B*, **66**:035412, 2002.

[54] Y. Hasegawa, R. Konno, H. Nakano, and M. Kohmoto. *Phys. Rev. B*, **74**: 033413, 2006.

[55] B. Partoens and F. M. Peeters. *Phys. Rev. B*, **74**:075404, 2006.

[56] C. Bena and G. Montambaux. *New J. Phys.*, **11**:095003, 2009.

[57] A. J. Leggett. *Lecture 5: Graphene I: Electronic band structure and Dirac fermions*. URL `http://media.iqc.ca/lectures/Leggett-2010/notes/lecture-5.pdf`.

[58] URL `https://www.tfkp.physik.uni-erlangen.de/download/research/DW-derivation.pdf`.

[59] J. W. McClure. *Phys. Rev.*, **108**:612, 1957.

[60] J. W. McClure. *Phys. Rev.*, **119**:606, 1960.

[61] Z. Q. Li, E. A. Henriksen, Z. jiang, Z. Hao, M. C. Martin, P. Kim, H. L. Stormer, and D. N. Basov. *Phys. Rev. Lett.*, **102**:037403, 2009.

[62] L. M. Zhang, Z. Q. Li, D. N. Basov M. M. Fogler, Z. Hao, and M. C. Martin. *Phys. Rev. B*, **78**:235408, 2008.

[63] M. S. Dresselhaus and G. S. Dresselhaus. *Adv. Phys.*, **51**:1, 2002.

[64] J. Nilsson, A. H. Castro Neto, F. Guinea, and N. M. R. Peres. *Phys. Rev . B*, **78**:045405, 2008.

[65] F. Guinea, A. H. Castro Neto, and N. M. R. Peres. *Phys. Rev . B*, **73**: 245426, 2006.

[66] E. McCann, D. S. L. Abergel, and V. I. Fal'ko. *Solid state Commun.*, **143**: 110, 2007.

[67] F. Guinea, A. H. Castro Neto, and N. M. R. Peres. *Solid state Commun.*, **143**:116, 2007.

[68] F. Guinea, A. H. Castro Neto, and N. M. R. Peres. *Eup. Phys. J. Spec. Top.*, **148**:117, 2007.

[69] M. Mucha-Kruczyński, A. Grishin O. Tsyplyatyev, E. McCann, V. I. Fal'ko A. Bostwick, and E. Rotenberg. *Phys. Rev. B*, **77**:195403, 2008.

[70] E. A. Henriksen, Z. Jiang, L-C. Tung, M. E. Schwartz, M. Takita, Y-J. Wang, P. Kim, and H. L. Stormer. *Phys. Rev. Lett.*, **100**:087403, 2008.

[71] A. B. Kuzmenko, I. Crassee, D. Van der Marel, P. Blake, and K. S. Novoselov. *Phys. Rev. B*, **80**:165406, 2009.

[72] A. Deshpande, W. Bao, Z. Zhao, C. N. Lau, and B. J. LeRoy. *Appl. Phys. Lett*, **95**:243502, 2009.

[73] L. Jing, J. Jr. Velasco, P. Kratz, G. Liu, W. Z. Bao, M. Bockrath, and C. N. Lau. *Nano. Lett.*, **10**:4000, 2010.

[74] J. Yan and M. S. Furher. *Nano. Lett.*, **10**:4521, 2010.

[75] R. C. Tatar and S. Rabii. *Phys. Rev. B*, **25**:4126, 1982.

[76] J.-C. Charlier, X. Gonze, and J.-P. Michenaud. *Phys. Rev. B*, **43**:4579, 1991.

[77] M. Inoue. *J. Phys. Soc. Japan*, **17**:808, 1962.

[78] O. P. Gupta and P. R. Wallace. *Phys. Stat. Sol. B*, **54**:53, 1972.

[79] G. Dresselhaus. *Phys. Rev. B*, **10**:3602, 1974.

[80] K. Nakao. *J. Phys. Soc. Japan*, **40**:761, 1976.

[81] K.-I. Sasaki and R. Saito. *Prog. Theor. Phys. Supplement*, **176**:253, 2008.

[82] C.-H. Park and N. Marzari. *Phys. Rev. B*, **84**:205440, 2011.

[83] S. Bae, H. Kim, Y. Lee, X. Xu, J.-S. Park, Y. Zheng, J. Balakrishnan, T. Lei, H. R. Kim, Y. I. Song, Y.-J. Kim, K. S. Kim, B. Özyilmaz, J.-H. Ahn, B. H. Hong, and S. Iijima. *Nature Nanotech.*, **5**:574, 2010.

[84] K. S. Novoselov, D. Jiang, F. Schedin, T. J. Booth, V. V. Khotkevich, S. V. Morozov, and A. K. Geim. *Proc. Natl Acad. Sci. USA*, **102**:10451, 2005.

[85] C. Casiraghi, A. Hartschuh, E. Lidorikis, H. Qian, H. Harutyunyan, T. Gokus, K. S. Novoselov, and A. C. Ferrari. *Nano. Lett.*, **7**:2711, 2007.

[86] I. Forbeaux, J.-M. Themlin, and J.-M. Debever. *Phys. Rev. B*, **58**:16396, 1998.

[87] Z. G. Cambaz, Gleb Yushin, S. Osswald, V. Mochalin, and Y. Gogotsi. *Carbon*, **46**:841, 2008.

[88] C. Enderlein. *Dissertation*, Graphene and its Interaction with Different Substrates Studied by Angular-Resolved Photoemission Spectroscopy:Freie Universitaet Berlin, 2010.

[89] K. S. Kim, Y. Zhao, H. Jang, S. Y. Lee, J. M. Kim, K. S. Kim J.-H. Ahn P. Kim, J.-Y. Choi, and B. H. Hong. *Nature*, **457**:706, 2009.

[90] X. Li, W. Cai, J. An, S. Kim, J. Nah, D. Yang, R. Piner, A. Velamakanni, I. Jung, E. Tutuc, S. K. Banerjee, L. Colombo, and R. S. Ruoff. *Science*, **324**:1312, 2009.

[91] URL http://www.physik.fu-berlin.de/einrichtungen/ag/ag-reich/lehre/Archiv/ss2011/docs/Nils_Krane-Handout.pdf?1359120846.

[92] A. K. Geim and K. S. Novoselov. *Nat. Mater.*, **6**:183, 2007.

[93] A. S. Mayorov. *Nano. Lett.*, **11**:2396, 2011.

[94] S. V. Morozov, K. S. Novoselov, M. I. Katsnelson, F. Schedin, D. C. Elias, J. A. Jaszczak, and A. K. Geim. *Phys. Rev. Lett.*, **100**:016602, 2008.

[95] K. I. Bolotin, K. J. Sikes, Z. Jiang, D. M. Klima, G. Fudenberg, J. Hone, P. Kim, and H. L. Stormer. *Solid State Commu.*, **146**:351, 2008.

[96] X. Du, I. Skachko, A. Barker, and E. Y. Andrei. *Nat. Nanotechnol.*, **3**:491, 2008.

[97] W. Zhu, V. Perebeinos, M. Freitag, and P. Avouris. *Phys. Rev. B*, **80**:235402, 2009.

[98] J.-C. Charlier, P. C. Eklund, J. Zhu, and A. C. Ferrari. Electron and Phonon Properties of Graphene: Their Relationship with Carbon Nanotubes:Berlin/Heidelberg: Springer–Verlag, 2008.

[99] J.-H. Chen, C. Jang, S. Xiao, M. Ishigami, and M. S. Fuhrer. *Nat. Nanotechnol.*, **3**:206, 2008.

[100] A. Akturk and N. Goldsman. *J. Appl. Phys.*, **103**:053702, 2008.

[101] F. V. Kusmartsev, W. M. Wu, M. P. Pierpoint, and K. C. Yung. *arxiv:1406.0809*, **3**, 2014.

[102] J.-H. Chen, C. Jang, S. Adam, M. S. Fuhrer, E. D. Williams, and M. Ishigami. *Nat. Phys.*, **4**:377, 2008.

[103] X. Li, K. M. Borysenko, M. B. Nardelli, and K. W. Kim. *Phys. Rev. B*, **84**: 195453, 2011.

[104] R. E. Prange and S. M. Girvin. *The Quantum Hall Effect (Springer, New York)*, 1990.

[105] A. H. MacDonald. *Quantum Hall Effect: A Perspective (Kluwer Academic, Dordrecht)*, 1990.

[106] K. I. Bolotin, F. Ghahari, M. D. Shulman, H. L. Stormer, and P. Kim. *Nature*, **462**:196, 2009.

[107] C. R. Dean, A.F. Young, P. Cadden-Zimansky, and L. Wang. *Nat. Phys.*, **7**: 693, 2011.

[108] M. R. Peterson and C. Nayak. *Phys. Rev. Lett.*, **113**:086401, 2014.

[109] D.-K. Ki, D. A. Abanin V. I. Fal'ko, and A. F. Morpurgo. *Nano. Lett.*, **14**: 2135, 2014.

[110] A. Kou, B. E. Feldman, A. J. Levin, B. I. Halperin, K. Watanabe, T. Taniguchi, and A. Yacoby. *Sciencexpress Report*, **345**:55, 2014.

[111] Yu. A. Bychkov and É. I. Rashba. *Pis'ma. Zh. Eksp. Teor. Fiz*, **39**:66, 1984.

[112] Z. Qiao, S. A. Yang, W. Feng, W.-K. Tse, J. Ding, Y. G. Yao, J. Wang, and Q. Niu. *Phys. Rev. B*, **82**:161414(R), 2010.

[113] W.-K. Tse, Z. Qiao, Y. Yao, A. H. MacDonald, and Q. Niu. *Phys. Rev. B*, **83**:155447, 2011.

[114] C. L. Kane and E. J. Mele. *Phys. Rev. Lett.*, **95**:226801, 2005.

[115] D. A. Abanin, R. V. Gorbachev, K. S. Novoselov, A. K. Geim, and L. S. Levitov. *Phys. Rev. Lett.*, **107**:096601, 2011.

[116] A. Ferreira, T. G. Rappoport, M. A. Cazalilla, and A. H. Castro Neto. *Phys. Rev. Lett.*, **112**:066601, 2014.

[117] J. Balakrishnan, G. K. W. Koon, A. Avsar, Y. Ho, J. H. Lee, M. Jaiswal, S.-J. Baeck, J.-H. Ahn, A. Ferreira, M. A. Cazalilla, A. H. Castro Neto, and B. Özyilmaz. *Nat. Commun.*, **5**:4748, 2014.

[118] E. Prada, P. San-Jose, L. Brey, and H.A. Fertig. *Solid State Commun.*, **151**: 1075, 2011.

[119] P. Maher, C. R. Dean, A. F. Young, T. Taniguchi, K. Watanabe, K. L. Shepard, J. Hone, and P. Kim. *Nat. Phys.*, **9**:154, 2013.

[120] A. Dyrdał and Józef Barnaś. *Solid State Commun.*, **188**:27, 2014.

[121] A. B. Kuzmenko, E. V. Heumen, F. Carbone, and D. V. D. Marel. *Phys. Rev. Lett.*, **100**:117401, 2008.

[122] J. Liu, A. R. Wright, C. Zhang, and Z. Ma. *Appl. Phys. Lett.*, **93**:041106, 2008.

[123] Q. Bao, H. Zhang, Y. Wang, Z. Ni, Y. Yan, Ze X. Shen, K. P. Loh, and D. Y. Tang. *Advanced Functional Materials*, **19**:3077, 2009.

[124] H. Zhang, Y. D. Tang, L. M. Zhao, Q. L. Bao, and K. P. Loh. *Optics Express*, **17**:17630, 2009.

[125] H. Zhang, Q. Bao, Y. D. Tang, L. Zhao, and K. P. Loh. *Appl. Phys. Lett.*, **95**:141103, 2009.

[126] H. Zhang, Y. D. Tang, R. J. Knize, L. Zhao, Q. Bao, and K. P. Loh. *Appl. Phys. Lett.*, **96**:111112, 2010.

[127] U. Kurum, B. Liu, K. Zhang, Y. Liu, and H. Zhang. *Appl. Phys. Lett.*, **98**: 141103, 2011.

[128] Z. Zheng, C. Zhao, S. Lu, Y. Chen, Y. Li, H. Zhang, and S. Wen. *Optics Express*, **20**:23201, 2012.

[129] H. Zhang, S. Virally, Q. Bao, K. P. Loh, S. Massar, N. Godbout, and P. Kockaert. *Optics Letters*, **37**:1856, 2012.

[130] V. P. Gusynin and S. G. Sharapov. *Phys. Rev. B*, **73**:245411, 2006.

[131] V. P. Gusynin, S. G. Sharapov, and J. P. Carbotte. *New J. Phys.*, **11**:095013, 2009.

[132] V. P. Gusynin, S. G. Sharapov, and J. P. Carbotte. *Phys. Rev. B*, **75**:165407, 2007.

[133] V. P. Gusynin, S. G. Sharapov, and J. P. Carbotte. *J. Phys. Condens. Matter*, **19**:026222, 2007.

[134] V. P. Gusynin, S. G. Sharapov, and J. P. Carbotte. *Phys. Rev. Lett.*, **98**: 157402, 2007.

[135] M. Koshino and T. Ando. *Phys. Rev. B*, **77**:115313, 2008.

[136] M. V. Strikha and F. T. Vasko. *Phys. Rev. B*, **81**:115413, 2010.

[137] V. P. Gusynin, S. G. Sharapov, and J. P. Carbotte. *Phys. Rev. Lett.*, **96**: 256802, 2002.

[138] T. Ando, Y. Zheng, , and H. Suzuura. *J. Phys. Soc. Jpn.*, **71**:1318, 2002.

[139] L. A. Falkovsky and A. A. Varlamov. *Eur. Phys. J. B*, **56**:281, 2007.

[140] T. Stauber, N. M. R. Peres, , and A. H. Castro Neto. *Phys. Rev. B*, **78**: 085418, 2008.

[141] V. P. Gusynin, S. G. Sharapov, , and J. P. Carbotte. *Int. J. Mod. Phys. B*, **21**:4611, 2007.

[142] Z. Q. Li, E. A. Henriksen, Z. Jiang, Z. Hao, M. C. Martin, P. Kim, H. L. Stormer, and D. N. Basov. *Nat. Phys.*, **4**:532, 2008.

[143] R. R. Nair, P. Blake, A. N. Grigorenko, K. S. Novoselov, T. J. Booth, T. Stauber, N. M. R. Peres, and A. K. Geim. *Science*, **320**:1308, 2008.

[144] K. F. Mak, M. Y. Sfeir, Y. Wu, C. H. Lui, J. A. Misewich, and T. F. Heinz. *Phys. Rev. Lett.*, **101**:196405, 2008.

[145] E. J. Nicol and J. P. Carbotte. *Phys. Rev. B*, **77**:155409, 2008.

[146] D. S. L. Abergel and V. I. Fal'ko. *Phys. Rev. B*, **75**:155430, 2007.

[147] M. Koshino and E. McCann. *Phys. Rev. B*, **79**:125443, 2009.

[148] D. S. L. Abergel, A. Russel, and V. I. Falko. *Appl. Phys. Lett.*, **91**:063125, 2007.

[149] X. Wang, M. Zhao, and D. D. Nolte. *Phys. Rev. B*, **95**:081102, 2009.

[150] R. W. Boyd. *Nonlinear Optics*, page Academic Press, 2008.

[151] L. Allen and J. H. Eberly. *Optical Resonances and Two-Level Atoms*, page Wiley and Sons, 1975.

[152] H. Haug and S. W. Koch. *Quantum Theory of Optical and Electronic Properties of Semiconductors*, page World Scientific, 2004.

[153] C. Gerry and P. Knight. *Introductory Quantum Optical*, page Cambridge University Press, 2005.

[154] L. Mandel and E. Wolf. *Optical Coherence and Quantum Optics*, page Cambridge University Press, 1995.

[155] P. Blake, E. W. Hill1, A. H. Castro Neto, K. S. Novoselov, D. Jiang, R. Yang, T. J. Booth, and A. K. Geim. *Appl. Phys. Lett.*, **91**:063124, 2007.

[156] Y. Y. Wang, Z. H. Ni, Z. X. Shen, H. M. Wang, and Y. H. Wu. *Appl. Phys. Lett.*, **92**:043121, 2008.

[157] J. S. Park, A. Reina, R. Saito, J. Kong, G. Dresselhaus, and M.S. Dresselhau. *Carbon*, **47**:1303, 2009.

[158] D. Graf et al. *Eur. Phys. J. Spl. Top.*, **148**:171, 2007.

[159] Y. Y. Wang, Z. h. Ni, T. Yu, Z. X. Shen, H. M. Wang, Y. H. Wu, W. Chen, and A. T. S. Wee. *J. Phys. Chem.*, **C112**:10637, 2008.

[160] Z. H. Ni, W. Chen, X. F. Fan, J. L. Kuo, T. Yu, A. T. S. Wee, and Z. X. Shen. *Phys. Rev. B*, **77**:115416, 2008.

[161] A. C. Ferrari, J. C. Meyer, V. Scardaci, C. Casiraghi, M. Lazzeri, F. Mauri, S. Piscanec, D. Jiang, K. S. Novoselov, S. Roth, and A. K. Geim. *Phys. Rev. Lett.*, **97**:187401, 2006.

[162] S. Pisana, M. Lazzeri, C. Casiraghi, K. S. Novoselov, A. K. Geim, A. C. Ferrari, and F. Mauri. *Nat. Mater.*, **6**:198, 2007.

[163] J. M. Dawlaty, S. Shivaramam, M. Chandrashekhar, F. Rana, and M. G. Spencer. *Appl. Phys. Lett.*, **92**:042116, 2008.

[164] P. A. George, J. Strait, J. M. Dawlaty, S. Shivaraman, M. Chandrashekhar, F. Rana, and M. G. Spencer. *Nano Lett.*, **8**:4248, 2008.

[165] S. Kumar, M. Anija, N. Kamaraju, K. S. Vasu, K. S. S. yam, A. K. Sood, and C. N. R. Rao. *Appl. Phys. Lett.*, **95**:191911, 200p.

[166] J. Shang, Z. Luo, C. Cong, J. Lin, T. Yu, and G. G. Gurzadyan. *Appl. Phys. Lett.*, **97**:163103, 2010.

[167] B. A. Ruzicka, L. K. Werake, H. Zhao, S. Wang, and K. P. Loh. *Appl. Phys. Lett.*, **96**:173106, 2010.

[168] H. Wang, J. H. Strait, Paul A. George, S. Shivaraman, V. B. Shields, M. Chandrashekhar, J. Hwang, F. Rana, M. G. Spencer, C. S. Ruiz-Vargas, and J. Park. *Appl. Phys. Lett.*, **96**:081917, 2010.

[169] M. Breusing, S. Kuehn, T. Winzer, E. Malić, F. Milde, N. Severin, J. P. Rabe, C. Ropers, A. Knorr, and T. Elsaesser. *Phys. Rev. B*, **83**:153410, 2011.

[170] URL `http://en.wikipedia.org/wiki/Graphene#cite_note-208`.

[171] Graphene Uses and Applications. URL http://www.graphenea.com/pages/graphene-uses-applications#.VJlPtP_AA.

[172] M. A. Rafiee, J. Rafiee, Z. Wang, H. Song, Z. Z. Yu, and N. Koratkar. *ACA Nano*, **3**:3884, 2009.

[173] Applied Graphene Materials Web site: Graphene dispersions. URL http://www.appliedgraphenematerials.com/products/graphene-dispersions/.

[174] I. I. Rabi. *Phys. Rev.*, **51**:652, 1937.

[175] E. G. Mishchenko. *Phys. Rev. Lett.*, **103**:246802, 2009.

[176] B. Dóra, K. Ziegler, P. Thalmeier, and M. Nakamura. *Phys. Rev. Lett.*, **102**:036803, 2009.

[177] P. N. Romanets and F. T. Vasko. *Phys. Rev. B*, **81**:241411(R), 2010.

[178] H. K. Avetissian, A. K. Avetissian, G. F. Mkrtchian, and Kh. V. Sedrakian. *Phys. Rev. B*, **85**:115443, 2012.

[179] H. K. Avetissian, G. F. Mkrtchian, K. G. Batrakov, S. A. Maksimenko, and A. Hoffmann. *Phys. Rev. B*, **88**:165411, 2013.

[180] F. Kadi and E. Malic. *Phys. Rev. B*, **89**:045419, 2014.

[181] K. L. Ishikawa. *Phys. Rev. B*, **82**:201402(R), 2010.

[182] Y. S. Ang, S. Sultan, and C. Zhang. *Appl. Phys. Lett.*, **97**:243110, 2010.

[183] A. R. Wright, J. C. Cao, and C. Zhang. *Phys. Rev. Lett.*, **103**:207401, 2009.

[184] Enamullah, V. Kumar, and G. S. Setlur. *Physica B*, **407**:4600, 2012.

[185] B. Partoens and F. M. Peeters. *Phys. Rev. B*, **75**:193402, 2007.

[186] M. Koshino and E. McCann. *Phys. Rev. B*, **83**:165443, 2011.

[187] V. Kumar, Enamullah, U. Kumar, and Girish S. Setlur. *Pramana- J. Phys.*, **83**:597, 2014.

[188] S. Y. Zhou, G. H. Gweon, A. V. Fedorov, P. N. First, W. A. de Heer, D.H. Lee, F. Guinea, A. H. Castro Neto, and A. Lanzara. *Nat. Mater.*, **6**:770, 2007.

[189] S. A. Jafari. *J. Phys.: Condens. Matter*, **24**:205802, 2012.

[190] R. Quhe, J. Zheng, G. Luo, Q. Liu, R. Qin, J. Zhou, D. Yu, S. Nagase, W. N. Mei, Z. Gao, and J. Lu. *NPG Asia Mater.*, **4**, 2012.

[191] M. Mucha-Kruczyński, D. S. L. Abergel, E. McCann, and V. I. Fal'ko. *J. Phys.: Condens. Matter*, **21**:344206, 2009.

[192] M. Mucha-Kruczyński, E. McCann, and V. I. Fal'ko. *Semicond. Sci. Technol.*, **25**:033001, 2010.

[193] A. Qaiumzadeh and R. Asgari. *New J. Phys.*, **11**:095023, 2009.

[194] T. G. Pedersen, A. P. Jauho, and K. Pedersen. *Phys. Rev. B*, **79**:113406, 2009.

[195] C. Triola and E. Rossi. *Phys. Rev. B*, **86**:161408(R), 2012.

[196] A. Varykhalov, D. Marchenko, J. S. Barriga, M. R. Scholz, B. Verberck, B. Trauzettel, T. O. Wehling, C. Carbone, and O. Rader. *Phys. Rev. X*, **2**: 041017, 2012.

[197] S. Y. Zhou, D. A. Siegel, A. V. Fedorov, and A. Lanzara. *Physica E*, **40**: 2642, 2008.

[198] G. Giovannetti, P. A. Khomyakov, G. Brocks, P. J. Kelly, and J. van der Brink. *Phys. Rev. B*, **76**:073103, 2007.

[199] A. Grüneis and D. V. Vyalikh. *Phys. Rev. B*, **77**:193401, 2008.

[200] A. Grüneis, K. Kummer, and D. V. Vyalikh. *New J. Phys.*, **11**:073050, 2009.

[201] D. A. Siegel, S. Y. Zhou, F. El. Gabaly, A. V. Fedorov, A. K. Schmid, and A. Lanzara. *Appl. Phys. Lett.*, **93**:243119, 2008.

[202] S. Y. Zhou, D. A. Siegel, A. V. Fedorov, and F. El Gabaly et al. *Nat. Mater.*, **7**:259, 2008.

[203] S. Kim, J. Ihm, H. J. Choi, and Y. Son. *Phys. Rev. Lett.*, **100**:176802, 2008.

[204] V. Kumar, Enamullah, Upendra Kumar, and Girish S. Setlur. *Physica B: Condensed Matter*, **436**:140, 2014.

[205] M. Koshino and T. Ando. *Phys. Rev. B*, **73**:245403, 2006.

[206] J. Cserti, A. Csordás, and G. Dávid. *Phys. Rev. Lett.*, **99**:113110, 2007.

[207] J. M. B. Lopes dos Santos, N. M. R. Peres, and A. H. Castro Neto. *Phys. Rev. Lett.*, **99**:256802, 2007.

[208] G. Li, A. Luican, J. M. B. Lopes dos Santos, A. Reina A. H. C. Neto, J. Kong, and E. Andrei. *Nat. Phys.*, **6**:109, 2009.

[209] A. Luican, G. Li, A. Reina, J. Kong, R. Nair, K. S. Novoselov, A. K. Geim, and E Andrei. *Phys. Rev. Lett.*, **106**:126802, 2011.

[210] W. Yan, M. Lui, R. F. Dou, L. Meng, L. Feng, Z. D. Chu, Y. F. Zhang, Z. F. Lui, J. C. Nie, and L. He. *Phys. Rev. Lett.*, **109**:126801, 2012.

[211] M. S. Dresselhaus and G. Dresselhaus. *Adv. Phys.*, **51**:1, 2002.

[212] E. I. Rashba. *Phys. Rev. B*, **79**:161409(R), 2009.

[213] P. Rakyta, A. Kormányos, and J. Cserti. *Phys. Rev. B*, **82**:113405, 2010.

[214] R. de Gail, M. O. Goerbig, F. Guinea, G. Montambaux, and A. H. Castro Neto. *Phys. Rev. B*, **84**:045436, 2011.

[215] Y. H. Wen, Z. D. Chu, and L Hi. *Phys. Rev. Lett.*, **111**:066803, 2013.

[216] V. Kumar, Enamullah, U. Kumar, and G. S. Setlur. *Eup. Phys. J. B*, **87**: 70, 2014.

[217] A. R. Wright and C. Zhang. *Phys. Rev. B*, **81**:165413, 2010.

[218] M. A. Pimenta, A. Marucci, S. A. Empedocles, M. G. Bawendi, E. B. Hanlon, A. M. Rao, P. C. Eklund, R. E. Smalley, G. Dresselhaus, and M. S. Dresselhaus. *Phys. Rev. B*, **58**:16016 (R), 1998.

[219] J. Maultzsch, S. Reich, C. Thomsen, H. Requardt, and P. Ordejon. *Phys. Rev. Lett.*, **92**:075501, 2004.

[220] S. Piscanec, M. Lazzeri, F. Mauri, A. C. Ferrari, , and J. Robertson. *Phys. Rev. Lett.*, **93**:185503, 2004.

[221] E. H. Hwang and S. Das Sarma. *Phys. Rev. B*, **77**:115449, 2008.

[222] T. Ando and M. Koshino. *JPSJ*, **78**:034709, 2009.

[223] T. Ando. *JPSJ*, **75**:124701, 2006.

[224] L. M. Malard, D. C. Elias, E. S. Alves, and M. A. Pimenta. *Phys. Rev. Lett.*, **101**:257401, 2008.

[225] T.-T. Tang, Y. Zhang, C.-H. Park, B. Geng, C. Girit, Z. Hao, M. C. Martin, A. Zettl, M. F. Crommie, S. G. Louie, Y. R. Shen, and F. Wang. *Nat. Nanotech.*, **5**:32, 2010.

[226] K. Ishikawa and T. Ando. *J. Phys. Soc. Jpn.*, **75**:084713, 2006.

[227] H. Suzuura and T. Ando. *J. Phys. Soc. Jpn.*, **77**:044703, 2008.

[228] E. Mariani and F. V. Oppen. *Phys. Rev. Lett.*, **100**:076801, 2008.

[229] H. Suzuura and T. Ando. *Phys. Rev. B*, **65**:235412, 2002.

[230] S. S. Kubakaddi. *Phys. Rev. B*, **79**:075417, 2009.

[231] R. Bistritzer and A. H. macDonald. *Phys. Rev. Lett.*, **102**:206410, 2009.

[232] J. K. Viljas and T. T. Heikkila. *Phys. Rev. B*, **81**:245404, 2010.

[233] M. Mucha-Kruczyńnski, I. L. Aleiner, and V. I. Fal'ko. *Phys. Rev. B*, **84**: 041404(R), 2011.

[234] E. Mariani and F. V. Oppen. *Phys. Rev. Lett.*, **100**:249901, 2008.

[235] E. Mariani and F. V. Oppen. *Phys. Rev. B*, **80**:155411, 2009.

[236] E. Mariani and F. V. Oppen. *Phys. Rev. B*, **82**:195403, 2010.

[237] L. M. Woods and G. D. Mahan. *Phys. Rev. B*, **61**:10651, 2000.

[238] Y.-W. Son, S.-M. Choi, Y. P. Hong, S. Woo, and S.-H. Jhi. *Phys. Rev. B*, **84**:155410, 2011.

[239] E. Mariani, A. J. Pearce, and F. Von Oppen. *Phys. Rev. B*, **86**:165448, 2012.

[240] A. J. Pearce, F. Cavaliere, and E. Mariani. *J. Phys.: Condens. Matter*, **25**: 375301, 2013.

[241] L. D. Landau and E. M. Lifshitz. *Theroy of Elasticity*, Pergamon:New yark, 1986.

[242] V. Kumar and G. S. Setlur. *Phonon Assisted Damping of Anomalous Rabi Oscillations in graphene systems*, Manuscript to be communicated.

Publications

Journal publications:

1. *Coherent non-linear electromagnetic response in twisted bilayer and few-layer graphene.*
   Vipin Kumar, Enamullah, Upendra Kumar and Girish S. Setlur, ***Pramana J. Phys.*** **83**, 597-617 (2014)
   http://link.springer.com/article/10.1007%2Fs12043-014-0808-4

2. *Coherent non-linear optical response in SU(2) symmetry broken single and bilayer graphene.*
   Vipin Kumar, Enamullah, Upendra Kumar and Girish S. Setlur, ***Physica B*** **436**, 140-148 (2014).
   http://dx.doi.org/10.1016/j.physb.2013.12.002

3. *Band structure effects on the nonlinear optical response of bilayer graphene.*
   Vipin Kumar, Enamullah, Upendra Kumar and Girish S. Setlur, ***Eup. Phys. J. B*** **87**, 70 (2014).
   http://dx.doi.org/10.1140/epjb/e2014-40887-8

4. *Nonlinear optical response of asymmetric monolayer graphene.*
   Vipin Kumar, Enamullah and Girish S. Setlur, ***Phys. Express*** **4**, 4 (2014). (Special Issue)
   http://www.cognizure.com/abstract.aspx?p=106637304

5. *Anomalous Rabi oscillations of AB and ABC- stacked graphene.*
   Vipin Kumar, Enamullah, Upendra Kumar and Girish S. Setlur, ***J. Nanosci. Lett.*** **4**, 32 (2014). (Special Issue)
   http://www.cognizure.com/abstract.aspx?p=109637320

6. *A theoretical study of pump-probe experiment in single layer, bilayer and multilayer graphene.*
   Enamullah, **Vipin Kumar**, Upendra Kumar and Girish S. Setlur, ***Pramana J. Phys.*** **82**, 6 (2014).
   http://dx.doi.org/10.1007/s12043-014-0756-z

7. *Quantum Rabi oscillations in graphene.*
   Enamullah, **Vipin Kumar**, Upendra Kumar and Girish S. Setlur, ***J. Opt. Soc. Am. B*** **31**, 3 (2014).
   http://dx.doi.org/10.1364/JOSAB.31.000484

8. *Linear optical response of highly non-equilibrium graphene.*
   Enamullah, **Vipin Kumar**, Upendra Kumar and Girish S. Setlur, ***J. Nanosci. Lett.*** **4**, 33 (2014). (Special Issue)
   http://www.cognizure.com/abstract.aspx?p=109637319

9. *Strain Effect on the Nonlinear Electromagnetic Response of 2D Carbon Based Material*
   Enamullah, **Vipin Kumar**, Upendra Kumar and Girish S. Setlur, ***Adv. Sci. Lett.*** **20**, 1459 (2014).
   http://dx.doi.org/10.1166/asl.2014.5523

10. *Band-anisotropy induced Bloch-Siegert shift in graphene.*
    Upendra Kumar, **Vipin Kumar**, Enamullah and Girish S. Setlur, ***J. Opt. Soc. Am. B*** **31**, 3042 (2014).
    http://www.opticsinfobase.org/josab/abstract.cfm?uri=josab-31-12-3042

11. *Cross-over of coherent Rabi oscillations in graphene.*
    Enamullah, **Vipin Kumar** and Girish S. Setlur, ***Physica B*** **407**, 4600 (2012).
    http://dx.doi.org/10.1016/j.physb.2012.08.005

12. *Phonon assisted damping of anomalous Rabi oscillations in graphene systems.*
    Vipin Kumar and Girish S. Setlur. (**Manuscript to be submitted**)

Conference proceedings:

1. **Vipin Kumar**, Enamullah and Girish S. Setlur, AIP Conf. Proc. **1591**, 1406 (2014).
   http://dx.doi.org/10.1063/1.4872975
2. **Vipin Kumar**, Enamullah and Girish S. Setlur, AIP Conf. Proc. **1536**, 351 (2013).
   http://dx.doi.org/10.1063/1.4810245
3. **Vipin Kumar**, Enamullah, Upendra Kumar and Girish S. Setlur, AIP Conf. Proc. **1536**, 266 (2012).
   http://dx.doi.org/10.1063/1.4810071


भारतीय प्रौद्योगिकी संस्थान गुवाहाटी
Indian Institute of Technology Guwahati

Vitae

Mr. Vipin Kumar, born in Uttar Pradesh, India, he received his B.Sc. degree in Physics as a main subject in 2006 and M. Sc. degree in Physics in 2008 from C S J M University, Kanpur, U. P., India. He qualified national level tests, CSIR-UGC NET and GATE. He joined Indian Institute of Technology Guwahati in 2010 for the award of Ph.D degree. He was awarded Junior and Senior Research Felloships by MHRD, India.